THE APPLICATION OF NETWORK MODELLING TECHNIQUES TO STEADY- AND UNSTEADY-STATE MULTIPHASE FLOW IN POROUS MEDIA

By

Steven Robert McDougall B.Sc.

Thesis submitted for the Degree of
Doctor of Philosophy

Department of Petroleum Engineering
Heriot-Watt University
Edinburgh

April 1994

To Hilary

CONTENTS

LIST OF FIGURES AND TABLES i

ACKNOWLEDGEMENTS ix

ABSTRACT x

INTRODUCTION 1
Background 1
Objectives 2
Thesis Content 3

CHAPTER 1 THE NATURE OF POROUS MATERIALS 7
1.1 Introduction 7
1.2 Macroscopic Parameters 8
1.2.1 Porosity 8
1.2.2 Permeability 10
1.3 Microscopic Pore Structure 12
1.3.1 Stereology 12
1.3.2 Pore Size Distributions 13
1.3.3 Co-ordination Number 14
1.4 Porous Media of Geological Origin 14
1.5 Fluid/Solid Interactions 16
1.5.1 Surface and Interfacial Tension 16
1.5.2 Adhesion and Cohesion 17
1.5.3 Wettability and Contact angle 18
1.5.4 Spreading Phenomena 19
1.5.5 Capillarity 20

CHAPTER 2 FLUID-FLOW ANALOGUES AND NETWORK MODELLING TECHNIQUES 22
2.1 Introduction 22
2.2 Conduit Models 22
2.3 Probabilistic Models 26
2.4 Empirical Models 27
2.5 Network Modelling 28
2.5.1 Previous Studies 28
2.5.2 The Basic Model 31

CHAPTER 3 SINGLE-PHASE FLOW 35
3.1 A New Predictive Model For Network Permeability. 35
3.2 Effective Medium Theory (EMT) 39
3.3 Percolation Theory 43
3.4 Comparisons Between The Extended Mean Radius Model, Effective Medium Theory And Percolation Theory. 49

CHAPTER 4 TWO-PHASE FLOW IN STRONGLY WATER-WET SYSTEMS 50
4.1 Introduction 50
4.2 Steady- and Unsteady-State Flow 50
4.3 The Relative Permeability Concept 51
4.4 Laboratory Determination of Relative Permeability 52
4.4.1 Steady-State Methods 53
4.4.2 Unsteady-State Methods 54
4.4.3 Centrifuge Methods 56
4.5 The Effects of Flowrate, Viscosity Ratio, and Interfacial Tension. 56
4.6 Relative Permeability Models 57
4.6.1 Capillary Models 58
4.6.2 Statistical Models 58
4.6.3 Empirical Models 59
4.7 Percolation Theory and Critical Exponents. 60
4.8 Saturation Predictions From Network Models. 63
4.9 Capillary Network Analogue of Two-Phase Flow. 66
4.9.1 Simulation Of Primary Processes 67
4.9.2 Secondary Displacement Processes 73

CHAPTER 5 TWO-PHASE FLOW IN MIXED-WET AND FRACTIONALLY-WET SYSTEMS 76
5.1 Introduction 77
5.2 Measurement Of Rock Wettability 80
5.2.1 The Amott Test 80
5.2.2 USBM Wettability Index 82
5.2.3 Imbibition Method 83
5.2.4 The Measurement Of Heterogeneous Wettability 83
5.3 Simulation Model And Topological Considerations 84
5.3.1 Model Set-Up And Implementation 84
5.3.2 Cluster Behaviour And Phase Trapping in Systems of Non-Uniform Wettability. 87
5.4 Simulation Of Capillary Pressure Curves 88
5.4.1 Capillary Pressure Curves From Strongly Wetted Systems 88
5.4.2 Waterflood Capillary Pressure Curves From Fractionally-Wet Systems 90
5.4.3 Waterflood Capillary Pressure Curves From Mixed-Wet Systems 92
5.5 Simulation Of Relative Permeability Curves 93
5.5.1 Fractionally-Wet Relative Permeabilities 94
5.5.2 Mixed-Wet Relative Permeabilities 95
5.6 Prediction Of Waterflood Performance 96
5.6.1 Displacement Efficiency In Fractionally-Wet Systems 96
5.6.2 Displacement Efficiency In Mixed-Wet Systems 98
5.7 A Proposed Method Of Wettability Measurement 98
5.7.1 Measurement Of Fractional Wettability 99
5.7.2 Measurement Of Mixed Wettability 100

CHAPTER 6 UNSTEADY-STATE FLOW AND VISCOUS/CAPILLARY COUPLING 101
6.1 Introduction 101
6.2 Unsteady-State Drainage Model 102
6.2.1 The Effect of Viscosity Ratio 106
6.2.2 The Effect of Flowrate 107
6.2.3 The Effect of Network Heterogeneity 108
6.3 Unsteady-State Imbibition Model 108
6.4 Unsteady-State Displacements in Finely Laminated Porous Media. 112
6.4.1 Geological Background 113
6.4.2 Simulation Details 116
6.4.3 Waterfloods in Water-Wet Systems 117
6.4.4 Waterfloods in Oil-Wet Systems 120
6.4.5 Recoveries in Water-wet and Oil-Wet Systems 122

CHAPTER 7 THREE-PHASE FLOW 124
7.1 Introduction 124
7.2 Current Difficulties Associated with Three-Phase Flow 125
7.2.1 Contradictory Experimental Results 126
7.3 Existing Analytical Models and Their Limitations 128
7.4 A Possible Solution Strategy: From Pore-Scale to Core-Scale. 131
7.5 Relevant Three-Phase Flow Physics 132
7.6 The Role of Network Modelling 134
7.7 The Effect of Connate Water and Spreading Co-efficient Upon Gas/Oil Capillary Pressure Measurements. 136
7.7.1 Introduction 136
7.7.2 Simulation Details 137
7.7.3 Results and Discussion 138
7.7.4 Comparisons with Published Data 139
7.8 Concluding Remarks on Three-Phase Flow 141

CHAPTER 8 CONCLUSIONS AND AREAS FOR FUTURE STUDY 142
8.1 Single Phase Flow 142
8.2 Two-Phase Flow in Strongly Water-Wet Systems 143
8.2.1 Primary Processes 143
8.2.2 Secondary Processes 145
8.3 Two-Phase Flow in Mixed-Wet and Fractionally-Wet Systems 145
8.4 Unsteady-State Flow and the Viscous/Capillary Force Balance 148
8.5 Three-Phase Flow 149
8.6 Practical Significance 150
8.7 Areas for Future Study 151

APPENDIX A PORE SHIELDING AND THE LIMITATIONS OF STANDARD MERCURY POROSIMETRY 152
Introduction 152
Laboratory Determination of Pore Size Distributions 152
Pore Shielding and the Accessibility Issue 153
Counter-Examples to the Standard Ritter and Drake Analysis 153
Network Simulations of Mercury Injection in Geological Media 157

APPENDIX B THE EXTENDED WASHBURN EQUATION AND ITS APPLICATION TO OIL/WATER DISPLACEMENTS 160

APPENDIX C SCALEUP AND THE VISCOUS/CAPILLARY FORCE BALANCE. 164

APPENDIX D RADIUS PROBABILITY DISTRIBUTION FUNCTIONS 167

APPENDIX E COMPUTATIONAL ALGORITHMS AND PROGRAMMING DETAILS 169
Introduction 169
The Model 170
Labelling of the Nodes 172
Labelling of the Bonds. 172
Sampling Radii from a Probability Distribution 174
Clusters and Clustering 176
Software and Hardware 180
Flow Diagrams of Programs 181

REFERENCES 182

LIST OF FIGURES AND TABLES

Figure 1.1 Darcy' s experiment. Water passes through a sand filter and the resultant pressure drop is measured in terms of hydraulic head.

Figure 1.2 Natural porous materials (x10): (a) beach sand, (b) sandstone, (c) limestone, (d) rye bread, (e) wood, (f) human lung (Collins, 1961).

Figure 1.3 (a) Serial sectioning, (b) branch-and-node representation of pore structure (Fischmeister, 1974).

Figure 1.4 The three "R"s: R_{cap} represents the pore entry radius, R_{vol} governs the pore volume, and R_{cond} relates to pore conductivity.

Figure 1.5 Schematic representation of co-ordination number (the number of pore elements that meet at a node).

Figure 1.6 Schematic of interfacial tension: attractive forces between liquid molecules at the surface and those in the interior exceed those of the competing air molecules. The result is a net inward pull leading to a contraction of the surface.

Figure 1.7 (a) The work of adhesion between two immiscible liquids equals the work required to separate unit area of the liquid-liquid interface, (b) the work of cohesion for a single liquid corresponds to the work required to pull apart a column of liquid of unit cross-sectional area.

Figure 1.8 Force balance acting on a liquid drop in equilibrium.

Figure 1.9 Dependency of the contact angle upon fluid pair and surface material (Benner and Bartell, 1941).

Figure 1.10 (a) A drop of non-spreading oil on a water surface, (b) a duplex film between air and water, (c) spreading of *n*-hexanol on water.

Figure 1.11 Capillary rise: water wets the bottom of the capillary, creating an upward component of interfacial tension which acts to draw fluid up.

Figure 2.1 Schematic representation of tortuosity.

Figure 2.2 Simple capillary bundle models: (a) straight capillaric model with all radii equal to the hydraulic radius, (b) radii sampled from a distribution, (c) serial type model (after Scheidegger, 1963)

Figure 2.3 Various network geometries (Koplik, 1982).

Figure 2.4 (a) Thin section of greywacke, (b) A small two-dimensional square lattice.

Figure 2.5 80x80 network simulation of capillary-dominated drainage: the overall picture is somewhat more convincing.

Figure 2.6 Three-dimensional $N_x x N_y x N_z$ network schematic. In practice, each element has a radius sampled from a distribution function.

Figure 2.7 Comparison of imbibition relative permeabilities (with and without trapping) using different-sized networks: (a) 5x5x5, (b) 10x10x10, (c) 15x15x15, (d) 20x20x20.

Figure 3.1 Log-log plot of total flowrate (Q) vs fluid viscosity for a 20x10x10 network.

Figure 3.2 Log-log plot of total flowrate (Q) vs pressure drop for a 20x10x10 network.

Figure 3.3 (a) Log-log plot of total flowrate vs cross-sectional area for a variety of network sizes, (b) flowrate vs network length.

Figure 3.4 Log-log plot of total flowrate vs mean radius: radii sampled from Uniform distributions.

Figure 3.5 Log-log plot of total flowrate vs mean radius: radii sampled from Cubic distributions.

Figure 3.6 Log-log plot of total flowrate vs mean radius: radii sampled from Log-Uniform distributions.

Figure 3.7 Log-log plot of total flowrate vs mean radius: radii sampled from Exponential distributions.

Figure 3.8 Log-log plot of total flowrate vs mean radius: radii sampled from Truncated Normal distributions with varying r_{bar}.

Figure 3.9 Log-log plot of total flowrate vs mean radius: radii sampled from Truncated Normal distributions with varying σ

Figure 3.10 Log-log plot of total flowrate vs mean radius: radii sampled from Triangular distributions.

Figure 3.11 Log-log plot of network permeability (k) vs $\langle r^2 \rangle^2$ for a variety of different pore-size distribution functions.

Figure 3.12 Log-log plot of network permeability (k) vs $\langle r^4 \rangle$ for a variety of different pore-size distribution functions.

Figure 3.13 Log-log plot of network permeability (k) vs median radius for a variety of different pore-size distribution functions.

Figure 3.14 Comparison of Equation (3.4) (solid line) with network simulation results for various distribution functions.

Figure 3.15 Effect of standard deviation (σ) upon network permeability for Uniform radius distributions.

Figure 3.16 Log-log plot of effective medium conductivity (g_m) vs mean radius for a Cubic radius distribution.

Figure 3.17 Log-log plot of effective medium conductivity (g_m) vs mean radius for a Log-Uniform radius distribution.

Figure 3.18 A pure percolation process on a regular square lattice. Yellow bonds are open, blue bonds are closed, red bonds belong to the spanning cluster: (a) p=0.04, (b) p=0.15, (c) p=0.255, (d) p=0.31, (e) p=0.49, (p=fraction of open bonds).

Figure 3.19 Schematic showing how flow must pass through bottleneck pores of radius R_p once a spanning cluster has formed.

Figure 3.20 Log-log plot of total flowrate vs percolation radius (R_p) for a Cubic radius distribution.

Figure 3.21 Log-log plot of total flowrate vs percolation radius (R_p) for a Uniform radius distribution.

Figure 3.22 Bimodal Uniform radius distribution. By fixing (B) and varying (A), the mean radius changes whilst the percolation radius remains fixed.

Figure 3.23 Log-log plot of total network flowrate vs mean radius: radii sampled from the distribution used by Berman et al.

Figure 4.1 Typical experimental imbibition relative permeability curves (Richardson et al, 1955).

Figure 4.2 Typical experimental drainage relative permeability curves (Corey and Rathjens, 1956).

Figure 4.3 Penn-State relative permeability apparatus showing the typical three core assembly (Geffen et al, 1951).

Figure 4.4 Hassler-type relative permeability apparatus (Hassler, 1944).

Figure 4.5 The effect of viscosity ratio (M) upon relative permeability (Odeh, 1959).

Figure 4.6 The effect of low interfacial tensions upon gas/oil relative permeability (Bardon and Longeron, 1978).

Figure 4.7 Number of clusters containing invaded fluid as a function of the invaded bond fraction.

Figure 4.8 Pure bond percolation process on a regular cubic network. The fraction of invaded (yellow) pores is denoted by p: (a) p=0.07, (b) p=0.13, (c) p=0.256 (the red spanning cluster is connected because of periodic boundary conditons), (d) p=0.256 (invading phase only). Note the dendritic structure of the invaded clusters. (e) p=0.3, (f) p=0.3 (invading phase only). Already, most of the invaded pores belong to the spanning cluster.

Figure 4.9 Plot showing fraction of bonds in spanning cluster vs ($p-p_c$) for a 20x10x10 network.

Figure 4.10 Number of clusters of size s vs s for a 20x10x10 network (the dotted line is the theoretical scaling).

Figure 4.11 Plots of p(R), $S_w(R)$ and $S_w(p)$ for (a) Uniform distribution, (b) Cubic distribution.

Figure 4.12 Saturation of the isolated and spanning clusters as a function of the total saturation for bottom-up filling.

Figure 4.13 Rayleigh distribution with $R_{min}=0$, $R_{max}=100$ and $\beta=1250$.

Figure 4.14 Schematic representation of spontaneous imbibition

Figure 4.15 Simulated imbibition relative permeability curves using a Rayleigh radius distribution.

Figure 4.16 Schematic of capillary-dominated drainage: numbers refer to pore radii; 13 largest, 1 smallest.

Figure 4.17 Simulated drainage relative permeability curves using a Rayleigh radius distribution.

Figure 4.18 Clustering behaviour of both water and oil during a low-rate imbibition simulation.

Figure 4.19 Trapping behaviour during a low-rate imbibition simulation (trapped pores contain oil).

Figure 4.20 Comparison between imbibition relative permeability curves with and without trapping of the nonwetting phase.

Figure 4.21 Schematic showing the "current bounding radius" concept: (a) imbibition, (b) drainage.

Figure 4.22 R-plots for imbibition with and without trapping: (a) p(R), (b) $S_w(R)$, (c) $k_{ro}(R)$ and $k_{rw}(R)$.

Figure 4.23 Experimental primary drainage — secondary imbibition relative permeabilities for a consolidated rock (Geffen et al, 1951).

Figure 4.24 Network simulation of the primary drainage — secondary imbibition cycle. Note the hysteresis effect in the nonwetting curves.

Figure 4.25 R-plots for primary drainage followed by secondary imbibition: (a) p(R), (b) $S_w(R)$, (c) $k_{ro}(R)$ and $k_{rw}(R)$.

Figure 4.26 $S_w(R)$ plots for primary drainage followed by secondary imbibition, with and without trapping of the nonwetting phase.

Figure 5.1 Distribution of oil-wet pores in a mixed-wet porous medium.

Figure 5.2 Distribution of oil-wet pores in a fractionally-wet porous medium.

Figure 5.3 The USBM wettability measurement technique (after Donaldson et al, 1969) — see text for details.

Figure 5.4 Waterflood capillary pressure simulations: (a) 100% water-wet network (imbibition), (b) 100% oil-wet network (drainage).

Figure 5.5 Waterflood capillary pressure curves for a variety of fractionally-wet networks: (a) α=0, (b) α=0.35, (c) α=0.5, (d) α=0.65, (e) α=1.0.

Figure 5.6 Pore filling sequences for waterfloods of fractionally-wet networks: (a) α=0, (b) α=0.35, (c) α=0.5, (d) α=0.65, (e) α=1.0.

Figure 5.7 For all $\alpha<\alpha^*$, the amount of water spontaneously imbibed by a fractionally-wet network will exceed that imbibed by a 100% water-wet network. The value of α^* is such that the volume weighted integrals corresponding to A_1 and A_2 are equal.

Figure 5.8 Effect of fractional wettability on capillary pressure curves derived experimentally from sandpack floods (after Fatt and Klikoff, 1959).

Figure 5.9 Waterflood capillary pressure curves for a variety of mixed-wet networks: (a) α=0, (b) α=0.25, (c) α=0.35, (d) α=0.5, (e) α=0.75, (f) α=1.0.

Figure 5.10 Pore filling sequences for waterfloods of mixed-wet networks: (a) α=0, (b) α=0.25, (c) α=0.35, (d) α=0.5, (e) α=0.75, (f) α=1.0.

Figure 5.11 Waterflood relative permeability curves for a range of fractionally-wet conditions: (a) α=0 -> α=1 envelope, (b) full range.

Figure 5.12 (a) Relative permeabilities from waterflood experiments on uniformly-wet Torpedo sandstone (after Owens and Archer, 1971). Measurements are based upon the effective oil permeability at S_{wi}, (b) Semi-log plot of simulated curves.

Figure 5.13 Waterflood relative permeability curves for a range of mixed wettability conditions: (a) α=0 -> α=1 envelope, (b) full range.

Figure 5.14 Recovery efficiencies for fractionally-wet networks, calculated via Buckley-Leverett analyses of the associated relative permeability curves.

Figure 5.15 Schematic calculation of average water saturation at breakthrough (S_{wf}) using the Welge tangent technique (Welge, 1952).

Figure 5.16 Recovery efficiencies for mixed-wet networks, calculated via Buckley-Leverett analyses of the associated relative permeability curves.

Figure 5.17 Experimental results (after Jadhunandan and Morrow, 1991) showing waterflood recovery efficiency vs wettability index.

Figure 5.18 Plots of (a) R-k_{ro} and (b) R-k_{rw}, from waterfloods of fractionally-wet networks.

Figure 5.19 Plots of (a) R-k_{ro} and (b) R-k_{rw}, from waterfloods of mixed-wet networks.

Figure 6.1 Schematic of a low-rate oilflood of a water-wet matrix. The nonwetting phase invades successively narrower pores.

Figure 6.2 Modification to the entry pressure requirements during unsteady-state drainage displacements.

Figure 6.3 Two-dimensional distorted network. Each node is displaced from (x, y) to a new position ($x+\varepsilon_x$, $y+\varepsilon_y$), where the ε_i are random numbers.

Figure 6.4 Drainage simulations on a 40x40 distorted network, showing the effect of viscosity ratio (κ) upon residual saturation and displacement efficiency. The sequence of displacement is white-yellow-orange-red, the trapped phase is black. Radii are chosen randomly from (0,100) and capillary effects are negligible. (a) κ=0.01, (b) κ=0.1, (c) κ=1.0, (d) κ=10, (e) κ=100.

Figure 6.5 Drainage simulations on a 40x40 distorted network, showing the effect of capillary number (Ca) upon residual saturation and displacement efficiency. The sequence of displacement is white-yellow-orange-red, the trapped phase is black. Radii are chosen randomly from (0,100). (a) Ca=1.0, (b) Ca=0.5, (c) Ca=0.35, (d) Ca=0.25.

Figure 6.6 Drainage simulations on a 40x40 distorted network, showing the effect of network heterogeneity upon residual saturation and displacement efficiency. The sequence of displacement is white-yellow-orange-red, the trapped phase is black. Radii are now chosen from (40,60). (a) κ=0.01, (b) κ=1.0, (c) κ=100.

Figure 6.7 Water of viscosity μ displaces air from a capillary tube of radius r. ΣP is the total effective pressure.

Figure 6.8 Two tubes of differing radius filling under viscous domination. The penetrated lengths satisfy the equation $x_1=(R_1/R_2)x_2$.

Figure 6.9 Two tubes of differing radius filling under capillary control. The penetrated lengths now satisfy the equation $x_1=(R_1/R_2)^{1/2}\ x_2$.

Figure 6.10 Typical pore element used for imbibition simulations. Two sets of roughness capillaries are used to explicitly model film-flow along surface irregularities.

Figure 6.11 Network simulations of waterfloods in homogeneous water-wet media using the Washburn approximation: (a) capillary-dominated, (b) viscous/capillary regime, (c) viscous-dominated.

Figure 6.12 The scale-dependency of the viscous/capillary force balance — from the pore-scale to the reservoir-scale.

Figure 6.13 The six heterogeneous systems used in this study: each contains an orientated layer of contrasting permeability.

Figure 6.14 Network simulations of waterfloods in homogeneous water-wet media using the extended Washburn equation: (a) capillary-dominated flow(scattered capillary fringe), (b) viscous/capillary coupling (frontal advance together with a narrow capillary fringe), (c) viscous-dominated flow (frontal advance).

Figure 6.15 Waterflood simulations in heterogeneous water-wet systems containing orientated layers of low permeability. Viscous forces increase vertically downwards: (a)-(c) low permeability horizontal, (d)-(f) low permeability vertical, (g)-(i) low permeability diagonal.

Figure 6.16 Waterflood simulations in heterogeneous water-wet systems containing orientated layers of high permeability. Viscous forces increase vertically downwards: (a)-(c) high permeability horizontal, (d)-(f) high permeability vertical, (g)-(i) high permeability diagonal.

Figure 6.17 Schematic showing the difference in viscous pressure gradients across layered systems. Darcy's law shows that pressure gradients will be greatest across low permeability layers.

Figure 6.18 Viscous-dominated waterflood of a water-wet system containing a vertical layer of low permeability. The permeability contrast between layers is approximately 100:1.

Figure 6.19 Network simulations of waterfloods in homogeneous oil-wet media: (a) capillary-dominated flow (capillary fingering), (b) viscous/capillary coupling, (c) viscous-dominated flow.

Figure 6.20 Waterflood simulations in heterogeneous oil-wet systems containing orientated layers of low permeability. Viscous forces increase vertically downwards: (a)-(c) low permeability horizontal, (d)-(f) low permeability vertical, (g)-(i) low permeability diagonal.

Figure 6.21 Waterflood simulations in heterogeneous oil-wet systems containing orientated layers of high permeability. Viscous forces increase vertically downwards: (a)-(c) high permeability horizontal, (d)-(f) high permeability vertical, (g)-(i) high permeability diagonal.

Figure 6.22 Plots showing recovery as a function of the viscous/capillary force balance: (a) systems containing low permeability heterogeneities, (b) systems containing high permeability heterogeneities

Figure 6.23 Network calculations can best be used for obtaining small-scale capillary-dominated flow parameters. These can then be used as input data for "geopseudo" scale-up studies.

Figure 7.1 A collection of water isoperms from the current literature.

Figure 7.2 A collection of gas isoperms from the current literature.

Figure 7.3 A collection of oil isoperms from the current literature.

Figure 7.4 Fluid hierarchies at the pore-scale: (a) positive spreading coefficient, (b) negative spreading coefficient.

Figure 7.5 (a) Various co-ordination numbers, (b) different pore geometries (cylindrical, biconical, general).

Figure 7.6 Schematic showing how oil films can improve displacement efficiency in a positive spreading system.

Figure 7.7 Series of network simulations of external gas drive with S>0 (blue-water, red-oil, green-gas): (a) primary oil-water drainage, (b) external gas drive up to breakthrough, (c) end of gas drainage (red oil clusters remain trapped).

Figure 7.8 Series of network simulations of external gas drive with S<0 (blue-water, red-oil, green-gas): (a) primary oil-water drainage, (b) external gas drive up to breakthrough, (c) end of gas drainage (large number of red oil clusters remain trapped).

Figure 7.9 Simulated capillary pressure curves for a variety of co-ordination numbers, showing the effects of connate water and spreading coefficient **(cylindrical pore geometry)**: (a) z=6, (b) z=4, (c) z=2.8.

Figure 7.10 Simulated capillary pressure curves for a variety of co-ordination numbers, showing the effects of connate water and spreading coefficient **(biconical pore geometry)**: (a) z=6, (b) z=4, (c) z=2.8.

Figure 7.11 Effect of z upon gas/oil capillary pressure curves (S_{wi}=0): (a) cylindrical pore geometry, (b) biconical pore geometry.

Figure 7.12 Experimental data of Dumoré and Schols (1974) showing the effects of connate water and spreading coefficient upon gas/oil capillary pressure curves. Bentheim cores and kerosene/Ondina17/water/air used.

Figure 7.13 Capillary pressure data from Longeron et al (1993). Clashach cores and *n*-heptane/methane mixtures used.

Figure 7.14 Capillary pressure data from Kalaydjian and Tixier (1991) using unconsolidated sandpacks.

Figure A1 Schematic of penetrometer used in mercury injection experiments.

Figure A2 Pore network consisting of tubes of different radii (numbers refer to relative sizes).

Figure A3 Mercury injection into the pore network.

Figure A4 (a) Uniform pore size distribution, (b) mercury intrusion schematic as P_c increases.

Figure A5 Illustration of the meaning of the Accessibility function, A(r), during the injection process.

Figure A6 The predicted S_{Hg} vs P_c relationship for a Uniform pore size distribution.

Figure A7 The three classes of heterogeneity considered in this study.

Figure A8 Simulated mercury intrusion curves for the laminated model. Each curve corresponds to a different ratio of low permeability to high permeability.

Figure A9 Simulated mercury intrusion curves for the isolated clast model.

Figure A10 Simulated mercury intrusion curves for the truly bimodal model.

Figure B1 Comparison between the Washburn approximation and the full energy equation for two capillary tubes of radii r_1=100μm and r_2=10μm. x(cm) is the penetrated length.

Figure B2 Blown-up region of Figure B1. The Washburn equation still predicts wider tubes filling first, but the full energy equation predicts more complex behaviour.

Figure E1 Three-dimensional pore network of nodal dimensions $N_x x N_y x N_z$.

Figure E2 Illustration of how bonds and nodes are identified.

Figure E3 Labelling of the nodes.

Figure E4 Labelling of the bonds.

Figure E5 (a) Probability density function for the bond radii, (b) the cumulative probability distribution.

Figure E6 Example of cluster labelling.

Table 3.1 Average Errors Between Predicted And Calculated Permeabilities.

Table 3.2 Percolation Thresholds for a Variety of Lattice Geometries (after Stauffer and Aharony, 1992).

Table 3.3 Average Errors Between Calculated Permeabilities And Those Predicted By Percolation Theory.

Table 3.4 Error Comparison Of Eq. (3.7) With EMT And Percolation Theory.

Table 4.1 Various Ascribed Values for the Critical Conductivity Exponent.

Table 5.1 Craig's Rules Of Thumb.

Table 7.1 The Effect Of Contacting History Upon Micromodel Wettability.

Table 7.2 Possible Saturation Histories During Three-Phase Displacements.

Table 7.3 Chronological Listing Of Three-Phase Relative Permeability Experiments.

Table 7.4 Chronological Listing Of Three-Phase Relative Permeability Models.

ACKNOWLEDGEMENTS

The author would first and foremost like to express his heartfelt thanks to Professor Ken Sorbie for his guidance and support throughout the past three and a half years. His contagious enthusiasm and seemingly limitless patience has made him a pleasure to work with: I hope that this thesis can repay him in some part for the kindness he has shown.

Thanks are also due to my colleagues within the Department of Petroleum Engineering, who have always attempted to answer my questions politely and sympathetically — even when the constant barrage often appeared to be totally aimless. More specific thanks are due to Cliff Ogle for his photographic expertise (and unwelcome golfing tips), Dave Parker for his computer trouble-shooting skills, and Eric Mackay for his invaluable work in designing the graphics interface used throughout this work.

None of this research would have been carried out without the financial assistance of BP Exploration Ltd. and the Petroleum Science and Technology Institute of Great Britain: the author is extremely grateful for their generous support. Invaluable discussions with Drs. Gasem Bayatt, Alistair Fletcher, Mike King, Martin Blunt and Chris Brown are also gratefully acknowledged.

ABSTRACT

The main aim of the work presented in this thesis is the derivation of single-phase and multi-phase flow parameters, such as permeability, relative permeability and capillary pressure, from microscopic considerations using three-dimensional network modelling techniques. The purpose has not necessarily been to calculate these for a specific porous medium, but rather to predict the factors that control them at the pore-scale. That is to say, quantitative predictions have been replaced by a variety of sensitivity studies.

A new predictive model for single-phase permeability is reported first, and is shown to form an important link between effective medium models and those derived from percolation theory. Some new analysis demonstrates that all three approaches are actually equivalent. Percolation concepts are more fully utilised in the modelling of immiscible two-phase flow, where both imbibition and drainage simulators are developed with the aim of broadening the understanding of the simultaneous flow of water and oil through reservoir rock. The network models are next extended to facilitate the study of flow through systems of heterogeneous wettability; i.e. water-wet networks which contain a fraction of pores that are preferentially oil-wet. Results demonstrate how the oil-wet pore fraction affects the associated relative permeability and capillary pressure curves. Furthermore, a novel test is proposed which could be used to determine the wettability of both frationally-wet and mixed-wet porous media.

Further development focusses upon augmenting the earlier steady-state models to deal with unsteady-state dynamics: some simulated unsteady-state waterfloods of finely laminated water-wet and oil-wet systems are presented, which clearly demonstrate the complex interaction between viscous and capillary forces and the underlying lamination structure of the porous medium. The work presented here has ultimately resulted in a simulator capable of interpreting a wide range of two- and three-phase laboratory displacements.

INTRODUCTION

Background

There is a saying in the oil industry that "oil is where you find it" — ruefully reflecting the fact that so often, and increasingly, it has to be extracted from some of the most inaccessible places on earth. Petroleum has been used for many centuries, primarily for heating and lighting, but it is only during this century that its influence upon global economics has become so profound. Indeed, the outstanding versatility of crude oil as a base manufacturing material should ensure its continued economic importance well into the next millennium.

Although hydrocarbon accumulations have been exploited all over the world and at a variety of depths beneath both land and sea, it is a painful fact that conventional recovery methods are not very effective. Figures relating to the beginning of 1984, for example, show that a staggering 68% of proven reserves were thought to be unrecoverable with present technology. The ever-increasing demand for hydrocarbons, coupled with the recognition that such materials constitute a finite resource, has consequently led to greater emphasis being placed upon the fundamental flow physics governing hydrocarbon production. Such fundamental issues are addressed in this thesis.

Petroleum (Gr. *petra*, rock, L. *oleum*, oil) is the general term used to describe all natural hydrocarbons, although in common usage it refers particularly to the liquid oils. As its etymology suggests, petroleum is usually found trapped within the interstices of a rock, into which it migrated from source rocks over a period of millions of years. Consequently, any attempt to understand the subsequent production from an oil well necessarily requires some knowledge of flow phenomena in porous media. More specifically, a clear understanding of fluid/solid interactions at the pore-scale is essential if accurate predictions

are to be made at the macroscopic level. The study of rock properties and how these relate to the fluids they hold in both static and flowing states is referred to as *petro-physics*, and the work described here attempts to investigate the sensitivity of a variety of multiphase displacements to some of the more important petrophysical parameters using pore-scale models.

Objectives

A long-standing issue concerning fluid flow in a porous medium is the calculation of transport coefficients in terms of associated pore-scale parameters. The pore structure of a real porous medium is usually so complex, however, that the explicit modelling of flow processes through it has posed a colossal problem to physicists and engineers alike. Consequently, this has remained one of the most intractable problems in statistical physics. The main objective of the work reported here has been to derive single-phase and multiphase flow properties, such as permeability, relative permeabilities and capillary pressures, from microscopic considerations using three-dimensional network modelling techniques. The purpose is not to calculate the parameters for a specific rock, but rather to predict what effectively controls them at the pore-scale. That is to say, quantitative predictions are replaced by a variety of *sensitivity* studies. This approach ties in rather well with current thinking in the petroleum industry: throughout reservoir description studies, there is always a degree of uncertainty associated with petrophysical input data, and so a *range* of production profiles is generally considered before any action is taken. By varying pore-scale parameters in the network model, such uncertainties can be analysed more effectively and related experimental data can also be better interpreted. Results from network simulations carried out as part of this thesis have also introduced new methods of data analysis, which serve to give greater insight into the pore-scale processes themselves.

Thesis Content

This thesis sets out to examine a variety of fundamental phenomena relating to immiscible flow in porous media, and reports upon the development and implementation of a pore-scale simulator capable of modelling them. Chapters 1 and 2 provide relevant background knowledge, whilst detailed simulation studies are presented in Chapters 3 to 7.

Chapter 1 gives a broad overview of the nature of porous materials and aims to describe a variety of fundamental concepts which relate to both pore structure and solid/fluid interactions. Material parameters discussed include porosity, permeability and pore size distribution, whilst descriptions of wettability and capillarity are used to give some insight into how fluid and solid interact. Consideration of such issues affords better understanding of many pore-scale processes and is essential if worthwhile progress is to be made later.

A discussion of fluid flow analogues is presented in Chapter 2: these include conduit, probabilistic and empirical models. The numerous refinements made to Fatt's (1956) early network models are also reviewed, and it is subsequently demonstrated how such studies have led to a vast improvement in the understanding of a great many diverse flow problems. The final section of the chapter describes the theory underlying the basic network model used in this work; additional features are added later and are explained in the relevant chapters.

A new predictive model for single-phase permeability is reported in Chapter 3. This is shown to form an important link between effective medium models and those derived from percolation theory, and some new analysis is presented which demonstrates that all three approaches are actually equivalent. The new model developed here is found to give the most accurate results.

In Chapter 4, the network modelling approach is used for the development of *two*-phase flow models, which attempt to capture some of the more interesting associated phenomena. The aim is to broaden the understanding of two-phase flow in porous media; more specifically, to the simultaneous flow of oil and water through reservoir rock. To this end, concepts from percolation theory are utilised more fully. The physical porous medium is once again simulated using a capillary network, but now each element may contain a different fluid: either water or oil. After briefly reviewing the relative permeability concept and its laboratory determination, attention is first focussed upon the simulation of steady-state primary displacement processes (both imbibition and drainage). The objective is to elucidate how factors such as phase trapping and film-flow affect microscopic two-phase flow processes and, in particular, the influence these may have upon the resulting relative permeability curves and residual saturations. Following this, some secondary processes are examined and simulation results are seen to successfully capture the well-documented hysteresis effect found between primary drainage and secondary imbibition relative permeability curves. It is also shown that this phenomenon can be explained simply in terms of the wettability assumptions made at the beginning of the simulation. Results demonstrate that the accepted way in which relative permeability curves are constructed and presented tends to disguise the underlying dynamics of the process under investigation. Related issues concerning accessibility and pore shielding are dealt with separately in Appendix A, where standard Ritter and Drake porosimeter analysis is shown to be fatally flawed.

Chapter 5 describes how the network model can be further extended to facilitate the study of flow through systems of heterogeneous wettability; i.e. water-wet networks which contain a fraction of pores which are preferentially oil-wet. By explicitly incorporating pore wettability effects into a steady-state model, it has been possible to explain many experimental observations from a

microscopic stand-point. Results are presented which show how α (the fraction of pores which are assigned oil-wet characteristics) affects resulting capillary pressure and relative permeability curves. Simulated capillary pressure data demonstrate that standard wettability tests (such as Amott-Harvey and free imbibition) may give spurious results when the sample is fractionally-wet in nature. The corresponding relative permeability curves have been used to calculate waterflood displacement efficiencies for a range of wettability conditions, and recovery is shown to be maximum at close to neutral conditions. Furthermore, a novel test is proposed which could be used to determine the wettability of both fractionally-wet *and* mixed-wet porous media. To date, no such satisfactory test exists.

The theoretical development of Chapter 6 focuses on extending the earlier steady-state models to deal with *u n*steady-state dynamics, ultimately producing a simulator capable of interpreting a wide variety of two- and three-phase laboratory displacements. Both unsteady-state drainage *and* imbibition models are considered. For the imbibition case, some new physics is presented which shows up the inadequacy of the Washburn equation at the micro-scale. Once the pore-level physics have been examined and extended, attention is turned towards sensitivity analyses relating to a variety of flow parameters, including; viscosity ratio, flowrate, and pore-scale heterogeneity. One area of great interest to the petroleum industry is the impact of geological structure upon recovery efficiency. Consequently, some unsteady-state waterflood displacements in finely laminated water-wet and oil-wet systems are considered next. Results clearly show how capillary and viscous forces interact in an extremely complex manner with the lamination structure of the porous medium. Sensitivities of the laminar oil capillary trapping mechanisms to factors such as the capillary/viscous force balance, lamina orientation and wettability are reported. The importance of scaling these effects in light of the underlying geological structure is also discussed.

Chapter 7 sets out to describe the current confusion surrounding a variety of three-phase flow phenomena and suggests a possible way forward towards greater understanding of three-phase flow generally. By focussing attention upon the relevant microscopic flow physics, it provides a cogent explanation as to why so much experimental work is inconsistent and contradictory. The first part of this chapter begins by examining previous experimental work and looks at the chronological development of three-phase flow research as a whole. The existing analytical models are then discussed and their shortcomings highlighted. The next section explains the need for an integrated research programme which builds upon our existing knowledge in a systematic way — from the pore-scale to the core-scale. The case for network modelling studies is also discussed. This is followed by some simulation results, which have been used to examine the role played by connate water and the spreading coefficient during three-phase displacements.

The final chapter of this thesis, Chapter 8, discusses the main findings of the investigation, and outlines their practical significance. Some areas for future study are also proposed.

CHAPTER 1 THE NATURE OF POROUS MATERIALS

1.1 Introduction

The notion of a "porous medium" immediately conjures up an intuitive picture: put in its crudest terms, a porous medium may be thought of as a solid with holes in it. Unfortunately, such a superficial definition is of little use when trying to describe such materials objectively, and a more precise formulation must be attempted. A cylindrical pipe, for example, would not generally be considered a porous medium, nor would a solid containing *isolated* holes. There is a tacit understanding that "real" porous media should be capable of sustaining fluid transport, implying a certain degree of interconnectedness within the underlying pore structure. In short, a truly porous material should have a specific permeability associated with it.

There are countless examples of porous materials in everyday life, each with its own particular pore structure and transport potential. These range from leather, wood, paper and textiles, to bricks, concrete and sand; even animal tissue and bones contain intricate pore networks. The need to understand such a vast array of permeable materials has consequently fostered a great deal of scientific interest from many diverse fields: soil mechanics, groundwater hydrology, industrial filtration, and petroleum engineering, to name but a few. Although the theme of fluid flow through porous media is a common feature of all of the disciplines listed above, each has its own technical terminology associated with the subject. For example, "dewetting", "desaturation" and "drainage" are all terms synonymous with the displacement of a wetting phase from the interstices of a porous material by a nonwetting phase. Throughout this thesis, however, the terminology used will be that generally encountered in the petroleum industry.

The aim of this chapter is to describe a variety of fundamental concepts which relate to both pore structure and solid/fluid interactions: consideration of these affords better understanding of a great many pore-scale processes

1.2 Macroscopic Parameters

As its name suggests, a macroscopic parameter is one which is used to describe a property of a porous medium which has been averaged over a continuum of porespace. This continuum is generally defined using the *representative elementary volume* concept, which sets out to define a locally homogeneous volume large enough to allow statistical averaging. The two parameters of most interest to the petroleum industry are *porosity* and *permeability*.

1.2.1 Porosity

Porosity (ϕ) is defined as the fraction of void space per unit volume of bulk material, i.e.

$$\phi = \frac{V_{void}}{V_{bulk}} \tag{1.1}$$

Values are often given in terms of percentages. Porosities can vary from close to zero in one extreme (as in metals and some igneous rocks), to almost one in the other (e.g. fibreglass). In the context of petroleum engineering, porosities of sandstones typically fall into the range 0.1 - 0.3, whilst limestone porosities are somewhat lower, typically 0.04 - 0.1 (Scheidegger, 1963). Note that porosity, in the general sense, refers to the *total* void fraction within a sample. In many instances, however, this may include isolated or dead-end porespace — porespace that plays little or no role during fluid flow. The term *effective porosity* has consequently been introduced to describe the fraction of interconnected void space which contributes to flow.

There are a variety of measurement techniques available for porosity determination, the most common of which are will now be described.

(1) Direct Method — The bulk volume is first measured and then the porous sample in compacted so as to destroy the internal voids. The resulting volume is therefore that corresponding to the solid matrix and the void volume can then be inferred.

(2) Optical Methods — The areal porosity of a polished section is calculated using stochastic analysis and the result applied to the three-dimensional sample.

(3) Imbibition Method — The porous sample is immersed in a wetting fluid under vacuum, until the entire pore volume has been invaded via spontaneous imbibition. This imbibed volume can be calculated by weighing the sample before and after imbibition. The bulk volume can be measured by immersing the filled sample in the same wetting fluid. Porosity is found as the ratio of these two measurements.

(4) Mercury Injection — Pore volume is found by injecting mercury into the sample at high pressure, whilst the bulk volume can be found by volumetric displacement in the same fluid.

(5) Gas Expansion Method — The basic principle behind the gas expansion method is direct measurement of the volume of air contained within the porespace. This is achieved by connecting the chamber containing the sample (the chamber having known volume and known pressure) to an evacuated chamber. When the valve between the two is opened, the ideal gas law can be used to derive the *effective* pore volume. Bulk volume must be independently measured.

(6) Density Method — The fact that the mass of a porous sample (M) is actually the mass of the solid matrix alone, means that

$$M = \rho_s V_s = \rho_B V_B$$

where s refers to the solid, B to the bulk, and the ρ_i are densities. From the definition of porosity, it follows that:

$$\phi = \frac{(V_B - V_s)}{V_B} = 1 - \frac{\rho_B}{\rho_s} \tag{1.2}$$

The best method to use for porosity measurements depends upon the material under investigation, although mercury injection and gas expansion methods tend to be the petroleum industry standards.

1.2.2 Permeability

The permeability of a porous medium relates to its potential for conducting fluid. If a sample is highly permeable, then fluid flows through it easily; if it is impermeable, no fluid transport occurs at all. This rather vague definition can be made more precise with reference to an early experiment carried out in 1856 by Henri Darcy (Figure 1.1). Darcy experimented with sand filters in the context of public water supply to the town of Dijon in France, and by varying a variety of flow conditions he derived the following relationship:

$$Q = \frac{-KA(h_2 - h_1)}{h} \tag{1.3}$$

where Q is the total volume flux and K is a "permeability constant" which depends upon the properties of the porous medium *and the fluid*. Equation (1.3) is what should properly be referred to as Darcy's Law, but this can be restated more conventionally as:

$$Q = \frac{-K' A(p_2 - p_1 + \rho g h)}{h} \tag{1.4}$$

where K' is a new permeability constant. It was found that this equation was still rather too vague, however; it said very little about the porous medium alone. It was not until the work of Nutting (1930), and later Wyckoff et al

(1933), that the situation was resolved. Given that the dimensions of the permeability constant are $M^{-1}L^3T$, it was proposed that the influences of fluid and matrix could be separated by rewriting K' as:

$$K' = \frac{k}{\mu} \tag{1.5}$$

where μ is the fluid viscosity and k is the "intrinsic permeability" of the material. There have been numerous verifications of this hypothesis, resulting in the consequent adoption of :

$$Q = -\frac{k}{\mu} A \frac{(p_2 - p_1 + \rho g h)}{h} \tag{1.6}$$

as the standard version of Darcy's Law. The unit associated with intrinsic permeability is the *Darcy* — a porous material has a permeability of 1 Darcy if a pressure difference of 1 atmosphere causes a fluid with viscosity equal to 1cP to flow at $1cm^3/s$ through a cube of material of dimensions 1cm x 1cm x 1cm. The dimensions of permeability are those of a length squared, with $1Darcy=0.987x10^{-12}m^2$.

Although k is assumed to be unique for a particular sample, it must be remembered that permeability values can sometimes be affected by the permeating fluid in more subtle ways. For example, clay deposits within a sandstone sample may swell up on contact with water, thereby reducing permeability. The same permeability measurement carried out using air would almost certainly give a different result (even after correction for the so-called gas "slip-effect" (Klinkenberg, 1941)).

Laboratory permeability measurements are usually performed using cylindrical core samples and inert fluids. In theory, one steady-state flow measurement should be enough to predict permeability using Darcy's Law, but in practice there is usually a degree of error associated with the determination of flowrate and pressure drop. It is more usual, therefore, for a range of experiments to be

undertaken at a variety of different flowrates, and a straight line fitted to the resulting Q vs ΔP plot. If a large number of permeability measurements are required in a very short space of time, a portable minipermeameter can be used (first introduced by Eijpe and Weber (1971)). Although requiring calibration, its rapid, non-destructive measuring capability is finding wide applicability, especially in the areas of core characterisation and geological outcrop studies.

1.3 Microscopic Pore Structure

1.3.1 Stereology

The preceding paragraphs dealt with statistically averaged quantities, such as porosity and permeability. This section focusses upon the actual pore structure itself and serves to underline the great difficulties involved in quantification at such a small scale. The photographs in Figure 1.2 clearly demonstrate the extreme irregularity of natural pore geometry, and so any concept of "pore radius" or "pore size" is necessarily a gross oversimplification. This has not prevented the majority of investigators from attempting to categorise porous media in just such a way, however.

Scanning electron microscopy (SEM) has enabled a wide variety of porous materials to be closely examined, yielding valuable information regarding the mineralogy and connectivity of two-dimensional sections. For modelling purposes, however, two-dimensional information is insufficient (as later chapters will demonstrate), and this has consequently led to the development of a number of techniques designed to reconstruct three-dimensional pore topology from two-dimensional data. Indeed, the only known methods of constructing three-dimensional models of natural porous samples rely entirely upon extrapolation from a collection of parallel "serial sections". Such stereological analyses include: the section diameter method (Chang and Dullien, 1976), the random point generating method (Yanuka et al, 1986), and autocorrelation techniques (Adler et al, 1990). These tasks are extremely

labour-intensive, however, and results largely depend upon the resolution of the original thin sections (a depth of about 10μm appears to be a lower limit (MacDonald et al, 1986)). A schematic of the process is illustrated in Figure 1.3.

1.3.2 Pore Size Distributions

Given the extreme complexity of pore structure, there seems little point in trying to impose conformity by attempting *quantitative* analysis using idealised pore geometries. Unfortunately, there appears to be no other option, and current mercury porosimetry techniques (described in more detail in Appendix A) still rely upon the simplistic assumption that porous media consist of bundles of circular capillary tubes. This is fine if only *qualitative sensitivities* are being examined (as in this work), but the extension to quantification must surely be a fallacious one.

A more profitable way forward may be to reject the notion of a pore size distribution altogether, and instead, consider a somewhat more abstract formulation. This is summarised in Figure 1.4 and will be referred to as the "3R's approach". Considering the process of oil displacing water from the pore element shown, it is clear that there are actually *three* associated pore "radii": one defines the capillary entry pressure (R_{cap}), another characterises the pore volume (R_{vol}), and a third governs the pore conductivity (R_{cond}). These may be related to one another (as is the case for cylindrical capillaries) or not. The only concern during the drainage process is that for each incremental increase in pressure, there is an associated incremental increase in nonwetting phase saturation, and a possible incremental increase in nonwetting phase conductivity (depending upon whether or not the invaded pore is a dead-end pore). The geometrical shape of the pore element itself is immaterial in such cases, as it is the consequent behaviour of the system that is really important. Recent work related to beadpack characterisation would support this more abstract approach (Bryant and Blunt, 1993).

1.3.3 Co-ordination Number

One measure of the interconnectedness of pore structure is the so-called co-ordination number (z): it is defined as the average number of branches meeting at a point (Figure 1.5). The co-ordination number plays an important role in determining such things as breakthrough and residual saturations during multiphase displacements, and is probably one of the most important parameters governing flow processes at the pore-scale. It is to be regretted that this fact appears to have been largely overlooked by the petroleum industry. Co-ordination numbers can vary greatly from system to system: from z=6 for a simple cubic sphere packing to $z \approx 2.8$ for Berea sandstone (Doyen, 1988; Dullien, 1979). This wide variation should clearly be taken into account when attempting to interpret flow behaviour.

1.4 Porous Media of Geological Origin

By far the most abundant porous materials on earth are geological in nature, with the high-porosity/high-permeability facies being of particular interest to the oil industry. It is vital for the petroleum geologist to understand not only the underlying depositional environment of any given reservoir, but also the associated pore structures and macroscopic parameters of each constituent rock-type. Some details are now presented.

For the purposes of this brief overview, geological materials can be *broadly* broken down into four main groups (as proposed by Dullien): dense rocks, volcanic rocks, indurated sedimentary rocks (those hardened by high temperature/high pressure/cementation), and non-indurated sediments.

(1) Dense Rocks — Examples are granite, dolerite, and gabbro. Porosities are generally less than about 2% and permeabilities less than 10mD. Although

dense rocks make up a large proportion of the earth's crust, they are of little interest to the oil industry because they have no inherent reservoir potential.

(2) Volcanic Rocks — Igneous intrusions and surface lava flows constitute a large proportion of these rocks. Solidified subsurface dykes and sills are dense and virtually impermeable; their presence in hydrocarbon reservoirs can cause great problems, acting as flow baffles during production. Conversely, if volcanic lava flows reach the surface, they may cool to form highly permeable aquifers.

(3) Indurated Sedimentary Rocks — The inherent economic viability of these rocks (or rather their contents) make them the most studied rocks of all. They can be typically categorised as shales, sandstones, and carbonates; other groups make up only a very small percentage.

Shales constitute about 50% of all sedimentary structures, with porosities ranging from 2- 25% (depending upon the depth of burial). Permeabilities lie in the 0.01-1.0mD range, making them ideal reservoir seals.

Sandstones make up about 25% of indurated sediments, with quartz generally being the dominant mineral. They are usually much more permeable than shales but are prone to cementation by minerals such as calcite and silica, which reduces their reservoir potential considerably. Typical porosities are 10-25% but these figures reduce with depth; sandstone below about 10km may have less than 5% porosity, for example. An important feature of sandstones is their stratified structure (due to the quasiperiodic nature of their deposition). Consequently, permeability variations can be large and samples should usually be treated as anisotropic (permeability measured across layers is nearly always less than that measured along layers). Lamination may even be evident at the

millimetre scale, making predictive modelling an even more awesome prospect.

Carbonate rocks consist mainly of calcite and dolomite, often with small amounts of quartz and clay material. Young carbonate rocks, such as coral reefs and atolls, can have high porosities and permeabilities ($\phi \approx 20\text{-}50\%$, $k \approx 1000D$). Unfortunately, unfractured carbonate reservoir material is older and compacted, yielding reduced permeabilities in the millidarcy range. Larger values may result in cases where chemical leaching and/or fracturing processes have occurred, and highly fractured carbonate oil reservoirs are of great economic importance.

(4) Non-Indurated Sediments — Unconsolidated sands have high porosities (30-40%) and high permeabilities (1-100D). Their primary use is in laboratory tests, where they are used to examine the effects of grain size and grain packing upon porosity and permeability.

Having outlined a variety of different phenomena relating to pore structure, attention now turns to the equally important area of fluid/solid interaction. Such considerations not only impact upon the physical state of a system, but are also responsible for the diverse range of flow behaviour that can take place within it.

1.5 Fluid/Solid Interactions

1.5.1 Surface and Interfacial Tension

It is well-documented that the molecules of a liquid are closely bound together by forces of molecular attraction, which serve to keep it as one cohesive assemblage of particles. Although these forces of cohesion act to cancel one

another in the interior of the liquid, the situation is somewhat different at the surface: at an air/liquid interface the cohesive forces of the underlying liquid far exceed those of the competing air molecules, resulting in a net inward pull (Figure 1.6). The system then behaves as if the liquid and air were separated by a uniformly stretched membrane, characterised by a *surface tension* (σ). The surface tension of a liquid is more precisely defined as the work required to increase the area of a surface isothermally by a unit amount; commonly used units are dynes/cm or N/m.

If, instead of a liquid/air system, a liquid/liquid system is considered, the tensile force is referred to as *interfacial tension* and is one of the most important parameters governing multiphase flow in porous media. The interfacial tension of a two fluid system generally lies between the surface tensions of the individual components: for crude-oil/water systems, typical values are in the range 10-30mN/m (Donaldson et al, 1969).

1.5.2 Adhesion and Cohesion

In this section, the concepts of adhesion and cohesion will be examined in order to investigate the link between surface (and interfacial) tension and the related free surface energies of the system. The *work of adhesion* is defined as the work required to separate a unit area of liquid-liquid interface to form two liquid-air interfaces (Figure 1.7a). In doing this, it is found that there is a loss of surface free energy associated with the *interfacial* tension of the system, but an increase in surface free energy corresponding to the two *surface* tensions. If the two liquids are labelled A and B, then the work required for separation can be written as (Shaw, 1970):

$$W_{adh} = \sigma_A + \sigma_B - \sigma_{AB} \qquad (1.7)$$

where σ_A and σ_B are the surface tensions, and σ_{AB} the interfacial tension.

The *work of cohesion* for a single liquid (A) corresponds to the work per unit area required for separation (Figure 1.7b). Reference to Equation (1.7) shows that this can be expressed as:

$$W_{coh} = 2\sigma_A \tag{1.8}$$

One obtains a much clearer insight into the underlying physics governing many pore-scale flow processes when surface tension is treated as a surface free energy parameter. This will prove particularly useful when describing spreading phenomena later.

1.5.3 Wettability and Contact angle

If a solid surface is contacted by a pair of fluids, one of them will tend to have a greater affinity for that surface than the other. This phase is identified as the *wetting* phase, whilst the other is known as the *nonwetting* phase. The wetting preference of a flat solid surface can be quantified by inspecting the contact angle and the associated force balance (Figure 1.8). This is due to the fact that the magnitude of the contact angle at equilibrium is intrinsically linked to the free surface energies of the system via Young's equation:

$$\sigma_{S1} - \sigma_{S2} = \sigma_{12}\cos\theta \tag{1.9}$$

where σ_{S1} represents the solid/fluid 1 surface free energy, σ_{S2} the solid/fluid 2 surface free energy, and σ_{12} the fluid-fluid interfacial tension. The value of the contact angle may lie anywhere from 0° to 180°, and is strongly dependent upon the fluid pair and surface material involved (Figure 1.9). If θ=90°, then σ_{S1}=σ_{S2} and neither fluid is wetting; the system is then described as neutral.

1.5.4 Spreading Phenomena

Consideration of the trigonometric term in Young's equation shows that mechanical equilibrium between two fluids and a solid surface is only possible if:

$$\sigma_{S1} - \sigma_{S2} < \sigma_{12} \qquad (1.10)$$

i.e. $\cos\theta$ must always be <1. If this condition is violated, however, the system is unstable and the wetting phase will spontaneously *spread* on the solid. Although quantification of this "spreadability" in fluid/solid systems is not possible at present (there is no current technique available for measuring either σ_{S1} or σ_{S2}), this is not a problem if the solid is replaced by a third fluid or a gas.

For example, if a drop of insoluble oil is placed on a clean water surface, it will generally behave in one of three ways. It will either:

(1) Remain as a lens without spreading on the water substrate (Figure 1.10a).

(2) Spread as a thin layer until it forms a "duplex" film (i.e. a film thick enough to support both a water-oil and an oil-air interface, Figure 1.10b).

(3) Spread as a monolayer, supporting excess oil in the form of equilibrium lenses (Figure 1.10c).

Now, if the contact area of the oil drop in Figure 1.10a is increased by a small amount δA, then the total free surface energy of the system will change by an amount $(\sigma_{oa}+\sigma_{ow}-\sigma_{wa}).\delta A$. If this change is negative, then the oil must spontaneously spread on the water substrate if thermodynamic equilibrium is to be achieved. The spreadability of the oil can therefore be quantified with recourse to a *spreading co-efficient*, defined by:

$$S_o = \sigma_{wa} - (\sigma_{ow} + \sigma_{oa}) \tag{1.11}$$

and so initial spreading occurs if this coefficient is either zero or positive.

It is evident from the above discussion that the spreading characteristics of oil/water/gas systems must have serious implications for a wide range of hydrocarbon recovery processes: it seems strange, therefore, that very little research appears to have been done in this area. The effect of the spreading coefficient upon three-phase displacements will be dealt with more fully later in Chapter 7.

1.5.5 Capillarity

Capillarity is defined rather vaguely as: "A phenomenon associated with surface tension, which occurs in fine bore tubes or channels" (Chambers Science and Technology Dictionary, 1992). The concept can perhaps be more fully understood by means of a fundamental example.

Consider the situation where a liquid is in contact with a glass capillary tube. If the adhesive forces of the liquid to the glass are greater than the cohesive forces in the liquid, then the interface will curve upwards towards the tube, forming a meniscus which intersects the tube wall at an angle θ (Figure 1.11). The fact that the meniscus is curved, means that there is now a non-zero vertical component of surface tension, which acts to pull liquid up the capillary. This continues, until the vertical component of surface tension is exactly balanced by the weight of fluid below, i.e. when:

$$\pi R^2 h \rho g = 2\pi R \sigma \cos\theta \tag{1.12}$$

$$h = \frac{2\sigma\cos\theta}{\rho g R} \tag{1.13}$$

where h is the height of the liquid column, R the capillary radius, and ρ the density of the fluid. Although the application of this simplistic example to flow in porous media may not be immediately obvious, it should serve to demonstrate how surface and interfacial tension forces can play a crucial role in determining fluid distributions at the pore scale. The full implications of capillary phenomena will become apparent in later chapters.

This chapter has outlined some of the more important issues regarding the effects of pore-scale parameters upon microscopic flow behaviour. The next chapter goes on to describe how the modelling of such complex processes can be attempted using mathematical analogues and network simulators.

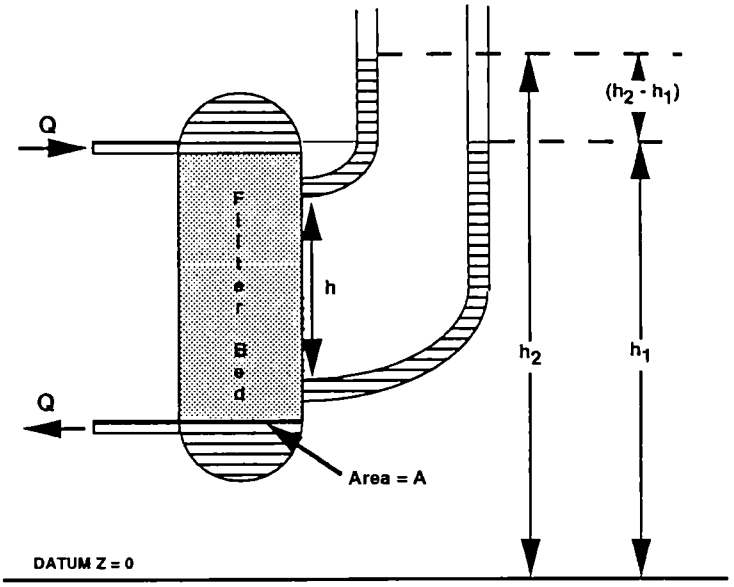

Figure 1.1 Darcy' s experiment. Water passes through a sand filter and the resultant pressure drop is measured in terms of hydraulic head.

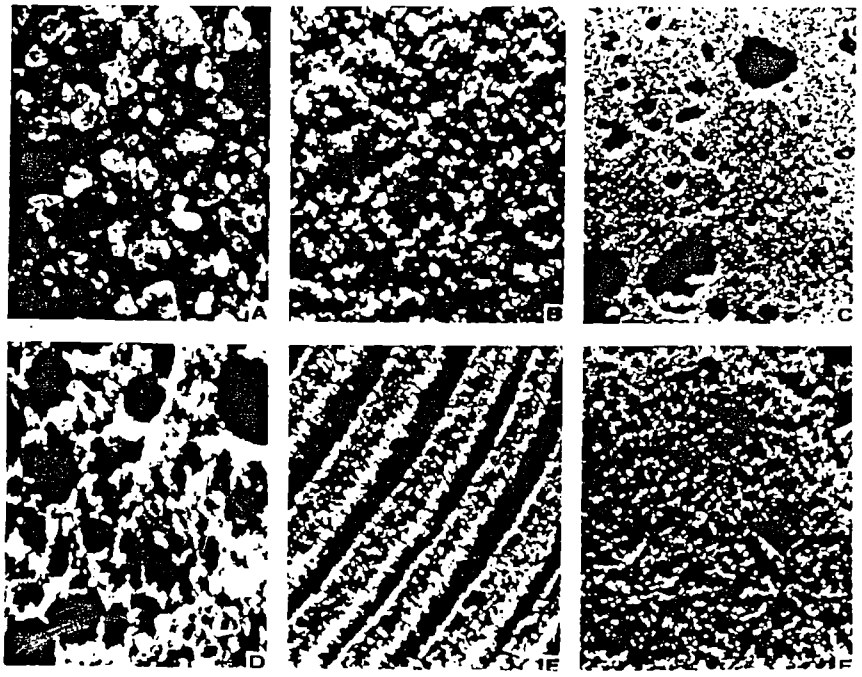

Figure 1.2 Natural porous materials (x10): (a) beach sand, (b) sandstone, (c) limestone, (d) rye bread, (e) wood, (f) human lung (Collins, 1961).

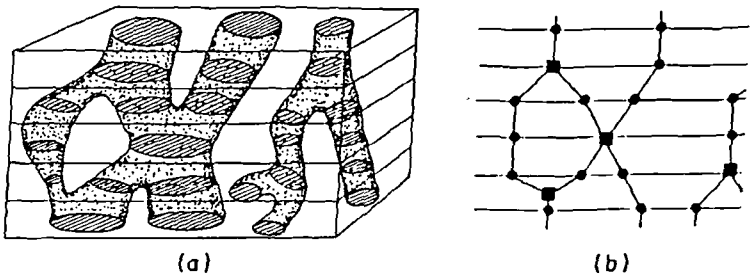

Figure 1.3 (a) Serial sectioning, (b) branch-and-node representation of pore structure (Fischmeister, 1974).

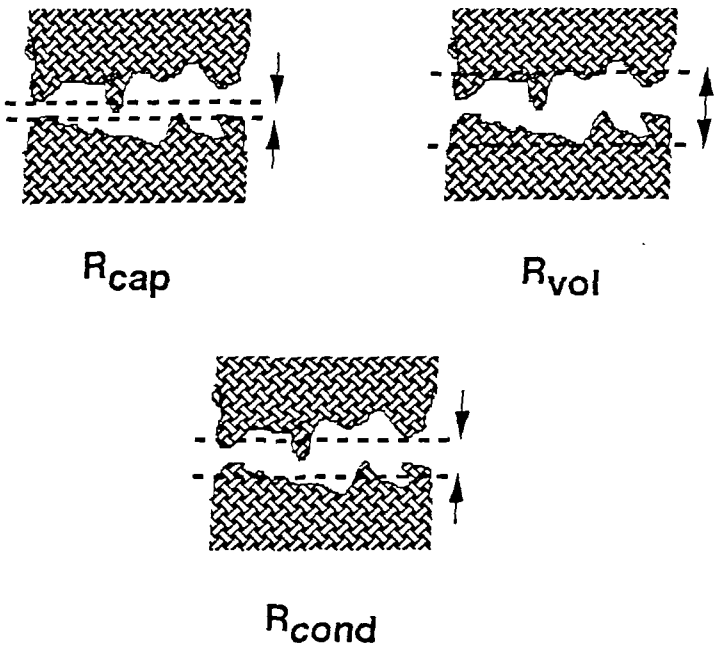

Figure 1.4 The three "R"s: R_{cap} represents the pore entry radius, R_{vol} governs the pore volume, and R_{cond} relates to pore conductivity.

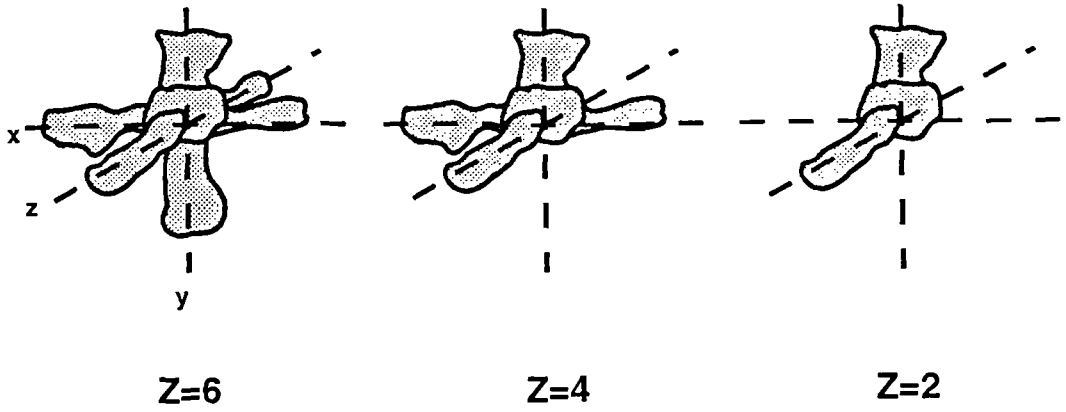

Figure 1.5 Schematic representation of co-ordination number (the number of pore elements that meet at a node).

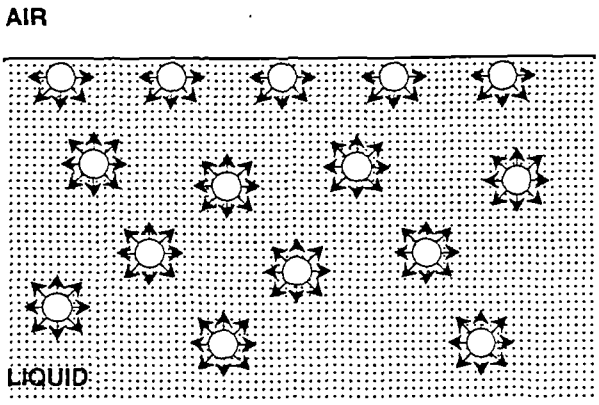

Figure 1.6 Schematic of interfacial tension: attractive forces between liquid molecules at the surface and those in the interior exceed those of the competing air molecules. The result is a net inward pull leading to a contraction of the surface.

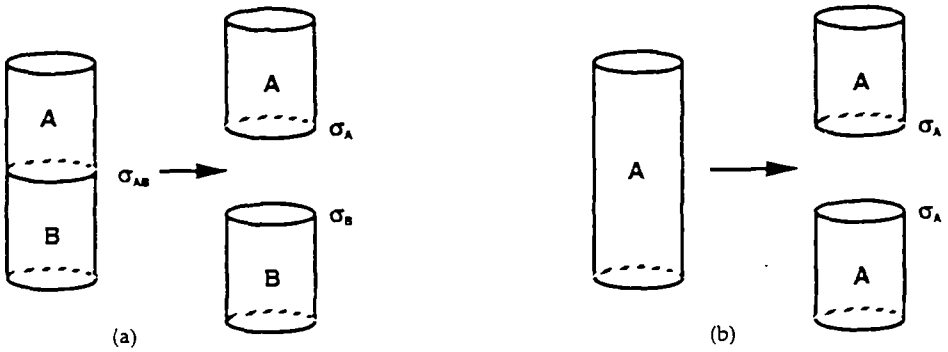

Figure 1.7 (a) The work of adhesion between two immiscible liquids equals the work required to separate unit area of the liquid-liquid interface, (b) the work of cohesion for a single liquid corresponds to the work required to pull apart a column of liquid of unit cross-sectional area.

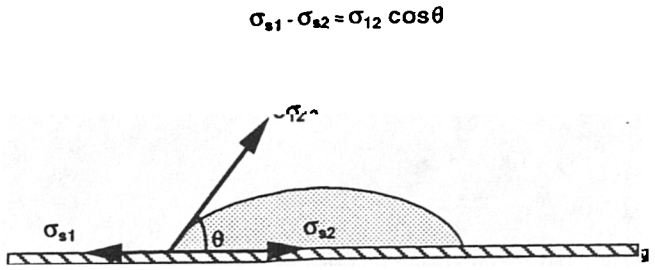

Figure 1.8 Force balance acting on a liquid drop in equilibrium.

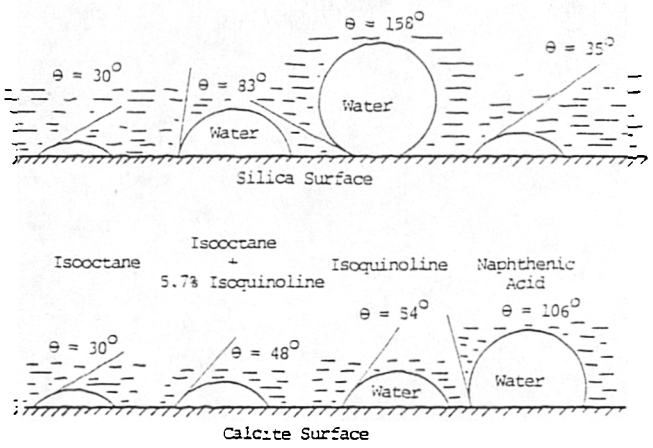

Figure 1.9 Dependency of the contact angle upon fluid pair and surface material (Benner and Bartell, 1941).

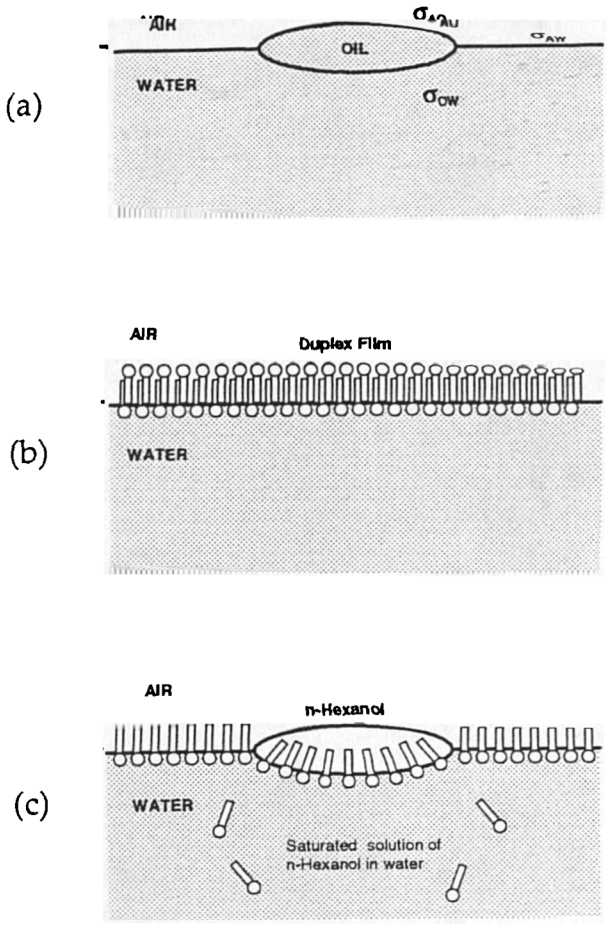

Figure 1.10 (a) A drop of non-spreading oil on a water surface, (b) a duplex film between air and water, (c) spreading of *n*-hexanol on water.

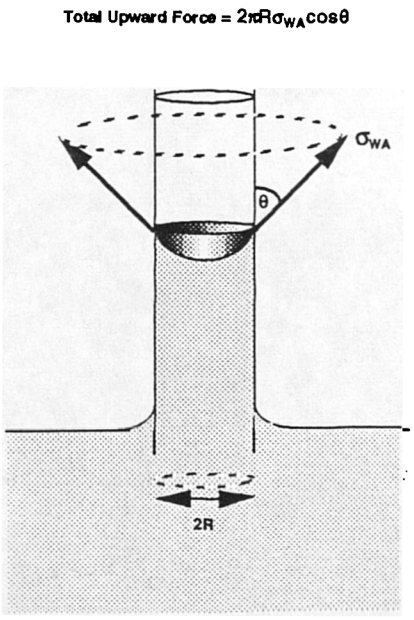

Figure 1.11 Capillary rise: water wets the bottom of the capillary, creating an upward component of interfacial tension which acts to draw fluid up.

CHAPTER 2 FLUID-FLOW ANALOGUES AND NETWORK MODELLING TECHNIQUES

2.1 Introduction

Examination of any photomicrograph immediately demonstrates why the modelling of fluid flow through a porous medium is such a formidable task: the underlying pore structure is extremely complex, with tortuous channels embedded throughout the solid matrix. Nevertheless, over the years there have been many attempts to encapsulate this structure into a simple, idealised analogue. Such models can generally be divided into four broad categories; (i) those which attempt to reduce the porous medium to a single representative conduit, (ii) probabilistic models, (iii) empirical correlations, and (iv) network models, where the medium is approximated by a lattice of connected conduits with distributed radii. A brief discussion of such analogues is now presented; more detailed descriptions can be found in the monographs of Scheidegger (1963) and Dullien (1979).

2.2 Conduit Models

This approach relies upon two main assumptions: (i) that a porous medium can be adequately characterised by a single channel having a characteristic radius, usually called the *hydraulic radius*, and (ii) that the effect of the interconnected pore structure can be contained within an empirical constant known as the *tortuosity factor*.

Carmen-Kozeny Model — One of the more notable correlations based upon conduit flow is that developed by Carmen and Kozeny (Carman, 1937, 1938, 1956; Kozeny, 1927). The theory utilises established hydraulic practice, in that the "equivalent" conduit is assumed to have a diameter, D_H, equal to four times the hydraulic radius. This hydraulic radius is usually defined as the flow cross-

sectional area divided by the wetted perimeter, but for flow in porous media it takes the form:

$$D_H = \frac{4 \times \text{Void volume of medium}}{\text{Surface area of channels in medium}} \tag{2.1}$$

By further assuming that the average interstitial velocity satisfies a form of Poiseuille's law, and that a Dupuit-Forchheimer relationship,

$$v_p = \left(\frac{v}{\phi}\right)\left(\frac{L_e}{L}\right) \tag{2.2}$$

can be used to relate the interstitial velocity (v_p) to tortuosity (L_e/L) and Darcy velocity (v), then the permeability of the system is given by:

$$k_{CK} = \frac{\phi D_H^2}{16 k_0 (L_e/L)^2} \tag{2.3}$$

where k_0 is rather vaguely referred to as a "shape factor". It should be noted, however, that the value of the effective flow path length, L_e, is seldom known (see Figure 2.1), and so most of the capillary models based upon Carman-Kozeny theory have to rely upon "geometrical parameters" to obtain realistic results.

Although a whole family of similar models exist, they differ only in the method of calculating D_H and the shape factors. The usual form of the Carmen-Kozeny equation is:

$$k_{CK} = \frac{\phi^3}{k_0 (L_e/L)^2 (1-\phi)^2 S_0^2} \tag{2.4}$$

where S_0 is the specific surface area per unit volume of the *solid*: the square of the length ratio is sometimes referred to as the tortuosity (T). A number of experiments have been carried out which claim to have substantiated the Carmen-Kozeny theory, but these generally prove to be little more than measurements of shape factors. Such models have little success in predicting permeability *a priori* due to the difficulty in obtaining a truly representative value for the tortuosity. Recent work by Katz and Thompson (1986, 1987) avoiding the use of this factor has resulted in better agreement with experiment.

Capillary Bundle Models (Figure 2.2) — These models characterise the porous medium using systems of capillary tubes with well-defined properties. Each different model contains tubes with different characteristics: they may be uniform and identical, for example, or uniform but with distributed radii, or periodically constricted and identical, etc.

If all tubes are identical (diameter=D) and lie parallel to the flow direction, then a combination of Poiseuille's law and Darcy's law gives:

$$k = \phi \frac{D^2}{32} \tag{2.5}$$

as a permeability predictor, where ϕ is the porosity. When applied to a real porous medium, however, D is a sort of "average" pore diameter which remains to be defined. A pseudo three-dimensional version of this model, in which 1/3 of the tubes are oriented in each co-ordinate direction can also be derived. The corresponding equation is simply:

$$k = \phi \frac{D^2}{96} \tag{2.6}$$

but, once again, a "typical" diameter must be calculated. Consequently, neither model is adequate for describing permeability without recourse to some empiricism. A more physical model was derived by Purcell (1949), who considered a *distribution* of tube diameters and replaced D^2 in Equation (2.6) with a squared average pore diameter defined by:

$$\overline{D}^2 = \int_{D_{min}}^{D_{max}} s^2 f(s)\, ds \qquad (2.7)$$

where f(D) is the diameter distribution function. Although not reported in any of the standard texts on the subject, the integral in Equation (2.7) is actually equivalent to:

$$\langle D \rangle^2 + \sigma_D^2 \qquad (2.8)$$

where <D> is the mean diameter and σ_D is the standard deviation of the distribution — this observation ties in nicely with a new permeability model to be described in the next chapter.

The parallel tube models outlined above are at one extreme of a spectrum of permeability predictors. The opposite extreme consists of models that assume all of the pore space to be *serially* lined up, as shown in Figure 2.2c. A similar analysis to that used earlier now gives:

$$k = \frac{\phi}{96} \frac{\left[\int f(D)\, dD / D^2\right]^2}{\int f(D)\, dD / D^6} \qquad (2.9)$$

where again, the factor 96 is introduced on the grounds that 1/3 of the capillaries are orientated towards each co-ordinate direction. Serial models will invariably lead to an underestimate of the permeability, however, whilst

parallel ones will tend to overestimate it. This is due to the fact that the total conductivity of a network of interconnected tubes must necessarily be greater than that obtained when all of the tubes are in series and less than that which results from placing all of the tubes in parallel. This is normally expressed through the Jensen inequality (c.f. Woodside and Messmer, 1961):

$$\frac{1}{\langle g^{-1} \rangle} < G < \langle g \rangle \tag{2.10}$$

where

$$\langle g \rangle = \int_{g\,\min}^{g\,\max} g\, f(g) dg \tag{2.11}$$

Here, G is the actual conductivity of a given network and the other two quantities are the conductivities that would result from systems where all the tubes were placed either in series or in parallel.

The main drawback with capillary bundle models is that they clearly do not take into account the interconnected nature of a real porous medium and neglect the fact that the fluid flow path may branch and rejoin.

2.3 Probabilistic Models

As their name suggests, probabilistic models involve the use of some kind of probability law. One of the most popular of these is the "cut-and-random-rejoin" model of Childs and Collis-George (1950), which has been further extended by Marshall (1958) and Millington and Quirk (1961). The underlying theory involves the sectioning of the porous sample into two parts perpendicular to the direction of flow. These are then joined together again in a random fashion, and statistical analysis is used to approximate the permeability of the subsequent hybrid. The analysis is based upon the assumption that the areal porosity is equal to the bulk porosity of the system, and so the fractional area of a section occupied by pores with capillary

diameters in the range ($D_e \rightarrow D_e + \delta D_e$) is equal to $\phi f(D_e) dD_e$, where f is the corresponding pore size distribution function. Further statistical considerations give the areal *overlap* between the two rejoined sections, and the final permeability estimate can be written as:

$$k = \frac{\phi^2}{32}\left\{\int_0^{\infty} f(D_e)\left[\int_0^{D_e} D_e'^2 f(D_e')dD_e'\right]dD_e + \int_0^{\infty} D_e^2 f(D_e)\left[\int_{D_e}^{\infty} f(D_e')dD_e'\right]dD_e\right\} \qquad (2.12)$$

Marshall also presented results which gave $k \propto \phi^2$, whereas Millington and Quirk derived a slightly different relationship, with $k \propto \phi^{4/3}$. Both authors claim to have predicted permeabilities in good agreement with experiment.

A more sophisticated model was developed by Haring and Greenkorn (1970), who modelled pore structure using randomly orientated, straight, cylindrical pores, with diameters and lengths sampled from a beta function. Therefore, in three dimensions, each pore is given four degrees of freedom: radius, length, and two angles of orientation. Although their analysis appears to be more involved than those described earlier, the final permeability predictor:

$$k = \frac{R_{max}^2}{24}\frac{(\alpha+1)(\alpha+2)}{(\alpha+\beta+2)(\alpha+\beta+3)}\phi \qquad (2.13)$$

where α and β are parameters of the beta function, has a similar form to other capillary models. This analogue has been criticised by Guin et al (1971a,b), who question the procedure of velocity weighting carried out by the original authors.

2.4 Empirical Models

There have been numerous attempts to derive correlations between permeability and other sample properties, such as porosity, capillary pressure,

grain size distribution, and electrical properties. The porosity/permeability relationship has perhaps been the most widely studied (see, for example, Mavis and Wilsey, 1936; Büche, 1937; Rose, 1945; Habesch, 1990), but correlations vary so much that no universally accepted formula can be adopted successfully. Indeed, it is quite straightforward to find two samples with identical porosities that have very different permeability properties, and so any poroperm correlation that may exist cannot be unique. Consequently, most empirical correlations contain "geometrical factors" which serve to fit experimental measurements without any real consideration of the underlying pore structure. Even the more recent attempts at permeability correlation require unappealing empirical constants to match experiment: for sandstones, Dullien (1990) has found a relationship of the form

$$k = (D_b/3.5)^2(\phi/32)\times 10^3 \quad (mD) \tag{2.14}$$

where D_b is the capillary pressure "breakthrough" diameter, and Chatzis (1980) has derived:

$$k = (85.63/P_{cb})^{2.71} \tag{2.15}$$

where P_{cb} is the mercury/air breakthrough capillary pressure in psi.

2.5 Network Modelling

2.5.1 Previous Studies

Models that account for the interconnected nature of porous media constitute a group of analogues which can truly be referred to as *network models*. Here, the medium is modelled using a system of *interconnected* capillary elements, which generally configure to some known lattice topology. A variety of lattices are shown in Figure 2.3. Although these network structures are somewhat idealised, the capillary radii are assigned randomly from a realistic pore size

distribution in an effort to partially reconstruct the actual porous medium under investigation.

A fully interconnected network was first used by Fatt (1956) for primary drainage studies. Although the two-dimensional lattice used was extremely small (200-400 tubes), the novelty of the approach encouraged great interest in the subject, and improvements on Fatt's primitive model were soon forthcoming (Rose ,1957; Dodd & Kiel ,1959). However, simulations using small lattices could never hope to capture the full behaviour of microscopic flow processes. Consider Figure 2.4, for example; such a small array of capillary tubes is clearly inadequate for simulating the rock matrix shown alongside: boundary effects will certainly have a major influence and saturation measurements will be of little utility. With the advent of high speed computers, however, much larger systems can now be constructed, with the result that microscopic flow behaviour can be more accurately simulated. Figure 2.5 shows a capillary dominated drainage process using an 80 x 80 square lattice, the details of which will be presented later: the resulting picture is somewhat more reassuring. The fractal capillary fingering is in excellent agreement with experimental observation (see Lenormand et al, 1988).

To date, there have been numerous refinements made to Fatt's small two-dimensional lattices in an attempt to simulate a wide range of different flow regimes: capillary-dominated flow (Lenormand and Zarcone, 1984; Diaz, Chatzis and Dullien, 1987; Tzakiroglou and Payatakes, 1991), viscous-dominated flow (Chen & Koplik, 1985; Chen & Wilkinson, 1985), intermediate cases (Koplik and Lasseter, 1984; Lenormand, Touboul, and Zarcone, 1988; Dias and Payatakes, 1986), miscible flow (Simon and Kelsey, 1971) and capillary flow through packs of circular obstacles (Cielpak and Robbins, 1988).

Several investigators have also exploited ideas from other branches of science, utilising techniques such as Effective Medium Theory (Koplik, 1981; Koplik et al, 1984) and Percolation Theory (Larson et al, 1981; Heiba et al, 1982; Wilkinson, 1986). Although these approaches have given qualitative insights into flow behaviour, no universally successful predictive formulae have been forthcoming.

Much research has been undertaken in an attempt to construct more realistic networks which better approximate Nature. These include: variable co-ordination number (Koplik and Lasseter, 1982; Chatzis, 1976), complex tube geometries (Dias and Payatakes, 1986), and even networks painstakingly recreated from serial sections of actual porous samples (Doyen, 1988; Yanuka et al, 1986). Once again, however, predictions are in poor agreement with experimental observations.

Only recently has it been computationally feasible to carry out studies using large three-dimensional networks. This extension is vital, however, if two or more phases are to flow simultaneously. Bicontinua are topologically impossible on a two-dimensional lattice, whereas well-connected three-dimensional networks permit the simultaneous flow of up to three phases. The ability to model interconnected multiphase flow has prompted several investigators to re-examine important issues such as relative permeability and capillary pressure more closely. Three-dimensional networks were used for capillary pressure calculations by Chatzis and Dullien (1977), and the first three-dimensional relative permeability simulations appear to have been carried out by Lin and Slattery (1982). Similar models have since been reported by Heiba et al (1982), and Mohanty and Salter (1982, 1983). The most recent investigations of Blunt et al (1990, 1991, 1992) and Bryant and Blunt (1992) have subsequently built upon these earlier works and have helped pave the way towards a greater understanding of relative permeability generally. Motivated

by the work of Lenormand et al (1988) in two-dimensions, and by Wilkinson's percolation approach, they studied various displacement mechanisms on regular cubic and irregular Voronoi networks. Modern day computer power enabled them to use networks containing up to 80,000 pore spaces, and models were also presented which explicitly accounted for the effects of viscous and buoyancy forces.

It is clear from this brief overview, that the pioneering studies of Fatt have consequently led to a vast improvement in the understanding of a great many diverse flow problems, several of which form the greater part of this thesis. The next section describes the construction of the basic network model used in this work; additional features will be added later and are explained in the relevant chapters.

2.5.2 The Basic Model

Many network models attempt to distinguish between "pores" and "throats", by building networks consisting of hollow spheres connected by thin capillary tubes. In such models, all of the liquid volume is assumed to be contained in the spherical pores with pressure differences being maintained by the throats (Lenormand, 1986). The approach taken in this work is somewhat more straightforward. The porous medium is initially modelled using a three-dimensional cubic network of what will be referred to as *pore elements;* unlike many previous studies, no distinction is made here between pores and throats. The author considers it debatable as to what constitutes a pore and a throat in a real porous medium, and the "3 R's approach" described in Chapter 1 gives a cogent reasoning as to why this is unimportant. It has also been shown by Cohen and Lin (1983) that the simple capillary tube model is appropriate for studying the flow properties of porous media, which is the problem investigated here. Moreover, this study focuses upon qualitative pore-scale

dynamics in a topological context and is not concerned with quantitative predictions relating to transport coefficients.

When more than one fluid is flowing through a network, phase occupancy during a given process (e.g. primary drainage, secondary imbibition etc.) may be characterised by a set of rules which, when combined with topological considerations (accessibility), give realistic saturation distributions throughout a displacement (see Chapter 4). This approach dispenses with microscopic unsteady state calculations to establish phase occupancies (e.g. Blunt and King, 1990, 1991) and is particularly well-suited to the modelling of capillary-dominated flow. However, since any increase or decrease in the saturation of a particular phase depends upon the spatial distribution of that phase, the computational effort saved in dispensing with unsteady state calculations is more than offset by the implementation of a *clustering algorithm* (Hoshen and Kopelman, 1976). This algorithm is essentially a "book keeping" exercise which locates and labels the phase clusters which are distributed throughout the network. These clusters are continually changing their structure during a displacement, and so the efficacy of the simulation as a whole is intrinsically linked to the efficacy of the clustering algorithm itself. A great deal of time and effort has been invested in achieving the optimum performance of this element of the network simulator. The precise computational details are dealt with more fully in Appendix E.

For most of the studies described in this thesis, the model used consisted of a three dimensional cubic network of capillary elements as shown in Figure 2.6. This simple lattice has dimensions $N_x \times N_y \times N_z$ where N_x, N_y, N_z are the number of nodes in the x, y and z directions respectively. Periodic boundary conditions have been assumed in the y and z directions in order to simulate larger systems and eliminate surface effects. The condition of no flow at these boundaries could equally have been applied, as it has been demonstrated that

there is no significant difference between these two types of boundary conditions for Nx, Ny, Nz ≥ 6 (Koplik, 1982). The pressure gradient is taken to be in the x direction.

Now, for a single element of radius r and length L, the flow Q is given by Poiseuille's law:

$$Q = \frac{\pi r^4}{8\mu} \frac{\Delta P}{L} \tag{2.16}$$

where μ is the viscosity and ΔP the pressure difference acting across the capillary. At each node (i, j, k), the sum of the flows Q_i must add up to zero (conservation of mass), and so:

$$\sum_{i=1}^{6} Q_i = 0 \tag{2.17}$$

This is essentially equivalent to Kirkchoff's law for a resistor network. Consideration of the whole network leads to a set of $(3.N_X.N_Y.N_Z+N_Y.N_Z)$ linear pressure equations, the solutions to which can then used to calculate the elemental flows (computational details are given in Appendix E). Summing the outlet flows yields the *total network flow,* which can then be substituted into Darcy's equation to give a value for the total network *permeability.* If the system contains more than one fluid, then the process is carried out for each fluid in turn; the resulting phase conductivities now being referred to as *effective permeabilities.* The modelling of multiphase flow is discussed more fully in later chapters.

Once a global geometry has been specified, a network is fully characterised by its dimensions and the radius and length of each constituent pore element. For most capillary-dominated simulations, the length of each element has been kept

constant and radii have been sampled from a variety of distribution functions (see Appendix D for a full list). Results have generally been calculated using networks of dimensions 15x15x15, equivalent to 10,350 interconnected pore elements, but some calculations have been performed using larger networks (up to 25x25x25). Unless explicitly stated, it is to be assumed that all the results presented are from runs using the former system. The size of the model was mainly limited by the computer power available; although larger networks were studied for confirmation purposes (their periodic inclusion is essential to justify general conclusions), simulations on a 15x15x15 network appear to exhibit all of the important features demonstrated by larger systems. To illustrate this point, a comparison between relative permeability curves calculated using networks of various sizes is shown in Figure 2.7. Clearly, no qualitative differences are evident between a 15x15x15 and a 20x20x20 realisation, even though the number of pores has more than doubled. The fact that qualitative behaviour is most important in this work, allows for slightly smaller models to be utilised, and it must also be remembered that large networks can take a prohibitively long time to run. These issues notwithstanding, however, 10,350 bonds still represent a vast improvement on early studies, which attempted to simulate flow processes using only 200-400 bonds.

The application of this simple model to single-phase flow problems is now considered.

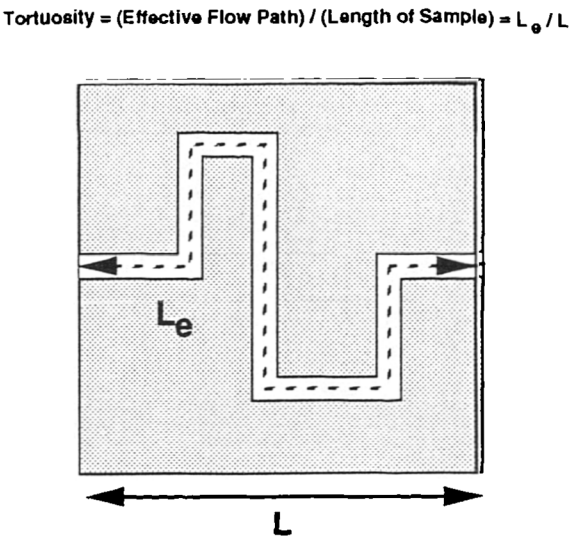

Figure 2.1 Schematic representation of tortuosity. The actual flowpath is longer than the sample length.

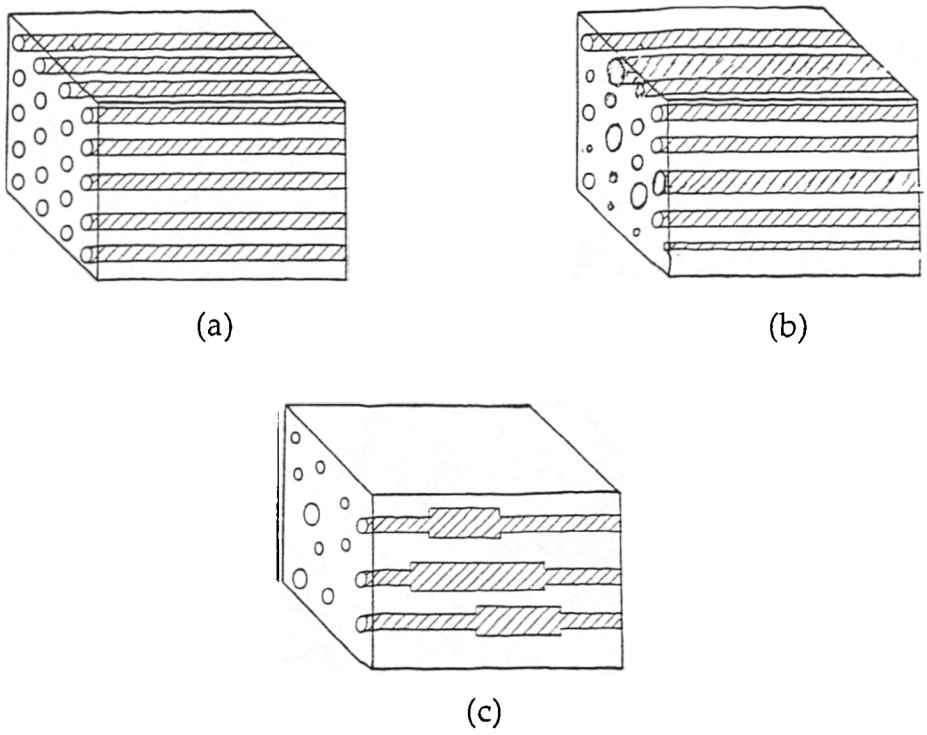

Figure 2.2 Simple capillary bundle models: (a) straight capillaric model with all radii equal to the hydraulic radius, (b) radii sampled from a distribution, (c) serial type model (after Scheidegger, 1963)

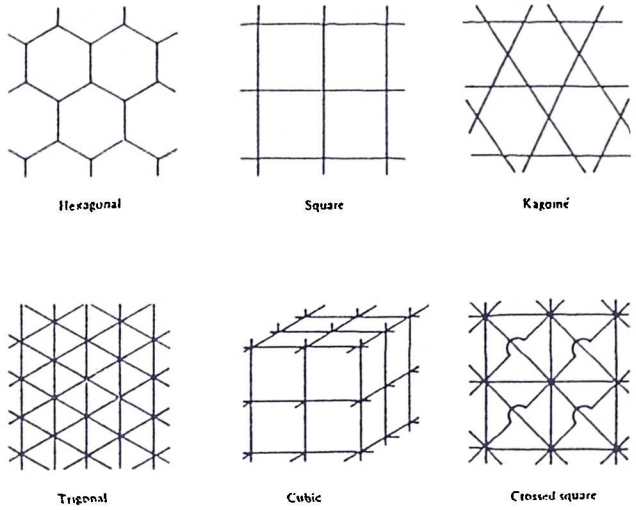

Figure 2.3 Various network geometries (Koplik, 1982).

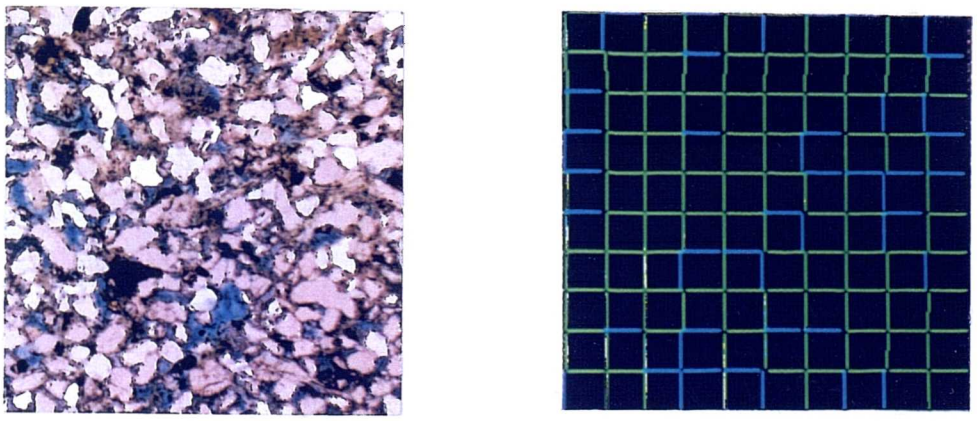

Figure 2.4 (a) Thin section of greywacke, (b) A small two-dimensional square lattice.

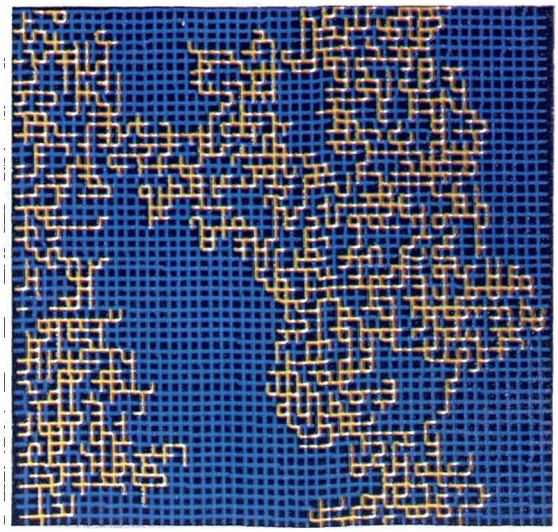

Figure 2.5 80x80 network simulation of capillary-dominated drainage: the overall picture is somewhat more convincing.

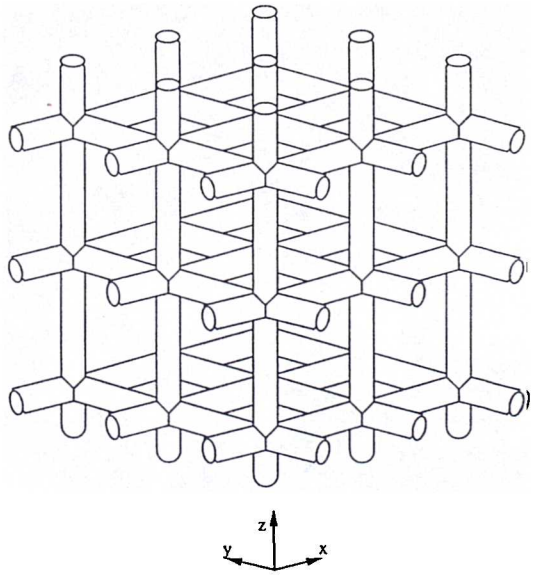

Figure 2.6 Three-dimensional $N_x x N_y x N_z$ network schematic. In practice, each element has a radius sampled from a distribution function.

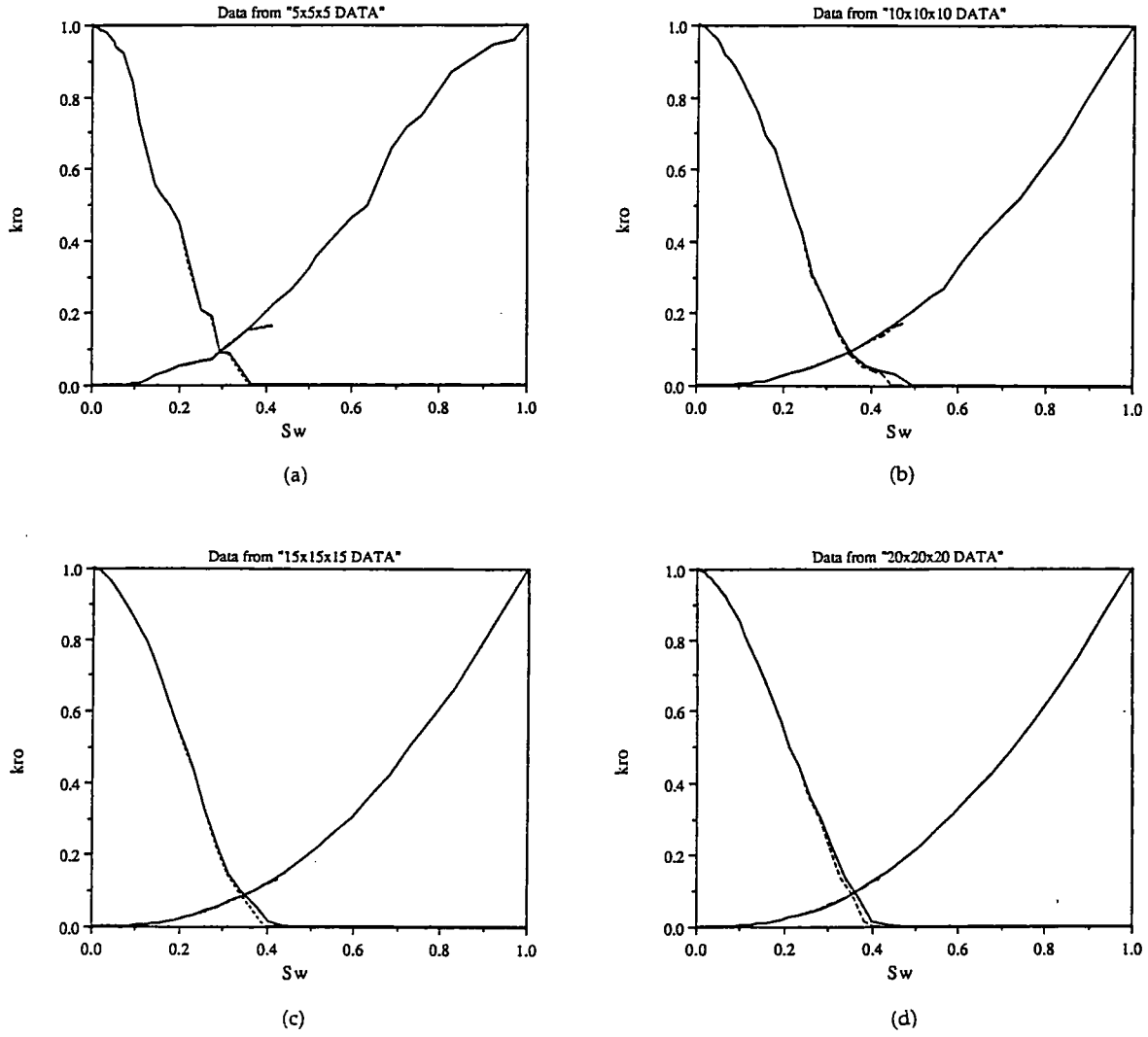

Figure 2.7 Comparison of imbibition relative permeabilities (with and without trapping) using different-sized networks: (a) 5x5x5, (b) 10x10x10, (c) 15x15x15, (d) 20x20x20.

CHAPTER 3 SINGLE-PHASE FLOW

3.1 A New Predictive Model For Network Permeability.

This section describes how the basic network model outlined in the previous chapter, can be used to calculate single-phase (absolute) permeability. An analytical model will also be discussed, as will its general applicability. The earlier aspects of this work have been described in O'Carroll and Sorbie (1993). Before dealing with these more involved issues, however, consider first a couple of simple calculations which can be used to check the basic running of the simulator: for convenience, the capillary length l (representing the distance between two adjacent nodes) will be taken as the basic unit of length. An expression for the flow through a single capillary element is given by Equation 2.16, which shows that each elemental flow has a simple functional dependency upon some of the system parameters: i.e. $Q \propto 1/\mu$ and $Q \propto \Delta P$. Through the linear nature of this equation, it is clear the *total* flow should also be inversely proportional to the fluid viscosity if the simulator is working properly. This has been confirmed numerically as illustrated in Figure 3.1. The linear relationship between total flow and the applied pressure difference has also been confirmed, as would be expected (see Figure 3.2). These straightforward preliminary tests are merely used to demonstrate that the network is behaving in a realistic manner, so that attention can now focus upon less obvious issues.

It is a well known result from percolation theory that the conductivity of a random network is proportional to the cross-sectional area of that network divided by its length (i.e. conductivity $\propto A/L$), where $A=N_yN_zl^2$ and $L=(N_x+1)l$ (Grimmett, 1989). This has also been confirmed numerically here and results are shown in Figures 3.3a and b. The preceding numerical results imply that an equation may be written for the total flow through the network of the form:

$$Q = \frac{A\Delta P}{\mu L} k \qquad (3.1)$$

where, by dimensional arguments, it is easy to see that k must have the dimensions of a length squared. In fact, k is the *permeability* as defined by Darcy's law (see Chapter 2). It would be desirable to relate k to geometrical parameters of the network, and so characteristic lengths associated with the system, such as the median and mean of the pore size distribution functions listed in Appendix D have been considered. It is important to stress that in all cases, a *series* of flow calculations was performed to minimise numerical error. Hence, the network permeability calculations presented are averages taken over a number of runs; typically 40 to 50. For such a series of calculations the individual networks will be different although they are all sampled from the same distribution and have the same mean. It is important to note that, by using a different set of random pores each time, it is guaranteed that only the statistical parameters of the distribution are being investigated and not a particular configuration.

The dependence of flow on mean radius for various radius distributions is illustrated in Figures 3.4 to 3.10. These results show that the mean radius appears to be an excellent parameter for characterising the flow, and hence the permeability, through a random capillary network. The possibilities of the permeability also depending upon the median, $\langle r^2 \rangle^2$, and $\langle r^4 \rangle$ of a given distribution were also investigated. Results are shown in Figures 3.11 to 3.13. It can be seen that the effect of these parameters on the flow was not the same for all distributions and that, consequently, there can be no unique formula covering all cases. Having studied the variation of flow with a variety of distribution parameters, it became apparent that the *mean* pore radius was still the most appropriate.

The fact that the flow is proportional to the fourth power of the mean radius (given by the slope of each best-fit line) permits the derivation of a single

formula which attempts to predict the permeability for all of the distributions considered. If all elements in the network had radii R, say, then the total flow through the network would be given by Poiseuille's law:

$$Q = \frac{\pi R^4 \Delta P}{8\mu(Nx+1)l} NyNz \tag{3.2}$$

Now, eliminating Q from Equations 3.1 and 3.2 gives:

$$k = \frac{\pi}{8l^2} R^4 \tag{3.3}$$

This must necessarily be the actual permeability of a network consisting of identical capillaries. Consequently, it is proposed that the permeability of a *random* network should be given by the equation:

$$k = \frac{\pi}{8l^2} < r >^4 \tag{3.4}$$

where <r> is the mean radius defined by:

$$< r >= \int_{R_{min}}^{R_{max}} r\, f(r)\, dr \tag{3.5}$$

The total flow through a network should then satisfy:

$$Q = \frac{\pi < r >^4 \Delta P}{8\mu(Nx+1)l} NyNz \tag{3.6}$$

Figure 3.14 shows a plot of the permeability as a function of the mean radius for a series of radius distributions. It is important to note that the line in Figure 3.14 is that *predicted* by Equation 3.4 and not a fit to the data. It is found that this equation predicts the permeability to a reasonable degree of accuracy for most

of the distributions studied, and runs performed on larger networks (20x20x20) have led to a significant improvement in the results.

Intuitively, however, one would not expect Equation (3.4) to be able to predict the permeability for *all* distributions. For example, it is a simple matter to find a uniform radius distribution having <r> = 40, say, which also happens to be the mean value of a cubic radius distribution in the range [1,50]. The very different shapes of these two distributions, obviously questions the accuracy of Equation (3.4). In order to clarify this issue further, permeabilites were calculated using networks characterised by distribution functions with identical <r> but differing standard deviations, σ. The uniform distribution is the "worst" case since it allows the greatest variation in radius. Results are shown in Figure 3.15. *It is quite clear that the standard deviation of the distribution (i.e. the amount of scatter of radius values) plays a crucial role in determining the total permeability of the network.* This effect was therefore incorporated into Equation 3.4, resulting in the extended form

$$k = \frac{\pi \langle r \rangle^4}{8 l^2} \left\{ 1 + \alpha \left(\frac{\sigma}{\langle r \rangle} \right)^2 \right\} \qquad (3.7)$$

where α is a parameter to be determined. Note that this result complements the model of Purcell (1949) very well indeed (cf. Equations 2.6-2.8)

After a few preliminary simulations, it soon became apparent that the α-values depended upon the distribution under investigation. Hundreds of network realisations were analysed for different ranges of each distribution, and values of α were then calculated from Equation (3.7). These are shown in Table 3.1 together with the average errors resulting from both Equations (3.4) and (3.7). The extended formula is clearly a more appropriate choice. The attraction of such a model lies in its sheer simplicity when compared to the more complex

approaches of the past, and it is surprising that this generalisation of the Poiseuille law does not seem to have been observed by other workers in this area.

Previously investigations have tended to focus upon two very different techniques: Effective Medium Theory (EMT) and Percolation Theory. In the following sections, the preceding results will be discussed in light of these theories, and some new analysis will be presented which demonstrates that all three approaches are actually equivalent.

3.2 Effective Medium Theory (EMT)

In studies of electrical flow in random conductor networks, results are usually discussed in terms of *elemental conductivities*. It is straightforward to apply such concepts to fluid flow, however, if pressure is associated with potential difference, flow with electrical current and flow resistance with electrical resistance. For fluid-flow networks, pore geometry and conductivity can be linked immediately by noticing that the associated radius and conductivity distributions, f(r) and h(g) respectively, are related to one another via the expressions $f(r)dr=h(g)dg$ and $g=r^4$: i.e. the probability of a pore having a radius between R and (R+δR) is the same as the probability of that pore having a conductivity between G and (G+δG). Thus, it is easy to show that $\langle g^{1/4} \rangle$ is the characteristic quantity corresponding to $\langle r \rangle$ for the random networks described earlier. However, for many years it has been known that there is another characteristic conductivity for a random network, the *effective medium conductivity*. This was originally derived in order to model hopping conductivity in conductor/insulator materials by Bruggeman (1935), and later by Landauer (1952). Kirpatrick (1973) presents an excellent description of this method. The main idea behind EMT is that the total conductivity of a random network can be reproduced by replacing each of the elements in the network by

elements possessing an "average" conductivity g_m. This "average" conductivity is defined via the implicit equation:

$$\int_{g_{min}}^{g_{max}} \frac{(g-g_m)h(g)}{\left\{g+\left(\frac{z}{2}-1\right)g_m\right\}}\,dg = 0 \qquad (3.8)$$

where z is the co-ordination number of the lattice (the number of conductors meeting at a node).

For example, consider the cubic radius distribution function defined by:

$$f(r) = Nr^3 \qquad (3.9)$$

where

$$N = \frac{4}{(R_{max}^4 - R_{min}^4)} \qquad (3.10)$$

It is straightforward to show that this radius distribution corresponds to a *uniform* conductivity distribution, and, for a regular network with z=6, the effective medium conductivity is found iteratively from the equation:

$$g_m = \frac{(R_{max}^4 - R_{min}^4)}{3\log\left(\frac{(R_{max}^4 + 2g_m)}{(R_{min}^4 + 2g_m)}\right)} \qquad (3.11)$$

The total flow across the network is then given by the relation:

$$Q = \frac{\pi g_m}{8\mu}\,\frac{\Delta P\, NyNz}{(Nx+1)l} \qquad (3.12)$$

and Darcy's law may be used to show that $k=(\pi g_m)/8l^2$. For a fuller account of EMT, see Koplik (1981, 1982) or David et al (1990).

The question arises as to whether or not Equation (3.8) holds for any probability density function (PDF). If this were to be the case, then the EMT model and the model developed in Section 3.1 could only be compatible if $g_m \propto \langle r \rangle^4$ for all distributions. Figure 3.16 shows that, for a cubic distribution, this appears to be the case: in fact, it can be shown that $g_m \approx 1.067 \langle r \rangle^4$. For a Log-Uniform distribution, however, such a proportionality does not seem realistic (Figure 3.17). Consequently, the true connection between the mean radius ($\langle r \rangle$) and the effective medium conductivity (g_m) for a general PDF must now be examined in more detail.

In general, a PDF must satisfy the equation:

$$\int_{R_{min}}^{R_{max}} p(r)\,dr = P(R_{max}) - P(R_{min}) = 1 \quad \text{where} \quad P(r) = \int p(r)dr \qquad (3.13)$$

This condition can be met by choosing f(r)=N.p(r), where:

$$N = \frac{1}{P(R_{max}) - P(R_{min})} \text{ is a normalisation factor}$$

and so,

$$\int_{R_{min}}^{R_{max}} f(r)dr = 1 \qquad (3.14)$$

After integrating by parts, the mean radius for any radius distribution is now given by:

$$\langle r \rangle = \int_{R_{min}}^{R_{max}} r\, f(r)dr = \left\{ R_{max}F(R_{max}) - R_{min}F(R_{min}) - \int_{R_{min}}^{R_{max}} F(r)dr \right\} \qquad (3.15)$$

Now, the formula connecting the radius and conductivity PDF is f(r)dr=h(g)dg, where $g=r^4$; and so:

$$h(g) = \frac{f(g^{1/4})}{4g^{3/4}} = \frac{d}{dg}\left(F\left(g^{1/4}\right)\right) \tag{3.16}$$

Substituting h(g) from (3.16) into (3.8) gives, after a little manipulation:

$$1 = \frac{z}{2} g_m \int_{R_{min}^4}^{R_{max}^4} \frac{1}{\left\{g + \left(\frac{z}{2} - 1\right) g_m\right\}} \cdot \frac{d}{dg}\left(F\left(g^{1/4}\right)\right) dg \tag{3.17}$$

Equations 3.15 and 3.17 now lead to an expression connecting the mean radius with the effective medium conductivity, namely:

$$< r > = \frac{2\left\{R_{max}F(R_{max}) - R_{min}F(R_{min}) - \int_{R_{min}}^{R_{max}} F(r)dr\right\}}{z g_m \int_{R_{min}^4}^{R_{max}^4} \frac{1}{\left\{g + \left(\frac{z}{2} - 1\right) g_m\right\}} \cdot \frac{d}{dg}\left(F\left(g^{1/4}\right)\right) dg} \tag{3.18}$$

Consider once again the cubic radius distribution with:

$$f(r) = \frac{4r^3}{\left(R_{max}^4 - R_{min}^4\right)}.$$

For a cubic lattice (z=6), Equation 3.18 gives:

$$< r > = \frac{4\left(R_{max}^5 - R_{min}^5\right)}{15 g_m \log\left\{\frac{R_{max}^4 + 2g_m}{R_{min}^4 + 2g_m}\right\}} \tag{3.19}$$

Similarly, for a Log-Uniform distribution, where:

$$f(r) = \frac{1}{r.\log\left(\frac{R_{max}}{R_{min}}\right)} \tag{3.20}$$

the relationship takes the form:

$$< r >= \frac{4(R_{max} - R_{min})}{3 \log \left\{ \frac{R_{max}^4 + 2g_m}{R_{min}^4 + 2g_m} \right\}} \qquad (3.21)$$

It should be noted that Equation (3.18) generally contains 4 variables: R_{min}, R_{max}, <r>, and g_m. So, in order to obtain <r> as a closed form *analytical* function of g_m, it is necessary to fix either R_{min}(or R_{max}), and then find R_{max}(<r>) (or R_{min}(<r>)) from (3.15). In general, this may pose a problem as these equations are usually transcendental and in some cases, even finding g_m from (3.8) can be extremely difficult: if a uniform radius distribution is considered, for example, g_m must be found from an incredibly complicated transcendental equation. Although analytical solutions are difficult to obtain, there is no problem in solving Equations (3.15) and (3.18) numerically.

The preceding analysis clearly demonstrates that there is close similarity between EMT and the mean radius model developed here; both characterise the network by an appropriately averaged quantity. Indeed, Equation (3.18) appears to be the first time that a precise relationship connecting g_m and <r> has been reported.

3.3 Percolation Theory

In the previous two sections, the process of fluid flow in a porous medium has been considered from the point of view of the fluid. However, it is also possible to consider the process as being determined by the geometry of the porous medium itself. One approach, which has since become known as *percolation theory*, was first used by Broadbent and Hammersley (1957) to investigate the flow of gas through carbon granules (for the design of gas masks to be used in coal mines). As well as describing the flow of fluids and

gases through porous media, their theory has subsequently been used to describe many other diverse processes; such as, the electrical properties of amorphous semiconductors, the behaviour of crystalline semiconductors containing impurities, and magnetic phase transitions. In the present context of fluid flow, percolation theory emphasises the topological aspects of problems, dealing with the connectivity of a very large number of elemental pores and describing the size and behaviour of connected phase clusters in a well-defined manner.

The primary focus of this section is to discuss how ideas from percolation theory can be applied more specifically to flow in a porous medium. As a simple, instructive analogue, consider first a two-dimensional square lattice of capillary elements as shown in Figure 3.18 The most pertinent concepts from percolation theory will now be discussed using this geometry. Consider the critical behaviour of the network. Assume that, initially, all of the tubes are blocked and that they are then opened *at random*. For any given geometry there is a unique fraction of tubes that must be open before flow across the network can commence; this critical fraction is called the *percolation threshold* (P_c) and for a simple square lattice has the value P_c=0.5 exactly (Figure 3.18(e)). One of the most incredible aspects of this result is that it is *independent of the radius distribution*; it only depends upon the topological structure of the network (actually, the co-ordination number (z) and the Euclidean dimension (d)). In fact, the percolation threshold and system topology are linked by the equation:

$$z.P_c = \frac{d}{(d-1)} \qquad (3.22)$$

(see Stauffer and Aharony, 1992). Table 3.2 shows percolation thresholds for a variety of two- and three-dimensional geometries. The square (2D) and cubic (3D) geometries have been used for calculations here. Although this work deals mainly with networks containing only 10,350 elements, (15x15x15 nodes),

P_c is obtained to a very reasonable degree of accuracy. Not surprisingly, calculations using networks with up to 20x20x20 nodes has improved upon this still further.

Now, if instead of random opening, the pores are opened systematically beginning with those of largest radius, it is clear that flow will commence once a cluster of large open pores spans the system. The radius at which this occurs is known as the *percolation radius*, R_p, and is defined implicitly by the equation:

$$P_c = \int_{R_p}^{R_{max}} f(r)dr \qquad (3.23)$$

where f(r) is the normalised tube radius distribution function and P_c the percolation threshold. It will be shown later that such size-dependent opening criteria play an important part in the interpretation of a wide variety of flow processes.

The relationship between the percolation radius and the total network conductivity has been studied in detail for a random resistor network by Ambegaokar, Halperin & Langer (1971) (AHL) and their conclusions will now be examined. They argued that the percolation radius completely characterises the electrical conductivity of the network; if true, their argument must be equally valid for a fluid-flow network. They claim that, just before P_c is reached, the system consists of large unconnected clusters of tubes. The insertion of tubes of radius R_p then connects a fraction of these clusters across the network and flow begins. At this point the flow is indeed dominated by these tubes because, no matter how large the conductivity of any cluster, the fluid must pass through single "bottleneck" tubes of radius R_p (Figure 3.19). However, they go on to say that *even when all of the pores in the network are open, the flow is still dominated by pores of size* R_p. Given the basic geometrical difference between a cluster which is just spanning the network and a fully

connected system, this assertion is not immediately convincing. However, further numerical investigation here showed that there appeared to be a direct relationship between the total flow and the percolation radius. Log-log plots of the network flow as a function of the percolation radius for Cubic and Uniform distributions are presented in Figure 3.20 and 3.21.

In order to explain these results, consider once again Equations (3.15) and (3.23):

$$< r >= \int_{R_{min}}^{R_{max}} r\, f(r)dr = \left\{ R_{max}F(R_{max}) - R_{min}F(R_{min}) - \int_{R_{min}}^{R_{max}} F(r)dr \right\}$$

and

$$P_c = \int_{R_p}^{R_{max}} f(r)dr$$

These combine to give:

$$F(R_p) = \frac{1}{R_{max}} \left\{ < r > + R_{min}F(R_{min}) - R_{max}.P_c + \int_{R_{min}}^{R_{max}} F(r)\,dr \right\} \qquad (3.24)$$

which is the relationship between <r> and R_p for any general PDF. For a uniform distribution:

$$R_p = 2(1 - P_c) < r > + R_{min}(2P_c - 1) \qquad (3.25)$$

and a cubic radius distribution gives:

$$R^4{}_p = \frac{(R^4_{max} - R^4_{min})}{R_{max}} \left\{ < r > + \frac{(R^5_{max} + 4R^5_{min})}{5(R^4_{max} - R^4_{min})} - R_{max}.P_c \right\} \qquad (3.26)$$

which becomes:

$$R_p \approx R_{max}\left(1 - \frac{4P_c}{5 < r >}\right)^{1/4} \quad \text{when} \quad R_{max} >> R_{min} \qquad (3.27)$$

Thus, for any given radius distribution, there is an equation linking the mean radius and the percolation radius. Given that the results presented earlier showed that <r> governs the total network flow, and given that <r> and R_p are intrinsically linked via Equation (3.24), it appears that the AHL conclusion is valid after all; namely, that the total network flow is indeed related to R_p. However, Table 3.3 shows that there is obviously no universal formula which relates the total flow to the percolation radius for all distributions, although a predictive equation may be written in the form:

$$k = \frac{\beta \ \pi R_p^4}{8 l^2} \tag{3.28}$$

with β as a parameter which varies from distribution to distribution.

Previous authors have utilised percolation theory to predict permeability, (Katz and Thompson, 1986, 1987; Thompson et al, 1987, 1988), and their predictions appear to be in good agreement with experiment. There is, however, a class of radius distributions for which the percolation radius cannot completely characterise the flow. These are called bimodal distributions and the case of a bimodal uniform distribution, shown in Figure 3.22, is now discussed. Consider a simple 3D cubic network, with P_C=0.2488 (cf. Table 3.2). Placing more than 25% of the pore radii in section (B) ensures that the percolation radius R_p lies in that sector. Now, the position of sector (A) can be varied, thus changing <r> while R_p remains constant. Hence the totai flow must vary, while R_p remains constant. This demonstrates that, in some cases, the percolation radius cannot completely determine the flow. It *can*, however, describe the flow for a bimodal uniform distribution when the percolation radius varies with the mean radius. It is only when R_p is fixed and <r> changes that this relationship breaks down.

This behaviour of bimodal distributions has been noted by Berman et al (1986), who also discuss other counter-examples to the AHL argument, one of which considers a conductivity distribution of the form:

$$h(g)=\frac{\alpha g_{\min}^{\ \alpha}}{g^{\alpha+1}} \quad g_{\min} < g < \infty \tag{3.29}$$

where $\alpha>1$ is a positive constant. The actual distribution considered by Berman et al set $\alpha=2$. More generally, however, it is straightforward to show that the average conductivity and resistance are given by:

$$\langle g \rangle = \left(\frac{\alpha}{(\alpha-1)} \right) g_{\min} \qquad \text{and} \qquad \langle g^{-1} \rangle = \left(\frac{\alpha}{(\alpha+1) g_{\min}} \right) \tag{3.30}$$

respectively. For $\alpha>1$, the average conductivity is clearly greater than the minimum conductivity g_{min}, but it can be demonstrated that this is not always true for the *percolation* conductivity, (g_p). This critical value is obtained from the conductivity equivalent of Equation (3.23) and is equal to:

$$g_p = \frac{g_{\min}}{p_c^{1/\alpha}} \tag{3.31}$$

If g_p is now to characterise the flow, then it must satisfy the Jensen inequality for the conductivity of the whole network (see Chapter 2). Substituting <g>, $\langle g^{-1} \rangle$ and g_p into the Jensen inequality leads to:

$$\left(\frac{\alpha-1}{\alpha} \right)^{\alpha} < P_c < \left(\frac{\alpha}{\alpha+1} \right)^{\alpha} \tag{3.32}$$

For a cubic lattice, with $P_c \approx 0.25$, this inequality is easily violated. For example, $\alpha=3$ gives $0.30 < P_c < 0.42$, which cannot be true. Thus it is clear that for this type of distribution, the percolation conductivity (and hence the percolation radius) cannot characterise the flow. Equation (3.4), derived in this work, *does*

appear to predict the correct power law behaviour, however, because it utilises the mean radius <r>. This is shown in Figure 3.23.

In most situations, it is clear that percolation theory can prove extremely useful when describing flow in a porous medium. It provides a simple description based upon the topology of the system, and the percolation radius nearly always characterises the flow through the network. Unfortunately, however, this property cannot be encapsulated into a single general formula valid for all distributions.

3.4 Comparisons Between The Extended Mean Radius Model, Effective Medium Theory And Percolation Theory.

It has already been shown that the three approaches described above are complementary; i.e. it is possible to define any one of <r>, g_m and R_p in terms of any other. Which approach yields the best results when applied to network models? The accuracy of each method is reflected in Table 3.4, from which it appears that the extended formula derived in this work (Equation 3.7) gives best results. This extended formula has the slight disadvantage that the parameter α has to be calculated for each distribution, but this may be quickly found after only a few network realisations. Indeed it should be remembered that all three approaches require some numerical analysis before any predictions can be made (including EMT, where g_m is usually found numerically from a transcendental equation).

With regard to single-phase transport, the new predictive permeability model described in this chapter has proven to be an important link between effective medium models and those derived from percolation theory. In the next chapter, the network modelling approach will be used once again; this time for the development of two-phase flow models.

Table 3.1 Average Errors Between Predicted And Calculated Permeabilities.

Distribution	α-Value	Ave. % Error Using 3.4	Ave. % Error Using 3.7
Uniform	1.465	43.0	0.9
Log-Uniform	0.05*	16.0	16.0
Truncated Normal	-0.355	7.2	4.7
Cubic	1.83	7.0	0.4
Exponential	1.005	0.35	0.2
Triangular	1.475	18.5	0.5

Table 3.2 Percolation Thresholds for a Variety of Lattice Geometries (after Stauffer and Aharony, 1992).

Lattice	Site	Bond
Honeycomb	0·6962	0·65271
Square	0·592746	0·50000
Triangular	0·500000	0·34729
Diamond	0·43	0·388
Simple cubic	0·3116	0·2488
BCC	0·246	0·1803
FCC	0·198	0·119
$d = 4$ hypercubic	0·197	0·1601
$d = 5$ hypercubic	0·141	0·1182
$d = 6$ hypercubic	0·107	0·0942
$d = 7$ hypercubic	0·089	0·0787

Table 3.3 Average Errors Between Calculated Permeabilities And Those Predicted By Percolation Theory.

Distribution	Ave. % Error Using $k=\pi R_p^4/(8a^2)$
Uniform	69.0
Log-Uniform	79.3
Truncated Normal	33.2
Cubic	41.0
Exponential	4.5
Triangular	53.7

Table 3.4 Error Comparison Of Eq. (3.7) With EMT And Percolation Theory.

Distribution	Ave. % Error Using (3.7)	Ave. % Error Using EMT (see below)	Ave. % Error Using Corrected Percolation Formula (see below)
Uniform	0.9	4.3	2.8
Log-Uniform	16.0	49.0	17.0
Truncated Normal	4.7	16.0	7.9
Cubic	0.4	0.5	0.5
Exponential	0.2	0.5	4.0
Triangular	0.5	1.5	2.5

Each distribution has been examined over several ranges: [1,10], [1,20], [1,50], [1,75], [1,100], and [1,200]. Values of α and β in the formulae below are averaged quantities which have been chosen in order to minimize the errors for a given *distribution.* They apply to the actual distributions themselves and not just to any particular range.

The formulae used in the above table are:

(i) Equation (3.7)

$$k = \frac{\pi}{8l^2}\langle r\rangle^4\left\{1+\alpha\left(\frac{\sigma}{\langle r\rangle}\right)^2\right\}$$

(ii) EMT Predictor

$$k = \frac{\pi g_m}{8l^2}$$

(iii) Corrected Percolation Predictor

$$k = \frac{\beta\pi R_p^4}{8l^2}$$

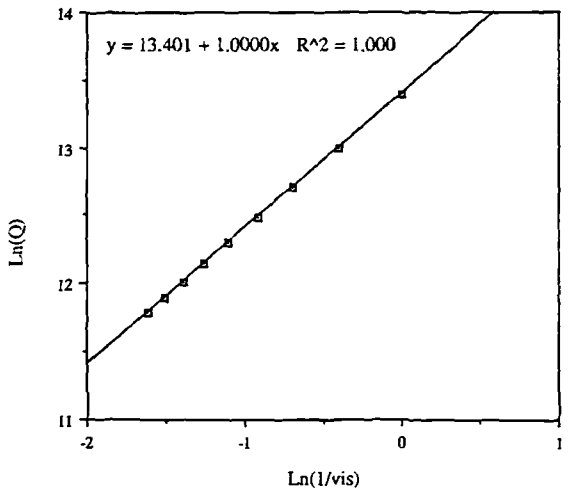

Figure 3.1 Log-log plot of total flowrate (Q) vs fluid viscosity for a 20x10x10 network.

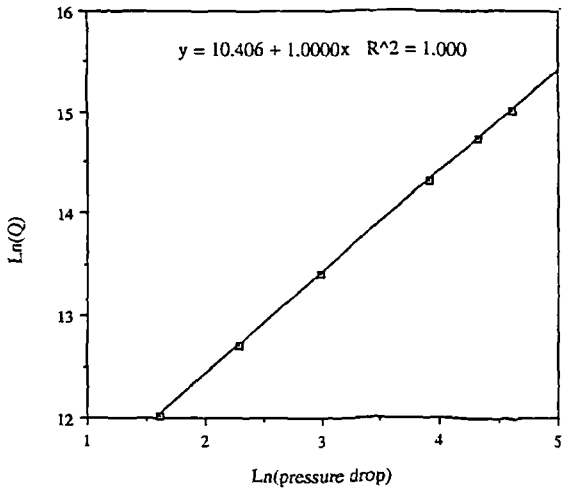

Figure 3.2 Log-log plot of total flowrate (Q) vs pressure drop for a 20x10x10 network.

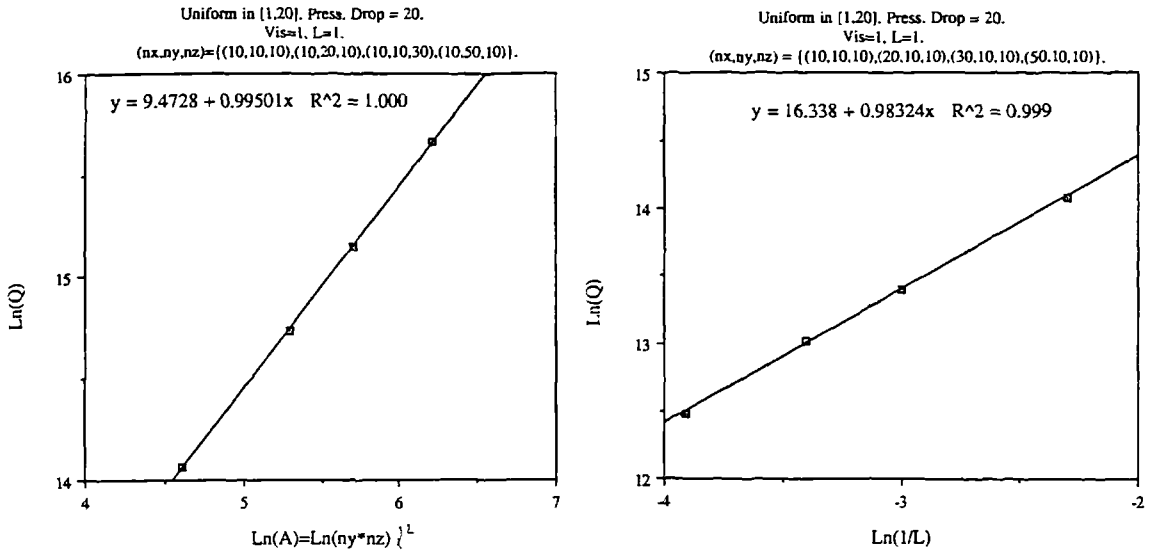

(a) (b)

Figure 3.3 (a) Log-log plot of total flowrate vs cross-sectional area for a variety of network sizes, (b) flowrate vs network length.

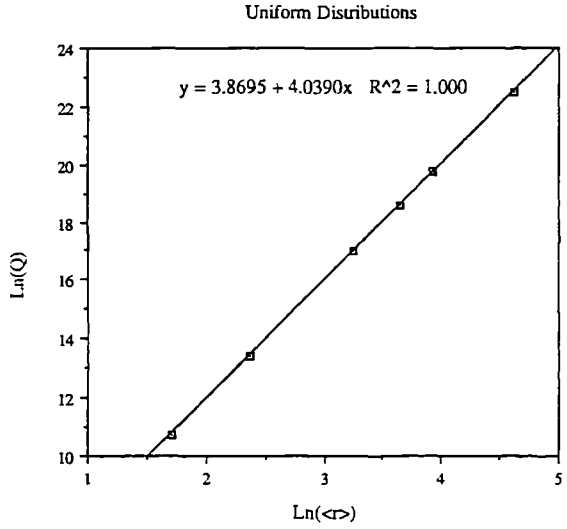

Figure 3.4 Log-log plot of total flowrate vs mean radius: radii sampled from Uniform distributions.

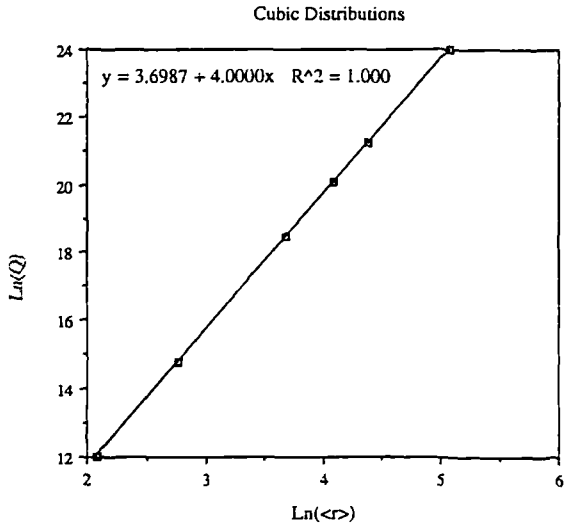

Figure 3.5 Log-log plot of total flowrate vs mean radius: radii sampled from Cubic distributions.

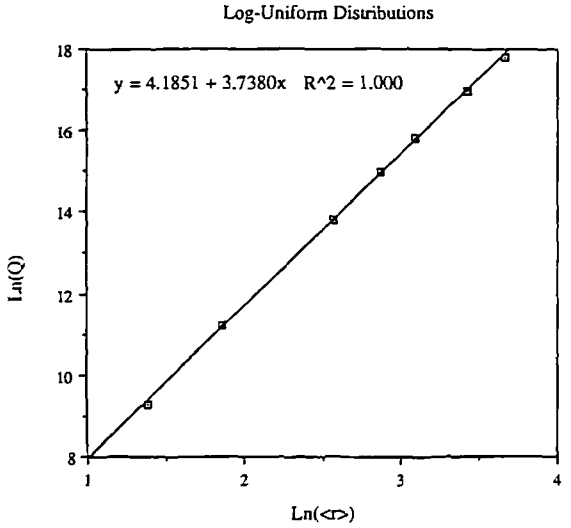

Figure 3.6 Log-log plot of total flowrate vs mean radius: radii sampled from Log-Uniform distributions.

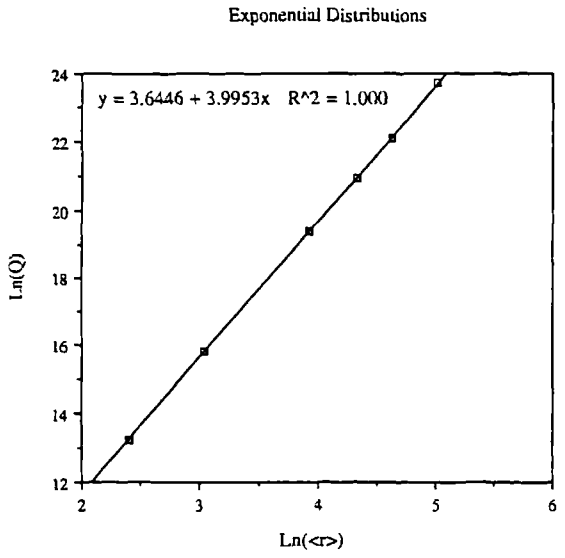

Figure 3.7 Log-log plot of total flowrate vs mean radius: radii sampled from Exponential distributions.

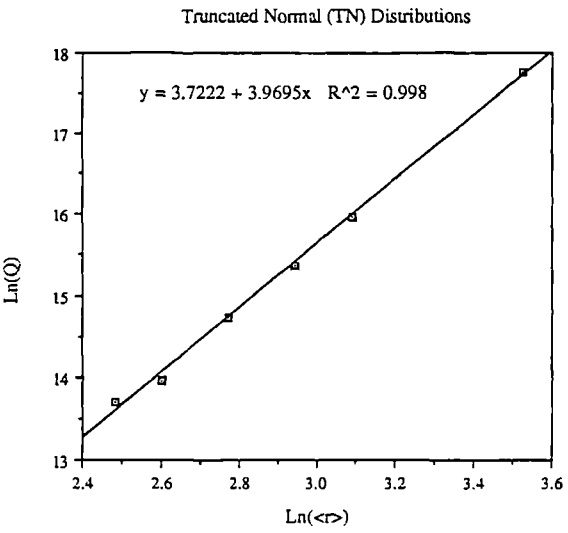

Figure 3.8 Log-log plot of total flowrate vs mean radius: radii sampled from Truncated Normal distributions with varying r_{bar}.

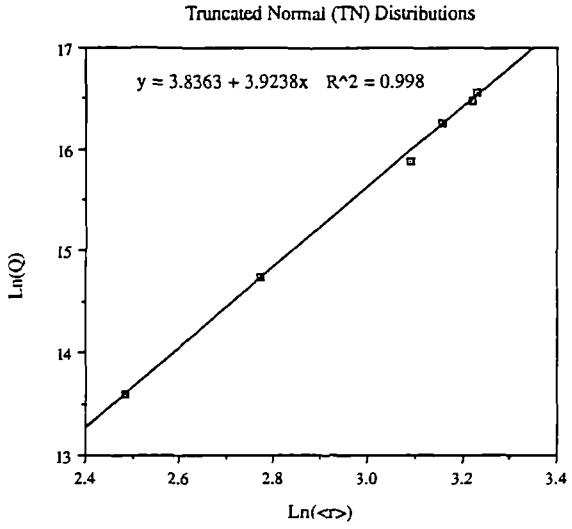

Figure 3.9 Log-log plot of total flowrate vs mean radius: radii sampled from Truncated Normal distributions with varying σ

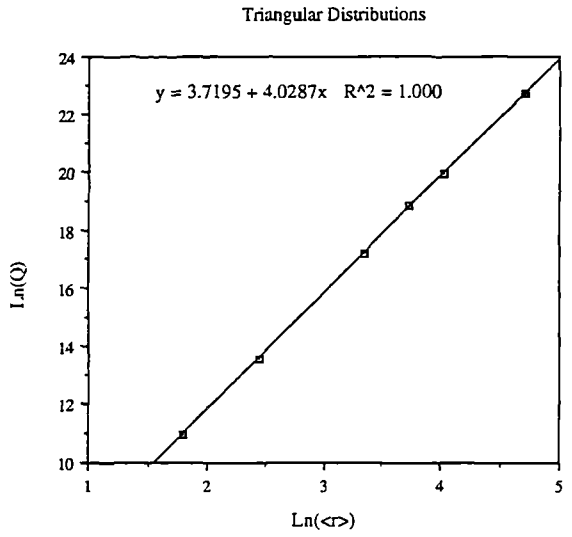

Figure 3.10 Log-log plot of total flowrate vs mean radius: radii sampled from Triangular distributions.

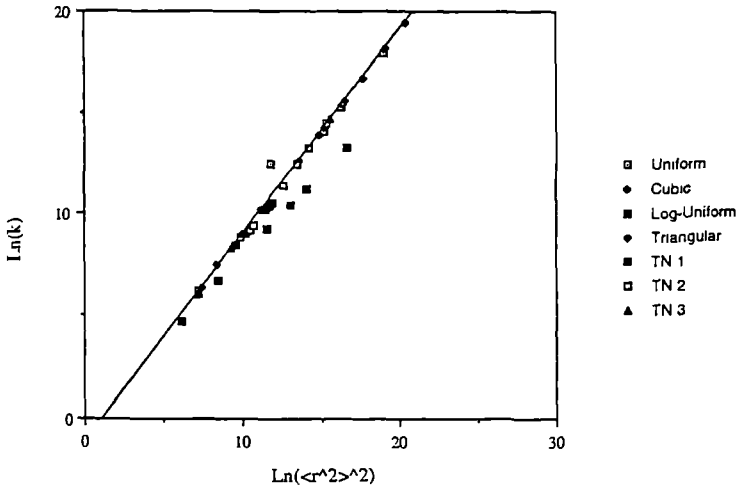

Figure 3.11 Log-log plot of network permeability (k) vs $\langle r^2 \rangle^2$ for a variety of different pore-size distribution functions.

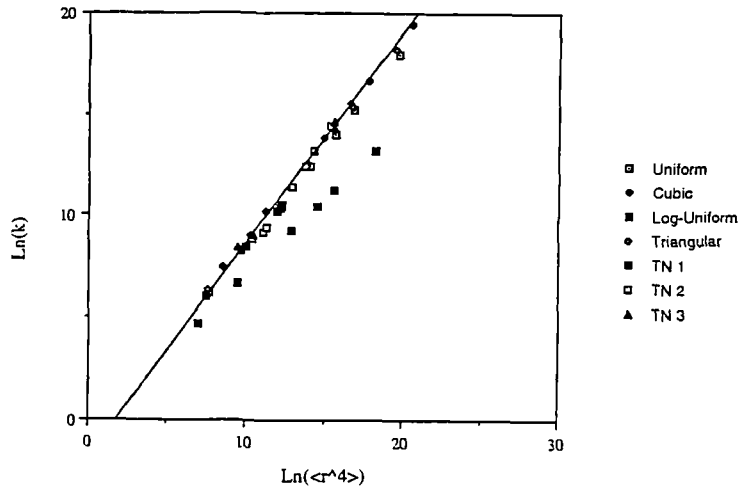

Figure 3.12 Log-log plot of network permeability (k) vs $\langle r^4 \rangle$ for a variety of different pore-size distribution functions.

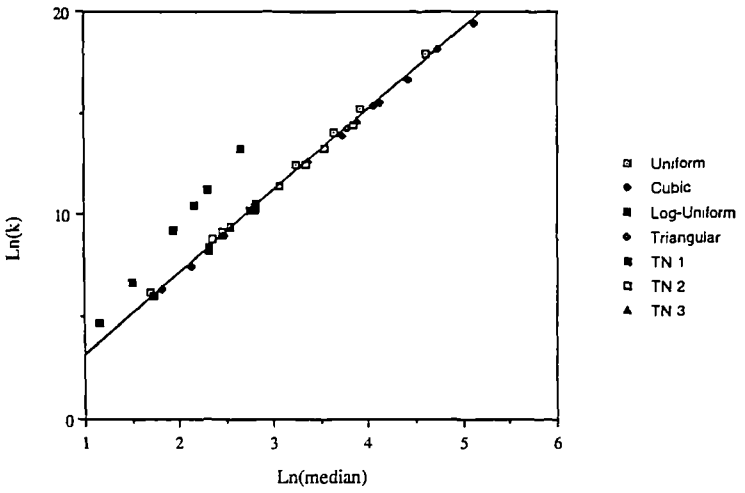

Figure 3.13 Log-log plot of network permeability (k) vs median radius for a variety of different pore-size distribution functions.

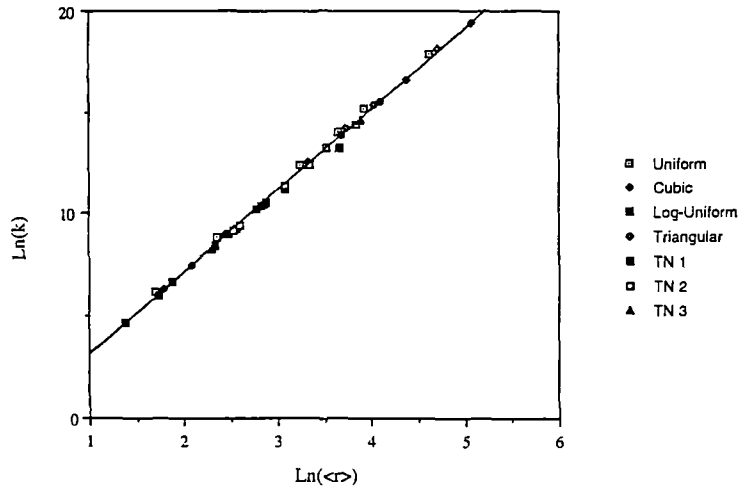

Figure 3.14 Comparison of Equation (3.4) (solid line) with network simulation results for various distribution functions.

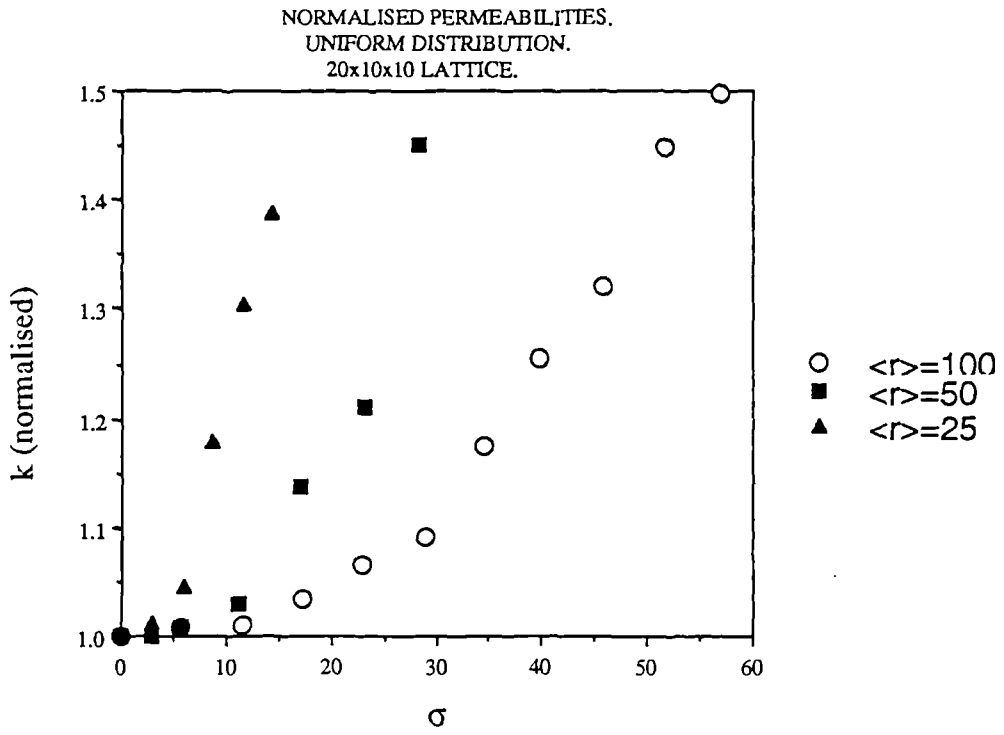

Figure 3.15 Effect of standard deviation (σ) upon network permeability for Uniform radius distributions.

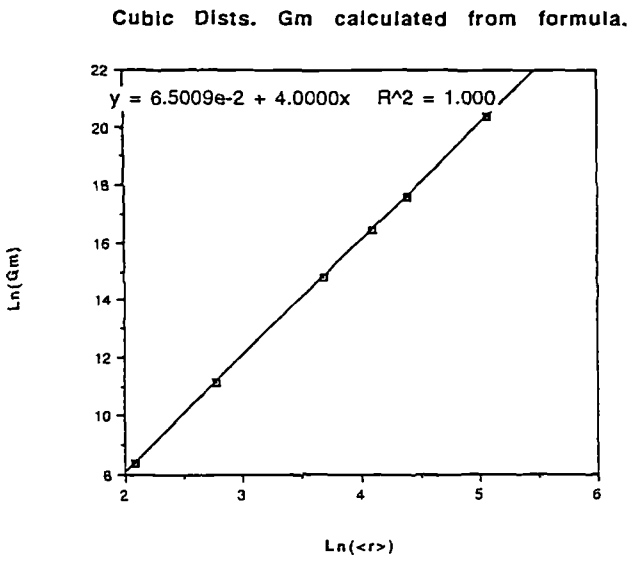

Figure 3.16 Log-log plot of effective medium conductivity (g_m) vs mean radius for a Cubic radius distribution.

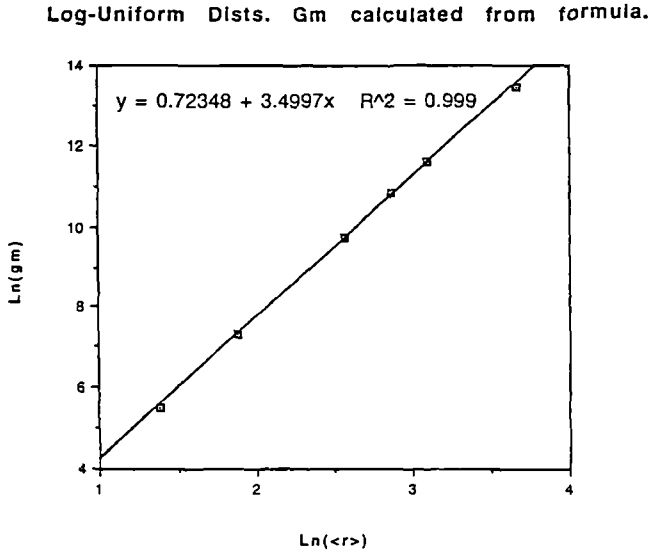

Figure 3.17 Log-log plot of effective medium conductivity (g_m) vs mean radius for a Log-Uniform radius distribution.

(a)

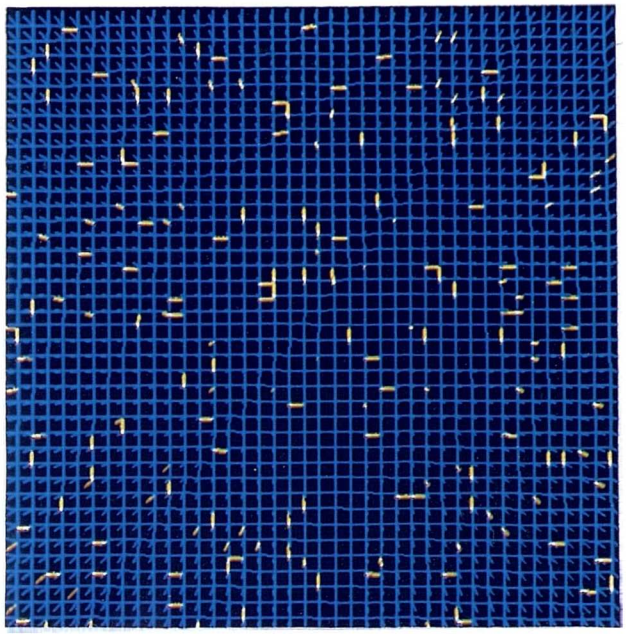

(b)

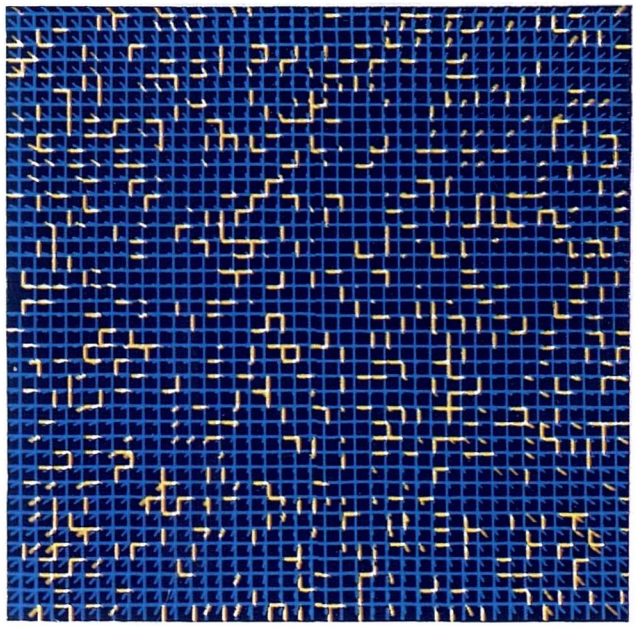

Figure 3.18 A pure percolation process on a regular square lattice. Yellow bonds are open, blue bonds are closed, red bonds belong to the spanning cluster: (a) p=0.04, (b) p=0.15, (c) p=0.255, (d) p=0,31, (e) p=0.49, (p=fraction of open bonds).

(c)

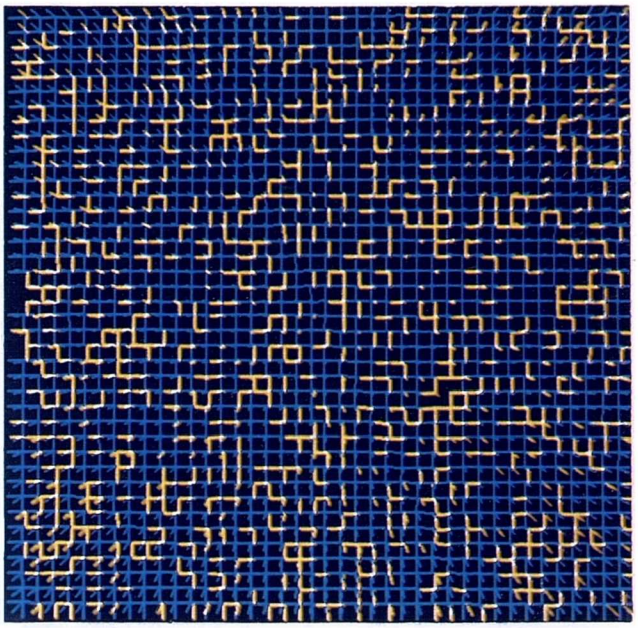

(d)

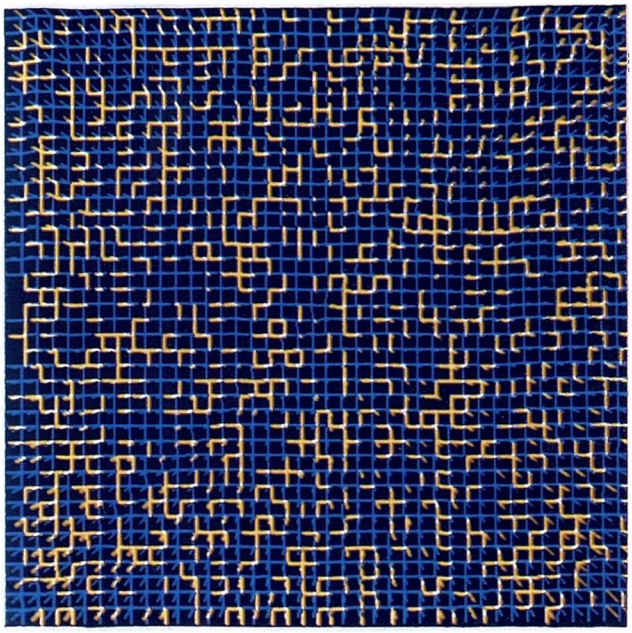

(e)

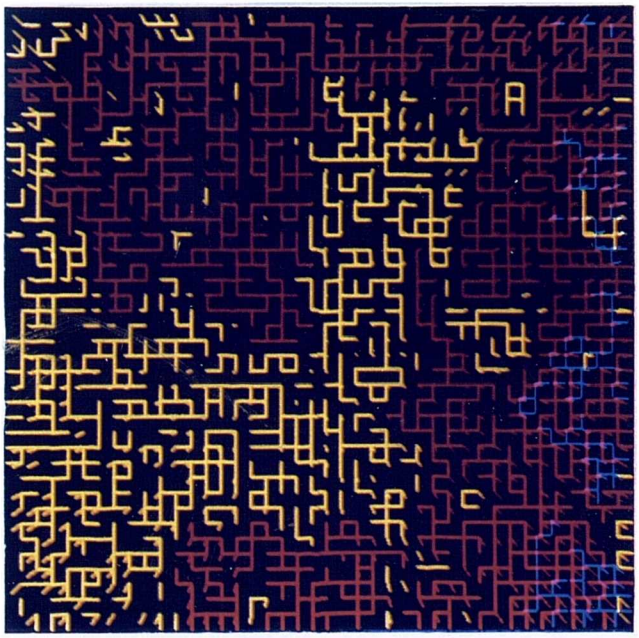

Figure 3.18 (Continued)

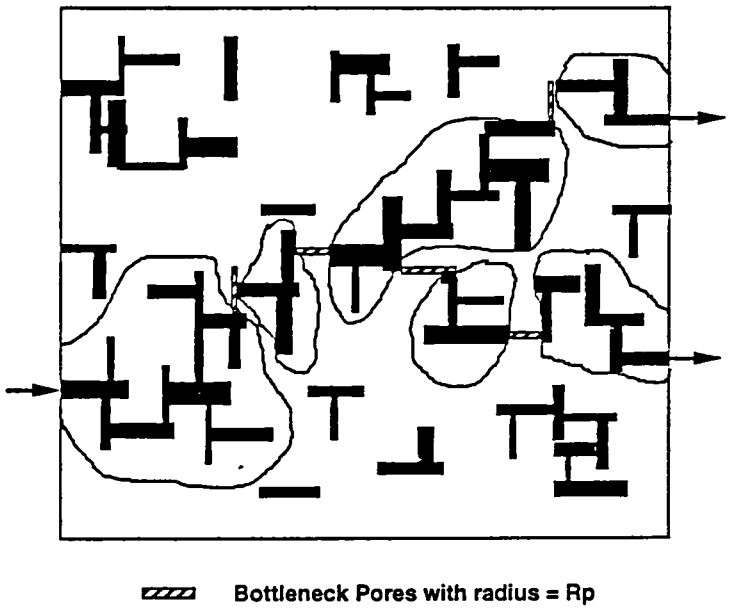

Figure 3.19 Schematic showing how flow must pass through bottleneck pores of radius R_p once a spanning cluster has formed.

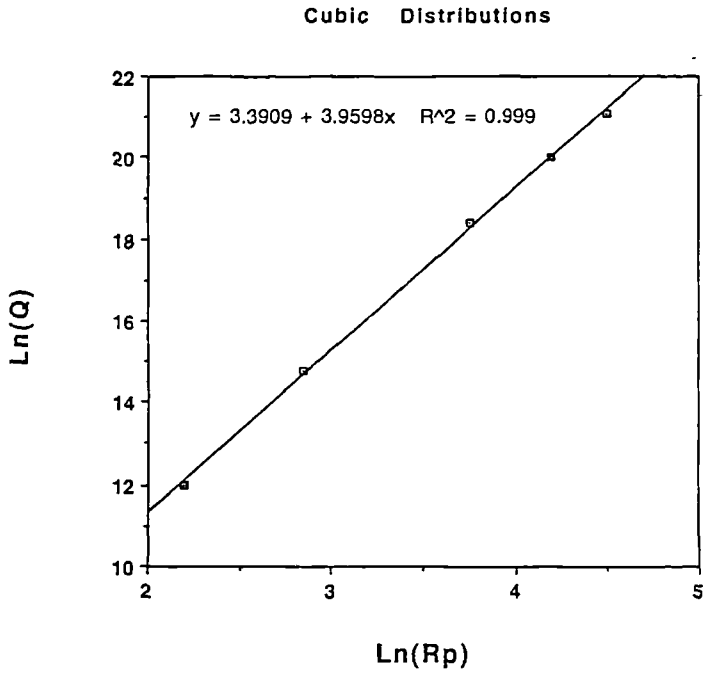

Figure 3.20 Log-log plot of total flowrate vs percolation radius (R_p) for a Cubic radius distribution.

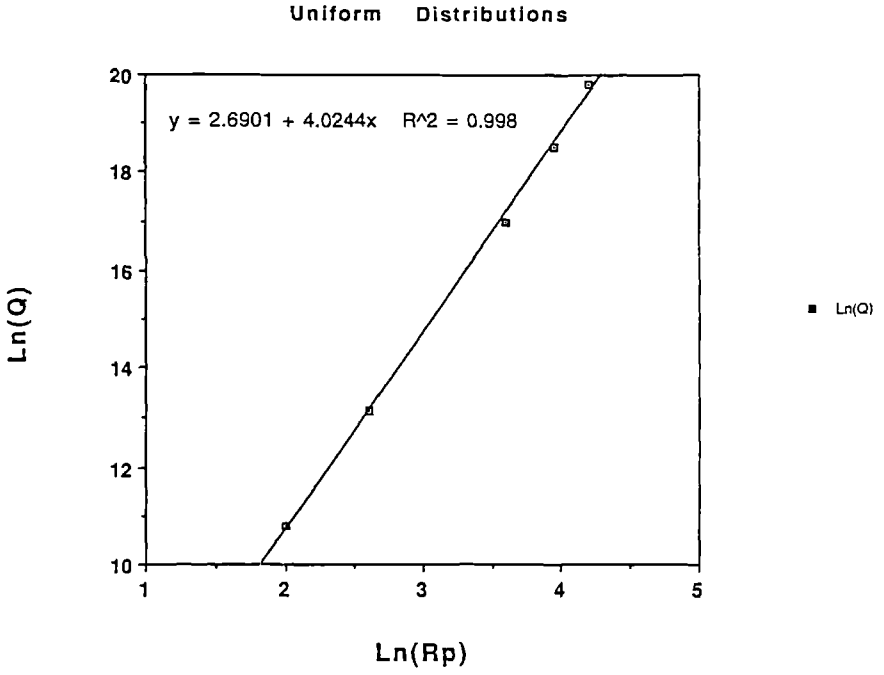

Figure 3.21 Log-log plot of total flowrate vs percolation radius (R_p) for a Uniform radius distribution.

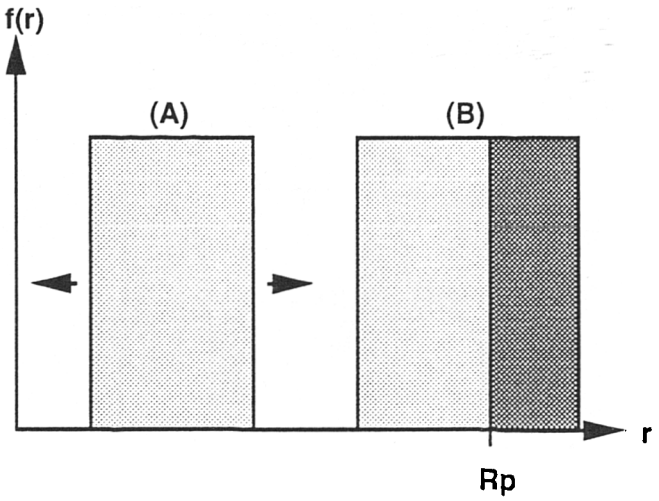

Figure 3.22 Bimodal Uniform radius distribution. By fixing (B) and varying (A), the mean radius changes whilst the percolation radius remains fixed.

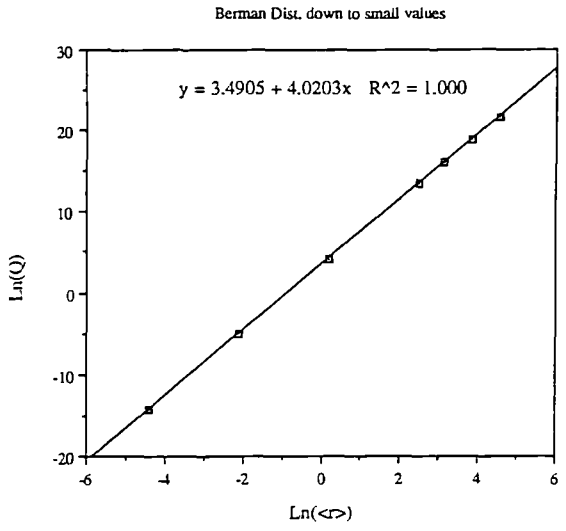

Figure 3.23 Log-log plot of total network flowrate vs mean radius: radii sampled from the distribution used by Berman et al.

CHAPTER 4 TWO-PHASE FLOW IN STRONGLY WATER-WET SYSTEMS

4.1 Introduction

The last chapter described how concepts from percolation theory could be used to describe the flow of a single liquid in a porous medium. The aim of this chapter is to broaden the understanding of *two*-phase flow in porous media; more specifically, to the simultaneous flow of oil and water through reservoir rock. To this end, concepts from percolation theory are utilised more fully. The physical porous medium is once again simulated using a capillary network, but now each element may contain a different fluid: either water or oil. In the parlance of percolation theory, this type of analogue is commonly known as a bond percolation model. Before dealing directly with percolation issues, however, it will be beneficial to first discuss some of the more general aspects of two-phase flow, such as phase distributions and relative permeabilities.

4.2 Steady- and Unsteady-State Flow

When dealing with any process involving multiphase flow, it is important to distinguish between steady-state and unsteady-state regimes. With regard to flow in porous media, the former is characterised by phase saturations that are invariant with time; that is, the volume flux of each fluid entering the system is the same as that leaving. Consequently, there are no pore-scale displacements of any kind once steady-state has been reached, and each phase tends to flow within its own tortuous network of pores. In contrast to this, unsteady-state flow is accompanied by almost continuous saturation changes, implying displacement of one fluid by another. Note that the two categories are seldom independent, however, as steady-state conditions can only be achieved once some degree of unsteady-state displacement has taken place to redistribute the phases.

Although the "channel flow concept" of steady-state flow outlined above appears to be generally valid (Craig, 1971), there are certain conditions under which this assumption may be questioned. If there is no strong wetting preference for the matrix, for example, or if the interfacial tension between the two fluids is very small, then a slug-like flow regime may develop. Alternatively, if the flow channels are rough and have an irregular cross-section (which is almost always the case in natural rock material), then the wetting phase will tend to line the channel walls and the nonwetting phase will usually reside in the centre of pores. Such phenomena can play a vital role in determining phase distributions during a variety of displacements, and their effects cannot always be overlooked.

4.3 The Relative Permeability Concept

For a single fluid in a porous medium, the permeability can be thought of as the ease with which the fluid flows through the sample. This is usually quantified by Darcy's law:

$$q = -\frac{k}{\mu}\nabla P \tag{4.1}$$

where q is the liquid velocity, μ the fluid viscosity and ∇P the pressure gradient. In single-phase flow, the permeability k depends mainly upon the geometry of the medium and in particular its degree of interconnectedness. When there are two immiscible liquids present, however, the permeability to one liquid will also depend upon the saturation of the other. The presence of this second liquid will effectively reduce the number of flow paths available to the first. Hence, as the phase saturations change, so too do the permeabilities. This concept was first postulated by Muskat and Meres (1936), and is based upon an extension of Darcy's law to two-phase flow, namely:

$$q_1 = -\frac{k_1}{\mu_1}\nabla P_1 \tag{4.2}$$

$$q_2 = -\frac{k_2}{\mu_2}\nabla P_2 \qquad (4.3)$$

when k_1 and k_2 are the *effective permeabilities* of fluids 1 and 2 at a given saturation. For convenience k_1 and k_2 are usually normalised by the absolute permeability (k), i.e. $k_{r1}=k_1/k$ and $k_{r2}=k_2/k$ to give *relative permeabilities,* although there are other definitions (Hornapour et al, 1986). The two Darcy equations consequently take the form:

$$q_1 = -\frac{kk_{r1}}{\mu_1}\nabla P_1 \qquad (4.2)'$$

$$q_2 = -\frac{kk_{r2}}{\mu_2}\nabla P_2 \qquad (4.3)'$$

Oil/water relative permeabilities are usually plotted as functions of water saturation and will depend (amongst other things) upon the interaction between the two liquids, characterised by the contact angle at the interface and the value of the interfacial tension. Although relative permeability is fairly easy to understand conceptually, there are many subtleties associated with it: some of these will become apparent later.

4.4 Laboratory Determination of Relative Permeability

Relative permeabilities can be measured using either steady-state or unsteady-state methods: unsteady-state measurements can usually be completed in a much shorter time, and have consequently become the oil industry standard. The question as to whether such rapid measurements are representative of conditions in the reservoir, however, is a matter of some debate.

4.4.1 Steady-State Methods

Steady-state methods are characterised by simultaneous injection of the two phases at a fixed ratio and known flowrates. Steady-state conditions are assumed to have been reached once the inlet and outlet fluxes of each phase have equilibrated and/or a constant pressure drop is seen to exist across the sample. This may take many hours or even days, depending upon the type of material under investigation and the measurement technique being used. Once equilibration has been reached, Darcy's law can be used for each phase in turn, resulting in a pair of relative permeability values valid at that particular saturation. The fluid flux ratio is then changed (whilst keeping the *total* flowrate constant), yielding a second set of data once a new steady-state has been achieved. Similar measurements for a number of different flux ratios can then be used to give a set of relative permeability curves which span the entire saturation range. Although the time involved in extracting such data is clearly an important concern, steady-state measurements performed at low rates should be considered most indicative of reservoir behaviour. Typical laboratory steady-state relative permeability curves are shown in Figures 4.1 and 4.2. Some of the more popular experimental techniques will now be discussed.

The Penn-State Method — Originally designed by Morse et al (1947), this technique has recently become one of the most popular. A typical apparatus is shown in Figure 4.3 and essentially consists of three similar core plugs mounted in a core holder with a pair of pressure tappings. Only the central plug is considered for measurement purposes; one of the two outer units acting as a mixer at the inlet, whilst the other serves to alleviate capillary end effects at the outlet. The three-plug assembly also facilitates dismantling of the test section for saturation measurements to be carried out. The method can be used for both liquid-liquid and liquid-gas measurements and has been used over a wide range of wettability conditions.

The Hassler Method — The laboratory apparatus used for this type of steady-state test is shown in Figure 4.4. Semi-permeable membranes are positioned at both the inlet and outlet ends of the core sample, which serve to separate the test fluids outwith the sample whilst permitting two-phase flow to take place within it. The importance of this is that allows the two pressure drops to be regulated independently, enabling equilibration of the capillary pressure at both ends of the core. This procedure is designed to provide a uniform saturation distribution throughout the system, and thus eliminate any capillary end effects.

The Dispersed-Feed Method — This technique was devised by Richardson et al (1952) in an attempt to introduce the fluids to the test sample in a more appropriate manner. It utilises an upstream dispersing medium in order to spread the wetting phase uniformly across the face of the test sample before entering it. The nonwetting phase is injected into radial grooves that are machined into the downstream end of the dispersing section, at its boundary with the core plug. A similar concept lies behind the Hafford apparatus, which injects nonwetting fluid directly into the sample, whilst the wetting phase must first pass through a central semi-permeable membrane. Again, the idea is to obtain more realistic injection behaviour.

Richardson et al (1952) have compared a variety of steady-state methods, and conclude that all four of the techniques outlined above should give very similar drainage relative permeability-saturation curves.

4.4.2 Unsteady-State Methods

Although unsteady-state relative permeability measurements can be made much more rapidly than those requiring steady-state equilibration, analysis of the resulting data is more difficult and open to a certain degree of ambiguity.

In unsteady-state tests, one phase is displaced directly from the core sample by the injection of another, at a rate high enough such that capillary pressure remains negligible. An analysis of the resulting production data, based upon the Buckley-Leverett frontal advance theory (Buckley and Leverett, 1942), then permits the determination of a relative permeability ratio (k_{rw}/k_{ro}). The relevant theory was given by Welge (1952), who demonstrated that:

$$f_o = \frac{1}{1 + \frac{\mu_o k_{rw}}{\mu_w k_{ro}}} \tag{4.4}$$

where f_o is the fraction of oil in the outlet stream, and the μ_i are viscosities. This was later extended by Johnson et al (1959), who developed a technique for calculating the *individual* relative permeabilities from the permeability ratio. Several other methods also exist (Saraf and McCaffery, 1982; Jones and Roszelle, 1978; inter alia).

In the past, much work has been carried out to compare these unsteady-state results with their steady-state equivalents. Unfortunately, although the outcomes appear to be broadly in agreement, there have been a number of exceptions (e.g. Schneider and Owens, 1970; Owens et al, 1965; Loomis and Crowell, 1962; Archer and Wong, 1971). The limitations of the unsteady-state approach for determining water-oil relative permeabilities have been discussed more fully by Craig (1971): the main concerns relate to the high pressure differentials involved (in excess of 50psi), and the fact that large viscosity ratios are often used in an attempt to extend the range of two-phase flow. The general applicability of the resulting data must consequently be called into question.

4.4.3 Centrifuge Methods

Although not commonly used, centrifuge techniques can provide useful results extremely rapidly, with the added bonus that they are thought to be free of the viscous fingering problems that accompany many other unsteady-state methods. They are, however, subject to problems associated with capillary end effect and cannot be used to quantify the relative permeability of the displacing phase. Such methods involve monitoring the production from samples that are initially saturated with one or two phases, with analytical techniques being used to back-out relative permeability values (see Van Spronsen, 1982, for a fuller account).

4.5 The Effects of Flowrate, Viscosity Ratio, and Interfacial Tension.

At sufficiently low flowrates, microscopic flow behaviour should always be capillary-dominated if the system has a strong wetting preference. At such rates, relative permeabilities in the medium saturation range should consequently be independent of the viscosity ratio, and this conclusion appears to have been borne out by many subsequent investigations (Leverett et al, 1939, 1941; Wyckoff and Botset, 1936; Saraf and Fatt, 1967; Levine, 1954). Near the endpoints, however, and in cases where the wetting phase is flowing only through thick films, there sometimes exists a strong hydraulic *coupling* between the two phases. As a result, the nonwetting phase may experience hydraulic slip and any analysis using Darcy's Law becomes invalid. If Darcy's law is applied regardless, however, nonwetting phase relative permeabilities greater than unity can often be the result: the experimental results of Odeh (1959) clearly demonstrate this effect (Figure 4.5). If high rates are used in relative permeability measurements, the subsequent flow behaviour will no longer remain capillary-dominated, and viscous forces will tend to take over. Moreover, if the associated viscosity ratio is high, then the less viscous invading fluid will begin to finger through the sample and a condition of uniform saturation will be impossible to achieve. With this in mind, it is clear

that such considerations should not be overlooked when attempting to interpret a wide variety of unsteady-state coreflood data.

The effect of interfacial tension upon relative permeabilities can also be significant. In cases where the experimental flowrate is high and the interfacial tension is small, the capillary forces become less significant and slugs of both fluids may begin to flow through the same network of pores. In fact, as the interfacial tension approaches zero, the relative permeability curves actually become straight diagonal lines: i.e. the total effective mobility of the system remains constant over the entire saturation range. Experimental results showing this effect are reproduced in Figure 4.6.

The full implications of the viscous/capillary force balance upon microscopic flow behaviour will be considered more fully in Chapter 6.

4.6 Relative Permeability Models

There are presently four broad categories of mathematical model in general use for the prediction of relative permeability curves: capillary models, statistical models, empirical models and network models. Capillary models take no account of the interconnected nature of a porous medium and are therefore inadequate in dealing with two-phase flow. Statistical models appear likewise, unless they specifically consider the tortuous structure within the porous medium. The fact that both have to rely upon a certain degree of empiricism if reasonable predictions are to be forthcoming, means that empirical formulae themselves are still currently the most popular. Recent improvements in computer capability, however, have motivated a number of studies (including the present one) to re-examine the two-phase capabilities of network modelling techniques.

4.6.1 Capillary Models

A typical example of the capillary analogue is the relative permeability model devised by Fatt and Dykstra (1951). It is an extension of the simple, single-phase capillary bundle model described in Chapter 3 and is based upon the assumptions that; (i) the length of each flow path (L_e) is greater than the actual length of the sample (L), and (ii) the length of each flow path may differ according to its diameter. After some analysis, the final result takes the form:

$$\frac{dk_i}{dS_i} = \frac{D_e^2 \phi L^2}{32 L_e^2} = \frac{D_e^2 \phi}{32T} \tag{4.5}$$

where D_e is an effective flow diameter and T is a "tortuosity function" which must be correlated with S_i before any complete solution can be attempted. As with all capillary models, the physical meaning of such parameters remains somewhat unclear.

4.6.2 Statistical Models

A wide variety of statistical models have been proposed in the past (see Honarpour et al, 1986), many of which attempt to encapsulate the underlying pore structure by the so-called "cut-and-random-rejoin" technique (Childs and Collis-George, 1950; Wyllie and Gardner, 1958). This model begins by considering a bundle of capillary tubes with diameters chosen from a probability distribution function f(D), within the range $D_{min} < D < D_{max}$. This bundle is then cut into many slices perpendicular to the tube axes, the short tube segments are then rearranged randomly, and finally the slices are reconstructed. A statistical analysis of the resulting sample, when combined with Laplace's equation, Poiseuille's law and Darcy's law, eventually yields the equations:

$$k_{rw} = S_{eff}^2 \frac{\int_0^{S_{eff}} \frac{dS_{eff}}{P_c^2(S_{eff})}}{\int_0^1 \frac{dS_{eff}}{P_c^2(S_{eff})}} \tag{4.6}$$

$$k_{rw} = (1 - S_{eff})^2 \frac{\int_{S_{eff}}^{1} \frac{dS_{eff}}{P_c^2(S_{eff})}}{\int_{0}^{1} \frac{dS_{eff}}{P_c^2(S_{eff})}} \tag{4.7}$$

where $S_{eff}=(S_w-S_{wi})/(1-S_{wi})$. Similar equations were also obtained by Burdine (1953) using hydraulic radius theory, and have been employed with varying degrees of success.

4.6.3 Empirical Models

Although the models described above yield relative permeability curves that are qualitatively reasonable, reproduction of experimental data is only achieved via the introduction of some form of empiricism. Many studies have subsequently relied entirely upon empirical curve fitting techniques. One of the most popular empirical correlations is that due to Corey (1954), who proposed the following:

$$k_{rw} \propto S_{eff}^4 \tag{4.8}$$

$$k_{rnw} \propto (1 - S_{eff})^2 (1 - S_{eff}^2) \tag{4.9}$$

However, it was soon discovered (not surprisingly) that the exponents in Corey's original equations would have to be varied in order to fit different materials. They were consequently generalised by Brooks and Corey (1964) to:

$$k_{rw} = S_{eff}^{(2+3\lambda)/\lambda} \tag{4.10}$$

$$k_{rnw} = (1 - S_{eff})^2 (1 - S_{eff})^{(2+\lambda)/\lambda} \tag{4.11}$$

$$S_{eff} = (P_{cb}/P_c)^{\lambda} \qquad (P_c \geq P_{cb}) \tag{4.12}$$

with P_{cb} representing the breakthrough capillary pressure and λ the "pore size distribution index". Both of these parameters have to be determined experimentally: S_{eff} vs P_c data is plotted on a log-log scale and a straight line fitted, the slope gives λ and the intercept with $S_{eff}=1$ is assumed to give P_{cb}. Many similar models exist, but their downfall lies in the fact that nothing can be predicted *a priori*.

It is quite apparent from this discussion that no satisfactory predictive model currently exists which can adequately account for the complex jumble of channels that pervade a porous medium. One of the most promising developments of recent years, however, has been the possibility of applying interconnected network models to the study of microscopic flow. Before describing how such a model has been utilised here, however, some related theory will first be examined.

4.7 Percolation Theory and Critical Exponents.

Percolation theory was discussed earlier in Chapter 3 with regard to single-phase flow. In this section, the concepts are extended to enable two-phase displacements to be considered. The real power of percolation theory is that it can be used to describe the behaviour of systems right down to percolation threshold. This consequently provides detailed information about a variety of features of the system: for instance, it provides a relationship between the mass of a phase spanning cluster (the number of pores in a cluster which connects a particular phase across two opposite faces of the network) and the total fraction of pores containing that phase. Percolation arguments also provide approximate formulae connecting the *conductivity* of each phase to the invaded pore fraction.

Some ideas from percolation theory will now be discussed in the context of a simple model of *two*-phase flow. This is not intended to be a definitive model, but rather a first step towards a more comprehensive treatment of the problem. Despite its simplicity, it will be seen that this model provides a good basis for the development of a realistic simulation. It also has the advantage of giving scaling criteria for the relative permeabilities of each phase during a simulation.

Begin by considering the case of approaching the percolation threshold at random. This means that, initially, all of the pores are filled with the defending fluid, and an increasing percentage of pores are filled with the displacing phase at random (i.e. the order of filling having no pore radii preference). This continues until the network is completely full of the invading phase; at any time, the fraction of invaded pores is denoted by p. This type of problem has been studied by Kirkpatrick (1973) using resistor networks, and by Wilkinson (1988) using capillary networks.

Consider now the *clustering behaviour* as the pores are filled at random. A cluster is an isolated pore or any collection of connected pores, and a quantity of particular interest is the total number of clusters in the network. A modified Hoshen-Kopelmann (1976) algorithm was used to follow the clustering process, the details of which are presented in Appendix E. Figure 4.7 shows the variation of the total number of clusters as a function of p, the fraction of invaded pores, for a regular cubic network. The overall form of this curve is the same for all of the distributions considered; this is as would be expected, of course, because it is the spatial distribution of invaded pores that is of most importance, not the size of individual capillaries. Note that by the time percolation threshold P_c is reached, there is a substantial decrease in the total number of clusters. This behaviour can be explained in the following manner; initially, as pores are invaded, the total number of clusters (N_{clus}) increases until a certain saturation is reached. These small clusters then begin to

aggregate to form extended clusters until, at $p=P_c\approx0.2488$, there is a cluster that crosses the entire network, the *spanning cluster*. This point is illustrated in the three-dimensional simulations shown in Figure 4.8. After $p=P_c$ has been reached, the system is dominated by the spanning cluster together with a few isolated clusters. The fractal, dendritic structure of this growing spanning cluster gives a fascinating insight into how phase distributions look in three dimensions. Note that in a finite system it is possible for a spanning cluster to form slightly above or below P_c and that there may be more than one (although throughout the work carried out here, consisting of many hundreds of calculations on large networks, no more than one spanning cluster has ever been found). In the case of an infinite system, there is a unique spanning cluster (Grimmett, 1989). Having briefly outlined the clustering behaviour of a typical random process, attention is now turned towards validating the model against well-documented percolation scaling exponents.

Denoting the fraction of pores in the spanning cluster by M(p), it is well known from percolation theory that M(p) scales as $(p-p_c)^\beta$ where $\beta\approx0.45$: Figure 4.9 shows the result of a typical run, which serves to highlight the problem of finite size effects when dealing with relatively small networks. The so-called critical exponents of percolation theory are derived from massive calculations using the latest computer technology, and so one can never hope to match these parameters exactly here: this is why a slightly different value of β has been obtained (0.355 as given by the slope of the best fit line). A second critical exponent can be used to characterise the cluster distribution of the displacing phase as it approaches percolation threshold. If $n_s(P_c)$ denotes the number of clusters of size s at the percolation threshold, it can be shown that the relevant scaling approximates $s^{-\tau}$ where $\tau\approx2.2$; see, for example, Stauffer (1985) or Efros (1986). The result of a small-scale simulation is shown in Figure 4.10. There is also an exponent which relates to the corresponding conductance of the network. This appears to scale as $(p-p_c)^t$, but there is still some uncertainty

relating to the value of t. Percolation theory suggests that it should be a universal quantity, at least in the vicinity of the percolation threshold, and Zapolitzky (1984) gives a value of t=2.0: further computations are currently on-going, however. Table 4.1 summarises the various values that have so far been proposed.

The main utility of these exponents lies in their application to larger systems and their associated scaling potential. Although they can be extremely useful in scale-up issues, their importance will not be over-emphasised in this work: this study is more concerned with sensitivity issues and pore-scale phenomena than quantitative extrapolation. The earlier details relating to clustering behaviour and percolation thresholds will prove most useful in the discussions that follow. One drawback with percolation theory is that it gives important scaling parameters in terms of the filled pore *fraction*. Laboratory measurements, however, deal with *saturations*, and so some way must be found to relate the two before further progress can be made.

4.8 Saturation Predictions From Network Models.

The saturation of a liquid in a porous medium is defined as:

$$S_i = \frac{\text{Volume of liquid i present}}{\text{Total pore volume available}} \qquad (4.13)$$

In the case of two-phase flow, the notation S_O will be used for the saturation of the nonwetting fluid (oil) and S_W for the wetting fluid (water). Assuming that all of the pore space is occupied by those liquids, the saturations must satisfy the condition:

$$S_o + S_w = 1 \qquad (4.14)$$

In the model presented so far, the amount of each liquid present in the system has been represented by the *fraction* of water-filled and oil-filled pores, (p and (1-p), respectively). These fractions must now be related to the saturations as defined here.

Assume for the moment that the network is being filled from the "bottom up" (i.e. the network is initially 100% oil). Then, if pores have been filled up to and including the radius value R, the water saturation is given by:

$$S_w(R) = \frac{\int_{R_{min}}^{R} \pi r^2 L f(r) dr}{V_{total}} \tag{4.15}$$

where

$$V_{total} = \int_{R_{min}}^{R_{max}} \pi r^2 L f(r) dr \tag{4.16}$$

where L is the pore length, f(r) the distribution of pore radii, and cylindrical pore geometry has been assumed.

Equation (4.15) for S_W can be related to the fraction p of water-filled pores through the equation:

$$p = \int_{R_{min}}^{R} f(r) dr \tag{4.17}$$

Consider, for example, the case of a uniform tube radius distribution:

$$f(r) = \frac{1}{R_{max} - R_{min}} \qquad R_{min} \le r \le R_{max} \tag{4.18}$$

$$p = \int_{R_{min}}^{R} f(r) dr = \frac{R - R_{min}}{R_{max} - R_{min}} \tag{4.19}$$

Equation (4.15) gives:

$$S_w(R) = \frac{\int_{R_{min}}^{R} r^2\, dr}{\int_{R_{min}}^{R_{max}} r^2\, dr} \tag{4.20}$$

Hence:

$$S_w(R) = \frac{R^3 - R_{min}^3}{R_{max}^3 - R_{min}^3} \tag{4.21}$$

Combining Equations (4.19) and (4.20) now leads to the expression:

$$S_w(p) = \frac{1}{R_{max}^3 - R_{min}^3}\left\{\left[\left(R_{max} - R_{min}\right)p + R_{min}\right]^3 - R_{min}^3\right\} \tag{4.22}$$

Similarly, for a Cubic radius distribution:

$$p = \frac{R^4 - R^4_{min}}{R^4_{max} - R^4_{min}} \tag{4.23}$$

$$S_w(R) = \frac{R^6 - R^6_{min}}{R^6_{max} - R^6_{min}} \tag{4.24}$$

and so

$$S_w(p) = \frac{1}{R^6_{max} - R^6_{min}}\left\{\left[\left(R^4_{max} - R^4_{min}\right)p + R^4_{min}\right]^{3/2} - R^6_{min}\right\} \tag{4.25}$$

The various curves are illustrated in Figure 4.11. Although saturations are measured directly during network calculations, these closed-form relationships constitute an extremely useful link between S_w and p, and can be used most effectively when attempting to assess residual saturations at the end of a displacement. Differences between measured saturations and those predicted

by Equation (4.15) serve to highlight issues such as accessibility and pore shielding, which will be covered later.

The expressions defined above are for the total saturation of one phase in the network. Within each phase a distinction can be made between the saturation of the spanning cluster, flowing cluster and isolated clusters. This is illustrated in Figure 4.12 for bottom up filling: note that after the onset of flow there is a sharp decrease in the saturation of isolated clusters. Another interesting point to note is that the flowing cluster forms a *subset* of the spanning cluster: its growth will consequently be less marked than that of the spanning cluster.

4.9 Capillary Network Analogue of Two-Phase Flow.

A detailed discussion now follows to determine the extent to which the capillary network model is an analogue for two-phase relative permeability experiments. The model calculates the total flow through two intertwined networks (one for each phase) over a range of saturation values. Inherent in this is the assumption that the flow is stationary, thus steady-state relative permeabilities are considered here: for work on dynamic relative permeabilities see Blunt and King (1990). Measured relative permeabilities depend upon the saturation histories, saturation of the fluids, porespace morphology, wetting characteristics of the fluids, the ratio of the fluid viscosities and the capillary number. Some of these factors have not yet been accounted for in the present model, but will be incorporated in the next two chapters.

The first topic to be considered will be the simulation of various primary processes via different network filling regimes. A primary displacement is one in which the network is initially 100% full of one (defending) phase, which is then gradually replaced by a second (invading) phase. When a *wetting* fluid is invading the network the process is known as primary *imbibition*; when a *nonwetting* fluid is invading, the process is termed primary *drainage*. The

objective here will be to elucidate the most important factors affecting microscopic displacements and, in particular, the influence these may have upon the resulting relative permeability curves and residual saturations. Both drainage and imbibition processes will be investigated, and the network is initially assumed to be strongly water-wet in all cases (results for a strongly oil-wet system may be inferred immediately). Phase-trapping will be incorporated into the model, whereby tubes containing the defending phase are invaded only if a continuous pathway exists connecting them to the outlet face of the network. If not, the defending fluid remains "trapped". The problem then becomes one of "percolation with trapping", a concept first described by Dias and Wilkinson (1986).

Following the primary simulations, some secondary processes will be examined which successfully capture the well-documented hysteresis effect found between primary drainage and secondary imbibition relative permeability curves. It will also be shown that this phenomenon can be explained simply in terms of the wettability assumptions made at the beginning of the simulation.

4.9.1 Simulation Of Primary Processes

This section reports on the simulation of primary displacements. In all that follows, the wetting phase is assumed to be water and the nonwetting phase oil. All realisations were performed using a 3D regular cubic network comprising 15x15x15 nodes (junctions) which contained 10,350 intersecting pore elements. A number of larger systems were used confirm the main results. Each pore in the network was assigned a radius from a modified Rayleigh distribution:

$$f(r) = \frac{2(r - R_{min})\, e^{\frac{-(r-R_{min})^2}{\beta}}}{\beta\left(1 - e^{\frac{-(R_{max}-R_{min})^2}{\beta}}\right)} \qquad r \in [R_{min}, R_{max}] \qquad (4.26)$$

where β is parameter which determines the degree of skewness. The particular distribution used is shown in Figure 4.13 where R_{min}=0, R_{max}=100, and β= 1250. It was felt that this form fell somewhere in between typical pore size distributions calculated by mercury porosimetry and photomicrography. The flow through each capillary element is again given by Poiseuille's law, and conservation of mass at each node leads to a set of linear pressure equations. At each step the total flow is calculated separately for *each* of the intertwined networks. The results are then converted into normalised permeabilities as functions of saturation.

Pore-Filling Regimes — Twelve rule-based filling regimes have been examined during this study (see Table 4.2), some of which were physically realistic whilst others were not. Some have incorporated phase-trapping and others have allowed all defending fluid to escape whether or not this was topologically possible. Here, attention will be restricted to only three processes; BU, BU-TRAP, and INV-PERC-TD-TRAP, as these demonstrate the salient features of all twelve rule-bases.

Consider first the case of a strongly water-wet rock which is initially 100% saturated with oil. Several possible displacement mechanisms have been identified in two dimensions (Lenormand and Zarcone, 1984), one of which is known as "snap-off". When brought into contact with the water phase, a strongly water-wet rock will spontaneously imbibe the wetting fluid via film flow along irregularities on the pore surfaces. In effect, the water slowly wets all internal grain surfaces and is essentially present everywhere in the matrix. As this imbibition process continues, the thin films begin to swell; eventually the thinnest pores will become completely filled with water and the original oil

will be displaced if an escape route exists (Figure 4.14). This continues with the gradual filling of progressively wider pores until no further displacement is possible since the oil phase becomes disconnected. The process is therefore one of pure bond percolation with the added constraint of phase trapping. In the terminology of this study, the model to be used is "Bottom-Up Filling with Trapping" (BU-TRAP). The resulting imbibition relative permeability curves are shown in Figure 4.15 and are seen to correlate well with experimental observations

The simulation of low-rate drainage processes is carried out using a "top-down invasion percolation model with hydraulic trapping of the wetting phase" (INV-PERC-TD-TRAP). In this case, the injected nonwetting phase first fills the largest pores *connected to the inlet face of the network,* and then proceeds along progressively narrower pathways, sequentially occupying smaller and smaller pores (Figure 4.16). This model, first proposed by Chandler et al (1982) and Wilkinson and Willemson (1983), is basically the displacement mechanism governing mercury porosimetry experiments, which are considered separately in Appendix A. The simulated drainage relative permeability curves are shown in Figure 4.17 and again correlate well with experimental observation.

Before comparing different filling regimes, two important results will first be presented. The first of these relates to cluster growth and the second demonstrates the qualitative effects of phase trapping.

Cluster Growth — Consider a pure bond percolation problem such as the "snap-off" imbibition study described above. The bonds are filled at random *positions* throughout the network and, as the process continues, the number of wetting clusters (groups of connected water bonds) increases with the invaded pore fraction (p). However, as described earlier, above a certain value of p, these small isolated groups join together to form larger aggregates; hence the total

number of clusters begins to decrease. At percolation threshold, one water cluster emerges which spans the entire network from inlet to outlet. Remember, that for a 3-dimensional, regular cubic network (z=6), $P_c \approx 0.2488$ (Stauffer, 1985). Hence, when approximately one quarter of the pores have been invaded, the wetting phase can flow freely across the network. As more and more pores are filled, the total number of water clusters continues to diminish. At $p \approx 0.5$, almost all of the invaded pores form one large cluster (a few small clusters still exist, but eventually even these are "connected up" by the spanning cluster). Symmetry arguments show that the clustering behaviour of the nonwetting phase is analogous to that of the wetting phase. The two curves are shown superimposed in Figure 4.18, where it is apparent that the point $p = 0.5$ is of primary importance. It is at this point that the network essentially consists of two large clusters; one of wetting fluid, the other of nonwetting fluid. This will clearly influence the trapping behaviour of the system because, up until this point, all of the defending fluid will have existed as one large cluster and so escape towards the outlet would always have been possible. That is to say, when $p < 0.5$, a continuous escape route of defending fluid will always be available, even though almost half of the network has already been invaded. Thus, whatever assumptions concerning pore occupancy exist for a given process, the system will have "forgotten" them once $p \approx 0.5$.

Phase Trapping — An example of the trapping behaviour of BU-TRAP is shown in Figure 4.19. It is evident that virtually no trapping has occurred up to $p \approx 0.5$. In fact, trapping only becomes significant close to the point where the defending phase loses hydraulic conductivity; i.e. when the defending phase is no longer able to flow across the network. Symmetry arguments show that this will occur when $p = P_f \approx 0.7512$, where P_f is the known as the "floodout" threshold (note that the percolation and floodout threshold values are not obtained exactly during these simulations due to the finite size of the networks

involved). This trapping behaviour is characteristic of all displacements, not only BU-TRAP, and will tend to operate only close to the percolation threshold in three dimensions.

Influence of Phase Trapping During Imbibition — Consider a pure bottom-up bond percolation process, with and without trapping (denoted BU-TRAP and BU, respectively). The resulting relative permeability curves are shown in Figure 4.20. It is immediately clear that trapping has had very little effect on the wetting phase curve and has merely terminated it prematurely at $S_W = 1-S_{or}$. The nonwetting curve, however, *has* been affected by phase trapping: as well as terminating at $S_W = 1-S_{or}$, the lower part of the curve has experienced a shift towards lower water saturations. The reasons for this shift are far from obvious, especially when the only data available are those used to plot the relative permeability curves themselves. The explanation for the observed differences is a subtle one, and depends largely upon the way in which the results are presented. The key to understanding how the various displacements progress is to plot relevant quantities as functions of the *current bounding radius* (R). This concept is illustrated in Figure 4.21, and demonstrates how the pore size distribution function can be used as an extremely useful interpretative tool. The relevant variables here are water saturation (S_W), relative permeabilities (k_{ro}, k_{rw}), and the fraction of invaded pores (p). These are plotted as functions of R in Figure 4.22.

Consider first how p varies as R is increased from $R_{min} = 0$ (Figure 4.22a). Without trapping this curve is simply the cumulative probability curve: all available pores are filled and displaced fluid is always permitted to escape whether or not this is physically possible. When trapping *is* allowed to occur, it only takes effect after $p \approx 0.5$ and only becomes marked at p close to P_f, i.e. when the defending phase becomes hydraulically discontinuous. Past this point (as R increases), only a small fraction of pores are able to be filled. These are pores

which are part of defending clusters that are still connected to the outlet face of the network. By the end of this process, approximately 25% of the pores remain trapped and it is these which constitute the residual oil saturation S_{or}.

Figure 4.22b shows the corresponding R-plots of water saturation. The discussion above dictates that these two curves must be identical up to $p \approx 0.5$, after which point they begin to diverge. Without trapping, $S_w(R)$ obviously terminates at $S_w = 1.0$, whilst trapping reduces this value to $S_w = 1\text{-}S_{or}$. It should be noted here that the structure of these curves is completely governed by; (i) the particular radius distribution in use (modified Rayleigh in this case), and (ii) the choice of volume function V(r). These caveats do not detract from the qualitative divergent behaviour of the curves, however, as trapping is a topological phenomenon independent of these issues.

The final step in understanding the effect of phase-trapping on imbibition processes is to examine the functions $k_{ro}(R)$ and $k_{rw}(R)$. These are shown in Figure 4.22c where it is immediately clear that trapping has had no effect on k_{ro} *at a given R*. This is because as the displacement takes place, the defending (oil) phase eventually begins to break up and is distributed in the network in the form of a spanning cluster together with smaller isolated clusters. Whether these isolated "islands" of oil are invaded or not, the oil permeability itself remains the same and this is governed only by the conductive spanning cluster. Hence, as the displacement continues and the oil phase continues to split, the actual conductivity of the oil remains totally unaffected by these divorced clusters, which may or may not eventually become displaced. In contrast to this, the wetting phase curve $k_{rw}(R)$ *is* affected by trapping. By allowing the invasion of isolated oil clusters, additional highly conductive flow paths are made available to the invading fluid. Therefore, once more than half of the pores have been invaded, and phase trapping has begun,

$$k_{rw}|_{\text{without trapping}} > k_{rw}|_{\text{with trapping}} \qquad (4.27)$$

Note the structure of these $k_{ro}(R)$ and $k_{rw}(R)$ curves: both are S-shaped. The reasons for this are quite obvious if one considers which pores are being invaded at each stage of the process.

The saturation and permeability shifts may now be considered together and their combined effects used to explain the resulting form of the relative permeability curves. Translating $k_{ro}(R)$ plots into $k_{ro}(S_w)$ plots implies a relative shift to the left for the lower section of the BU-TRAP curve (i.e. towards lower water saturations). A similar shift affects the upper part of the corresponding wetting phase curve, but in this case, the saturation shift is offset by the wetting phase permeability shift. That is to say, the two effects cancel one another, resulting in wetting phase relative permeability curves which follow identical paths up to $S_w = 1\text{-}S_{or}$. This is an important result, since it demonstrates how relative permeability curves can disguise the underlying dynamics of the process under investigation. Although they appear to show that trapping has no effect on the wetting phase, they hide the fact that this is essentially the combined product of two conflicting events. The following section demonstrates how such a phenomenon can cause a great deal of confusion when attempting to interpret a variety of flow processes.

4.9.2 Secondary Displacement Processes

Secondary displacement processes are displacements carried out on a porous medium which is already partially saturated with the displacing phase. For example, if a primary drainage experiment is followed by a waterflood, the process is called *secondary imbibition*. This cycle exhibits an hysteresis effect between the primary drainage and secondary imbibition nonwetting relative permeability curves, but very little variation is evident in the wetting phase curves and the hysteresis effect is usually considered to be negligible in this

case: typical experimental curves are shown in Figure 4.23. Various theories relating to pore size distribution and matrix cementation have been put forward in an attempt to explain this phenomenon, but network modelling of the various secondary processes provides important clues as to the real causes of hysteresis in porous media. These simulations are now described in detail.

Simulation Studies of Secondary Processes — Both secondary drainage and secondary imbibition have been studied, but for brevity only the primary drainage-secondary imbibition scenario will be discussed here. The simulation is shown in Figure 4.24. The similarity to experimental curves is striking and the hysteresis effect is clearly duplicated in the case of the nonwetting phase. The wetting phase curve shows little sign of deviation which is also in general agreement with experimental findings. In order to explain these effects, the relevant variables must once again be plotted as functions of a current bounding radius, R. Plots of p(R), $S_W(R)$, $k_{rO}(R)$ and $k_{rW}(R)$ are presented in Figure 4.25. The explanations given earlier help to interpret their various curvatures, but cannot account for the almost identical nature of the $k_{rO}(R)$ curves resulting from primary drainage and secondary imbibition. In order to explain this phenomenon, a step by step analysis of the distribution of invaded pores must be considered. A schematic snapshot of the phase distributions during the primary drainage process may be compared with the corresponding snapshot taken during the secondary imbibition stage of the cycle (i.e. at the same R). The mechanics of the imbibition process means that the corresponding phase distributions are virtually identical and remain so up until trapping begins. This explains why $k_{rO}(R)$ and $k_{rW}(R)$ take almost the same values during secondary imbibition as they did during primary drainage.

Having described and explained the nature of the various R-plots, the causes of the observed hysteresis effect may now be examined. As in the previous example, the saturation and permeability shifts associated with the wetting

phase act to cancel one another. Hence, no hysteresis effect is evident between the wetting phase relative permeability curves. Now consider the nonwetting curves. It has already been shown that the $k_{ro}(R)$ curves are virtually identical, and so the hysteresis must be entirely due to the shift in water saturation. At first glance, it appears that saturation variations evolve because of trapping of the nonwetting phase; in fact, trapping is *not* the main cause of the disparity. Figure 4.26 shows how the water saturation would have evolved had trapping not been permitted. Although the size of the shift would have been marginally reduced (remember that once $R > 40$, $k_{ro}(R) = 0$ anyway), it is quite clear that large saturation differences would still have existed even in this scenario. It can therefore be concluded that the observed hysteresis is actually generated by the curvature of $S_w(R)$ resulting from the *primary drainage* stage of the cycle. This in turn is related to the physics of the drainage process itself, and the associated issue of *accessibility*. The subject of accessibility is most easily discussed in relation to mercury porosimetry displacements, and a thorough discussion in Appendix A serves to emphasise its importance.

The next chapter describes how the network model can be further extended to the study of flow through systems of heterogeneous wettability; i.e. water-wet networks which contain a fraction of pores which are preferentially oil-wet.

Table 4.1 Various Ascribed Values for the Critical Conductivity Exponent.

Method of Derivation	Critical Exponent (t)
Computer Simulation	$1.6\pm0.1_{a,b,c}$, 1.87_{d}
Experimental	2.0_{e},$1.9\pm0.2_{f}$
Theoretical	$1.95\pm0.3_{g}$

(a) S. Kirkpatrick, Rev. Mod. Phys., **45**, 574 (1973)
(b) J. P. Straley, Ann. Israel Phys. Soc., **5**, 353 (1983)
(c) I. Webman, J. Jortner and M. H. Cohen, Phys. Rev. B, **16**, 2593 (1977)
(d) P. M. Adler and H. Brenner, Ann. Rev. Fluid Mech., **20**, 35 (1988)
(e) D. Adler, L. P. Flora and S. D. Senturia, Solid State Comm., **12**, 9 (1973)
(f) B. Abeles, H. L. Pinch and J. I. Gittleman, Phys. Rev. Lett., **35**, 247 (1975)
(g) R. Fisch and A. B. Harris, Phys. Rev. B, **18**, 416 (1978)

TABLE 4.2. Filling Regimes.

TD	TD-BACK	INV-PERC-TD	BU	BU-BACK	INV-PERC-BU
Top-down filling. Pores are filled sequentially (beginning with the largest) regardless of their position in the network. Defending fluid is always permitted to escape.	Top-down filling with backbone growth. Filling begins as in TD, up until p=pc. Thereafter, only the *spanning cluster* is allowed to grow. Again, all defending fluid may escape.	Invasion percolation (top-down). Invading fluid first fills the largest pores *connected to the inlet*, and then these clusters grow by sequentially occupying smaller and smaller pores.	Bottom-up filling. Pores are filled sequentially (beginning with the smallest) regardless of their position in the network. Defending fluid is always permitted to escape.	Bottom-up filling with backbone growth. Filling begins as in BU, up until p=pc. Thereafter, only the *spanning cluster* is allowed to grow. Again, all defending fluid may escape.	Invasion percolation (bottom-up). Invading fluid first fills the smallest pores *connected to the inlet*, and then these clusters grow by sequentially occupying larger and larger pores.

The remaining six filling regimes are the same as the six above, except that defending fluid may become trapped when no escape route exists to the outlet face of the network. Such regimes carry the suffix -TRAP.

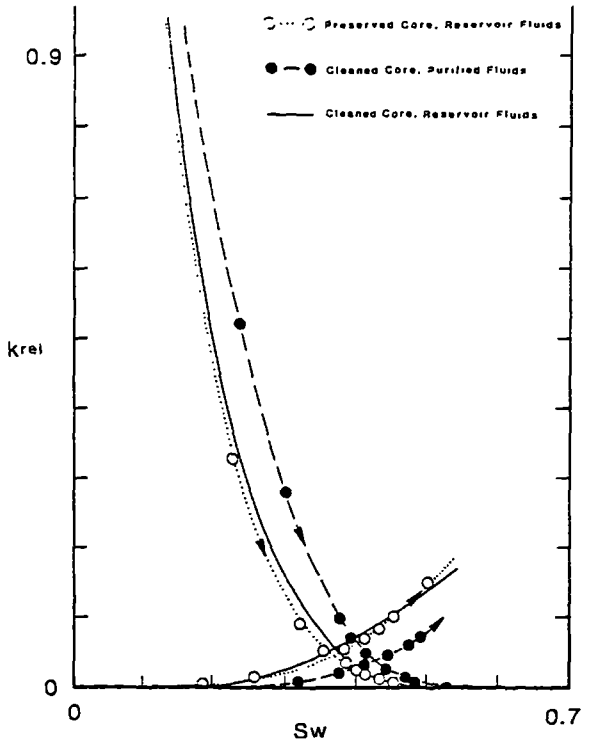

Figure 4.1 Typical experimental imbibition relative permeability curves (Richardson et al, 1955).

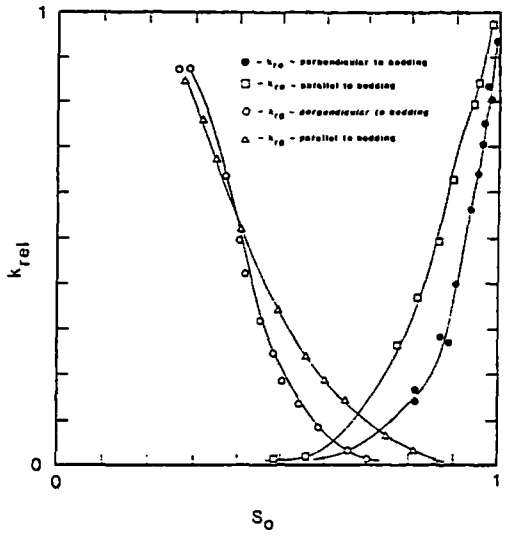

Figure 4.2 Typical experimental drainage relative permeability curves (Corey and Rathjens, 1956).

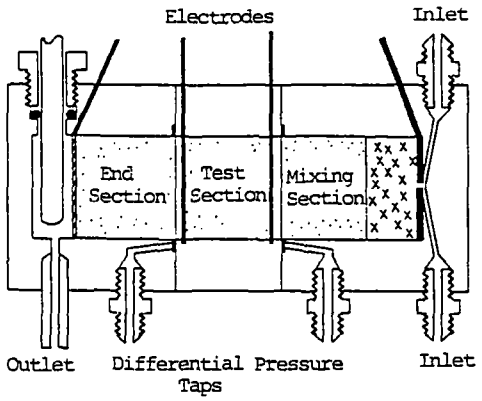

Figure 4.3 Penn-State relative permeability apparatus showing the typical three core assembly (Geffen et al, 1951).

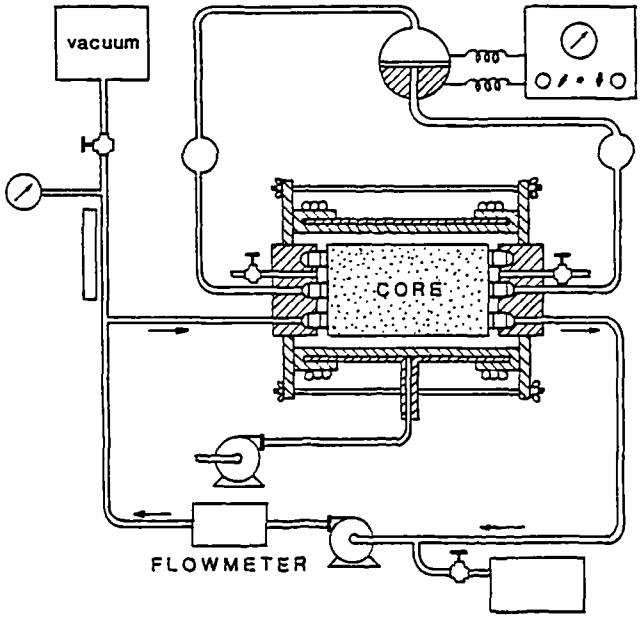

Figure 4.4 Hassler-type relative permeability apparatus (Hassler, 1944).

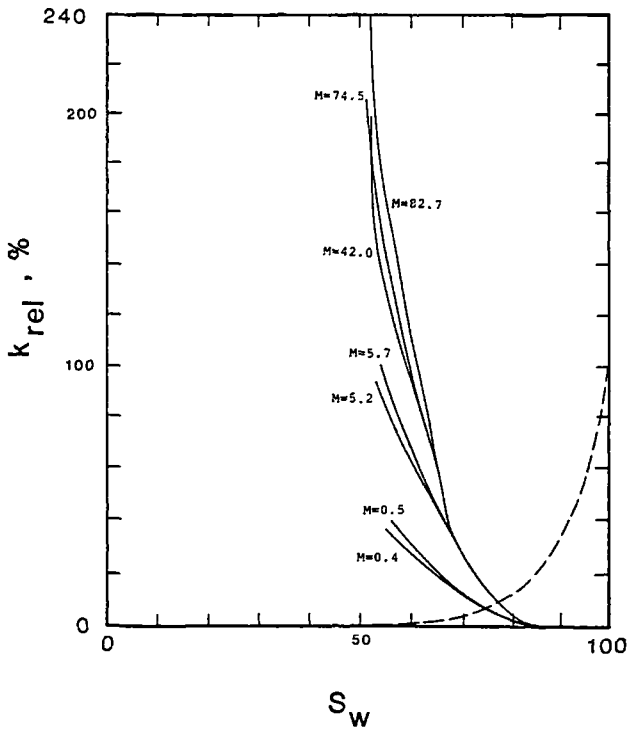

Figure 4.5 The effect of viscosity ratio (M) upon relative permeability (Odeh, 1959).

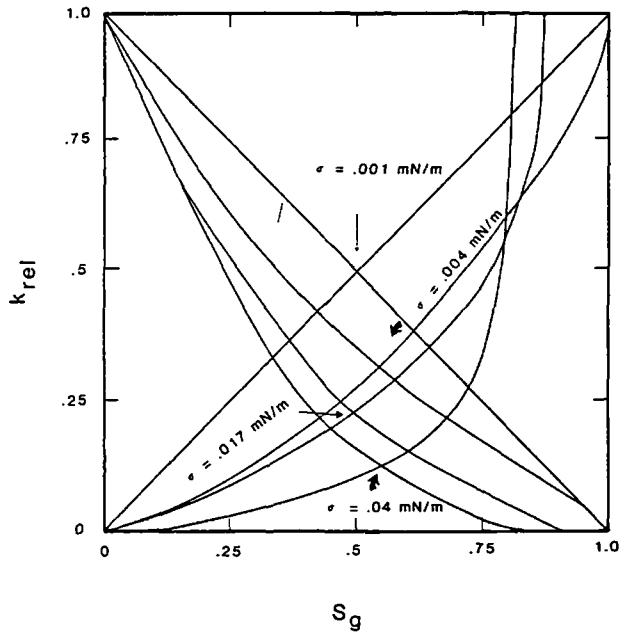

Figure 4.6 The effect of low interfacial tensions upon gas/oil relative permeability (Bardon and Longeron, 1978).

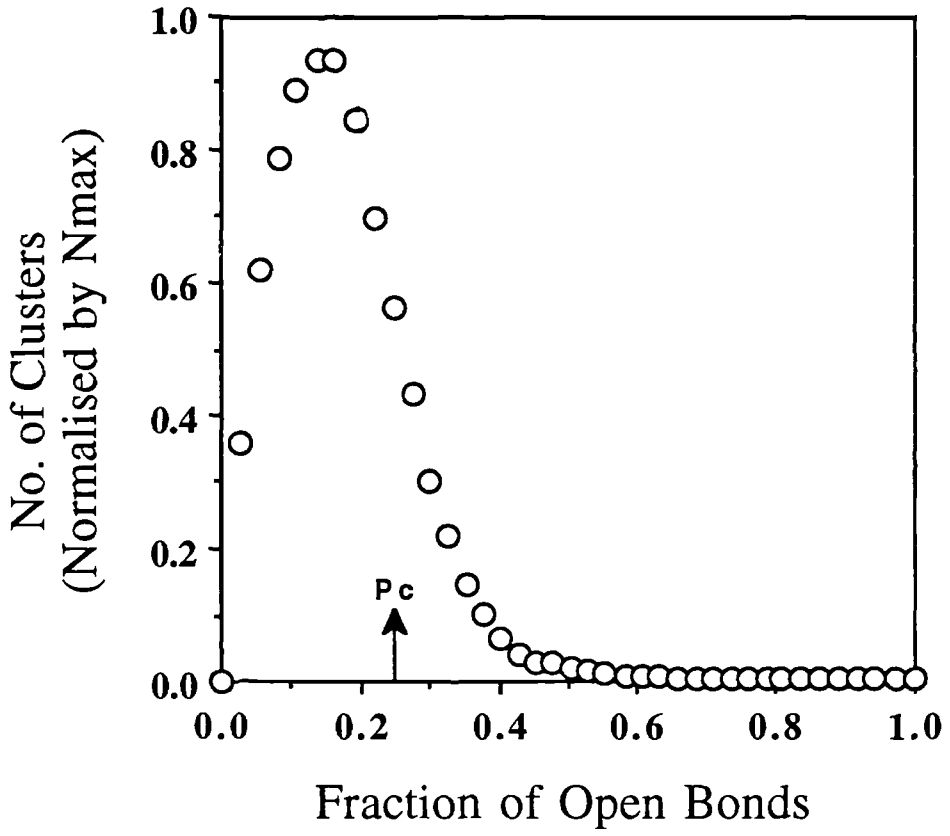

Figure 4.7 Number of clusters containing invaded fluid as a function of the invaded bond fraction.

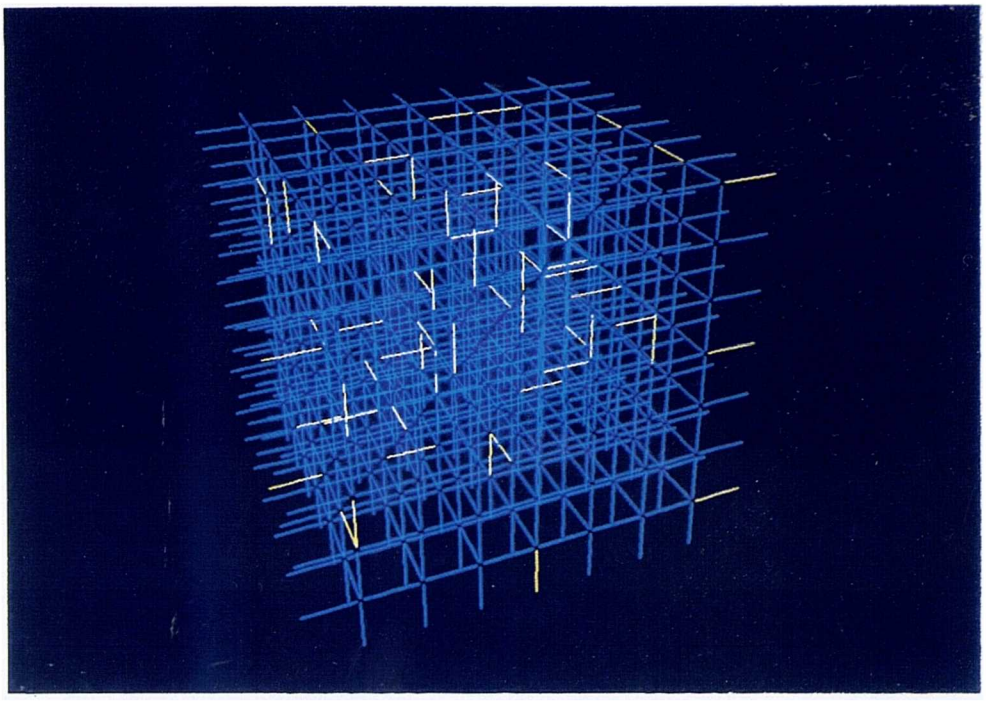

(a)

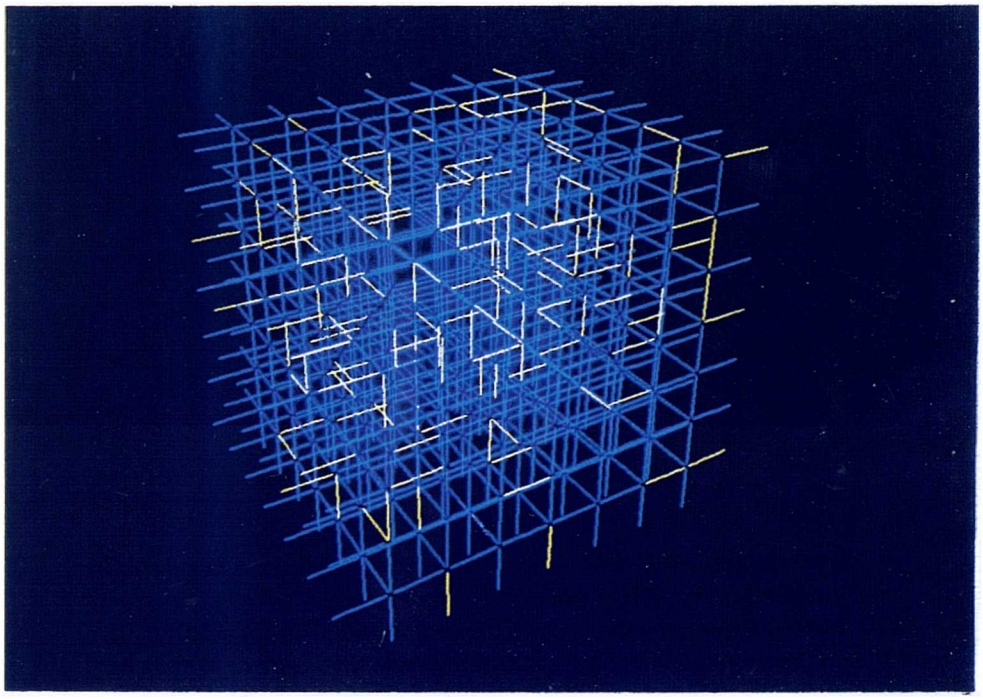

(b)

Figure 4.8 Pure bond percolation process on a regular cubic network. The fraction of invaded (yellow) pores is denoted by p: (a) p=0.07, (b) p=0.13, (c) p=0.256 (the red spanning cluster is connected because of periodic boundary conditons), (d) p=0.256 (invading phase only). (e) p=0.3, (f) p=0.3 (invading phase only).

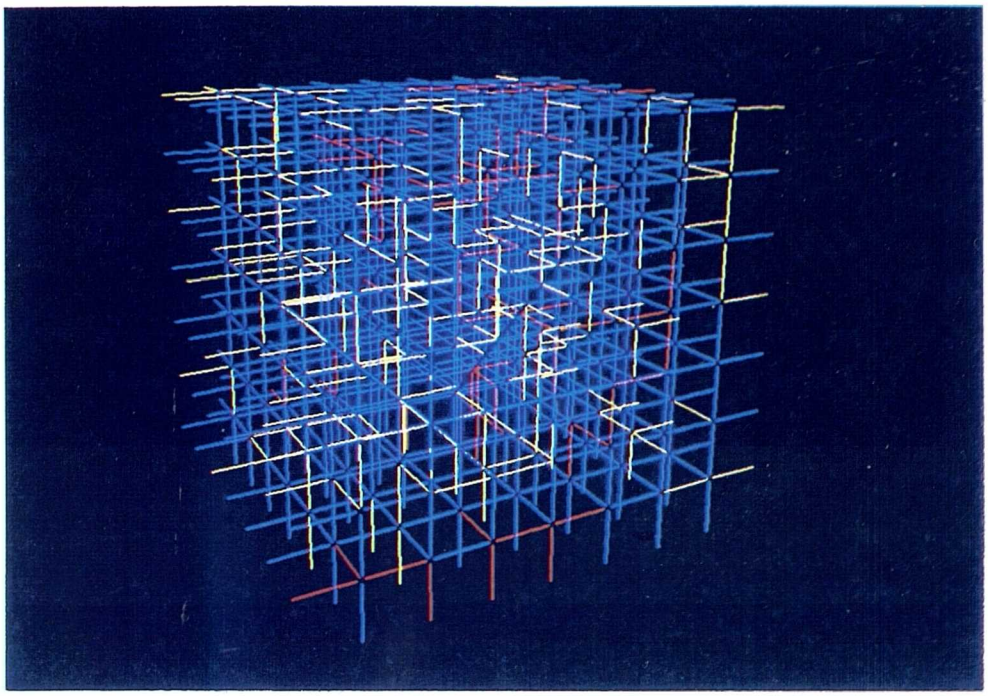

(c)

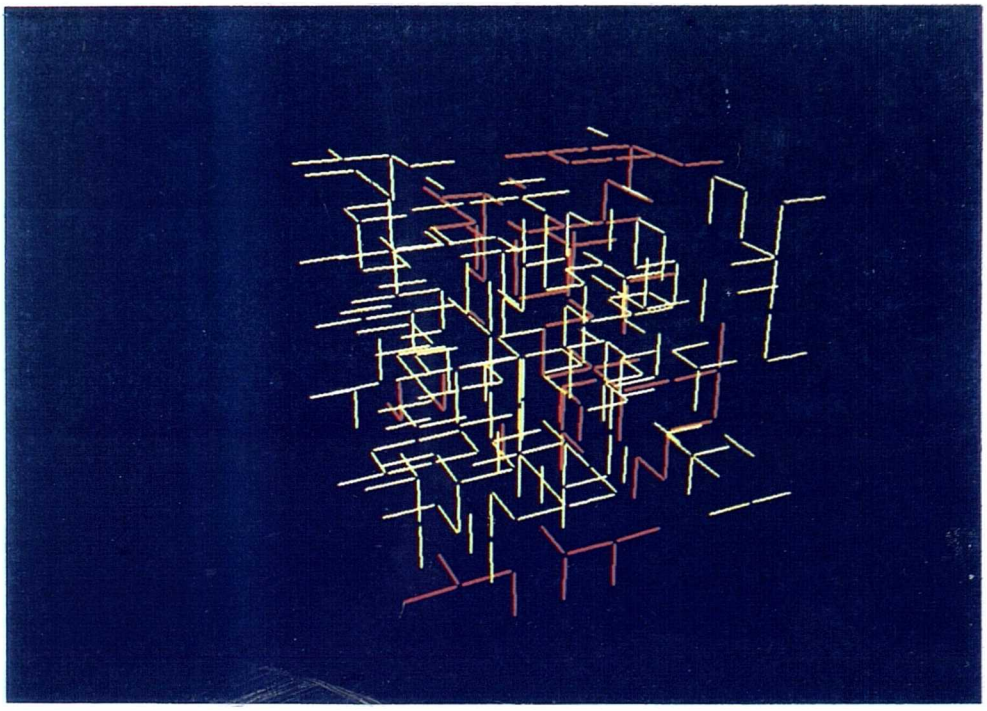

(d)

Figure 4.8 (Continued)

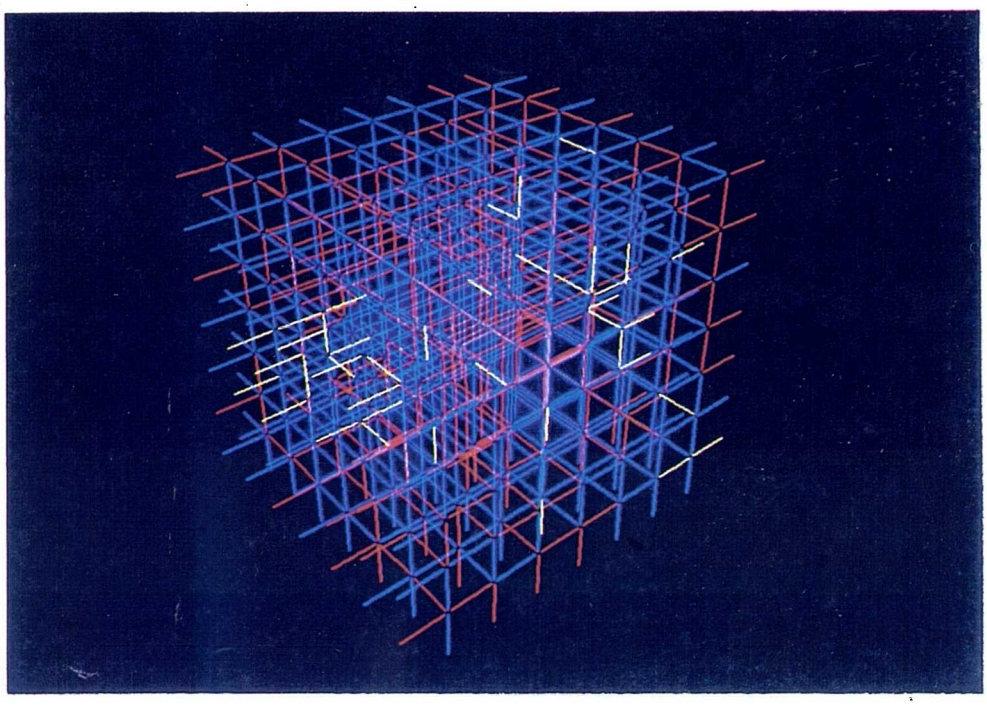

(e)

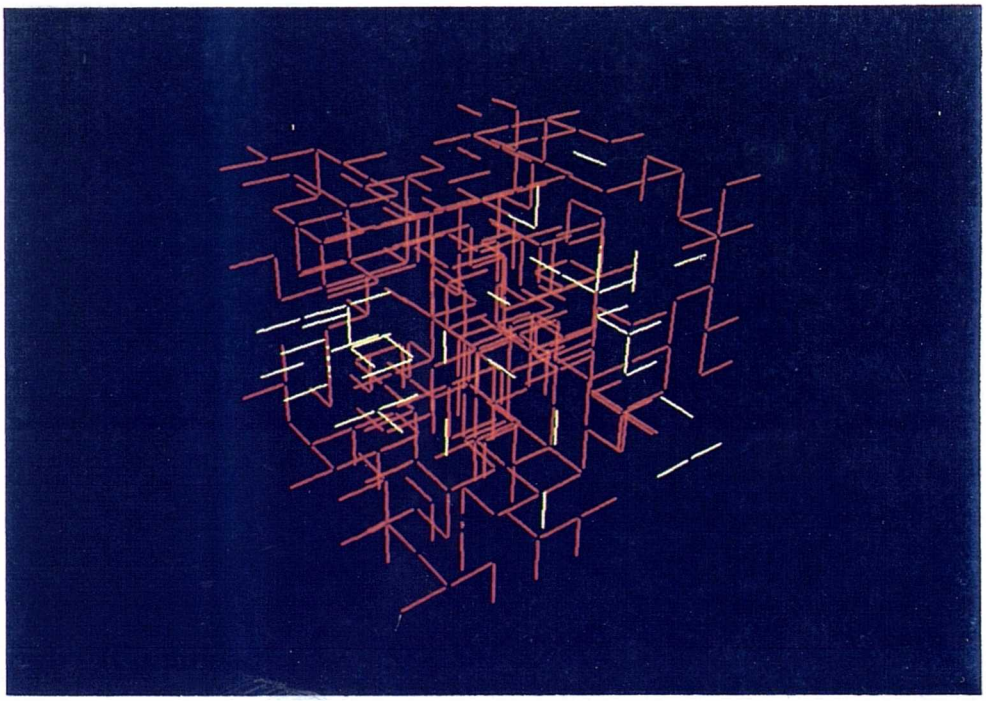

(f)

Figure 4.8 (Continued)

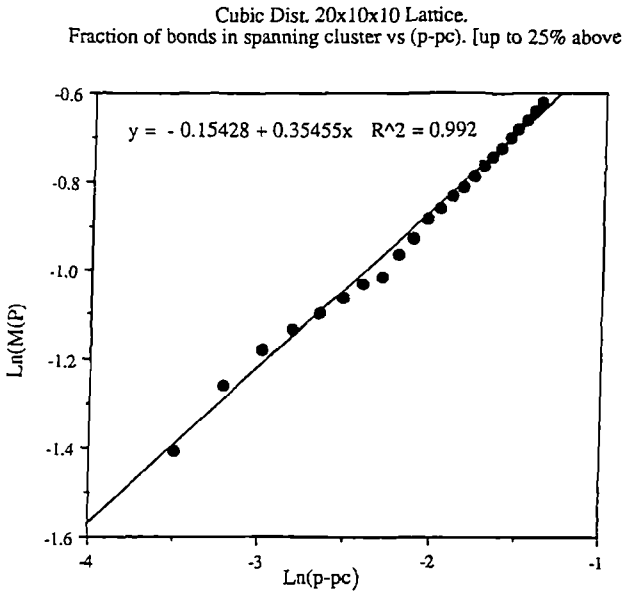

Figure 4.9 Plot showing fraction of bonds in spanning cluster vs $(p-p_c)$ for a 20x10x10 network.

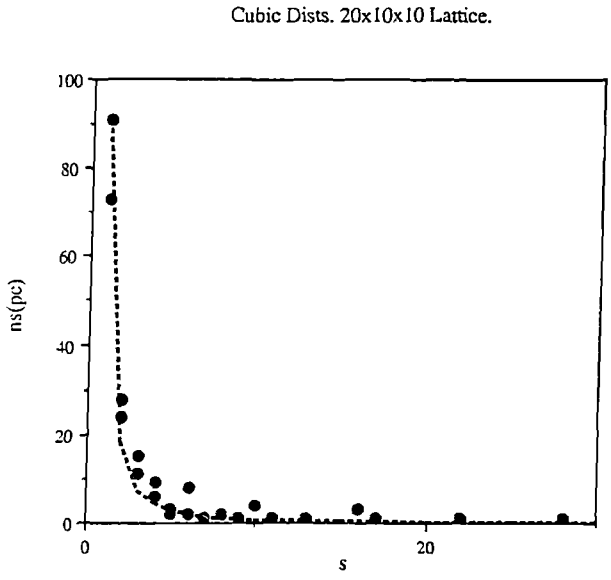

Figure 4.10 Number of clusters of size s vs s for a 20x10x10 network (the dotted line is the theoretical scaling).

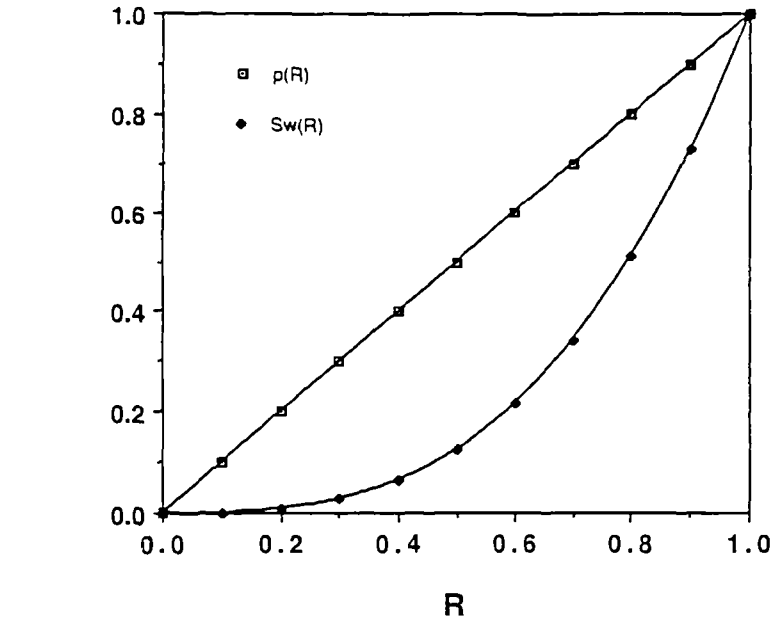

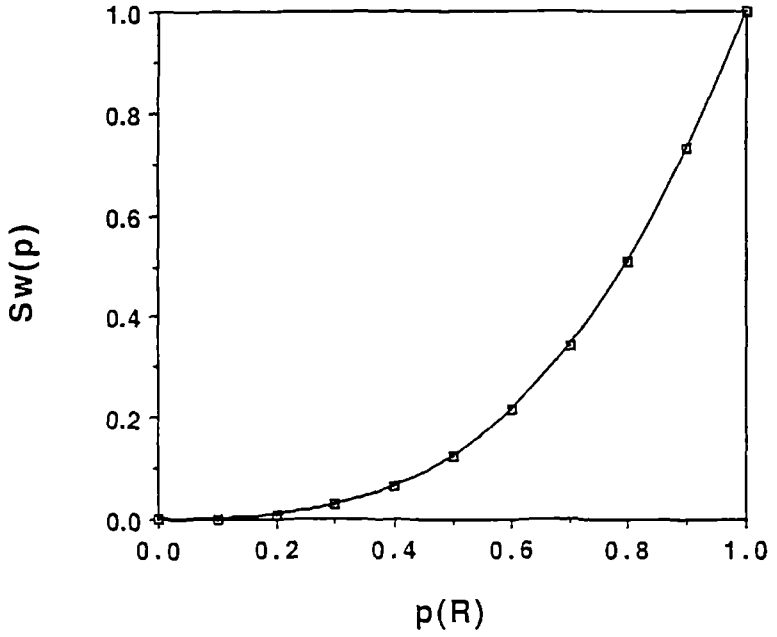

Figure 4.11(a) Plots of p(R), $S_w(R)$ and $S_w(p)$ for Uniform distribution.

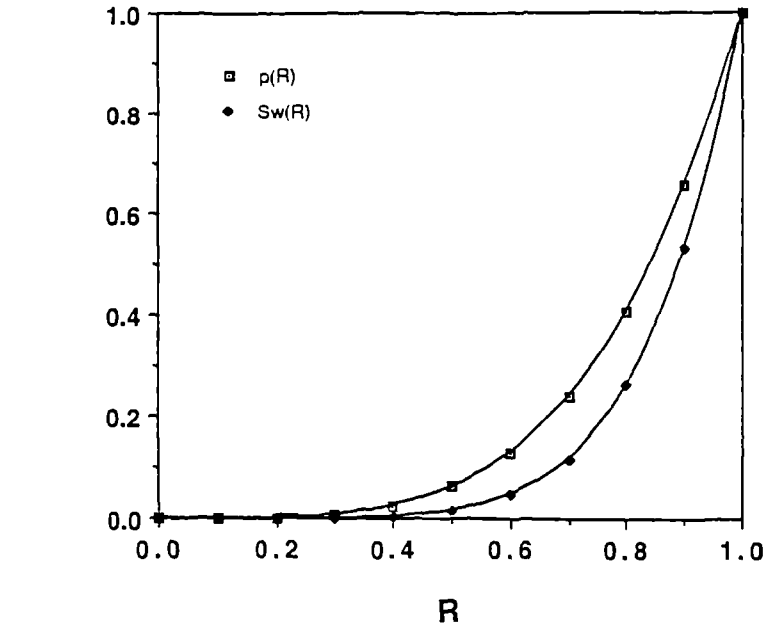

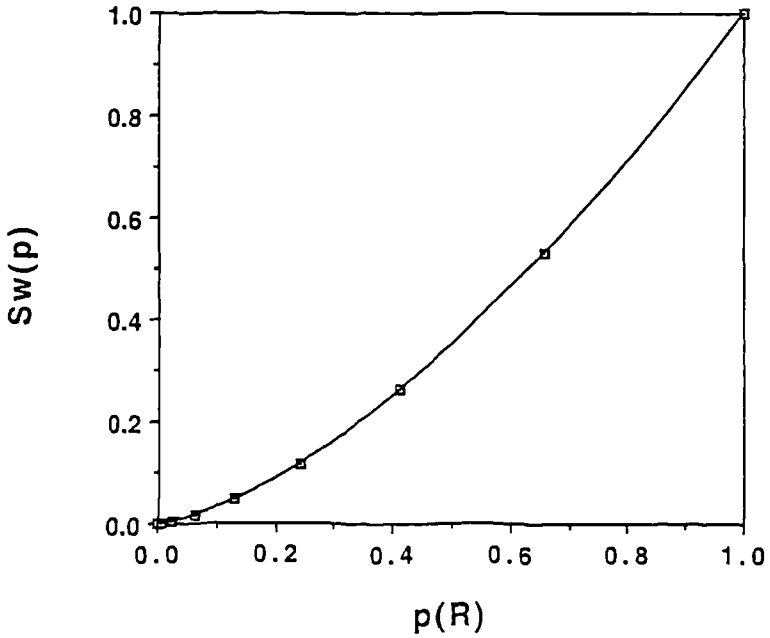

Figure 4.11(b) Plots of p(R), $S_w(R)$ and $S_w(p)$ for Cubic distribution.

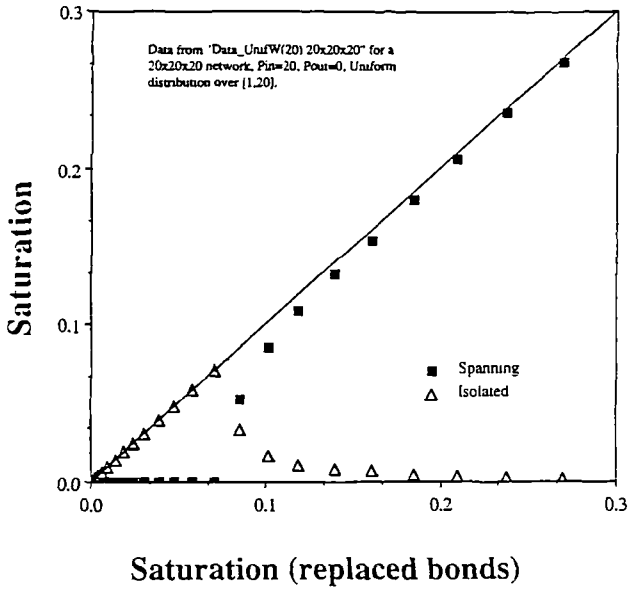

Figure 4.12 Saturation of the isolated and spanning clusters as a function of the total saturation for bottom-up filling.

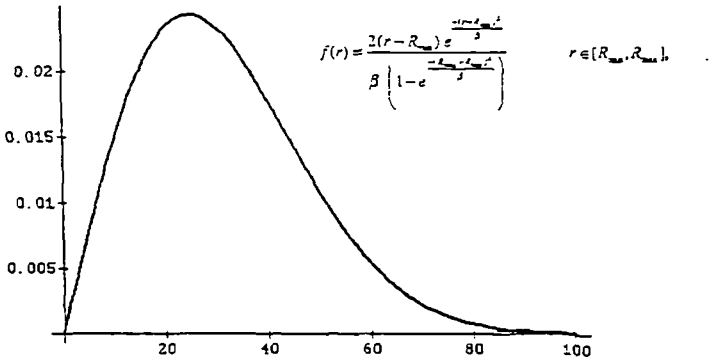

Figure 4.13 Rayleigh distribution with $R_{min}=0$, $R_{max}=100$ and $\beta=1250$.

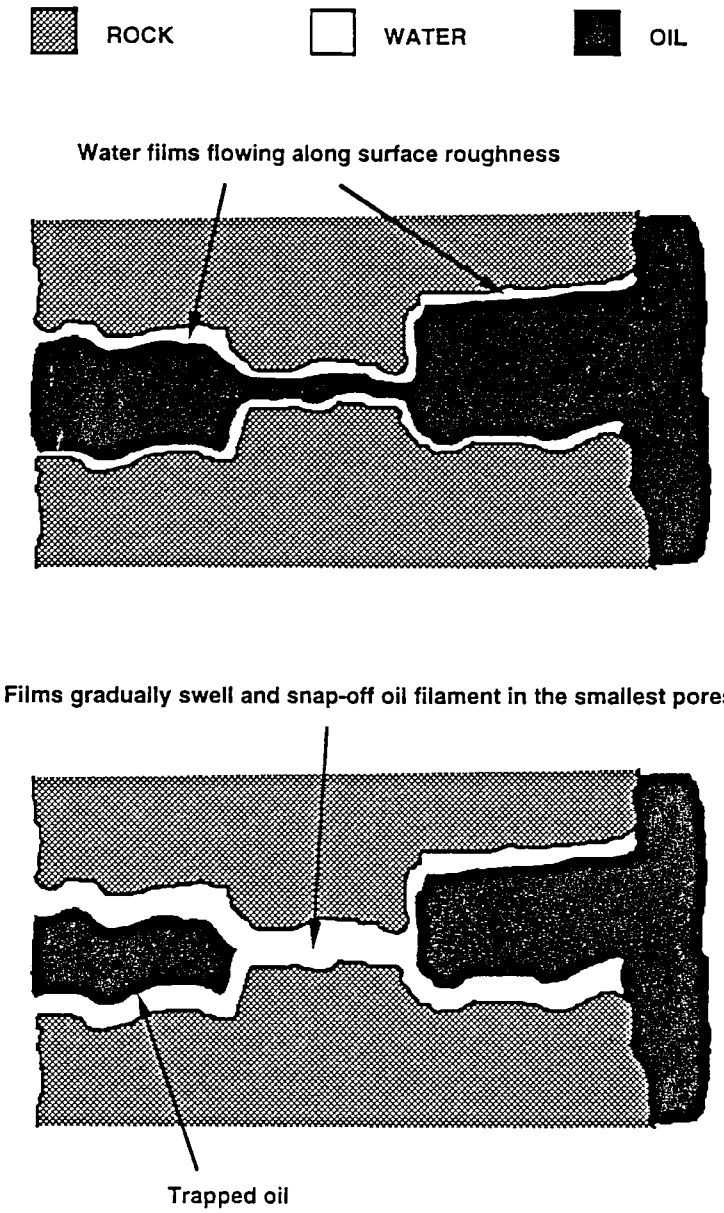

Figure 4.14 Schematic representation of spontaneous imbibition

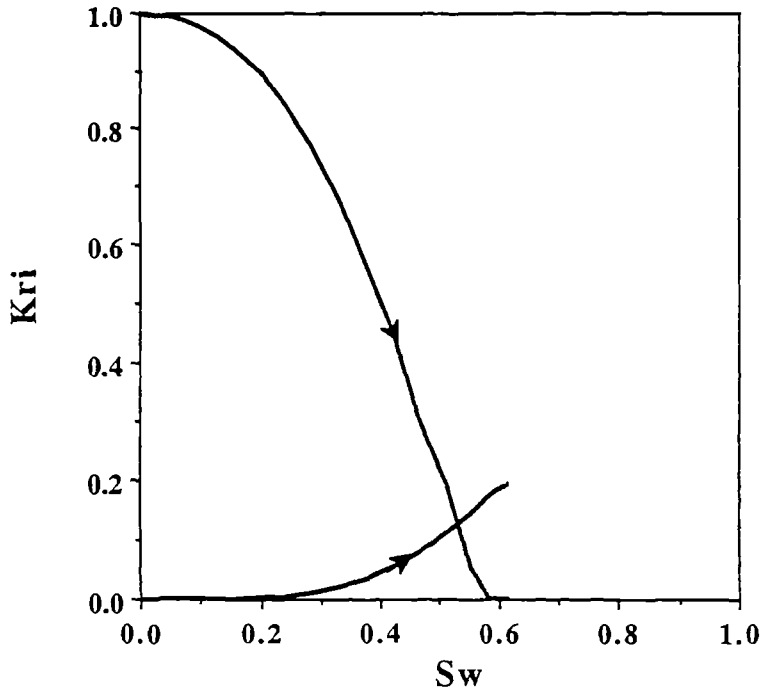

Figure 4.15 Simulated imbibition relative permeability curves using a Rayleigh radius distribution.

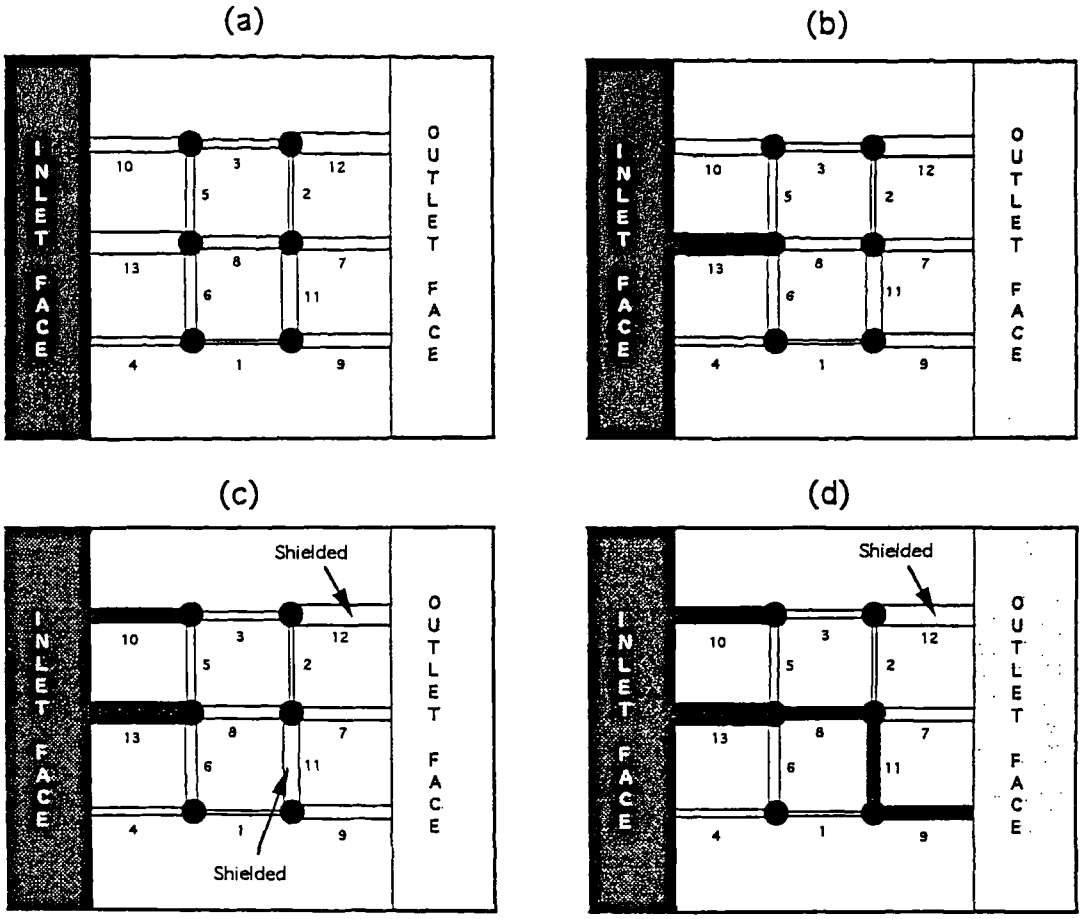

Figure 4.16 Schematic of capillary-dominated drainage: numbers refer to pore radii; 13 largest, 1 smallest.

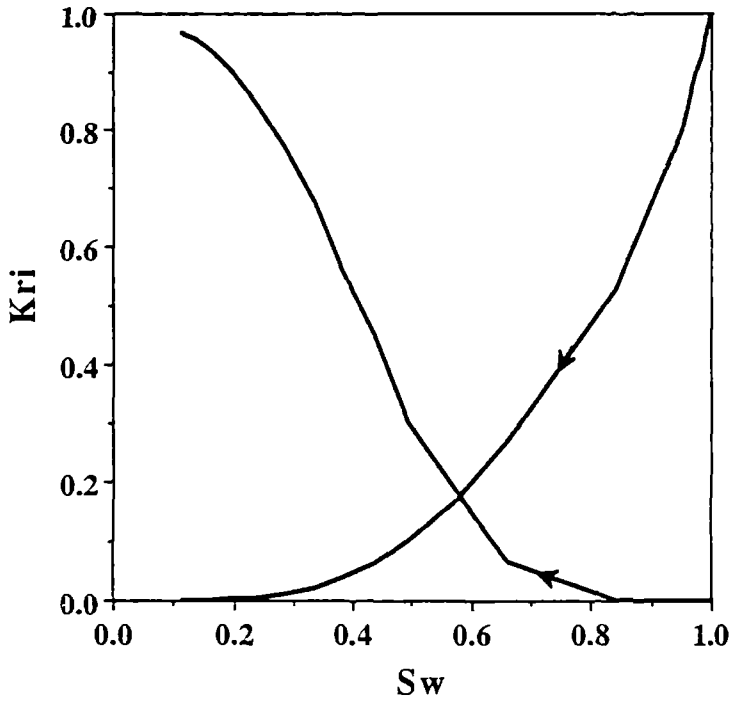

Figure 4.17 Simulated drainage relative permeability curves using a Rayleigh radius distribution.

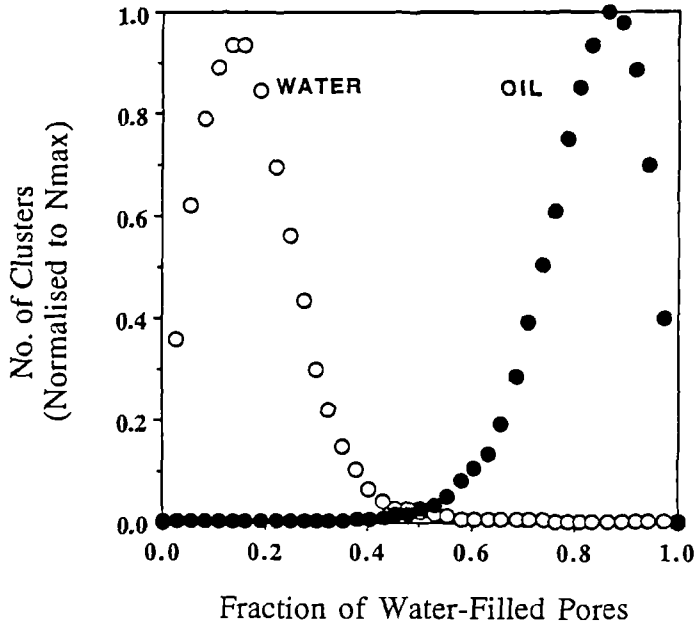

Figure 4.18 Clustering behaviour of both water and oil during a low-rate imbibition simulation.

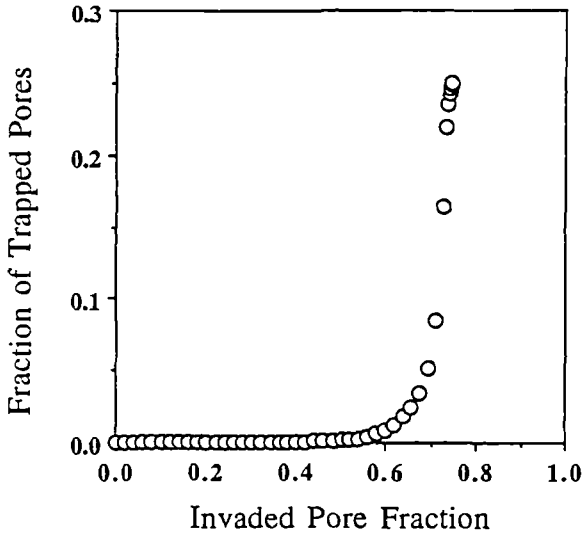

Figure 4.19 Trapping behaviour during a low-rate imbibition simulation (trapped pores contain oil).

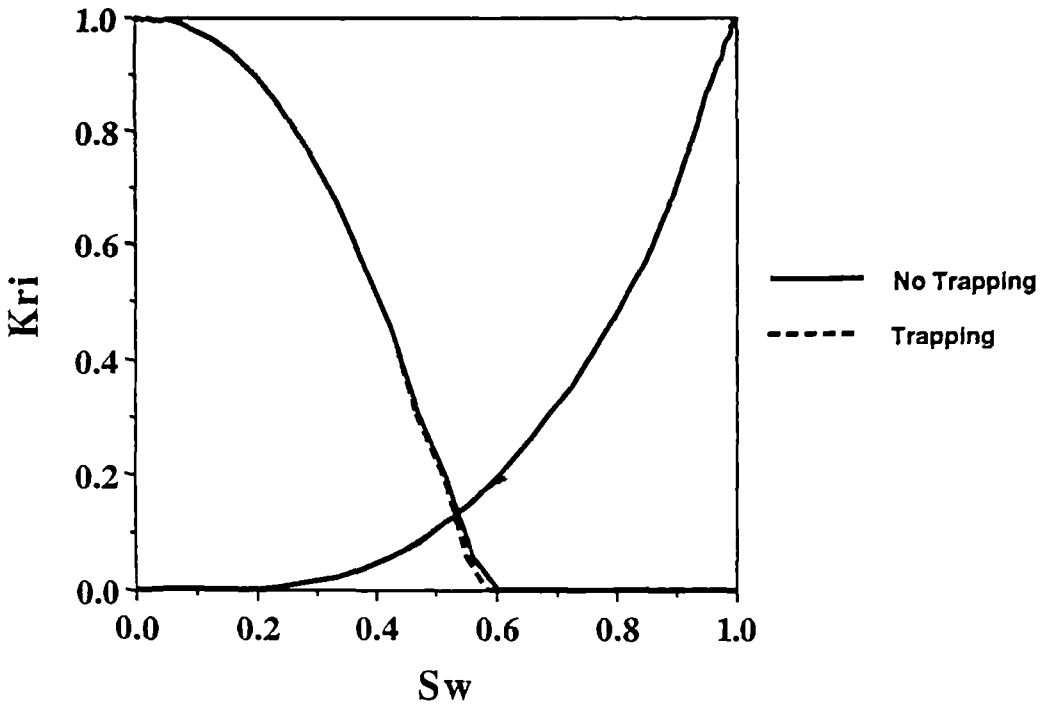

Figure 4.20 Comparison between imbibition relative permeability curves with and without trapping of the nonwetting phase.

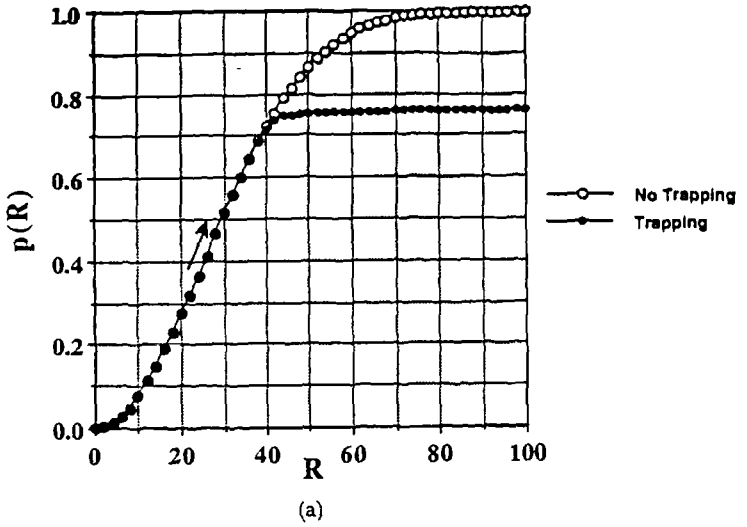

(a)

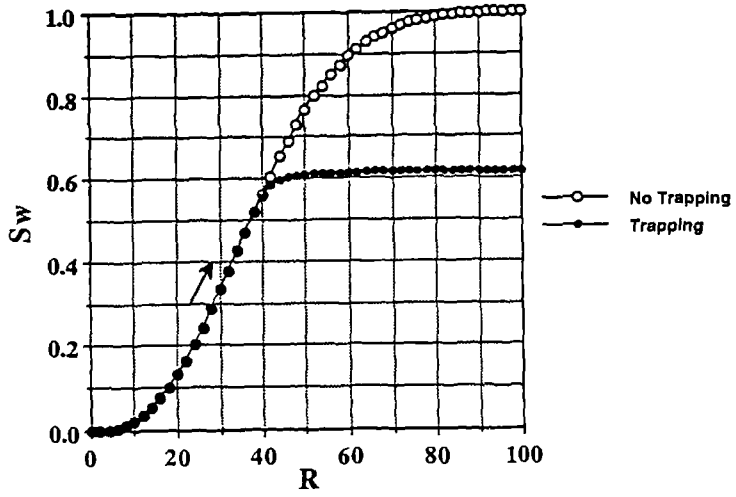

(b)

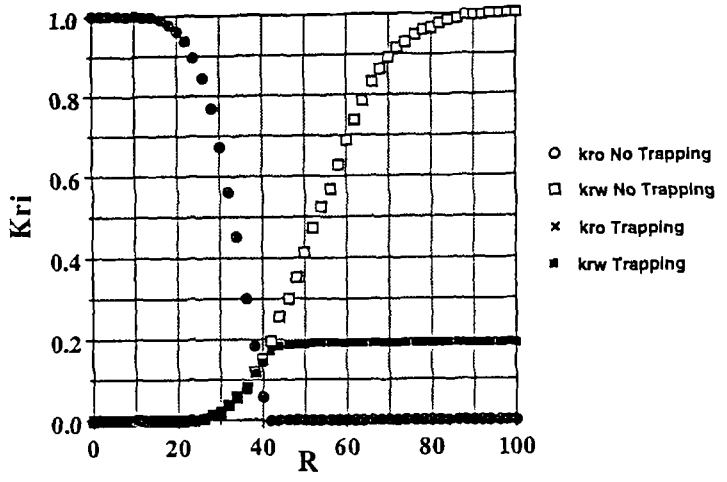

(c)

Figure 4.22 R-plots for imbibition with and without trapping: (a) p(R), (b) $S_w(R)$, (c) $k_{ro}(R)$ and $k_{rw}(R)$.

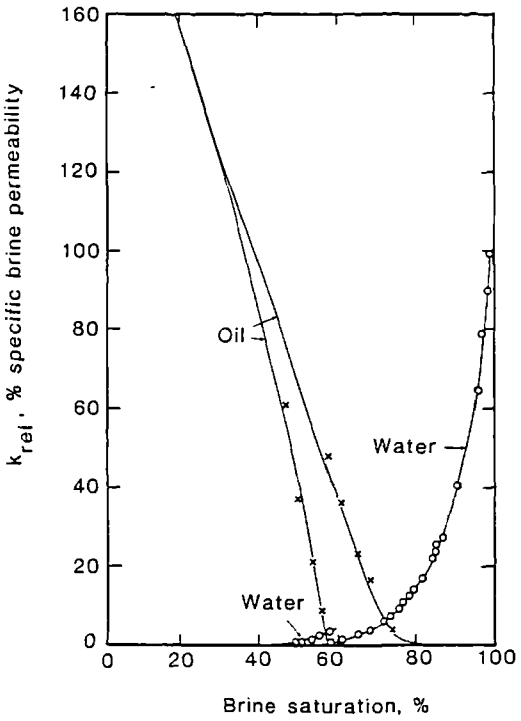

Figure 4.23 Experimental primary drainage — secondary imbibition relative permeabilities for a consolidated rock (Geffen et al, 1951).

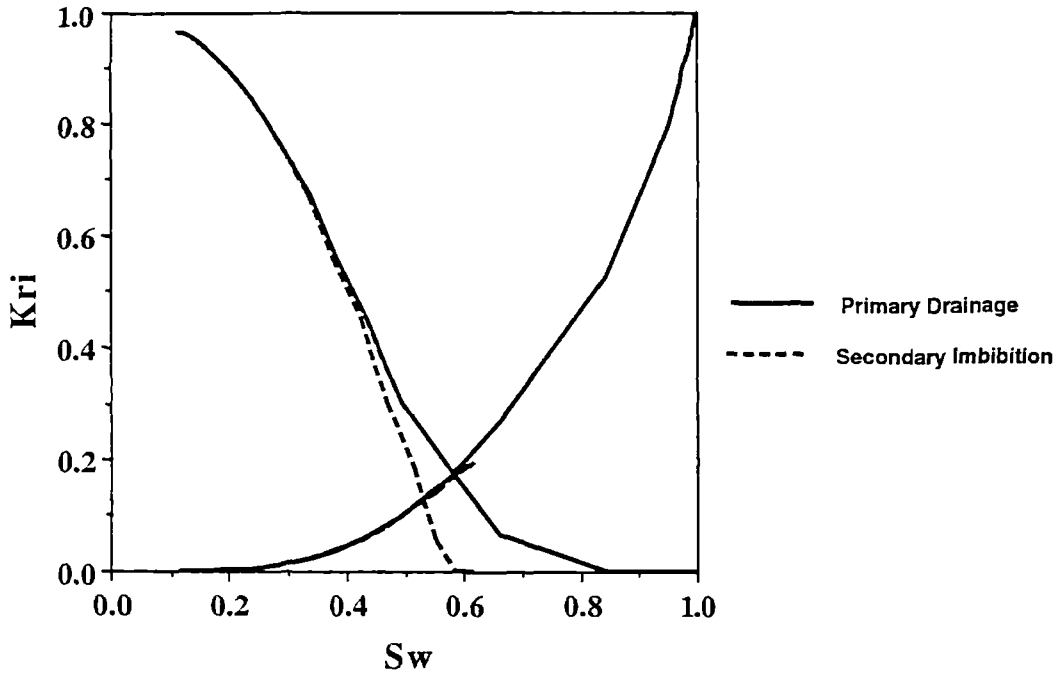

Figure 4.24 Network simulation of the primary drainage — secondary imbibition cycle. Note the hysteresis effect in the nonwetting curves.

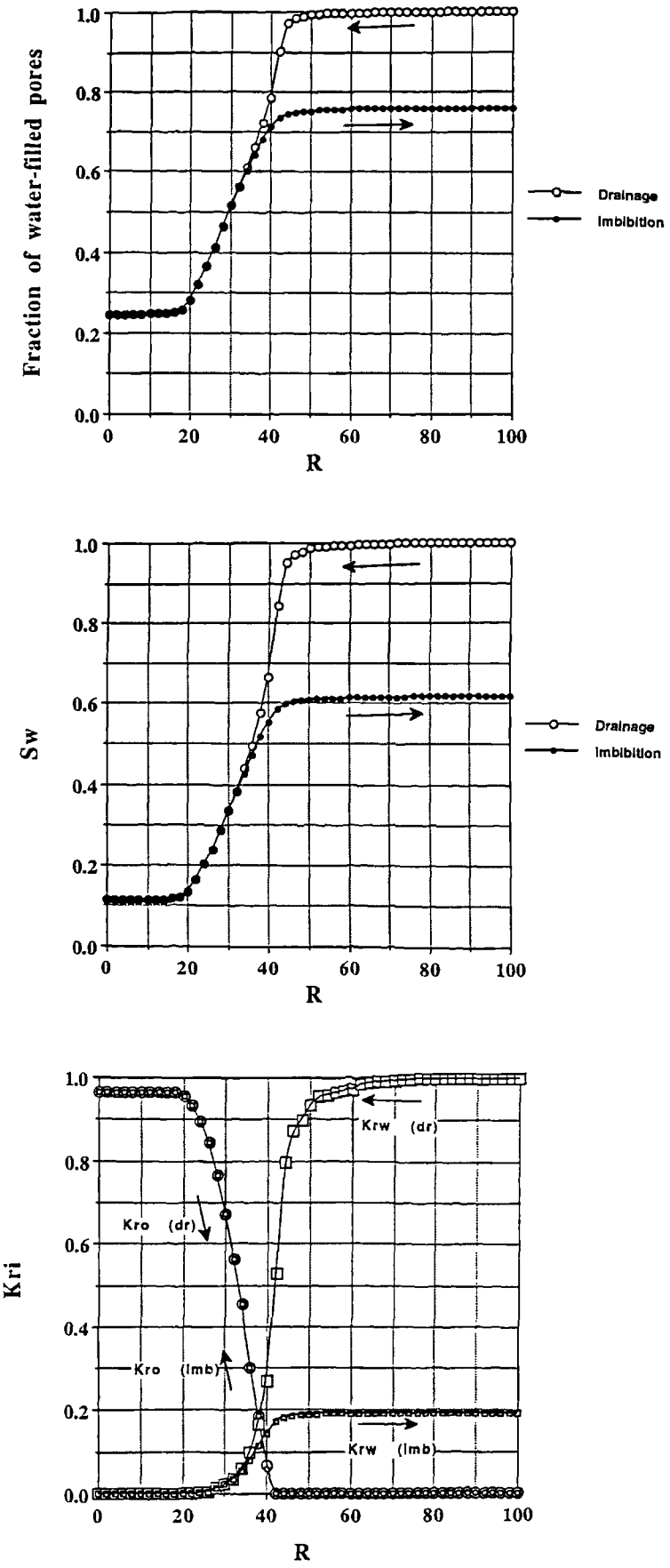

Figure 4.25 R-plots for primary drainage followed by secondary imbibition: (a) p(R), (b) $S_w(R)$, (c) $k_{ro}(R)$ and $k_{rw}(R)$.

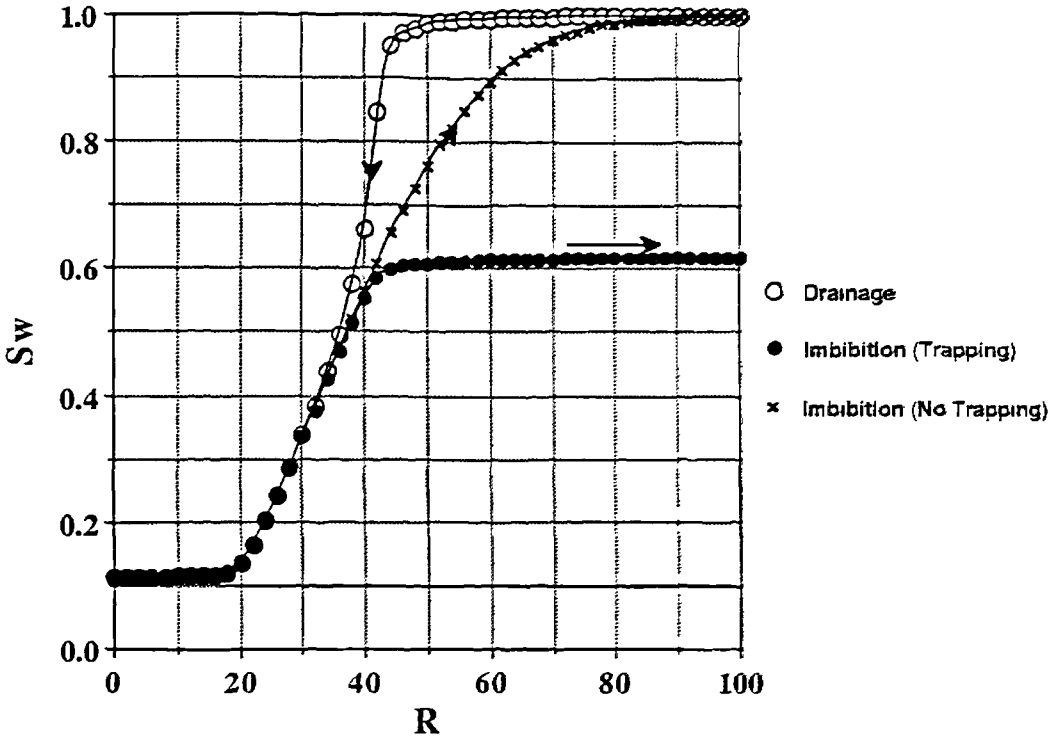

Figure 4.26 $S_w(R)$ plots for primary drainage followed by secondary imbibition, with and without trapping of the nonwetting phase.

CHAPTER 5 TWO-PHASE FLOW IN MIXED-WET AND FRACTIONALLY-WET SYSTEMS

This chapter focusses upon displacements in systems of heterogeneous wettability. By explicitly assigning wettability characteristics to each pore, it has been possible to explain many experimental observations from a microscopic standpoint. The effects of wettability upon relative permeability and capillary pressure curves have been closely analysed, as have the corresponding variations in microscopic displacement efficiency. An important consequence of these investigations has been the proposal of a new wettability test, based upon the simultaneous measurement of nonwetting phase relative permeability and capillary pressure. This test could be used to determine the wettability of both mixed-wet *and* fractionally-wet media — to date, no such satisfactory test exists.

The wettability characteristics of a porous medium play a major role in a diverse range of measurements including: capillary pressure data, relative permeability curves, electrical conductivity, waterflood recovery efficiency and residual oil saturation. This study describes the development and implementation of a pore-scale simulator capable of modelling multiphase flow in porous media of nonuniform wettability. This has been achieved by explicitly incorporating pore wettability effects into the steady-state models described in the previous chapter.

Results are presented which show how α (the fraction of pores which are assigned oil-wet characteristics) affects resulting capillary pressure and relative permeability curves. Simulated capillary pressure data demonstrate that standard wettability tests (such as Amott-Harvey and free imbibition) may give spurious results when the sample is fractionally-wet in nature. The corresponding relative permeability curves have been used to calculate

waterflood displacement efficiencies for a range of wettability conditions, and recovery is shown to be maximum at close to neutral conditions.

5.1 Introduction

Throughout the current literature, there exists much conflicting evidence pertaining to the effect of rock wettability on a variety of flow parameters and displacement processes. The wettability characteristics of a rock will completely govern the location and flow of any associated pore fluids and will thus greatly affect the capillary pressure and relative permeability properties of the system. Wettability conditions depend mainly upon rock mineralogy and the history of oil deposition (although other factors, such as brine pH and the asphaltene content of the crude, are also important). In the past, however, it was assumed that all petroleum reservoirs were strongly water-wet: this assumption was based upon the fact that the majority of sandstone reservoirs originated in aqueous environments - oil migration only occurring at a much later stage. A second basis for such an assumption was that almost all sedimentary rocks are water-wet when cleaned. However, the existence of oil-wet reservoirs had been demonstrated by Nutting as early as 1934, and more recent studies have shown that strongly water-wet reservoirs are actually the exception rather than the rule (Treiber et al, 1972; Chilingar and Yen, 1983; Morrow, 1991).

In any given rock sample, wettability may either be *uniform* or *non-uniform*. In the former case, the wettability of the entire porespace is the same (100% oil-wet, 100% water-wet, or 100% "intermediate"-wet) and the wetting and nonwetting phase contact angles will essentially remain constant throughout the system. In the non-uniform case, however, the rock may show heterogeneous wettability, with variations in wetting preference from pore to pore (say, 70% oil-wet pores, 30% water-wet pores). Non-uniform wettability can be further subdivided into two subclasses: *mixed-wettability* and *fractional-*

wettability. The term "mixed" wettability was first introduced by Salathiel (1973) to describe systems where the oil-wet pores correspond to the largest in the sample, the small pores remaining water-wet (Figure 5.1). Such situations may arise when oil migrates to water-wet reservoirs and preferentially fills the larger interstices. The wettability characteristics of these pores may then be altered by the adsorption of polar compounds and/or the deposition of organic matter from the original crude, thereby rendering them oil-wet. Fractional wettability, however, is generally related to the rock matrix itself and is due to the differences in surface chemistry of the constituent minerals. Because of these variations, crude oil components may adsorb onto some pore walls whilst ignoring others. This, in effect, means that fractionally-wet rock contains oil-wet pores of all sizes (Figure 5.2).

As earlier chapters have demonstrated, the technique of network modelling has been widely used in the past, but usually in an attempt to quantify flow parameters (Koplik et al, 1982; Doyen, 1988) or fit experimental data (Lin and Slattery, 1982). Quantitative prediction has proved unsuccessful whilst the fitting of experimental data is straightforward and uninformative. The author believes that network modelling should be used to examine the *sensitivities* of a given process to a variety of phenomena and this is the approach taken here. Very few studies have been reported which attempt to simulate flow in networks of heterogeneous wettability. Mohanty and Salter (1983) used a pore and throat model to investigate the effect of wettability on a variety of primary and secondary displacements but considered only one mixed-wet regime (25.5% PV oil-wet). Heiba et al (1983) utilised a Bethe network to approximate pore connectivity and described displacements in terms of pore-filling sequences - schematic representations using the pore size distribution curve of the lattice. They studied two non-uniform systems, both of which appear to be fractionally-wet in nature, and produced simulated capillary pressure and relative permeability curves. It is to be regretted, however, that the use of

Bethe lattices is still not generally accepted, although comparisons with results from regular networks clearly demonstrate their effectiveness.

The simulator described in this work is used to systematically investigate the vital role played by wettability at the pore scale in both fractionally-wet *and* mixed-wet media, and to explain how this influences the measurement of capillary pressure, relative permeability, and waterflood recovery efficiency. The ultimate goal of this study is to propose a new wettability test which may eventually be utilised in the laboratory. In order to enable comparisons to be made between this and current methods, some of the most common techniques used today are reviewed briefly in the next section.

The pore-scale simulator itself is described in Section 5.3, together with details of the input pore-size distributions and pore wettability characteristics. The *wettability* clustering behaviour is also briefly reviewed. Simulated capillary pressure curves are presented in Section 5.4 for a variety of oil-wet pore fractions. Results from a fractionally-wet system demonstrate that standard techniques may attribute incorrect wettability properties to such media. Variations in relative permeability behaviour are shown in the simulations of Section 5.5. The model curves are shown to be in excellent qualitative agreement with corresponding experimental results. In Section 5.6, the simulated relative permeability data are used to investigate the waterflood behaviour of the various systems. The variation in recovery efficiency with wettability is investigated and is shown to be optimum at close to "neutral" conditions. The phenomena described in earlier sections are exploited in Section 5.7, where a novel technique is proposed for the determination of rock wettability. The method precludes the need for saturation measurements, requiring instead the determination of nonwetting phase relative permeability as a function of capillary pressure.

5.2 Measurement Of Rock Wettability

Many methods already exist for determining the wettability of a porous medium, although the vast majority of these give only a qualitative indication (see Anderson, 1987, for a full account of both qualitative and quantitative methods). Currently, there are two techniques used for the quantitative measurement of rock wettability; the Amott method and the U.S. Bureau of Mines (USBM) method. A third, the contact angle method, is used primarily in the context of pure fluids/artificial core experiments and will not be considered here. The most widely used qualitative technique of wettability measurement is the "imbibition method", and this will be discussed later. It should be noted, however, that no proven method appears to exist which can determine the wettability characteristics of *fractionally-wet* or *mixed-wet* media.

5.2.1 The Amott Test

The Amott test (Amott, 1959) attempts to correlate the ratio of spontaneous to forced imbibition with the average wettability of the sample. It is based upon the fact that water will spontaneously imbibe along water-wet pathways in a porous medium, but will require to be overpressured if it is to enter oil-wet pores. Having centrifuged the test core under brine until the residual oil saturation (S_{or}) has been reached, the wettability measurement is performed as follows:

(1) The core is immersed in oil for 20 hours and the volume of water displaced over this period by the spontaneous imbibition of oil is measured ($V_{w\,sp}$).

(2) The core is then centrifuged under oil until irreducible water saturation (S_{wi}) is reached (forced oil imbibition). The total volume of water displaced during stages (1) and (2) is then calculated ($V_{w\,tot}$).

(3) The core is next immersed in *water* for 20 hours and the volume of *oil* displaced over this period by the spontaneous imbibition of water is measured ($V_{o\,sp}$).

(4) The core is then centrifuged under water until residual oil saturation (S_{or}) is reached (forced water imbibition). The total volume of oil displaced during stages (3) and (4) is then calculated ($V_{o\,tot}$).

The wettability of the sample is computed using two ratios:

(1) The "displacement-by-oil" ratio,

$$\delta_o = \frac{V_{w\,sp}}{V_{w\,tot}} \tag{5.1}$$

and (2) The "displacement-by-water" ratio,

$$\delta_w = \frac{V_{o\,sp}}{V_{o\,tot}} \tag{5.2}$$

Samples that are preferentially water-wet have $\delta_W>0$ and $\delta_O=0$. Similarly, oil-wet cores have $\delta_O>0$ and $\delta_W=0$. Both displacement ratios are zero for neutrally-wet media. Although Amott suggested allowing 20 hours for the completion of spontaneous imbibitions, this may be an underestimate — Anderson (1987) recommends a maximum period of 2 weeks. Premature termination of spontaneous imbibition will give rise to smaller displacement ratios and lead to an underestimate in the degree of water- or oil-wetness of the core. A slight modification to the Amott method was proposed by Boneau and Clampitt (1977) and Trantham and Clampitt (1977) whereby the water imbibition is carried out first. The wettability of the sample is then given by the "Amott-Harvey relative displacement index":

$$I = \delta_w - \delta_o = \frac{V_{o\,sp}}{V_{o\,tot}} - \frac{V_{w\,sp}}{V_{w\,tot}} \qquad (5.3)$$

The value of I varies from +1 (water-wet) to -1 (oil-wet), but it should be noted that Amott tests are generally unable to give an accurate measurement of wettability at near neutral conditions.

5.2.2 USBM Wettability Index

The USBM method (Donaldson et al, 1969, 1981) examines the work required for one phase to displace another. The main advantages in using such a test are that it gives very rapid results and is more sensitive near neutral wettability. It does not, however, take any account of spontaneous imbibition and so partially ignores the microscopic displacement mechanisms actually occurring in the reservoir itself. The procedure is as follows:

(1) Core is driven to S_{wi} by centrifuge.

(2) The core is then centrifuged under brine, at incremental speeds, until the capillary pressure reaches -10 psi (brine drive). At each increment, the volume of expelled oil is measured.

(3) Next, the sample is centrifuged under oil until a capillary pressure of +10 psi is reached (oil drive). At each stage, the volume of expelled brine is measured.

(4) Plots of capillary pressure vs brine saturation are then constructed as shown in Figure 5.3.

The USBM wettability index is then given by:

$$W = \log\left(\frac{A_1}{A_2}\right) \qquad (5.4)$$

where A_1 and A_2 are respectively the areas under the oil-drive and brine-drive capillary pressure curves. The core is considered to be oil-wet if $W<0$ and water-wet if $W>0$; the *degree* of wetness is given by $|W|$.

Sharma and Wunderlich (1985) have introduced the idea of a combined Amott/USBM wettability test, whereby spontaneous imbibition is allowed before centrifuging. Under most circumstances this should improve the accuracy of the USBM method, but it will be demonstrated later that in some instances this may not actually be the case.

5.2.3 Imbibition Method

This is the most frequently used qualitative measurement of rock wettability. Its popularity is due to the fact that it requires no specialised laboratory equipment and gives results in a very short time. The test sample (initially at S_{wi}) is submerged in brine beneath a graduated cylinder, and the rate and amount of free brine imbibition is recorded. Clearly, if a large volume of brine is quickly imbibed, then the core is water-wet; slower imbibition of a smaller volume implies a more weakly water-wet medium. If the sample fails to imbibe brine, then it is driven to S_{or} and submerged in oil. The oil-wetness of the core is then deduced in an analogous manner. In some cases, both brine *and* oil may be imbibed; this indicates a mixed- or fractionally-wet rock.

5.2.4 The Measurement Of Heterogeneous Wettability

Given the comments made in the Introduction concerning the origins of oil reservoirs, it is difficult to imagine how any such accumulation can reside in a rock matrix whose wettability is *not* heterogeneous in nature. It is surprising, therefore, that there appears to be no accepted method of determining the wettability characteristics of such systems. Indeed, the current literature regarding related experimental work is sparse and contradictory.

A nuclear magnetic resonance (NMR) technique has been proposed by Brown and Fatt (1956) to measure fractional wettability but, unfortunately, the relationship between thermal relaxation rate and core wettability is far from certain. Brown and Fatt found a linear relationship between the two, whilst Kumar et al (1969) presented a linear relationship between wettability and relaxation *time* (the *inverse* of relaxation rate). Dye adsorption techniques were successfully performed on fractionally-wet sandpacks by Holbrook and Bernard (1958), but the existence of clays in consolidated cores gave rise to problems. Neither the NMR nor the dye adsorption techniques are in regular use today, although there seem to be no effective alternatives. The determination of *mixed* wettability has proved even more difficult to achieve and, to date, there appear to be no reliable techniques available. The intrinsic difficulties associated with experimental wettability measurement have therefore prompted the current investigation using numerical simulations at the pore scale.

5.3 Simulation Model And Topological Considerations

5.3.1 Model Set-Up And Implementation

The results presented in this chapter come from simulations performed on a 3D regular cubic network comprising 20x20x20 nodes which contains 24,400 intersecting pore elements. Once again, in order to simulate larger systems, periodic boundary conditions are imposed across planes perpendicular to the direction of the applied pressure gradient. As in the previous chapter, each pore in the network is assigned a "radius" from a modified Rayleigh distribution. In reality, it is very difficult to determine what exactly constitutes a pore or a throat in a real rock sample, and so the notion of a "pore size distribution" may appear somewhat simplistic. However the rationale behind this study is that such a porous medium can simply be thought of as a collection of interconnected void spaces (see Chapter 2). Although the exact properties of these voids are unknown, each element will have associated with

it three "radii": one governing pore volume, one governing pore conductance, and the third governing pore entry pressure. In general, all three will differ from one another, but it is assumed tacitly here (not unreasonably) that all three are interrelated. Recent work by Bryant and Blunt (1992) relating to pores in random sphere packs has indeed shown this to be the case. For the special case of cylindrical pore elements, pore volume (V), pore conductance (g), and pore entry pressure (P_e) are given respectively by:

$$V(R) = \pi R^2 L \qquad g(R) = \frac{\pi R^4}{8L} \qquad P_e(R) = \frac{2\sigma\cos\theta}{R} \tag{5.6}$$

where R is the pore radius and L its length. Unfortunately, the geometry of a real pore is far more complex than this, and no such simple relationships exist. However, on the basis of geometrical analyses, it has been postulated (Heiba et al, 1982, 1983) that pores of random geometry can be described by the following proportionalities:

$$V(R) \propto R^{\nu}, \quad 0 \le \nu \le 2; \qquad g(R) \propto R^{\mu}, \quad 2 \le \mu \le 4; \qquad P_e(R) \propto \frac{1}{R} \tag{5.7}$$

where R is the radius governing pore entry pressure (the parameter which is typically measured in mercury porosimetry experiments). For reasons which will be explained in Section 5.5, the exponents chosen for this study are ν=1 and μ=4. The pore entry radii are assigned to each pore element from Equation (4.26) and corresponding volumes and conductances are found from Equation (5.7). The conductances are then used to derive elemental flows and conservation of mass at each node leads to a set of linear pressure equations which are solved to give the pressures at each node. Having obtained the pressure field for each phase in turn, relative permeabilities can then be calculated.

One of the advantages of using microscopic network simulators is that physical properties can easily be ascribed to each pore individually. Here, the wettability of each pore is controlled so that some are preferentially wetted by water and others by oil; the fraction of pores wetted by oil is denoted by α. The wetting phase contact angle is taken to be zero in both oil-wet and water-wet pores, i.e. pore walls are very strongly wetted by the corresponding wetting phase. In all that follows, the term "cluster" refers to any group of connected pores containing the same phase, whilst a "spanning cluster" is a cluster which spans the network — connecting the inlet face of the network to the outlet face.

Each simulation begins with the network 100% saturated with oil, and water is then introduced at the inlet face. Each waterflood consists of the following two stages:

(1) Water is first allowed to spontaneously imbibe via film flow *but only along continuous water-wet pathways which have access to the inlet.* Accessible water-wet pores are then assumed to become filled via a "snap-off" mechanism (Lenormand and Zarcone 1984, inter alia), whereby the smallest pores are filled first followed by the next smallest and so on. The defending oil phase can escape from a pore by draining along a pathway of oil-filled pores which connect it to the outlet.

(2) Once spontaneous imbibition has ceased, the invading water is conceptually over-pressured (i.e. a negative capillary pressure is applied) and now acts as a nonwetting fluid. The displacement is modelled using an invasion percolation process (Chandler et al, 1982; Wilkinson and Willemson, 1983), and the water next fills the *largest* oil-wet pores connected to either the inlet face of the network or the invading water cluster. If, at any time during the forced imbibition, water-wet pores are contacted by the invading cluster, then they are filled spontaneously if the defending oil can escape. Throughout forced imbibition, oil may escape in two different ways: either

(a) by draining along a pathway of oil-*filled* pores which connect it to the outlet, or

(b) by draining via film flow along a pathway of oil-*wet* pores to the outlet.

Both fractionally-wet and mixed-wet cases are considered, whereby oil-wet pores are either of random size or correspond to the largest pores in the network. Clustering algorithms (following Hoshen and Kopelman, 1976) have been developed which permit the labelling of both oil clusters and water clusters as well as clusters of oil-*wet* and water-*wet* pores. Note that the fluid clusters are a dynamic phenomenon, whilst the "wettability clusters" remain static during a given process.

Before going on to report the various simulation results, it will be beneficial to briefly describe the more complex clustering behaviour of the system.

5.3.2 Cluster Behaviour And Phase Trapping in Systems of Non-Uniform Wettability.

Consider a pure bond percolation problem such as the spontaneous imbibition model described earlier. Now, however, not only are there clusters of oil- and water-filled pores, but also oil- and water-*wet* pores. The behaviour of the phase clusters has already been described in Chapter 4, so consider now the consequences of the wettability clustering. Consider a system where all pores are initially oil-wet. The wettability characteristics of a fraction of pores are now altered at random positions throughout the network, so that there now exists a small fraction (p) of randomly-scattered water-wet pores. As more and more pores are made water-wet, the number of water-wet clusters (groups of connected water-wet pores) increases with the water-wet bond fraction (p). As before, above a certain value of p, these small isolated groups begin to join together to form larger aggregates; hence the *total* number of water-wet clusters

begins to decrease. Eventually, one cluster emerges which spans the entire network from inlet to outlet. The value of p at which this occurs will be called the *wettability percolation threshold* P_{cw}. For a cubic network, P_{cw}=0.2488, and so once approximately one quarter of the pores have been designated as water-wet, films of the displacing water phase can flow freely through the network. As still more pores are made water-wet, the total number of clusters continues to diminish until, at $p \approx 0.5$, almost all of the water-wet pores form one large cluster. Symmetry arguments show that the clustering behaviour of the oil-wet pores is analogous to that of the water-wet pores. The clustering behaviour of both wettability types is analogous to the phase clustering shown in Figure 4.18. The point $p = 0.5$ is again seen to be of primary importance: it is at this point that the network essentially consists of two large clusters; one of water-wet pores, the other of oil-wet pores. This will clearly influence the trapping behaviour of the system, because all of the defending oil will have access to a large oil-wet cluster and so escape towards the outlet will always be possible by film-flow. That is to say, when $p < 0.5$, a continuous escape route of oil-wet pores will always be available, even though almost half of the network has been made water-wet. The structure of the water-wet clusters is also extremely important, because spontaneous imbibition can only take place via film-flow of water along these pathways.

5.4 Simulation Of Capillary Pressure Curves

5.4.1 Capillary Pressure Curves From Strongly Wetted Systems

Whenever an oil/water interface becomes curved, the pressure jump across it will increase until an equilibrium is reached between it and the opposing interfacial tension forces. The pressure jump at which this balance is attained is given by Laplace's equation:

$$p_c = p_o - p_w = \sigma\left(\frac{1}{r_1} + \frac{1}{r_2}\right) \qquad (5.8)$$

where σ is the interfacial tension between the two fluids, and r_1 and r_2 are the two principal radii of curvature. The pressure difference p_c is known as the *capillary pressure* and is conventionally taken to be the pressure in the nonwetting phase minus the pressure in the wetting phase. For drainage of a water-wet circular capillary (radius R) and zero contact angle, this relationship becomes:

$$p_c = p_o - p_w = \frac{2\sigma}{R} \tag{5.9}$$

Notice that the capillary pressure can become negative if $p_w > p_o$. Such a situation could arise if the capillary was oil-wet, for instance, resulting in a reversal of the interfacial curvature. The combination of "negative" and "pressure" may at first seem confusing, but the term is merely an artefact of conventional terminology. The concept of negative capillary pressure will be central to the latter part of this section.

When discussing displacements in porous media of heterogeneous wettability, the terms imbibition and drainage become somewhat misleading. All results presented in this chapter relate to waterfloods, which may be a *combination* of conventional imbibition and drainage processes. When the network consists of 100% water-wet pores, the waterflood is a pure imbibition process; if all of the pores are oil-wet, however, the process is drainage with water as the nonwetting phase. When the network contains a mixture of water-wet and oil-wet pores, the waterflood initially proceeds as an imbibition, but eventually the water has to be forced into oil-wet pores and the displacement becomes one of drainage.

Waterflood capillary pressure curves corresponding to 100% water-wet and 100% oil-wet networks are shown in Figure 5.4 — in both cases the network was initially 100% saturated with oil. There are no oil-wet pathways available

to the trapped oil in the former case, and so a large residual oil saturation is the result. In the latter scenario, however, all pores are oil-wet, resulting in the gradual escape of all "trapped" oil via a film-flow mechanism. Experimentally, imbibition is a very difficult process to control, and it would appear from the literature that this can only be achieved if the pressure in the oil phase is gradually reduced so as to enable only pores having radii up to the current pore entry radius to be accessed. This is why imbibition capillary pressure curves are shown here as actual curves and not merely as straight lines running along the horizontal axis ($p_c/\sigma=0$).

It should be noted that the capillary entry pressure at which a pore of radius R is filled during *imbibition* is only half that given for drainage by Equation (5.9), i.e.

$$p_c\big|_{imb} = p_o - p_w = \frac{\sigma}{R} \qquad (5.10)$$

(see Lenormand and Zarcone (1984) for a full explanation). It will become clear that this greatly influences the shape of waterflood capillary pressure curves resulting from displacements in media of heterogeneous wettability. In all of the capillary pressure curves that follow, $p_c>0$ indicates that the process is imbibition, a negative p_c indicates drainage.

5.4.2 Waterflood Capillary Pressure Curves From Fractionally-Wet Systems

The simulated capillary pressure curves from fractionally-wet networks are displayed in Figure 5.5, whilst the corresponding pore filling sequences are shown in Figure 5.6. These pore filling sequences are a useful way in which to analyse each waterflood as they show exactly how each stage of the displacement proceeds.

For the strongly water-wet network (α=0, Figure 5.5a), water-wet surfaces exist throughout the entire network, and so all pores satisfying the pore entry criteria are accessible through film-flow. The topological structure of the model means that at the end of the waterflood, oil remains trapped as isolated ganglia in what are essentially the largest pores in the network (about 75% of the pores having been invaded). The sharp tailing-off of the curve at $S_w \approx 0.61$ is almost entirely due to this phase trapping, the shape of the pore size distribution itself only having a minimal effect. The corresponding filling sequence (Figure 5.6a) shows that residual oil saturation is reached when $R \approx 45$ ($p_c/\sigma \approx 0.022$). Reducing the capillary pressure below this value has no effect whatsoever upon the trapped oil - it is disconnected from the outlet and the absence of any oil-wet pores precludes any escape via film flow.

With α=0.35, a rather interesting phenomenon becomes apparent. *Although 35% of the pores are now oil-wet, a larger volume of water has imbibed than did when the entire network was water-wet.* The rather subtle reason for this is clear from Figure 5.6b; because of the distribution of oil-wet pores in fractionally-wet media, the imbibition of water now ends with oil remaining in pores of all sizes. This surprising effect will actually be seen for a range of α as shown in Figure 5.7. Only when the volume-weighted integral of oil-wet pores becomes greater than $S_{or}(\alpha=0)$ will the system behave in a more predictable manner. Notice also that the tailing-off of the capillary pressure curve is more gradual than before — this is because as p_c decreases, there are always some water-wet pores whose radii fulfil the current pore entry requirements. The cluster growth results of Section 5.3.2 show that with only 35% of the pores oil-wet, the invading water has been able to fill almost every water-wet pore during imbibition. This means that all remaining oil-filled pores are in contact with the water phase. Once the imbibition stage of the displacement has ended, the invading water is then forced into the *largest* oil-wet pores. The fact that the maximum pore radius is 100 means that no further displacement occurs until

p_c/σ=-2/100=-0.02 (the factor -2 appears because the process is now drainage with water as the nonwetting phase). This creates a discontinuity in the slope of the capillary pressure curve as the waterflood changes from imbibition to drainage. As the displacement continues, some oil escapes via a pathway of oil-filled pores whilst the remainder eventually drains through films. If enough time is allowed for film drainage to occur, only a small amount of residual oil will remain at the end of the flood.

As the fraction of oil-wet pores is increased still further, the volume of water spontaneously imbibed decreases whilst the extent of forced displacement increases. This trend is mirrored in the experimental data of Fatt and Klikoff (1959), who used fractionally-wet sandpacks containing mixtures of oil-wet and water-wet grains. Their results are shown in Figure 5.8 (notice that these relate to oilfloods giving inverted capillary pressure curves).

With α increasing, fewer and fewer water-wet pathways become available to the invading water during imbibition. Eventually, as α approaches 0.75, no spanning cluster of wetting phase will exist after imbibition (the number of water-wet pores is below the wettability percolation threshold). This reduction in water clusters at the end of imbibition means that many pores satisfying the capillary entry criteria during drainage are no longer *accessible* to the invading phase. Consequently, the curvature of the capillary pressure curve during the early stages of drainage becomes more and more pronounced as $\alpha \rightarrow 1$. Finally, when α=1 the curve has the characteristic structure of typical drainage experiments, with very little displacement of the wetting phase occurring until a specific displacement pressure has been reached.

5.4.3 Waterflood Capillary Pressure Curves From Mixed-Wet Systems

The simulated capillary pressure curves from mixed-wet networks are given in Figure 5.9, whilst the corresponding pore filling sequences are shown in Figure

5.10. As α increases, the trend in the corresponding capillary pressure curves is more straightforward than in the fractionally-wet regime. As expected, an increase in the fraction of oil-wet pores results in a decrease in the amount of spontaneous imbibition and an increase in the amount of drainage. The extent of spontaneous imbibition is now a clear indication of the degree of water-wetness of the sample.

The most interesting aspect of these curves is the form of the discontinuity as the process switches from imbibition to drainage. At the end of imbibition the curves no longer tail off gradually, but come to an abrupt end - subsequent reductions in capillary pressure towards zero yield no additional displacement: the explanation for this becomes clear once the corresponding pore filling sequences have been examined. Notice that when α=0.25, additional oil was recovered during drainage: this would not be expected in an infinite system, however, because a vanishingly small volume of oil would actually lie on the spanning cluster of oil-wet pores at percolation threshold (see Stauffer and Aharony, 1992). This additional recovery is due to a finite size effect relating to the networks used in the study.

Although the simulator used for these studies is based upon very simple pore occupancy rules, it has clearly demonstrated the possible effects of wettability on waterflood capillary pressure curves. Results presented here would support the belief that coreflood capillary pressure experiments should only be done using native state cores (Anderson, 1987). In many cases, the use of cleaned cores for capillary pressure measurements could give very inaccurate results.

5.5 Simulation Of Relative Permeability Curves

The choice of volume and conductance exponents used for each pore element was referred to earlier in Section 5.3.1. The particular values used, namely ν=1 and μ=4, were chosen so as to model the relative permeability curves resulting

from experimental waterfloods performed on very strongly water-wet and very strongly oil-wet porous media. The key features of such curves were presented by Craig (1971) who indicated the differences between the two in the form of several rules of thumb. Many subsequent experimental studies have agreed with these ideas (Donaldson and Thomas, 1971; Shankar and Dullien, 1981; inter alia). Craig's rules of thumb are given in Table 5.1 and these features have been used to "anchor" the simulation model. Once the model has been anchored, its sensitivity to a variety of wettability conditions can then be investigated. Understanding the resulting variations in relative permeability curves is an extremely important issue, as such curves are often used as input data for large-scale reservoir simulations.

5.5.1 Fractionally-Wet Relative Permeabilities

Relative permeability curves were computed for a variety of α values and several are shown in Figure 5.11. It is evident that as the oil-wet pore fraction increases from 0 to 1, the curves (and the crossover point) show a general shift towards lower water saturations. The oil curves change from being convex to concave in appearance whilst the water curves exhibit the reverse behaviour. Curves tend to lie within the 100% water-wet/100% oil-wet envelope. Increasing the oil-wet pore fraction has two effects: at low water saturations the oil permeability decreases with increasing α, whilst at high water saturations the water permeability *increases* with α. Note also, that the residual oil saturation decreases, tending towards 0 as the fraction of oil-wet bonds approaches approximately 0.5 (because at this point, oil-wet pores basically form one large cluster which can always conduct escaping oil via film-flow; see Figure 4.8 for an indication of what p=0.5 would look like). The endpoint water relative permeability consequently increases with α.

To date, the author is unaware of any equivalent steady-state experimental data with which to compare these predictions. Fatt and Klikoff (1959) performed

constant-rate waterflood experiments using fractionally-wet sand mixtures and the changes in the relative permeability ratio which they reported are similar to changes encountered by Mungan (1966) who varied the wettability of the whole system *uniformly* between oil-wet and water-wet (see Anderson, 1987). The implication is that fractionally-wet porous media should have relative permeability characteristics similar to "equivalent" uniformly-wet samples. The results presented here suggest that this may indeed be the case. By plotting the curves of Figure 5.11 on semi-log axes, the simulation results can be compared to the experimental curves of Owens and Archer (1971) whose experiments were performed on *uniformly*-wet Torpedo sandstone. Their results are shown in Figure 5.12 There is good qualitative agreement between the two, giving further credence to the above hypothesis.

5.5.2 Mixed-Wet Relative Permeabilities

The relative permeability curves from mixed-wet networks, computed for a variety of α values, are shown in Figure 5.13. Although the general trend is not quite as obvious as that emerging from the fractionally-wet simulations, it is apparent that once again the oil curve loses curvature and the water curve gains curvature as the oil-wet pore fraction increases. In contrast to the fractionally-wet case, however, the crossover point does not steadily move towards lower water saturations. For α between 0 and 0.5, it actually shifts to higher saturations; only when $\alpha > 0.5$ does it begin to moves back towards lower values.

The precise structure of relative permeability curves plays a vital role in determining reservoir performance and efficiency. The results described above show that experiments performed on unrepresentative core samples may yield inaccurate curves and subsequently lead to incorrect field predictions. The precise effect of reservoir wettability on waterflood performance is now examined in more detail.

5.6 Prediction Of Waterflood Performance

The relative permeability curves described above can now be used in the conventional fractional flow equations enabling the construction of a family of fractional flow curves. Buckley-Leverett analyses can then be carried out to uncover how the microscopic displacement efficiency is expected to be influenced by the wettability of the system. In the somewhat sparse literature on non-uniform systems there is much disagreement regarding this question. Donaldson et al (1969) and Emery et al (1970) performed waterflood experiments using core plugs which had been aged in crude for varying periods of time. Both studies showed that the more water-wet the rock, the more efficient the displacement. Conversely, Kennedy et al (1955), Amott (1959) and Salathiel (1973) have all shown that the most efficient recovery takes place at close to neutral conditions. The precise wettability details are unclear from study to study and so a systematic investigation of both fractionally- *and* mixed-wet systems is undertaken here.

5.6.1 Displacement Efficiency In Fractionally-Wet Systems

Buckley-Leverett analyses (with μ_w=1cP and μ_o=7cP) were performed using the simulated relative permeability curves of Figure 5.11. Figure 5.14 shows how the displacement efficiency varies with the water-wet pore fraction. At breakthrough it is clear that the displacement in the strongly water-wet system is more efficient than that in the strongly oil-wet regime, and this is in complete agreement with experimental evidence. The most surprising aspect of the results, however, is that the *most* efficient displacement actually takes place in a system containing approximately 50% oil-wet pores. That is to say, oil production at breakthrough is maximised when half the sample is oil-wet and half is water-wet. As each waterflood continues, the displacement efficiencies increase - more in some cases than others. For instance, once breakthrough has occurred in the strongly water-wet network, relatively little additional oil is

subsequently recovered. For the strongly oil-wet case, however, the low efficiency at breakthrough is countered by a large increase in recovered oil as the displacement continues. Note that even after many pore volumes have been injected (and the *economic* residual oil saturation has been passed), the maximum recovery is still achieved in weakly oil-wet systems containing a mixture of oil-wet and water-wet pores.

The reasons for such a phenomenon are not immediately clear, but its existence means that many of the heuristic arguments relating wettability to recovery efficiency are certainly not valid here. These arguments are based upon the form of the water fractional flow equation and the structure of the associated relative permeability curves. The water fractional flow equation is given by:

$$f_w(S_w) = \frac{1}{\left\{1 + \frac{\mu_w k_{ro}(S_w)}{\mu_o k_{rw}(S_w)}\right\}} \qquad (5.11)$$

where μ_o and μ_w are the oil and water viscosities respectively. At breakthrough, the average water saturation in the sample is equal to the slope of the tangent to the fractional flow curve drawn from the point $S_w=S_{wi}$ (see Figure 5.15). This is wholly governed by the mobility ratio in Equation (5.11) which in turn depends upon the corresponding relative permeability values. The heuristic argument goes as follows: as the oil-wetness of the sample increases then, for fixed S_w, oil relative permeability values decrease and water relative permeability values increase (see Figure 5.11). This means that at any S_w, the fractional flow of water (f_w) increases as the oil-wetness increases and hence so do the slopes of the corresponding tangents. The obvious conclusion to draw must therefore be that waterfloods of strongly water-wet media are most efficient at breakthrough, with this efficiency steadily decreasing as the media become more and more oil-wet. This argument supports the early results of Donaldson et al (1969) and Emery et al (1970), but in fact the situation

is not as clear-cut as this. Closer examination of Figure 5.11 shows that the above assumptions concerning relative permeability trends need not be valid here for water saturations greater than about 0.55. The oil permeabilities do not follow the trend exhibited at low S_w once:

$$S_w > S_w^* \tag{5.12}$$

where S_w^* is the crossover point of the relative permeability curves when $\alpha=0$. This happens to be exactly the saturation range which characterises the average water saturation at breakthrough and so the above argument becomes invalid. The precise explanation for the maximum displacement efficiency occurring at $\alpha \approx 0.5$ is not obvious even in the controlled environment of simulation, but is clearly linked to pore topology and the structure of oil relative permeability curves close to the endpoints.

5.6.2 Displacement Efficiency In Mixed-Wet Systems

Plots of displacement efficiency vs water-wet pore fraction for mixed-wet networks are shown in Figure 5.16 The qualitative features of these curves are similar to those found for the fractionally-wet systems, but the variation in recovery is greater here (about 15%). Again, the most efficient displacement takes place in a system containing approximately 50% oil-wet pores. Recent studies by Jadhunandan and Morrow (1991) have indicated that recovery should be optimal at close to neutral conditions in mixed-wet media. Their results are illustrated in Figure 5.17 and comparison with Figure 5.16 shows that the calculations carried out here reproduce their observations very satisfactorily.

5.7 A Proposed Method Of Wettability Measurement

In Chapter 4, it was demonstrated that the way in which conventional relative permeability curves are plotted effectively disguises the underlying dynamics

of the process under investigation. It was shown that a step-by-step analysis of the displacement could be better understood by plotting relative permeabilities as functions of the "current bounding radius" — the radius characterising the current value of the capillary entry pressure (i.e. $R \propto 1/p_c$). By plotting such curves for a range of wettability conditions, it is hoped that a new method of wettability measurement may be found which eliminates problems associated with current techniques (described in Section 5.2). An additional advantage associated with the methods described below, is that they do not require saturation determination at any stage.

5.7.1 Measurement Of Fractional Wettability

It was demonstrated in Section 5.4.2 that the amount water spontaneously imbibed by a fractionally-wet medium need not necessarily be an indication of the extent of its water-wetness: it was shown that a 100% water-wet network could imbibe *less* water than a 65% water-wet network. This difficulty may be overcome by examining the corresponding R-k_{ro} and R-k_{rw} curves during the imbibition stage of each waterflood. These are shown for a variety of wettability conditions in Figure 5.18. Clearly the water relative permeabilities are of little use for the prediction of wettability, but the oil curves follow a distinct pattern. As the number of oil-wet pores increases, the R-k_{ro} curves fan out and terminate at progressively higher values of k_{ro}. These results show that such a method may prove extremely useful for distinguishing a wide range of wettability conditions. Percolation theory dictates that curves for $0.75 \leq \alpha \leq 1.0$ will collapse onto the single $\alpha=1.0$ curve and so this technique may not differentiate between oil-wet and strongly oil-wet media. Fortunately, however, wettabilities within this range should be correctly identified by spontaneous imbibition tests (see Section 5.2.3). It is hoped that analysis of R-k_{ro} curves resulting from waterfloods on water-wet to mildly oil-wet media could overcome the problems associated with standard measurement techniques described above.

5.7.2 Measurement Of Mixed Wettability

The corresponding R-k_{ro} and R-k_{rw} curves for mixed-wet systems are shown in Figure 5.19 and are clearly structurally different from those derived from fractionally-wet networks. Either set of curves could be utilised for wettability measurement, although greater resolution would be obtained by using R-k_{ro} plots. Note that the standard imbibition test should prove adequate for quantifying the wettability of mixed-wet media, *but only if the assumption of mixed wettability can be shown to have been correct at the outset.* The tests suggested here may be able to distinguish not only the extent of oil wetness in a sample, but also its spatial distribution: i.e. whether mixed-wet or fractionally-wet conditions exist.

Results presented in this chapter support the argument that only native-state cores should be used for laboratory analysis, as any alteration in matrix wettability will invariably lead to inaccurate (and possibly very costly) conclusions: waterfloods performed on cleaned or weathered material would almost certainly result in an erroneous prediction of reservoir efficiency. The main conclusion to be drawn from this study is that a clear understanding of the role played by wettability at the pore scale is essential if accurate predictions are to be made at a macroscopic level.

TABLE 5.1 CRAIG'S RULES OF THUMB

	WATER-WET	**OIL-WET**
Connate water saturation	Usually greater than 20-25% PV	Generally less than 15% PV. Often less than 10%.
Water saturation at which $k_{ro}=k_{rw}$	Greater than 0.5.	Less than 0.5.
Value of k_{rw} at maximum water saturation ($1-S_{or}$).	Usually less than 0.3.	Greater than 0.5 and approaching 1.0

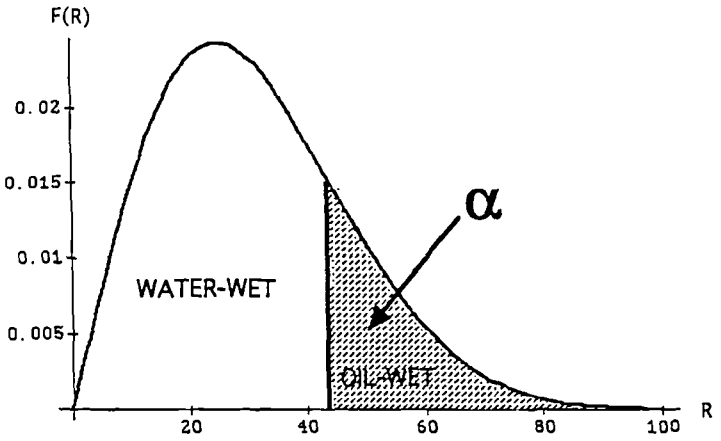

Figure 5.1 Distribution of oil-wet pores in a mixed-wet porous medium.

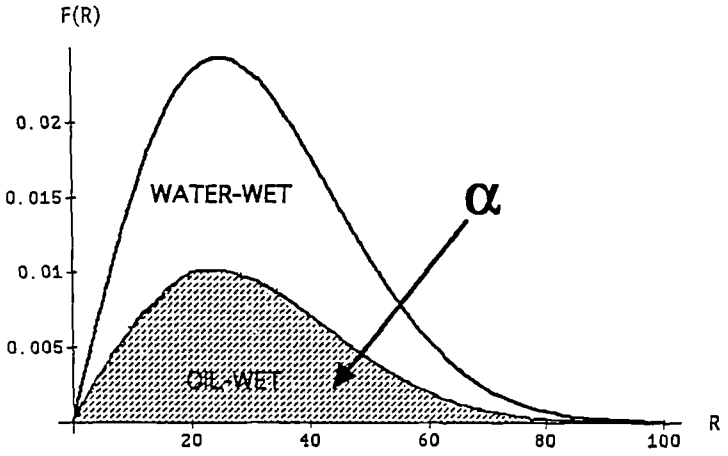

Figure 5.2 Distribution of oil-wet pores in a fractionally-wet porous medium.

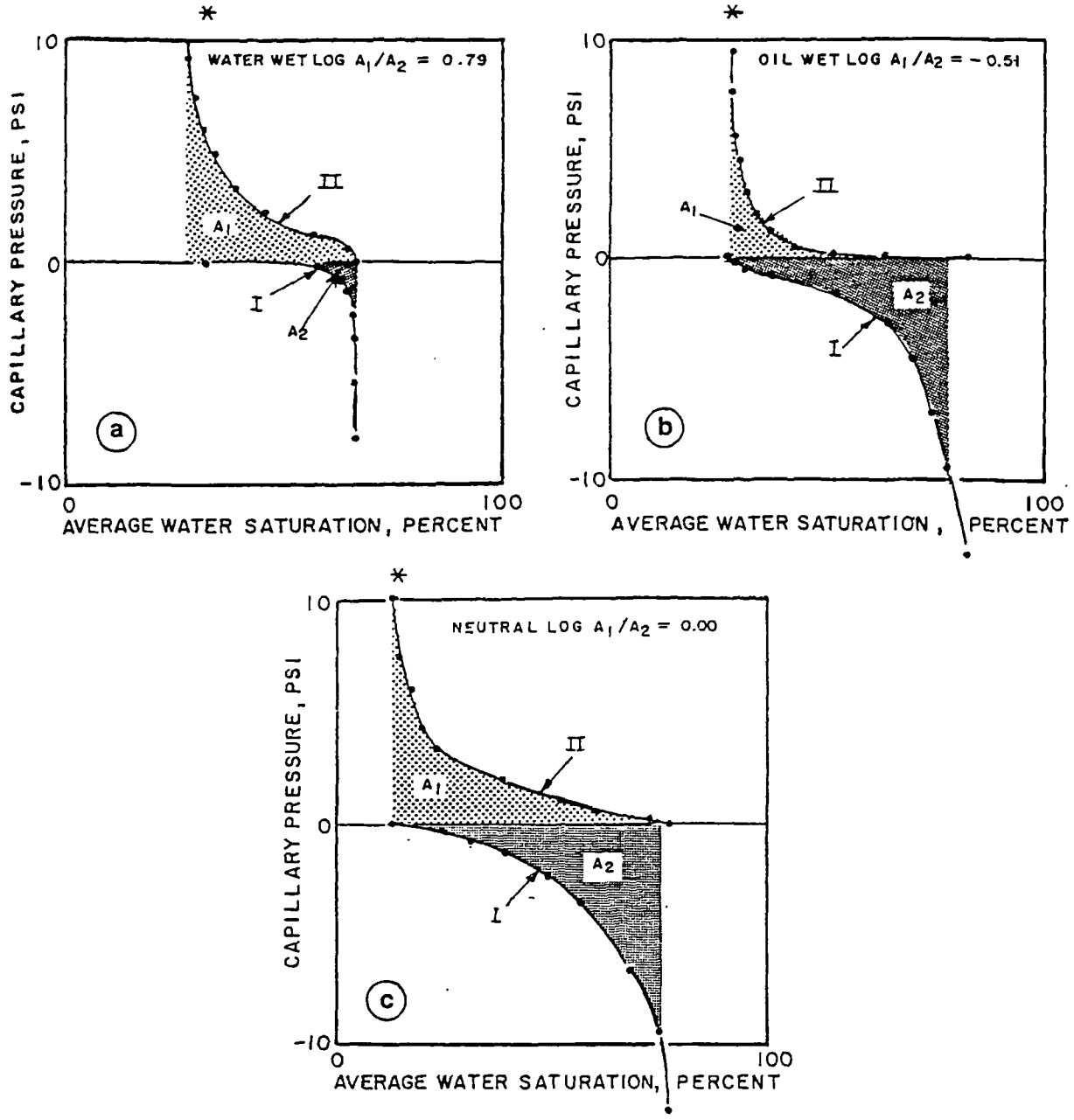

Figure 5.3 The USBM wettability measurement technique (after Donaldson et al, 1969) — see text for details.

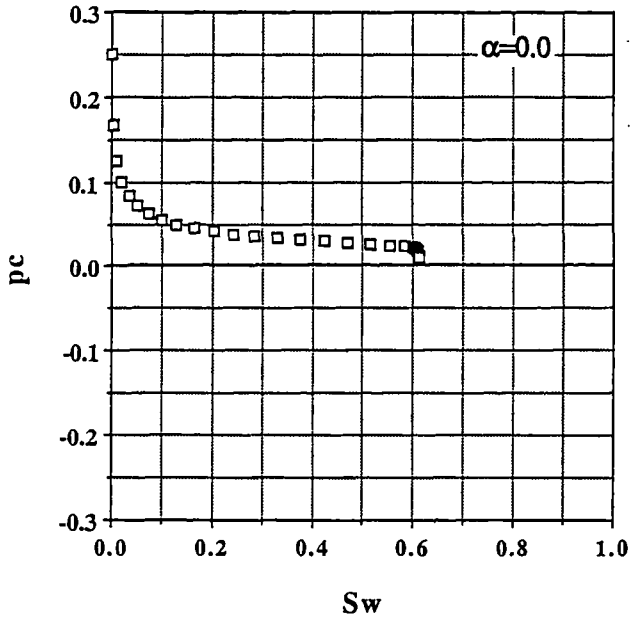

(a)

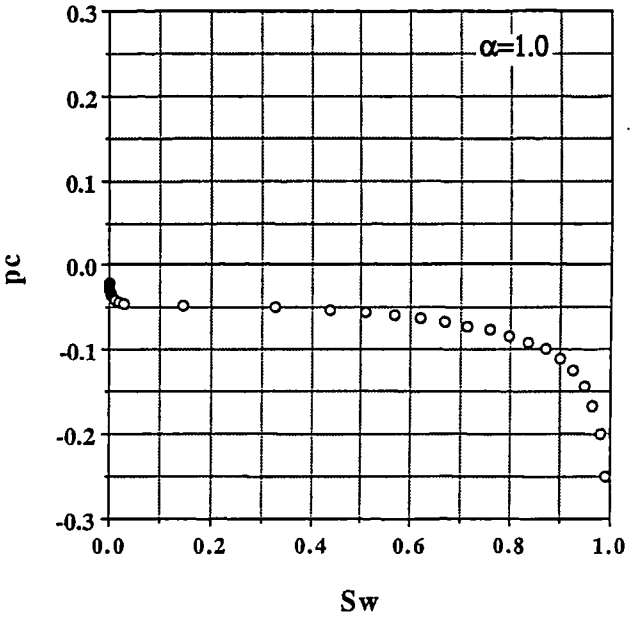

(b)

Figure 5.4 Waterflood capillary pressure simulations: (a) 100% water-wet network (imbibition), (b) 100% oil-wet network (drainage).

(a)

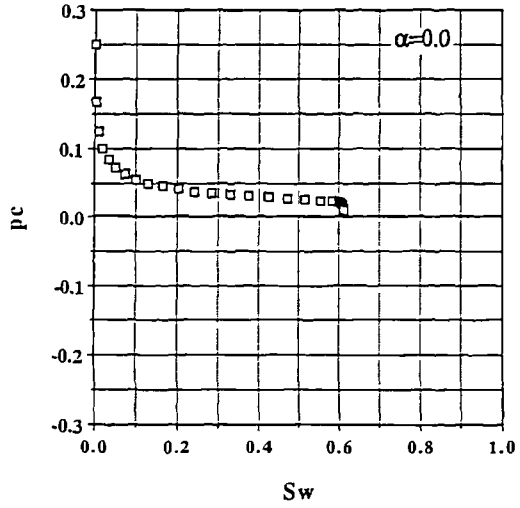

(b)

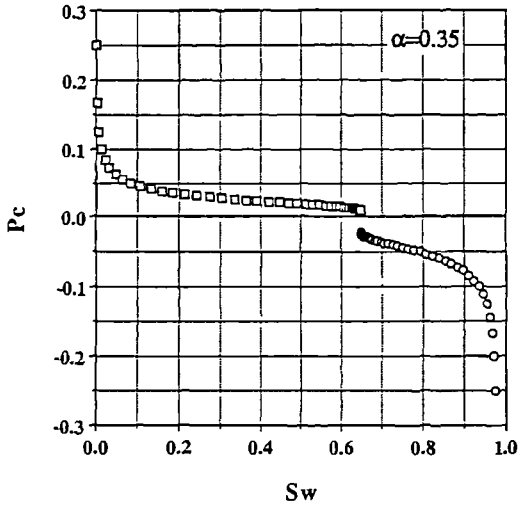

(c)

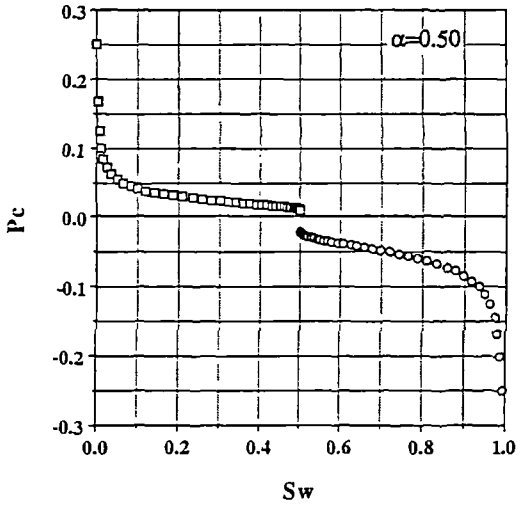

Figure 5.5 Waterflood capillary pressure curves for a variety of fractionally-wet networks: (a) α=0, (b) α=0.35, (c) α=0.5, (d) α=0.65, (e) α=1.0.

(d)

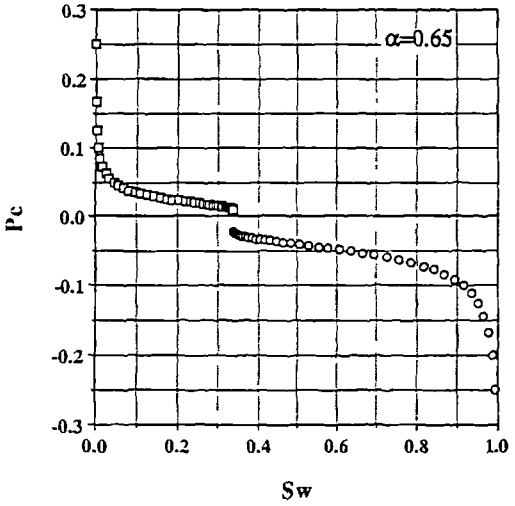

(e)

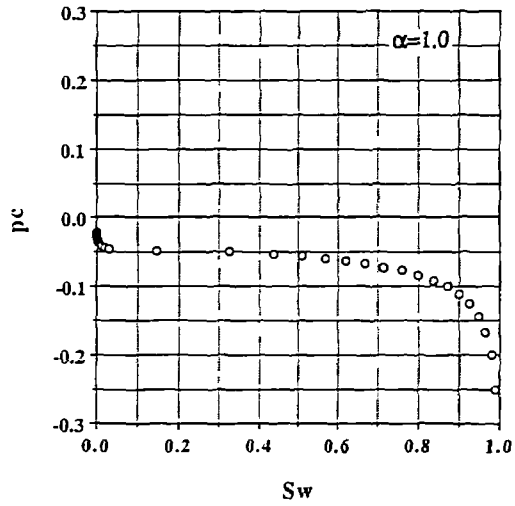

Figure 5.5 (Continued)

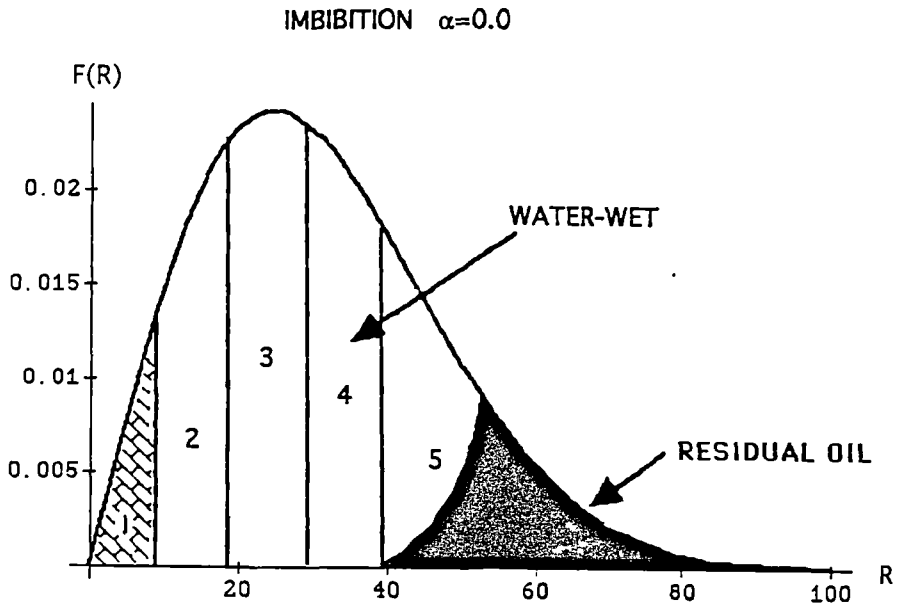

(a)

Figure 5.6 Pore filling sequences for waterfloods of fractionally-wet networks: (a) α=0, (b) α=0.35, (c) α=0.5, (d) α=0.65, (e) α=1.0.

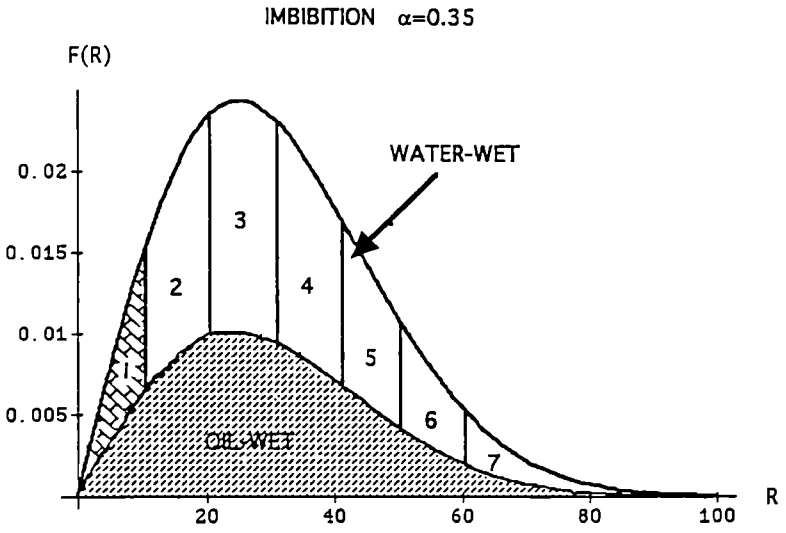

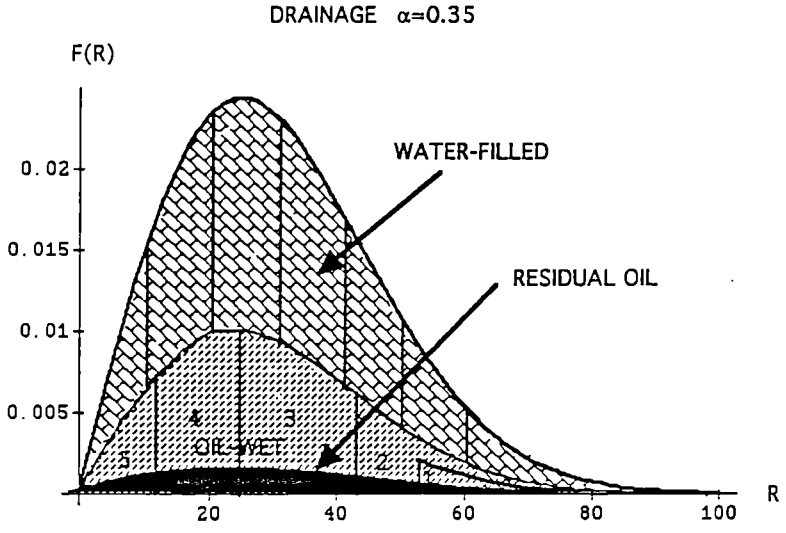

(b)

Figure 5.6 (Continued)

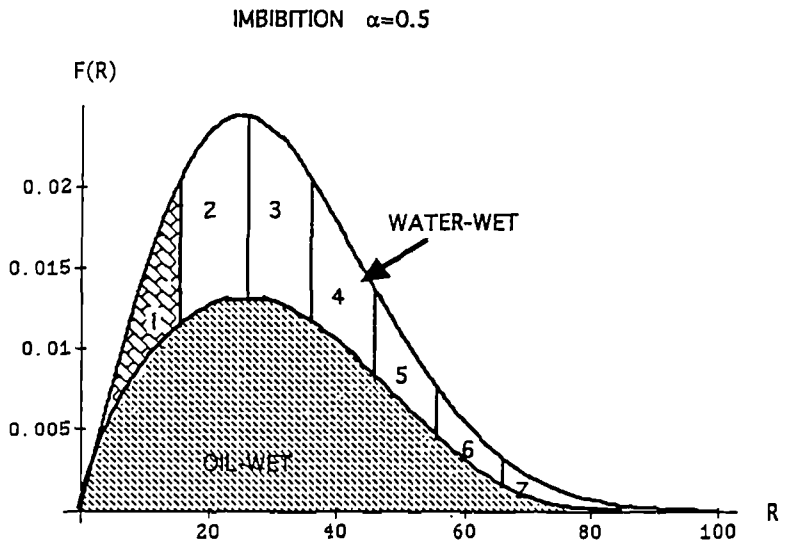

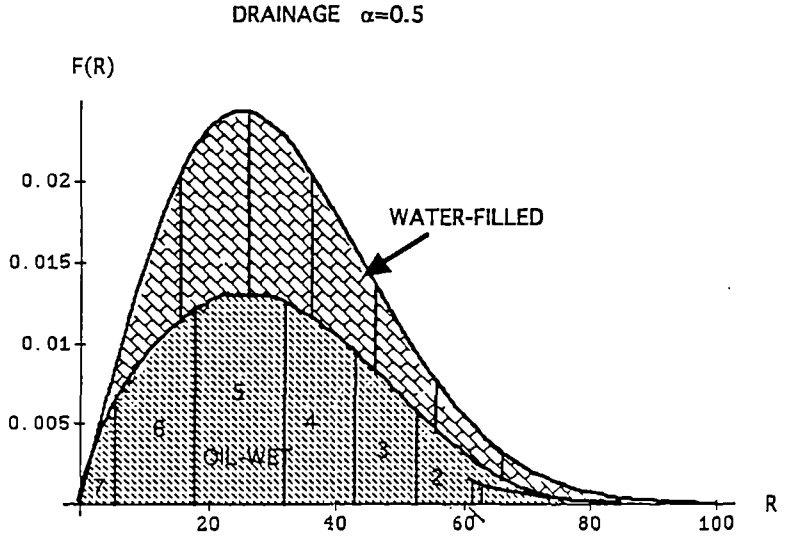

(c)

Figure 5.6 (Continued)

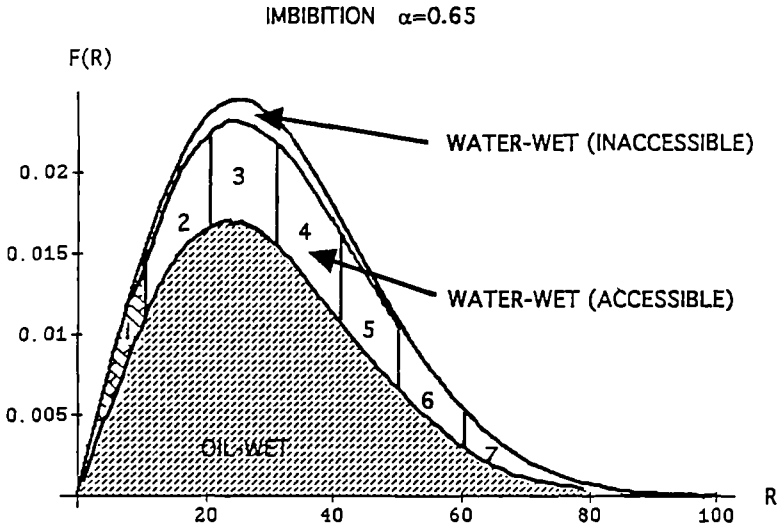

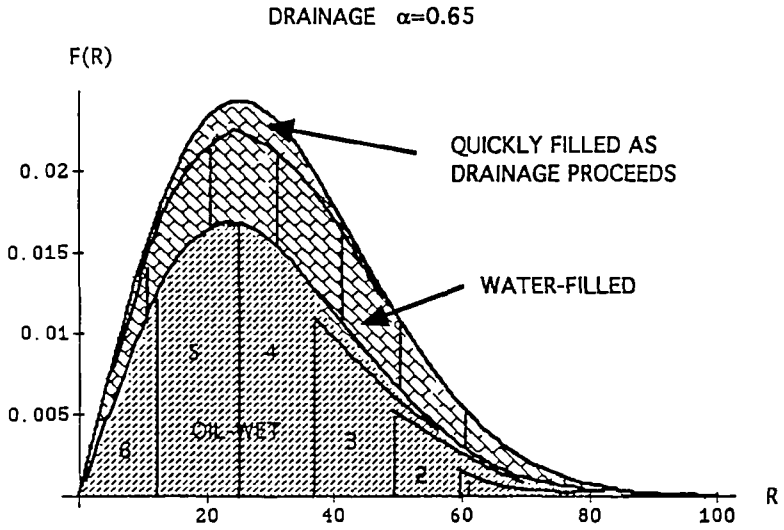

(d)

Figure 5.6 (Continued)

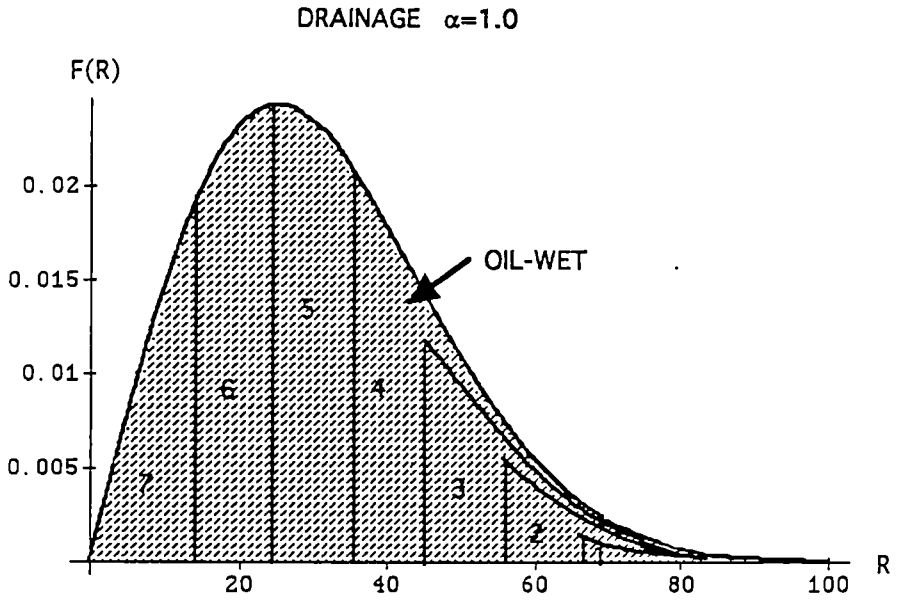

(e)

Figure 5.6 (Continued)

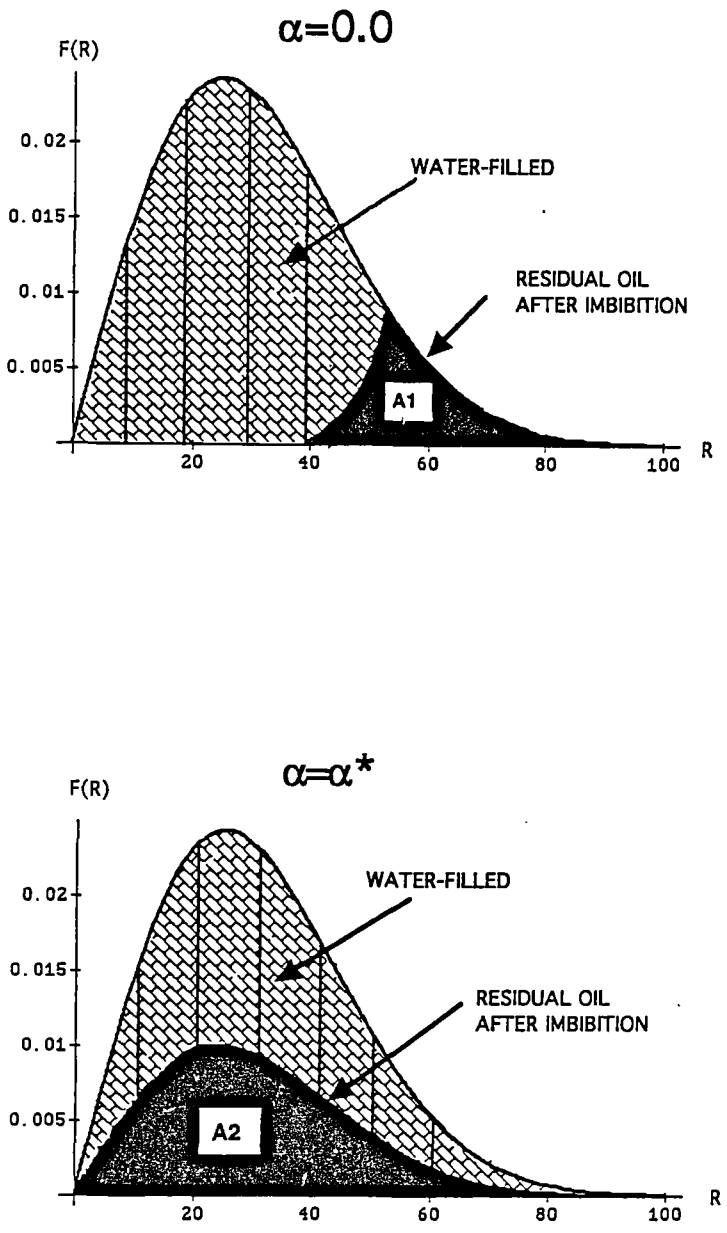

Figure 5.7 For all $\alpha<\alpha^*$, the amount of water spontaneously imbibed by a fractionally-wet network will exceed that imbibed by a 100% water-wet network. The value of α^* is such that the volume weighted integrals corresponding to A_1 and A_2 are equal.

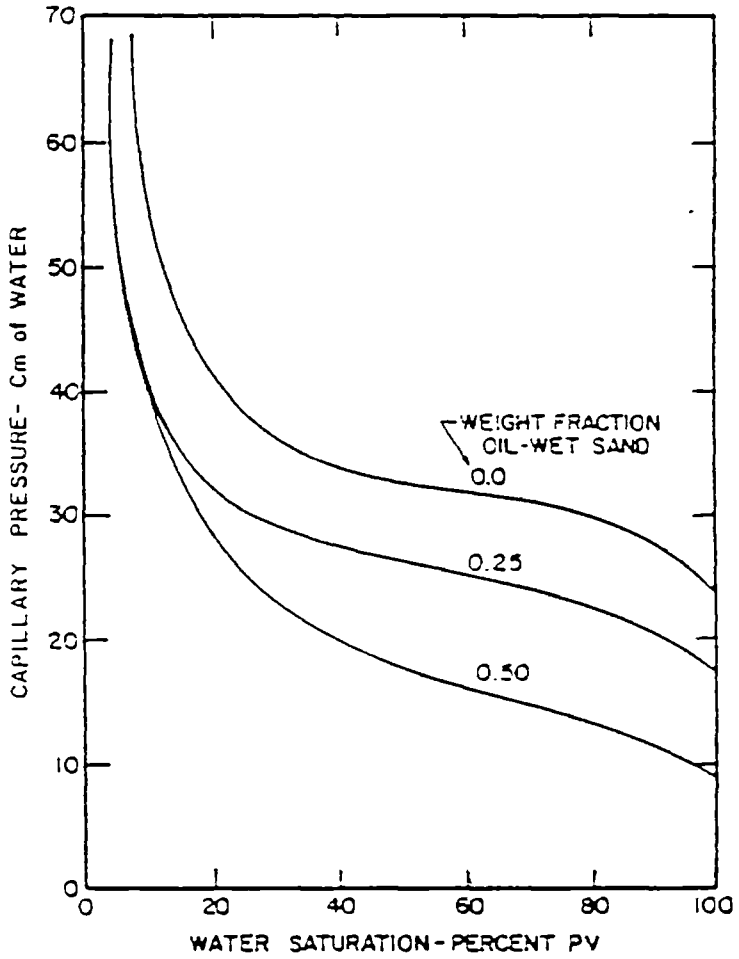

Figure 5.8 Effect of fractional wettability on capillary pressure curves derived experimentally from sandpack floods (after Fatt and Klikoff, 1959).

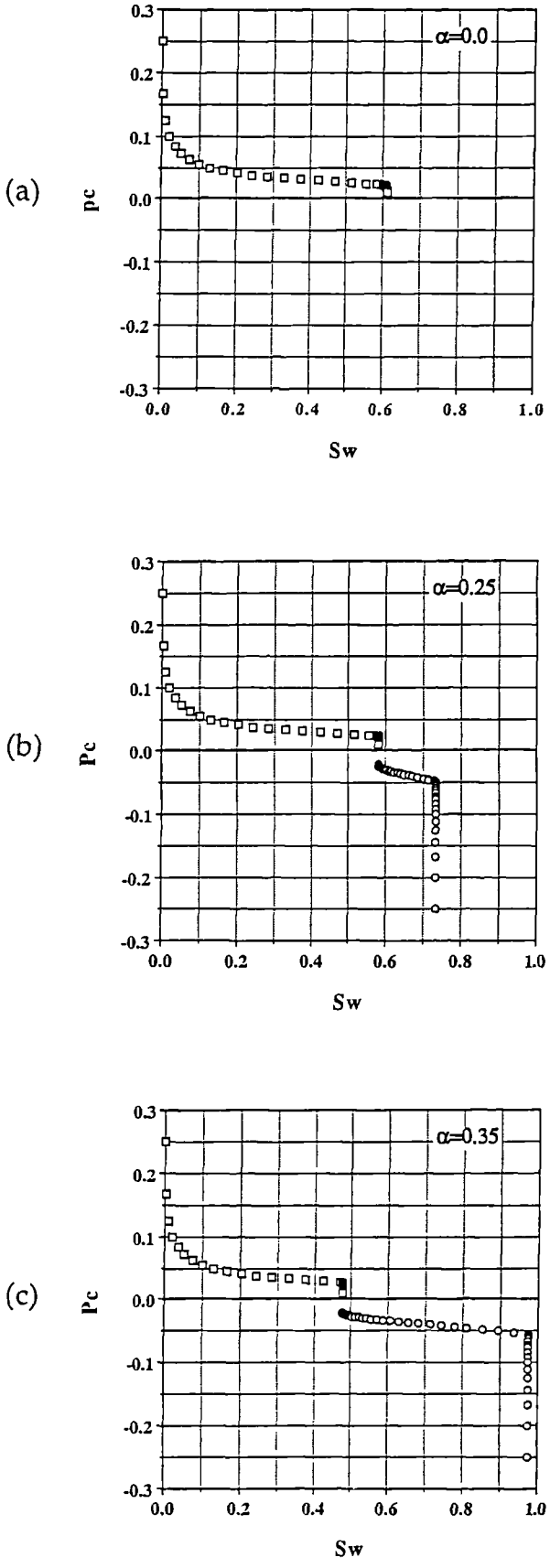

Figure 5.9 Waterflood capillary pressure curves for a variety of mixed-wet networks: (a) α=0, (b) α=0.25, (c) α=0.35, (d) α=0.5, (e) α=0.75, (f) α=1.0.

(d)

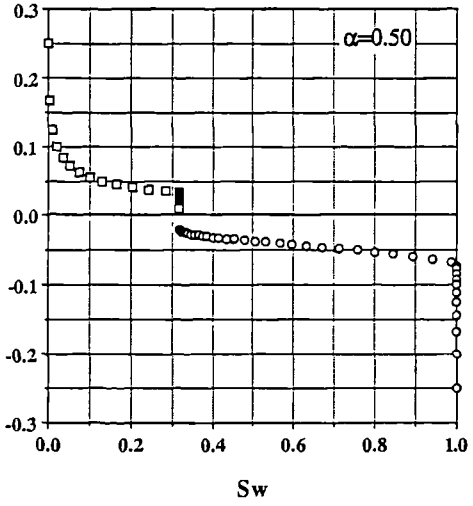

(e)

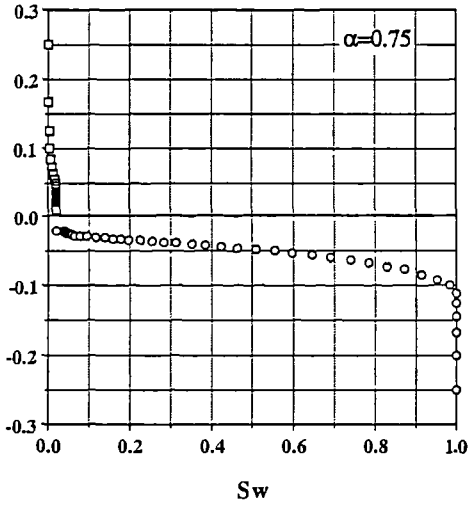

(f)

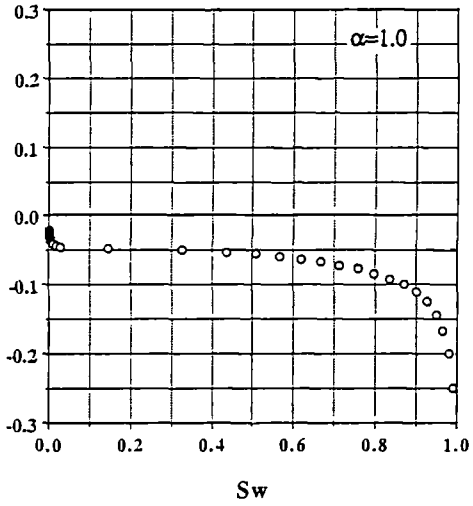

Figure 5.9 (Continued)

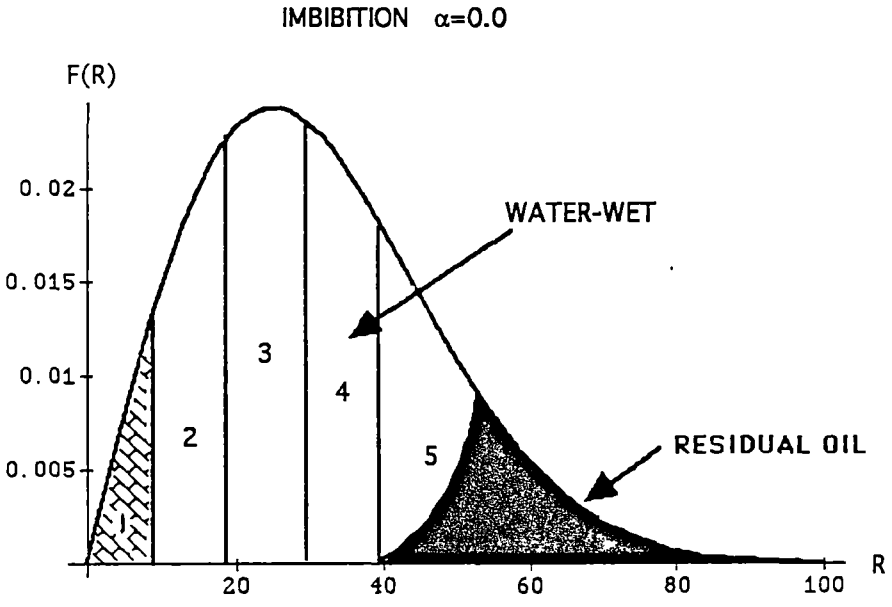

(a)

Figure 5.10 Pore filling sequences for waterfloods of mixed-wet networks: (a) α=0, (b) α=0.25, (c) α=0.35, (d) α=0.5, (e) α=0.75, (f) α=1.0.

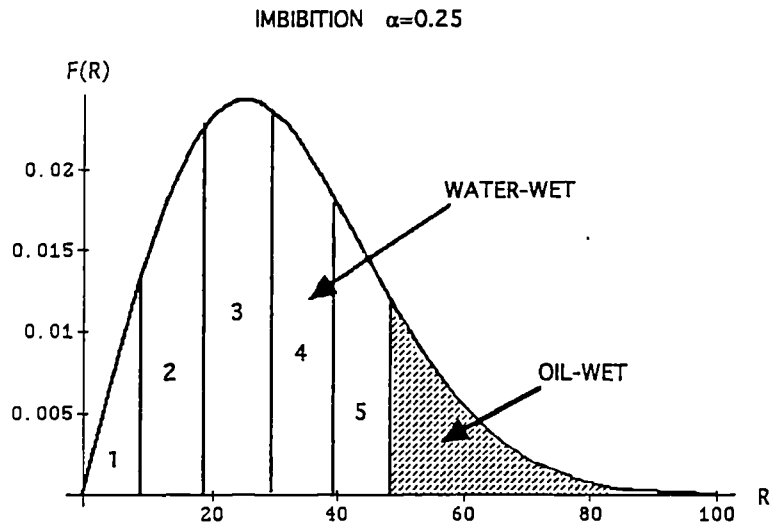

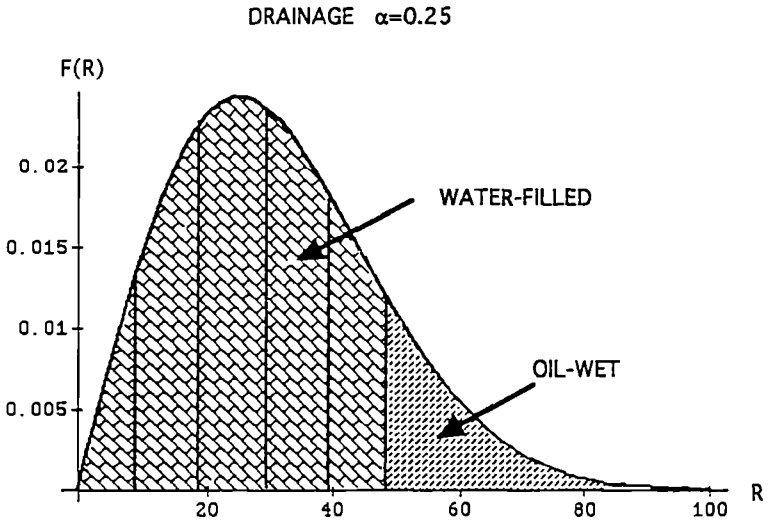

(b)

Figure 5.10 (Continued)

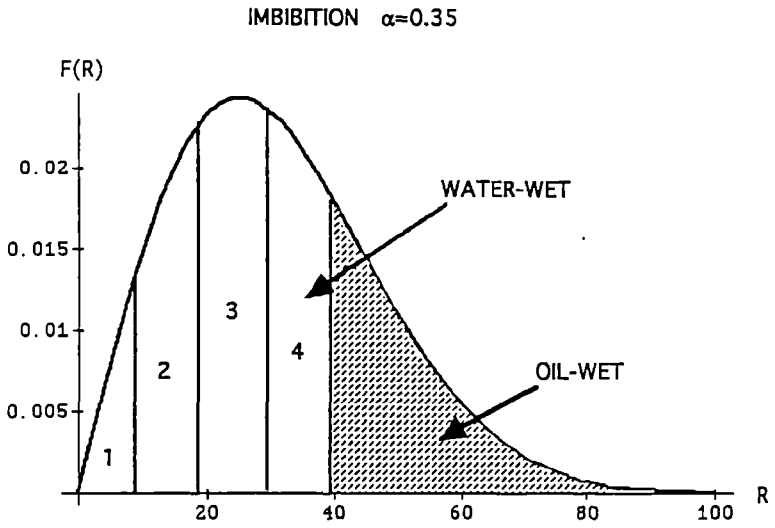

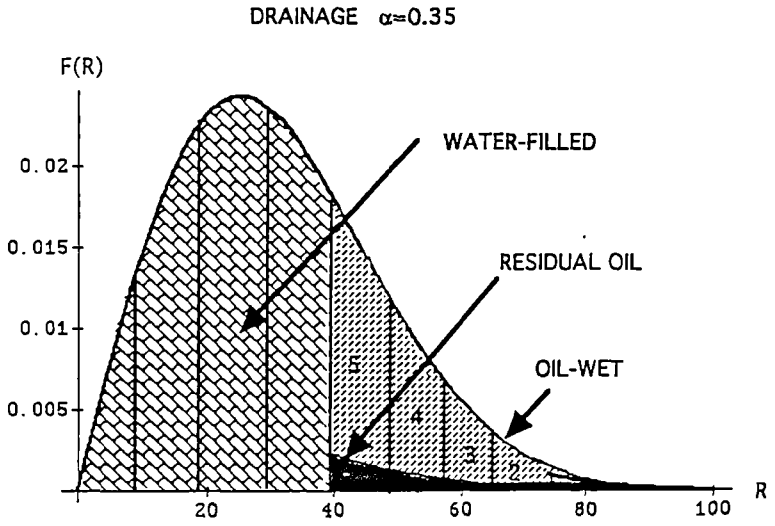

(c)

Figure 5.10 (Continued)

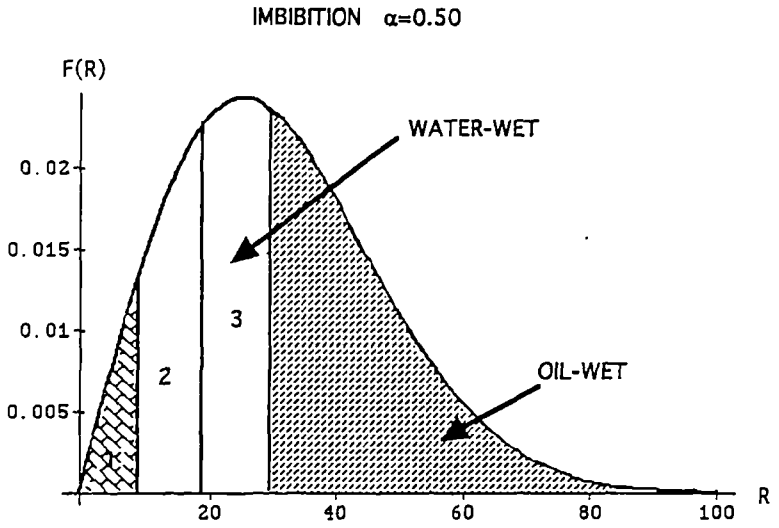

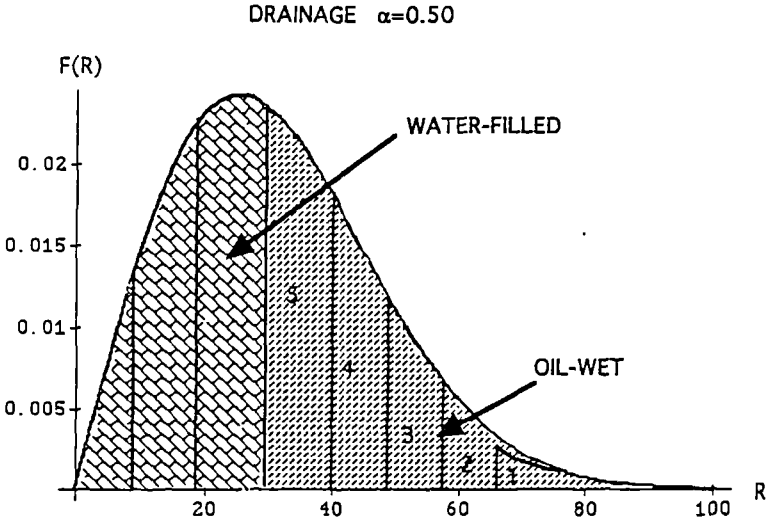

(d)

Figure 5.10 (Continued)

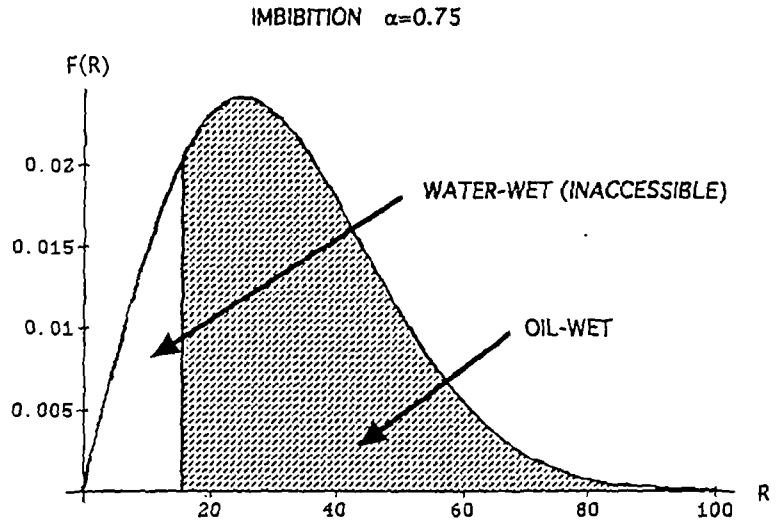

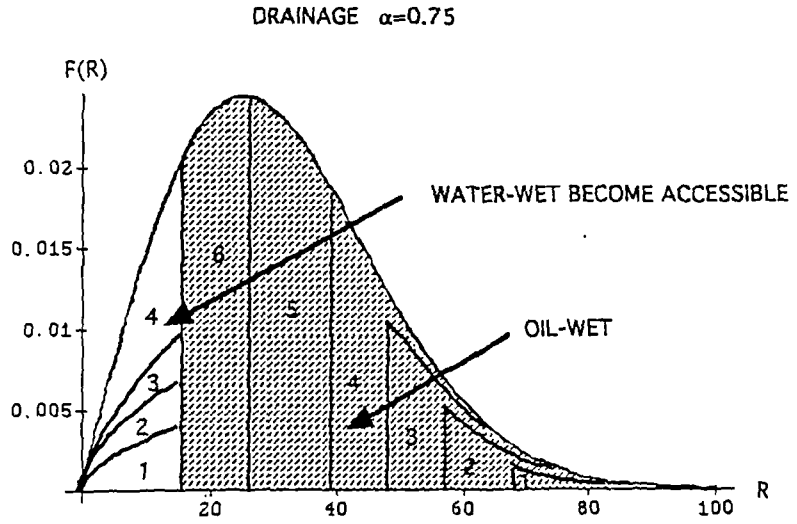

(e)

Figure 5.10 (Continued)

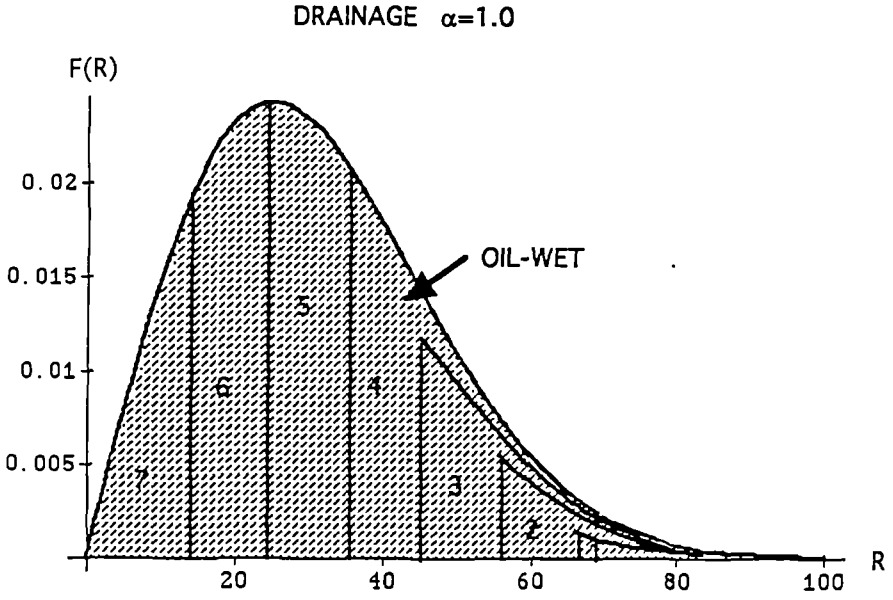

(f)

Figure 5.10 (Continued)

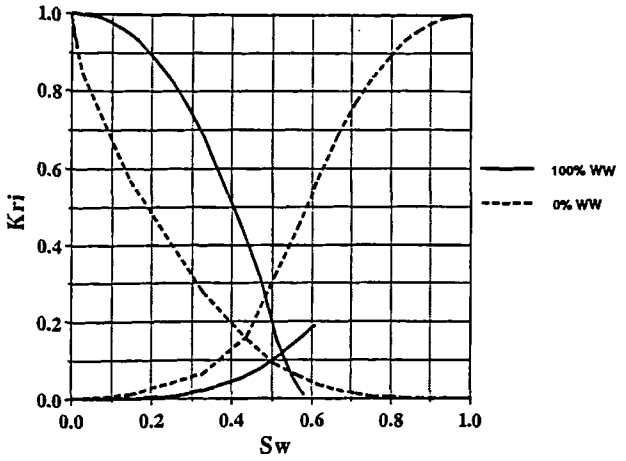

(a)

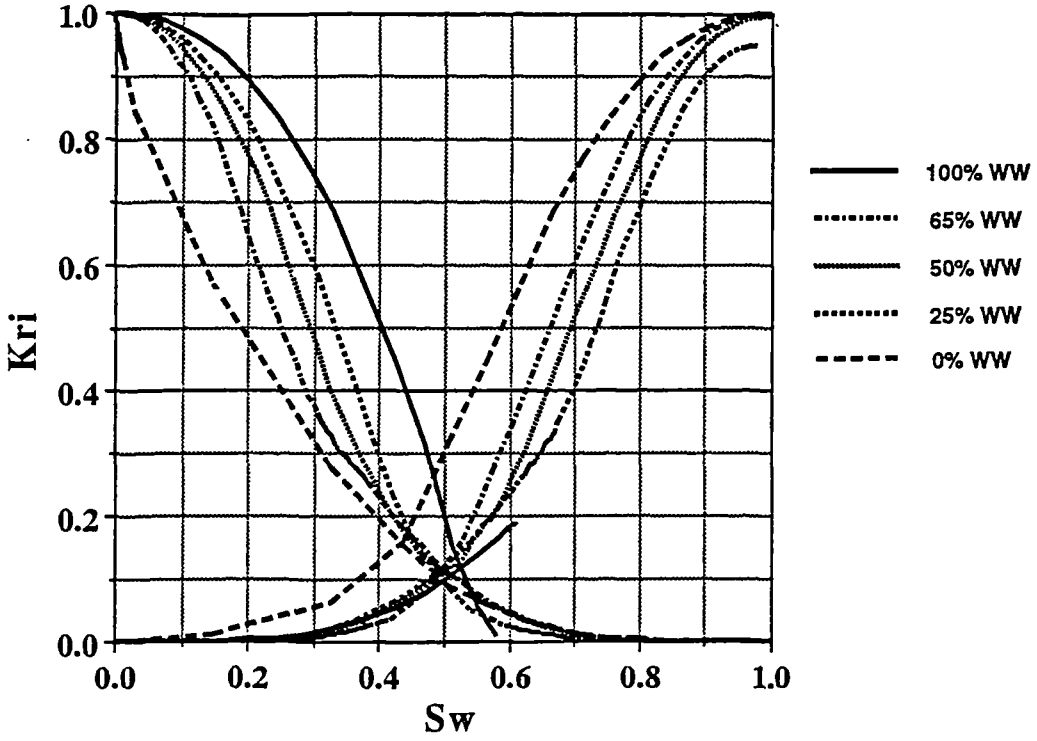

(b)

Figure 5.11 Waterflood relative permeability curves for a range of fractional –wettability conditions: (a) α=0 -> α=1 envelope, (b) full range.

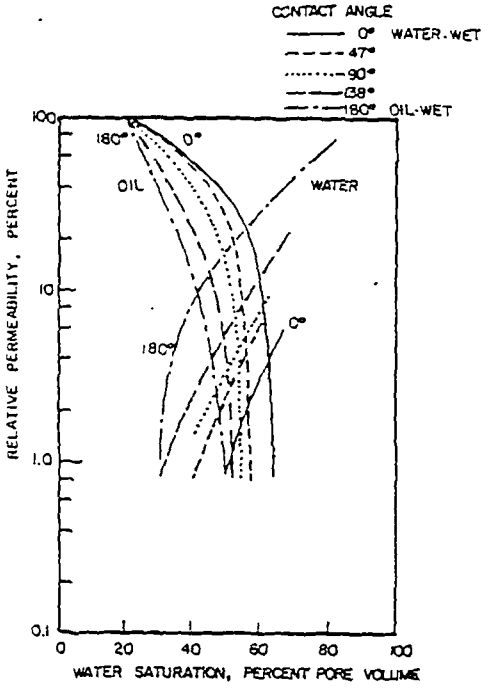

(a)

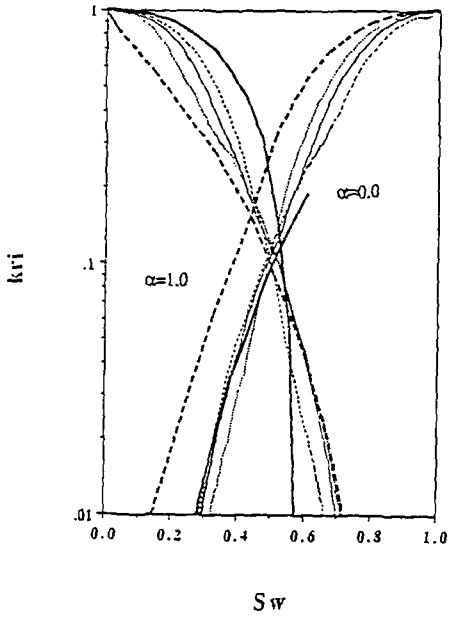

(b)

Figure 5.12 (a) Relative permeabilities from waterflood experiments on uniformly-wet Torpedo sandstone (after Owens and Archer, 1971). Measurements are based upon the effective oil permeability at S_{wi}, (b) Semi-log plot of simulated curves.

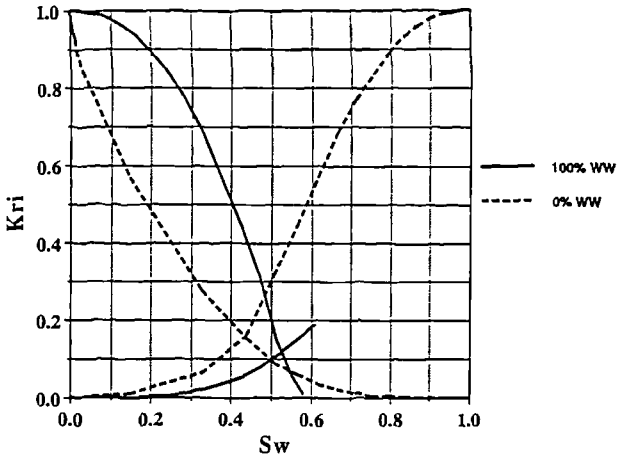

(a)

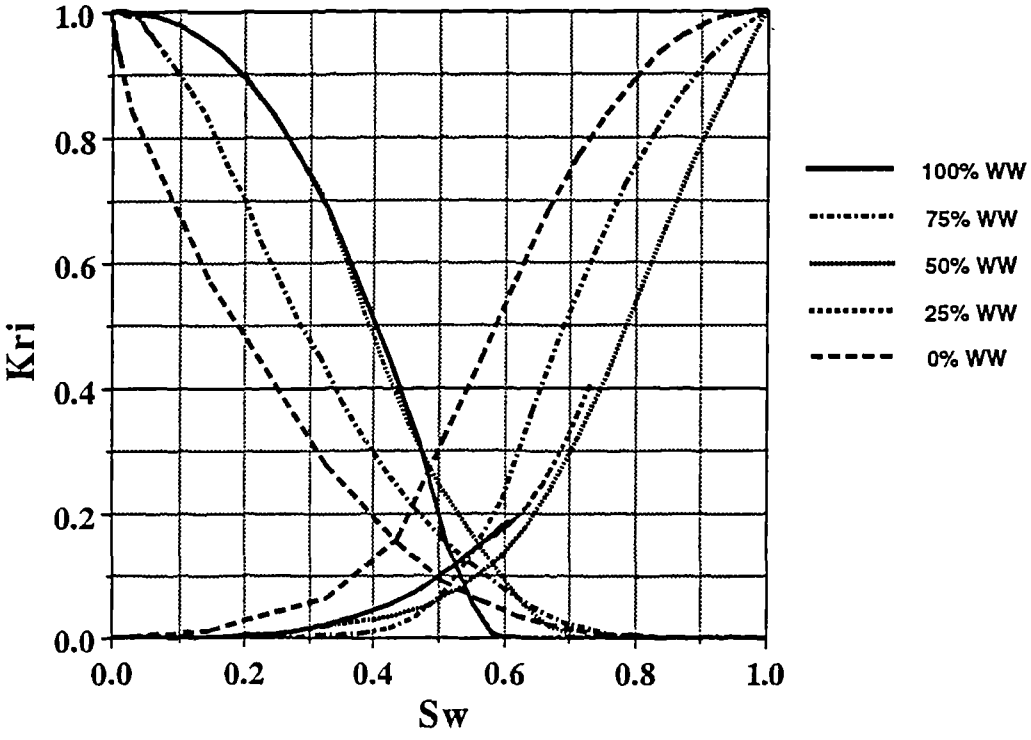

(b)

Figure 5.13 Waterflood relative permeability curves for a range of mixed wettability conditions: (a) $\alpha=0$ -> $\alpha=1$ envelope, (b) full range.

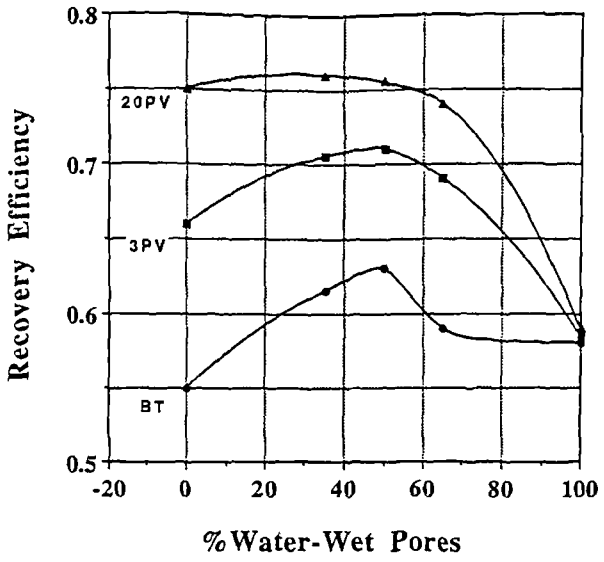

Figure 5.14 Recovery efficiencies for fractionally-wet networks, calculated via Buckley-Leverett analyses of the associated relative permeability curves.

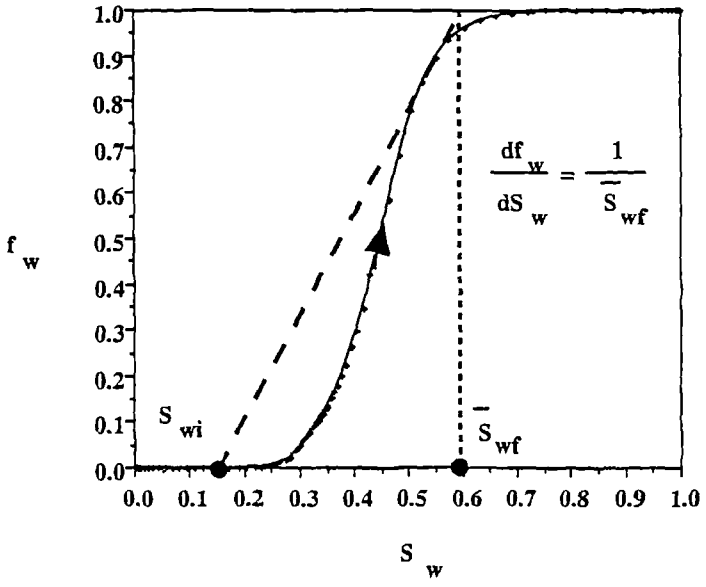

Figure 5.15 Schematic calculation of average water saturation at breakthrough (S_{wf}) using the Welge tangent technique (Welge, 1952).

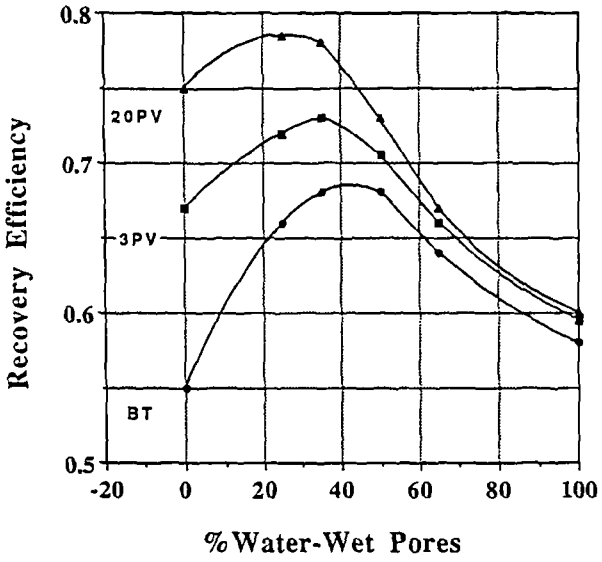

Figure 5.16 Recovery efficiencies for mixed-wet networks, calculated via Buckley-Leverett analyses of the associated relative permeability curves.

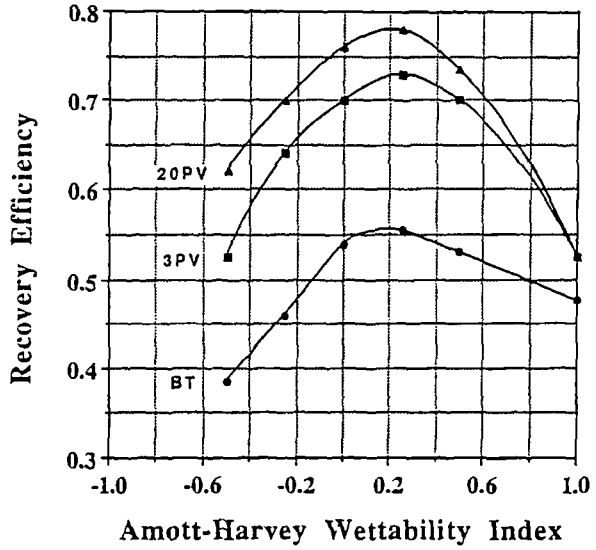

Figure 5.17 Experimental results (after Jadhunandan and Morrow, 1991) showing waterflood recovery efficiency vs wettability index.

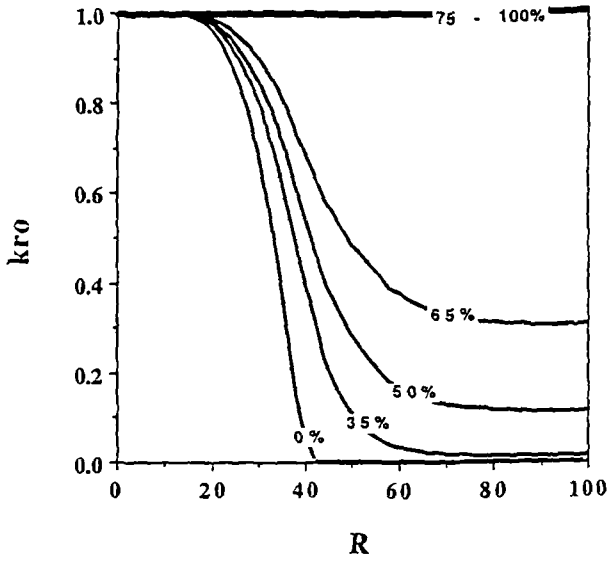

(a)

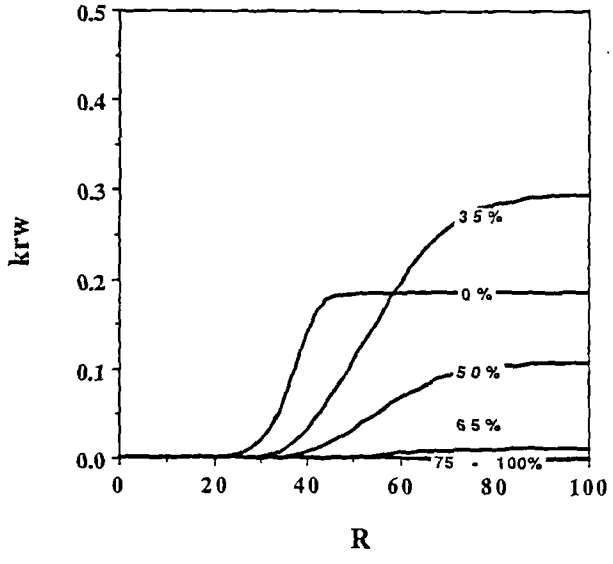

(b)

Figure 5.18 Plots of (a) R-k_{ro} and (b) R-k_{rw}, from waterfloods of fractionally-wet networks.

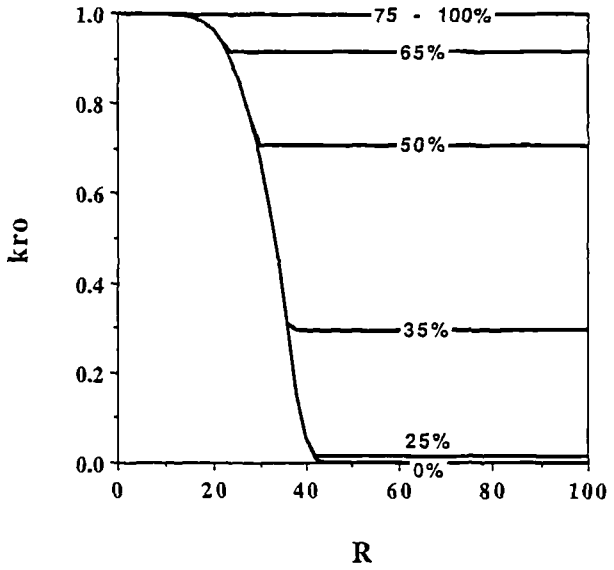

(a)

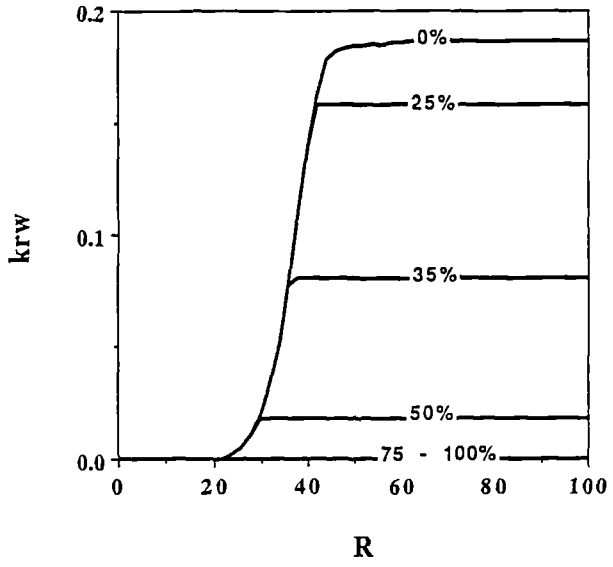

(b)

Figure 5.19 Plots of (a) R-k_{ro} and (b) R-k_{rw}, from waterfloods of mixed-wet networks.

CHAPTER 6 UNSTEADY-STATE FLOW AND VISCOUS/CAPILLARY COUPLING

6.1 Introduction

The work described above has clearly demonstrated how pore topology and matrix wettability can affect a variety of petrophysical parameters (capillary pressure, relative permeability, etc.). It should be remembered, however, that the simulations of Chapters 4 and 5 assumed that displacements were being performed at a very low flowrate. Hence all previous results relate mainly to capillary-dominated steady-state flow processes. This chapter focuses on extending these steady-state models to deal with unsteady-state dynamics, with a view to ultimately producing a simulator capable of interpreting a wide variety of two- and three-phase laboratory displacements.

Steady-state three-phase flow is seldom, if ever, truly achieved in the laboratory — precise control of gas flow is a formidable task (Idris, 1990) and slug flow is difficult to avoid. This is one reason why unsteady-state issues have to be addressed. Differential displacement rates are also a feature of unsteady-state processes; for instance, fluid transport through film-flow and bulk fluid transfer will generally have different characteristic timescales associated with them. Such considerations imply that the existing steady-state network model would be somewhat inadequate in dealing with such flow phenomena; consequently, new unsteady-state physics must be introduced which better approximate observed flow behaviour. This is no trivial task, however.

Three-phase displacements will be discussed in greater detail in Chapter 7. This chapter presents analysis and simulation of *two*-phase unsteady-state flow; both unsteady-state drainage *and* imbibition models will be considered.

6.2 Unsteady-State Drainage Model

The unsteady-state flow of fluid through a porous medium at typical reservoir rates will generally occur under the influence of at least three associated forces: capillary, viscous and gravitational. Results presented here correspond to displacements under capillary/viscous control; gravitational forces will not be considered.

The invasion percolation model of drainage discussed in Chapter 4 was only valid for capillary-dominated flow; the addition of viscous pressure forces adds a further degree of complexity to the pore-scale dynamics. Consider first the mechanics of an equilibrium drainage displacement, such as a low rate oilflood of a water-saturated water-wet core (Figure 6.1). As the displacing oil is forced into the porous sample at incrementally higher pressures, it is able to overcome successively larger capillary entry thresholds and thereby fills up smaller and smaller pores. An external pressure must be applied to the oil before any invasion can occur because of interfacial tension forces acting to oppose the motion. By performing the oilflood at a very low rate, pressure gradients set up *within* the system are so small as to be negligible when compared to the large pressure differences across the oil/water interfaces. When such displacements are carried out at a higher rate, however, these viscous pressure gradients within the sample may no longer remain insignificant.

Once large viscous pressure gradients have been set up within a system, the hierarchy of pore filling events can be dramatically altered. Consider the section of water-wet pore network shown in Figure 6.2. The invading oil ganglion would next fill pore 1 if the oilflood were taking place at a very low rate, because all three viscous pressure gradients (ΔP_1, ΔP_2, ΔP_3) would be comparatively small and pore 1 has the lowest capillary entry threshold ($\sim 1/r_1$). If, however, a high rate flood was underway, then the pore entry requirements would be as follows:

Threshold pressure to enter pore 1= $2\sigma\cos\theta/r_1 + \Delta P_1$

Threshold pressure to enter pore 2= $2\sigma\cos\theta/r_2 - \Delta P_2$

Threshold pressure to enter pore 3= $2\sigma\cos\theta/r_3 + \Delta P_3$

Hence, even though pore 2 is the narrowest of the three available, it can still be filled before the others if:

$$\Delta P_2 > 2\sigma\cos\theta\left(\frac{1}{r_2}-\frac{1}{r_1}\right)-\Delta P_1 \qquad (6.1)$$

and

$$\Delta P_2 > 2\sigma\cos\theta\left(\frac{1}{r_2}-\frac{1}{r_3}\right)-\Delta P_3 \qquad (6.2)$$

These ideas are used explicitly in the unsteady-state drainage simulator. An initial pressure gradient is set across the entire network and pressures are found at each node as described previously. The magnitude and direction of the pressure drop across every *available* pore in the network is then determined: these are the microscopic viscous pressure gradients. Note that "available" pores are those that are connected either to the inlet face of the network or the invading oil cluster. Once all viscous pressure gradients have been found, the *total entry pressure* for each pore can be calculated as:

$$P_{entry} = \frac{2\sigma\cos\theta}{r_i} + \Delta P_i \qquad (6.3)$$

where r_i is the radius of pore i and ΔP_i the viscous pressure drop across it. Note that depending upon its sign, ΔP_i may help or hinder invasion of a pore (the ΔP_i are taken to be positive in the positive x, y, and z directions). All of these checks must be made throughout the network at every time step, a task requiring massive computational effort. When the entry pressure of each pore has been calculated, the pore with the minimum threshold is invaded by the

nonwetting fluid: the pore is labelled as being oil-filled and the viscosity of the pore fluid becomes that of oil.

At very high rates, some of the ΔP_i may be so large that the corresponding threshold pressures become negative, i.e. oil may be convected or "sucked in" along certain pores. This means that the displacement is no longer constrained by interfacial tension forces acting at oil/water interfaces, and so more than one pore may be invaded simultaneously. In such cases, the displacement proceeds until one pore has been completely filled with invading fluid, and the interim positions of all other menisci *within* pores are noted. The network pressure field is recalculated and the flood continues.

Throughout all simulations, the total flowrate (Q) is kept constant. At unit viscosity ratio ($\mu_O=\mu_W$) this poses no particular problems; the pressure field within the network remains completely unchanged during a displacement - the flow through a pore will be the same whether it is transporting oil or water. Once the viscosities of the invading and defending fluids differ, however, the global pressure field changes during the flood. For instance, if high viscosity oil displaces low viscosity water at a constant rate, then the total pressure gradient across the system must increase with time. Because it is the *pressures* that are controlled during simulations and not the flows, a rather subtle technique must be used to reproduce this behaviour. When a pore has just been invaded, the pressure equations are solved as before to give a new *total* flowrate (Q'). Because of the viscosity difference between the invading and defending fluids, this new flowrate will not be the same as the old flowrate (Q). The two can be made identical, however, if each nodal pressure (p_i) is replaced by:

$$p_i^{new} = p_i^{old} \times \frac{Q}{Q'} \qquad (6,.4)$$

This means that simulations can be conducted at constant flowrate simply by modifying the nodal pressures in the network. Although this initially appears rather unphysical, it is merely solving the problem "inside-out". In a typical experiment, the flowrate is kept constant and the pressures can be measured: here, the pressure field is derived before the flowrate is known. The modification to the pressure field is not merely an artefact of the numerical method, however; such a modification will actually be seen in a physical system if the total flowrate of injected fluid is maintained and the viscosity ratio is not unity.

Another consideration when dealing with large viscous flows is the topology of the network itself. Simulations performed using regular square or cubic networks exhibit a flow bias parallel to the macroscopic pressure gradient. This will tend to reduce transverse flow and lead to unrealistic results. The problem is overcome by distorting the system in such a way that pores become randomly orientated, whilst the global structure of the network remains intact. The method is shown in Figure 6.3: each inner node of the network is displaced from its original position (x, y, z) to a new position $(x+\varepsilon_1, y+\varepsilon_2, z+\varepsilon_3)$, where the ε_i are random numbers. Although the ε_i can take any values, they are generally chosen from the range [0, 0.5] as this avoids pores crossing one another (the graphical output becomes rather messy if pores cross). The positions of inlet and outlet nodes remain unchanged in order to maintain the overall network structure. Once the nodal positions have been determined, the new pore lengths are calculated using simple trigonometry. The distorted network therefore contains pore elements with a variety of radii *and* lengths.

With the pore-level physics in place, attention will now turn to the sensitivity of drainage displacements to a variety of flow parameters, including; viscosity ratio, flowrate, and pore-scale heterogeneity. The following sections expand upon earlier work by Lenormand et al (1986), who present an impressive series

of micromodel studies and numerical simulations using regular lattices and narrow pore size distributions (phase trapping is not considered, however).

6.2.1 The Effect of Viscosity Ratio

Throughout this study, the viscosity ratio (κ) will be defined as:

$$\kappa = \frac{\mu_{displaced\ fluid}}{\mu_{displacing\ fluid}} \tag{6.5}$$

Five viscosity ratios have been examined in total, ranging from very favourable ($\kappa << 1$) to very unfavourable ($\kappa >> 1$). Figure 6.4 shows a series of drainage floods carried out on a 40 x 40 distorted network with pore radii chosen randomly from the range [0,100] and $\kappa \in \{0.01, 0.1, 1, 10, 100\}$. Figure 6.4a shows a simulation of the migration of nonwetting fluid at a favourable viscosity ratio of 100:1 (κ =0.01). The displacement is essentially one of frontal advance — the raggy appearance of the front is due to the pore-scale heterogeneity of the network. Such a picture may be characteristic of large-scale oil migration into an aquifer or processes where water displaces gas (eg a WAG process). Increasing κ towards 1 causes the front to become less and less uniform (Figure 6.4b), and once the fluid viscosities are matched, the underlying heterogeneity of the network can be clearly seen (Figure 6.4c). The finger-like structure of the flood front identifies paths of high and low conductivity, the combined effects of which result in the bypassing of a large region of the pore space.

When the viscosity ratio is made unfavourable, the injected fluid streams across the system and breaks through very quickly (Figure 6.4d). This is a microscopic view of the phenomenon of viscous fingering and characterises the flow behaviour in cases where water or gas is used to displace a heavy oil. Large regions of the porespace remain unswept resulting in a high residual oil

saturation and poor displacement efficiency. The fingering gradually worsens as κ increases (Figure 6.4e).

6.2.2 The Effect of Flowrate

Whenever the flowrate of a displacement is varied, so too is the ratio of viscous to capillary forces at the porescale. The results presented below, show that this will have serious consequences for flood efficiency. The viscous/capillary ratio is characterised by the Capillary Number (Ca), defined here as:

$$Ca = \frac{\mu_{displacing} Q}{\sigma A} \tag{6.6}$$

where $\mu_{displacing}$ is the viscosity of the displacing fluid, Q is the total flowrate, σ is the interfacial tension, and A is the cross-sectional area of the system. It is clear that the displacement becomes more capillary dominated as Ca decreases. If σ , A, and $\mu_{displacing}$ are all kept constant, then the viscous/capillary force ratio can be investigated merely by varying the total flowrate Q.

Figure 6.5 demonstrates the effect of flowrate upon the pore-scale dynamics of a *favourable* 100:1 drainage displacement. As the flowrate is reduced, the capillary forces begin to dominate the displacement: instead of frontal advance, the invading fluid starts to finger. This time, the fingering is not caused by the viscosity difference (remember that κ is favourable anyway) but is entirely due to the influence of capillarity. Capillary fingering has a very different structure when compared to that of viscous fingering: capillary fingers loop in all directions, whereas viscous fingers tend to grow parallel to the principal flow direction. The flowrate in Figure 6.5a is only four times greater than that in Figure 6.5d, yet the displacements are dramatically different.

6.2.3 The Effect of Network Heterogeneity

The simulations shown in Figure 6.6 demonstrate how the degree of microscopic heterogeneity can affect flow behaviour. It depicts three drainage processes carried out at different κ on a network of pores whose radii were randomly chosen from the interval [40,60]. Although the system has the same mean radius as those described above, the distribution of radii is now much narrower. Comparison with Figure 6.4 shows that narrowing of the pore size distribution results in a more layered form of displacement. The crossover between frontal advance and viscous fingering is still observed, but the reduction in transverse flow results in elongated lenses of bypassed wetting phase and more severe streaming at unfavourable κ.

The results discussed above have clearly demonstrated the need for greater understanding of unsteady-state pore-scale processes. Viscosity ratio, capillary number, and pore size distribution (microscopic heterogeneity) interact in a very complex manner and all have a major influence on multiphase flow behaviour.

6.3 Unsteady-State Imbibition Model

The physics governing imbibition processes is still not very well understood and urgently requires further investigation. The earliest relevant analysis was carried out by Washburn in the 1920s and dealt with the case of water displacing air in a capillary tube. By assuming steady-state flow and Poiseuille's law (neither of which is strictly true) he obtained the following equation for the velocity of the water-air interface:

$$\frac{dx}{dt} = \frac{\Sigma P}{8r^2 \mu x}\left(r^4 + 4\varepsilon r^3\right) \qquad (6.7)$$

where x is the length of penetration, r is the tube radius, μ the water viscosity, and ΣP the *total* effective pressure (Figure 6.7). The second term in the bracket

relates to a slip condition. The total effective pressure will generally consist of three separate contributions: capillary pressure (P_c), hydrostatic pressure (P_g), and an externally applied viscous pressure (P_v). Equation (6.7) can be integrated to give:

$$x^2 = \frac{\sum P}{4\mu}\left(r^2 + 4\varepsilon r\right)t \tag{6.8}$$

Consider now two special cases:

(i) $P_c=P_g=0, P_v=\Delta P$

With no capillary or gravitational forces (and $\varepsilon=0$), the time taken to fill the capillary is given by:

$$t_f = \frac{4L^2\mu}{r^2\Delta P} \tag{6.9}$$

where L is the total tube length. This implies that under viscous domination, wide tubes fill up quicker than narrow ones ($t_f \sim 1/r^2$). Hence, if two tubes of differing radii but identical length are subjected to the same external pressure gradient (Figure 6.8), then at any time $t<t_f$, the penetrated lengths satisfy:

$$x_1 = \frac{r_1}{r_2}x_2 \tag{6.10}$$

If $r_1>r_2$, tube 1 will fill first and the water/air interface in tube 2 will have moved a distance:

$$x_2^* = \frac{r_2}{r_1}L. \tag{6.11}$$

(ii) $P_v=P_g=0, P_c=2\sigma\cos\theta/r$

Consider next a situation where the flow is entirely capillary dominated. The time for complete penetration is now given by:

$$t_f = \frac{2\mu L^2}{r\sigma\cos\theta} \tag{6.12}$$

Once again, the Washburn approximation predicts that wide tubes fill quicker than narrow ones — *even under capillary domination*. Now, however, the penetrated lengths satisfy:

$$x_1 = x_2\sqrt{\frac{r_1}{r_2}} \tag{6.13}$$

(Figure 6.9) Wider capillaries filling first under capillary domination seems somewhat counter-intuitive. It is well known that water-wet porous media spontaneously imbibe water along surface irregularities, filling up smaller pores first. This anomaly requires further investigation and will be discussed later.

Washburn's equation can easily be generalised to describe *two*-phase flow in a capillary tube. The general equation governing the displacement of, say, oil by water is:

$$\frac{dx}{dt} = \frac{r^2\sum P}{8[\mu_w x+\mu_o(L-x)]} \tag{6.14}$$

where μ_w and μ_o are the water and oil viscosities respectively. It was hoped that Equation (6.14) could be implemented on the network, giving imbibition simulations over a range of flow conditions. To this end, surface roughness was explicitly incorporated into each pore element. A typical element is shown

in Figure 6.10: every pore was equipped with two sets of "roughness capillaries" to allow for differential film flow and film swelling. Simulations carried out at three different rates are shown in Figure 6.11: the Washburn approximation has resulted in three fairly similar displacements. The floods were performed at unit viscosity ratio, and so the fingering patterns are caused solely by network heterogeneity. The reduction in fingering with reduced flowrate can be explained with reference to Equations (6.10) and (6.13): if pore 1 is the first to fill, then the meniscus in pore 2 will have penetrated further under capillary domination (low flowrate, Equation (6.13)) than it would have under viscous domination (high flowrate, Equation (6.10)).

The most striking feature of the flood patterns shown in Figure 6.11 is that they do not correspond to physically realistic imbibition displacements. The result from the high rate flood may be reasonable, but low rate imbibition should be characterised by snap-off events in small pores throughout the system. The inadequacy of the current model implies that either the simplistic assumptions concerning pore roughness are at fault, or the Washburn approximation itself is invalid. The latter, however, has been verified experimentally for standard capillary tubes (Fisher and Lark, 1979) and is generally accepted as being a valid approximation in laminar flow regimes. If the Washburn approximation is valid *at the pore-scale*, one must conclude that flow along surface roughness cannot be modelled using simple circular roughness capillaries.

Although the Washburn equation has been shown to hold for displacements in *standard* capillary tubes, closer analysis carried out as part of this work reveals that it may be in error when applied at length scales typical of *microscopic* flow processes. Indeed, it has already been shown above that the sequence of pore-filling events predicted by Washburn is completely at odds with that observed in the laboratory. The subsequent analysis carried out as part of this thesis has led to the formulation of an *extended* Washburn equation and its coupling to an

extended pore-doublet model. Details of this theory, together with a discussion of associated pore metering effects, are presented in Appendix B. Equations derived from this theoretical study have been incorporated into the network code, and form the basis of unsteady-state imbibition simulations reported below. Figure 6.12 is a schematic of how the displacements should proceed once the new physics has been implemented on homogeneous networks: frontal advance at high rates; pure percolation at low rates; frontal advance preceded by a capillary fringe at intermediate rates. The importance of flowrate upon residual oil saturation and displacement efficiency is clearly illustrated.

Having extended the earlier network model by incorporating unsteady-state flow physics, a wide variety of displacements can now be examined in more detail. One area of great interest to the petroleum industry is the impact of geological structure upon recovery efficiency. Some relevant microscopic systems will be considered next.

6.4 Unsteady-State Displacements in Finely Laminated Porous Media.

Recent work on fluid flow upscaling in clastic facies has demonstrated the importance of both the small scale lamination structure and the local viscous/capillary force balance. This section presents a pore-scale analysis of unsteady-state imbibition and drainage processes, which attempts to elucidate the interaction between capillary and viscous forces during waterfloods in such finely laminated porous media. Network simulation studies have been performed to evaluate their combined effect upon "residual" oil trapping and microscopic displacement efficiency.

The three main purposes of this study are (i) to demonstrate these small scale structure/force balance mechanisms from first principles (i.e. from microscopic modelling at the pore scale); (ii) to examine sensitivities of the laminar capillary

trapping mechanisms to various factors; (iii) to comment on aspects of the pore to core upscaling of these effects in the light of the recently proposed "geopseudo" methodology. Results will demonstrate how small-scale lamination can greatly affect the larger-scale dynamics of a flood, especially where the principal flow direction is across the lamina as in cross-bedded systems. Sensitivity studies have been undertaken to examine the effects of lamina orientation and matrix wettability: a range of lamina structures has been considered under both water-wet and oil-wet conditions. The importance of scaling these effects in the light of the underlying geological structure will also be discussed.

6.4.1 Geological Background

It is very well-documented that permeability variations in an oil reservoir will greatly affect the amount of oil recovered from it (Weber, 1991; Lake et al, 1991). The precise effects of such heterogeneities depend upon the actual oil recovery process employed and on the associated balance of forces (scaling groups) (Ringrose et al, 1993a): such heterogeneities are present at many length scales from kilometres down to millimetres. Although accurate flow predictions through such systems may initially appear to be intractable, there are often underlying geological structures which can help to reduce the complexity of the problem.

The deposition of clastic sediments is generally characterised by quasi-periodic events, resulting in a hierarchy of layered structures: lamina, lamina set, bedform, etc. (Pettijohn et al, 1964; Allen, 1982; Fritz and Moore, 1988), and wider recognition of these geological building blocks has recently led to an improved understanding of the influence of heterogeneities on fluid flow (Ringrose et al, 1993b; Corbett et al, 1992). It is the *scale-dependent interaction* of sedimentary structure with flow process which ultimately determines both how the flow should be appropriately scaled up and how the residual oil is

distributed after a displacement process such as waterflooding. It is important, therefore, to study heterogeneities at all scales down to the smallest level.

Layered systems at the reservoir scale have already been widely studied (Stiles, 1949; Goddin et al, 1966; Ypma, 1983). More recently, however, attention has focussed upon the effect of small-scale heterogeneity on reservoir performance. In a classic study, Kortekaas (1983) investigated the effects of festoon crossbedding at the centimetre scale, and found that waterflooding parallel to the layers (laminae) gives much better recovery than that resulting from across-layer flow. In the latter case, large amounts of residual oil are left behind in the *high* permeability laminae (for water-wet systems) through a capillary trapping mechanism. These findings have been confirmed in the more recent studies by Ringrose et al (1993) and Corbett et al (1992), who describe recovery efficiency using a variety of deterministic and stochastic permeability fields. In addition to extending the original concepts of Kortekaas, these workers also addressed the issue of fluid flow scaleup and have developed the "geopseudo" approach. Other workers have also discussed the importance of small scale capillary phenomena in heterogeneous systems: in experimental rock slabs (Hartkamp, 1991), in flow simulations employing fractal permeability fields (Van Batenburg et al, 1991) and in displacement calculations using geologically based models of braided stream deposits (Hoimyr et al, 1993).

The details of the oil capillary trapping mechanism referred to above are the central concern of this work. The three main aims are as follows:
(i) to demonstrate these small scale structure/force balance mechanisms from first principles i.e. from the microscopic physics of drainage and imbibition at the pore scale using a network simulator;

(ii) to examine *sensitivities* of the laminar oil capillary trapping mechanisms to various factors such as capillary/viscous balance, lamina orientation and wettability;
(iii) to comment on aspects of the pore to core upscaling of these effects in the light of the "geopseudo" methodology referred to above.

Network modelling techniques are used to study the impact of various lamination structures on waterflood recovery efficiency in both water-wet and oil-wet systems. By incorporating the unsteady-state dynamics and varying flowrate, it has been possible to examine the interaction between capillary and viscous forces over a variety of length scales. When coupled to the underlying heterogeneity of the system, this viscous/capillary balance is found to be responsible for a range of interesting flow behaviour.

Heterogeneous networks have recently been used by Ferrand and Celia (1992) to study the drainage capillary-pressure relationship in layered media. Although their results were restricted to the capillary-dominated regime, they clearly indicate how heterogeneities can significantly affect capillary pressure curves. The simulators developed here can be used to examine the sensitivities of a given displacement to various combinations of flow parameters (viscosity ratio, flowrate, matrix wettability, etc.) and are capable of modelling three-dimensional systems. The results presented in this chapter, however, are restricted to unit mobility floods in two-dimensions: the effects of capillary/viscous balance (related to system size), layer orientation and wettability are the primary concerns here. The relationship between system size and the balance of forces is discussed in more detail in Appendix C.

Results will show that displacement efficiencies and residual oil saturations are strongly dependent upon the capillary/viscous force balance, layer orientation

and matrix wettability. The distribution of bypassed oil at a variety of length scales will also be discussed.

6.4.2 Simulation Details:

All realisations were performed using a 2D network comprising 40 x 40 nodes (junctions) which contained 4,840 intersecting pore elements (bonds). A number of larger systems were used to confirm the main results and each pore in the network was assigned a radius from a modified Rayleigh distribution (cf. Equation 4.26).

Six different layered systems have been studied in total as shown in Figure 6.13. Each consists of two basic "building blocks" — one of high permeability and porosity (k=944mD, ϕ=21%) and one of lower permeability and porosity (k=102mD, ϕ=5%). The six configurations are: lower permeability horizontal (LH), lower permeability vertical (LV), lower permeability diagonal (LD), higher permeability horizontal (HH), higher permeability vertical (HV) and higher permeability diagonal (HD). Pore radii in the low permeability layers are two-thirds the size of those in the high permeability zones. Simulations have been carried out on each layered network at three different rates, under both water-wet and oil-wet conditions (i.e. six simulations per network). This means that 36 different flow regimes have been investigated in layered systems. Six runs were also performed on homogeneous networks for comparative purposes. The three rates selected for the simulations were chosen in order to highlight the most interesting (and surprising) aspects of the viscous/capillary force balance at different length scales (remember that flow rate and system size are intimately related via the scaling groups as discussed in Appendix C). The lowest rate was selected to ensure that displacements were entirely capillary-dominated; low-rate results therefore correspond to flow through systems that are heterogeneous at the small (<1cm) scale. The highest rate was that applicable at the viscous-dominated larger scale, whilst the medium flow rate

was chosen to examine the effect of viscous-capillary coupling at some intermediate scale. The results will be described below in terms of the basic mechanisms which are predicted by the model and, where appropriate, some interpretation of these results in terms of *scale* will be made.

6.4.3 Waterfloods in Water-Wet Systems

The scale-dependency of the viscous/capillary force balance has already been shown schematically in Figure 6.12: capillarity dominates at the very small scale, whilst viscous forces begin to control the displacement as the system size (or flow rate) increases. The effect of varying the force balance in homogeneous (unlayered) systems is reproduced in the simulations of Figure 6.14. The imbibition model used to derive these results involves the implementation of the extended Washburn equation described in Appendix B. The colours represent the time evolution of each displacement: white pores are those filled first, followed by yellow, orange and red. Residual oil exists as black clusters of uninvaded pores.

At the small scale (Figure 6.14a), the displacement is characterised by film flow along surface roughness, with water invasion occurring primarily in small pores along a scattered capillary fringe. At larger scales, viscous forces become more effective. The flood now appears to proceed via frontal advance, with a narrow capillary fringe fingering ahead of the bulk flow (Figure 6.14b). At the scale of viscous domination, the water front proceeds in a piston-like manner (Figure 6.14c).

Simulations using water-wet, *layered* networks are presented in Figures 6.15 and 6.16 in which the lamina permeability is lower or higher, respectively, than the surrounding matrix. The first few simulations will be described in more detail, in order to communicate the basic mechanisms responsible for the results.

Low Permeability Horizontal Layer (LH): Figures 6.15a-c clearly demonstrate the scale-dependent effects of the viscous/capillary force balance. When the flood is capillary dominated, water preferentially fills the low permeability layers first (Figure 6.15a); this results in poor recovery at breakthrough. As the flood continues, water sweeps through the high permeability layers and ultimately leaves residual oil distributed evenly throughout the system.

For the intermediate viscous/capillary case, viscous forces convect water into the high permeability layers, whilst capillary forces simultaneously pull water along the low permeability zones (Figure 6.15b). This demonstrates that viscous-capillary coupling can be *constructive* when flooding takes place parallel to bedding — the front is smeared across the entire width of the system.

At larger scales (higher rates; Figure 6.15c), the dominant viscous forces cause water to flow primarily along the high permeability layers. A small amount of capillary crossflow takes place, but oil mainly becomes trapped in the *low* permeability zone. These results show that flow behaviour can completely change as viscous forces increase. Hence, recovery mechanisms are strongly dependent upon system size and the correlation length of the heterogeneity under investigation

Low Permeability Vertical or Diagonal Layer (LV and LD): The consequences of flooding *across* both vertical and diagonal laminae are clearly shown in Figures 6.15d-i. For the lowest and intermediate rates, regions of oil remain trapped in the high permeability region upstream of the low permeability lamina in complete agreement with the work of Kortekaas and Ringrose et al described earlier.

At the small scale, the displacement begins with capillary forces drawing wetting films through the system (Figures 6.15d and g). As before, these films

swell and initially displace oil from the smallest pores. Once the films reach the low permeability strip, however, capillarity draws wetting fluid into it preferentially and fills it up long before water has had time to sweep the high permeability zone upstream of it.

Although increased viscous effects improve displacement efficiency at larger scales, a quantity of oil still remains trapped in the high permeability lamina (Figures 6.15e and h). What is the trapping mechanism operating at these larger scales? Once viscous forces begin to dominate, the trapping can no longer be caused by capillarity, as capillary forces are becoming less and less influential. The answer to this apparent anomaly is shown schematically in Figure 6.17. Trapping is now caused by the differential pressure gradients acting across different layers within system. Darcy's law shows that viscous pressure gradients in the low permeability layer are much larger than those in the areas of high permeability. This trapping mechanism becomes more influential as the permeability contrast between layers increases. Figure 6.18 shows a viscous-dominated waterflood in a network where the permeability contrast is approximately 100:1 — the effect is clearly much more dramatic.

It is the variation in the viscous/capillary force balance *from layer to layer* that is responsible for the variety of flow behaviour described throughout this section. Intuitively, one may expect regions of high permeability to fill up very quickly — these results demonstrate that waterflooding *across* layers of high permeability may have quite the opposite effect.

High Permeability Horizontal Layer (HH): The flooding of a water-wet system with a high permeability horizontal lamina in a lower permeability matrix is shown in Figures 6.16a-c. As expected, under capillary domination, water once again imbibes along the low permeability layers, giving poor recovery at breakthrough (Figure 6.16a). As viscous forces increase, however, the flood

front begins to straighten (Figure 6.16b). Under viscous domination, water preferentially fills the high permeability lamina first (Figure 6.16c). The change in the viscous/capillary force balance has again reversed the flow behaviour.

High Permeability Vertical or Diagonal Layer (HV and HD): Capillary dominated waterfloods in networks with flow across high permeability vertical or diagonal laminae terminate with oil remaining in the high permeability zone (Figures 6.16d, e, g, h). Again, these results can be interpreted from the dynamics discussed above: wetting films pervade at the small scale, whilst differential viscous pressure gradients operate at the large scale. The evolution of the viscous-dominated floods (Figures 6.16f and i) seems somewhat counter-intuitive: one would expect the high permeability region to be well swept at the end of the displacement. In fact, the larger viscous pressure gradients set up within the downstream low permeability layer may cause the invading water to burst through and bypass much of the oil in the high permeability zone.

6.4.4 Waterfloods in Oil-Wet Systems

The effect of the viscous/capillary force balance in homogeneous *oil-wet* networks is shown in Figures 6.19a-c. Film-flow of water during waterfloods in an oil-wet medium (drainage) is not an issue. Capillary-dominated flows are now characterised by *capillary fingering* (Figure 6.19a). In contrast to the imbibition simulations discussed in Section 6.4.3, capillary forces in drainage processes act to *oppose* intrusion. The invading water first fills the largest available pores, and only proceeds along a narrower channel once the capillary pressure has exceeded associated capillary entry thresholds. Once viscous forces become influential, the displacements become more and more piston-like in appearance, as pore entry thresholds are more easily overcome as reported previously by Lenormand et al (1988).

Low Permeability Horizontal Layer (LH): For drainage displacements with low permeability horizontal laminae, the same qualitative behaviour occurs at all scales: water begins by filling the high permeability layers and breaks through having swept only a small fraction of the low permeability region (Figures 6.20a-c). Although a large fraction of the porespace remains unswept in this layer, the *volume* of oil remaining is relatively small.

Low Permeability Vertical or Diagonal Layer (LV and LD): Displacement results in Figures 6.20d-i demonstrates dramatically how the distribution of residual oil after waterflooding *across* layered oil-wet media is strongly scale dependent. Under capillary domination, low permeability regions act as temporary flow barriers (Figures 6.20d and g), with the result that high permeability regions upstream can be well-swept before water continues towards the outlet.

Once viscous forces become important, however, some very interesting features emerge (Figures 6.20e and h). The fact that larger viscous pressure gradients are set-up within the low permeability lamina, means that flow in low permeability regions may be viscous-dominated, whilst flow upstream may still remain capillary-dominated. Figures 6.20e and h show how this affects the displacement: water fingers through the high permeability strip until it reaches the low permeability vertical. It then bursts into this tight layer in the form of "triangular fans" (structural dispersion). The ultimate outcome is that oil remains trapped in both high and low permeability zones. At larger scales (when capillary effects become negligible), the differential pressure gradients across layers still play a large part in dictating the final distribution of trapped oil.

High Permeability Horizontal Layer (HH): Drainage displacements for a high permeability horizontal lamina proceed in a similar manner to the (LH) case for an oil wet system since water fills the high permeability region first, with the

low permeability layers remaining only partially swept (Figures 6.21a-c). Note that when capillarity dominates, the low permeability regions are virtually unswept at breakthrough, whilst as viscous forces increase all layers are partially swept. Displacements in each layer become progressively more piston-like as viscous forces increase.

High Permeability Vertical or Diagonal Layer (HV and HD): Once again, across-layer flow in oil-wet systems is seen to be dramatically scale-dependent (Figures 6.21d-i). Under capillary domination (small-scale), water fingers through the low permeability region closest to the inlet until it meets the contrasting high permeability lamina (Figures 6.21d and g). Capillary entry thresholds are much lower in this coarser layer, and so the water sweeps this region immediately - leaving oil behind predominantly in the low permeability region upstream. This behaviour is reversed, however, as viscous forces start to become important. Figures 6.21e and h, for example, show how the large viscous pressure gradients across the low permeability laminae can cause regions of *high* permeability to remain unswept.

6.4.5 Recoveries in Water-wet and Oil-Wet Systems

Oil recoveries from all of the above simulations are summarised in Figure 6.22 The residual or "remaining" oil fraction is (1 - Recovery). The high levels of remaining oil in certain cases (e.g. all water-wet cases under capillary control) is partly a function of the 2D nature of the network and the scale of the heterogeneity. However, the sensitivity predictions are thought to be essentially correct: recoveries from systems with diagonally-orientated layers tend to fall between those containing vertically- and horizontally-orientated ones.

Results presented above have clearly shown that capillary and viscous forces interact in a very complex manner with the lamination structure of the porous

medium. Whilst this section has set out to examine displacements in laminated systems over a range of notional lengthscales, results should be interpreted with some degree of caution. The fact that clastic reservoirs tend to be stratified *aggregates*, means that scale-up procedures must honour geological structure *at all scales*. Network simulators are best used to examine sensitivity issues relating to *capillary-dominated* systems, whilst large-scale behaviour is better predicted using conventional black oil simulators. A useful way to utilise network calculations may to use them to calculate a variety of small-scale transport parameters (relative permeabilities, capillary pressures, etc.) and to use these as input data for a "geopseudo" scale-up. The process is summarised schematically in Figure 6.23.

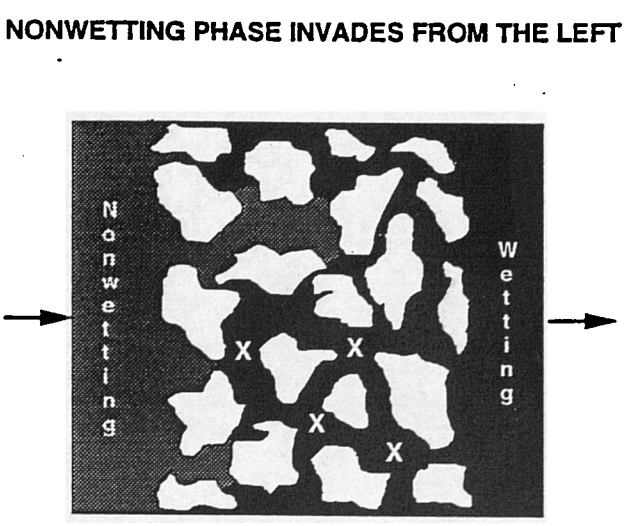

Figure 6.1 Schematic of a low-rate oilflood of a water-wet matrix. The nonwetting phase invades successively narrower pores.

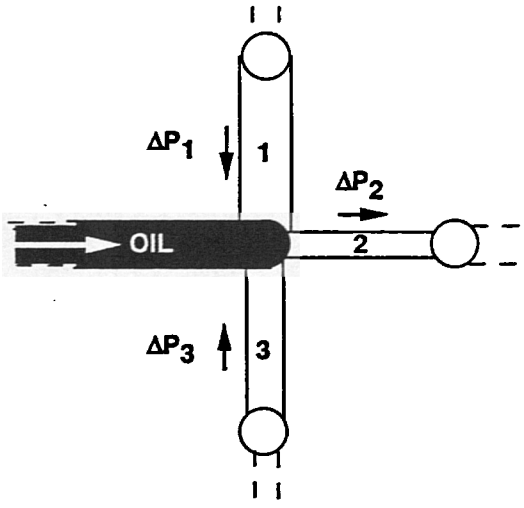

Figure 6.2 Modification to the entry pressure requirements during unsteady-state drainage displacements.

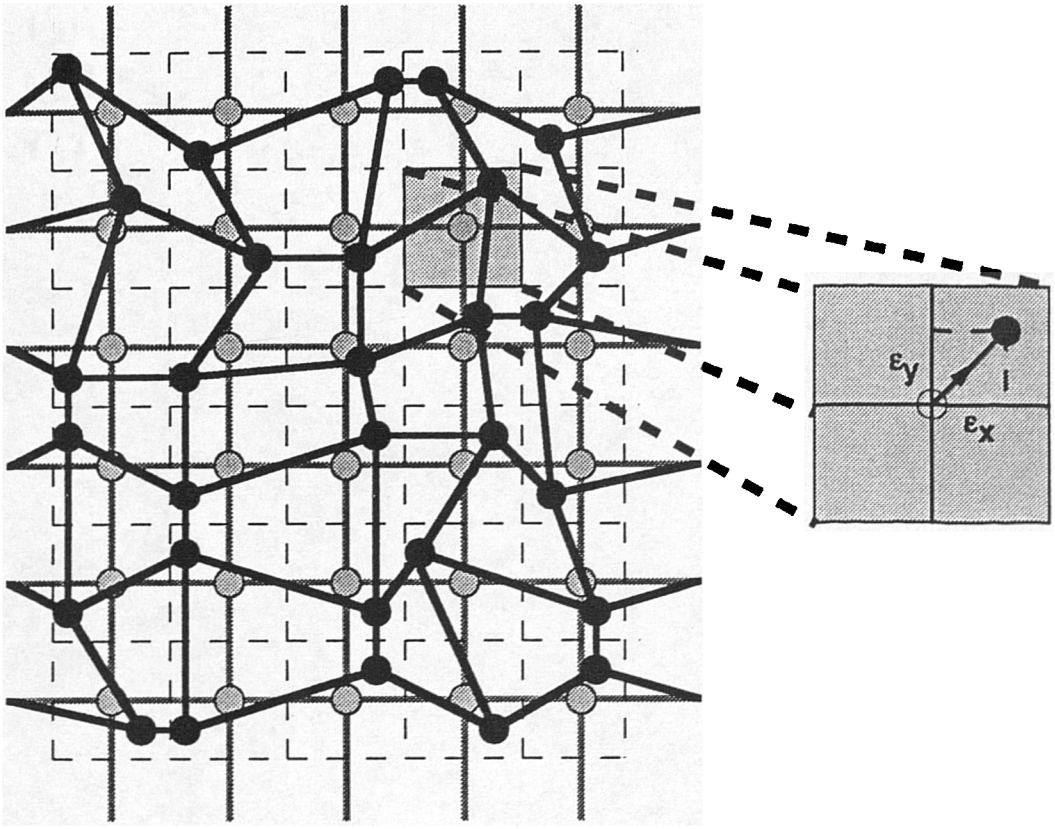

Figure 6.3 Two-dimensional distorted network. Each node is displaced from (x, y) to a new position ($x+\varepsilon_x$, $y+\varepsilon_y$), where the ε_i are random numbers.

(a)

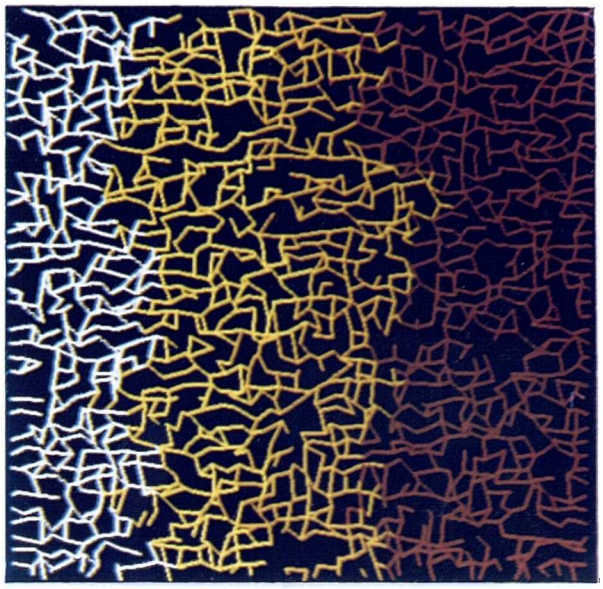

(b)

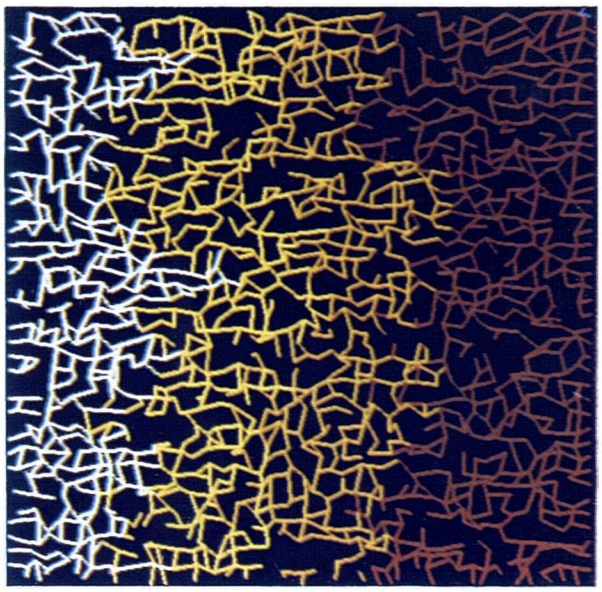

Figure 6.4 Drainage simulations on a 40x40 distorted network, showing the effect of viscosity ratio (κ) upon residual saturation and displacement efficiency. The sequence of displacement is white-yellow-orange-red, the trapped phase is black. Radii are chosen randomly from (0,100) and capillary effects are negligible. (a) κ=0.01, (b) κ=0.1, (c) κ=1.0, (d) κ=10, (e) κ=100.

(c)

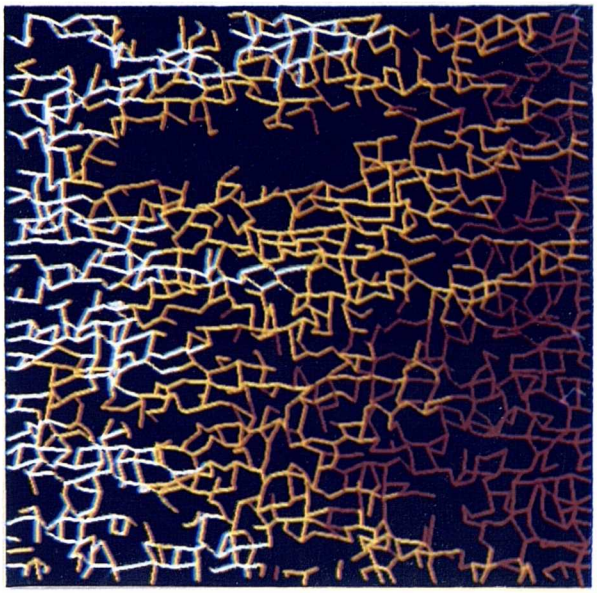

(d)

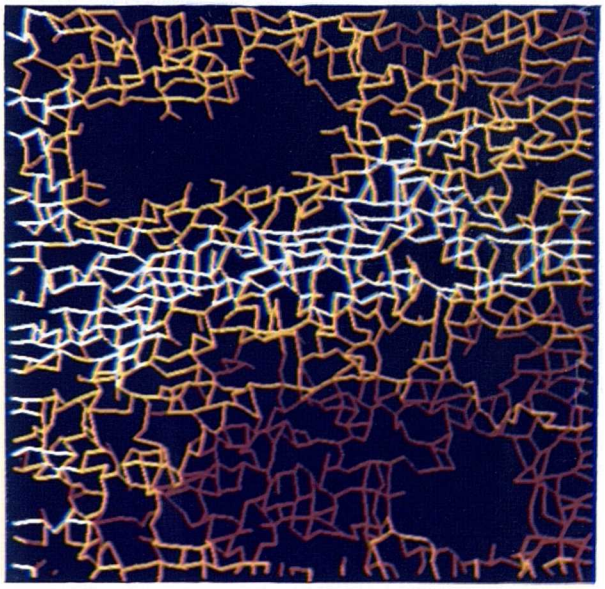

(e)

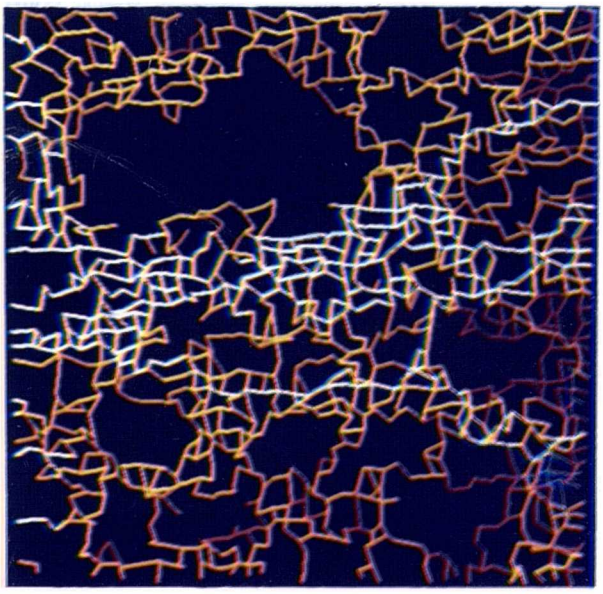

Figure 6.4 **(Continued)**

(a)

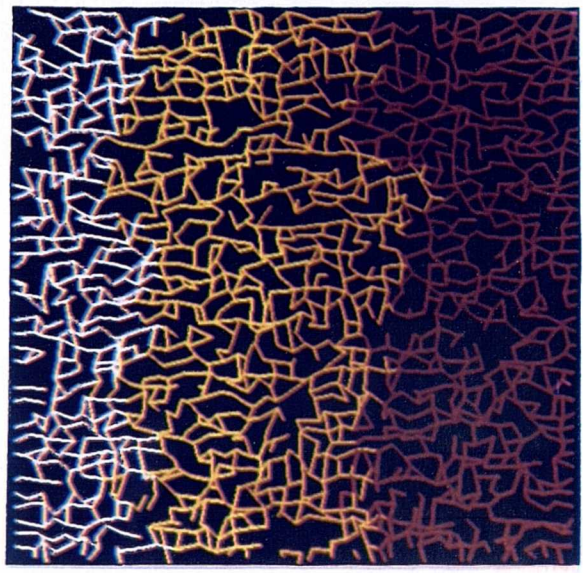

(b)

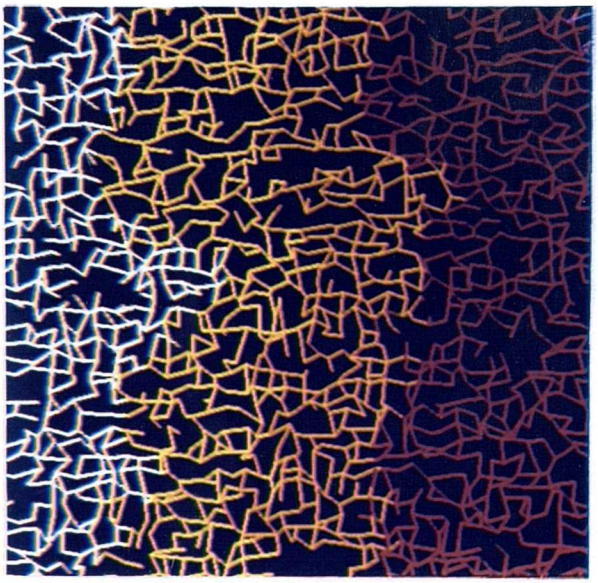

Figure 6.5 Drainage simulations on a 40x40 distorted network, showing the effect of capillary number (Ca) upon residual saturation and displacement efficiency. The sequence of displacement is white-yellow-orange-red, the trapped phase is black. Radii are chosen randomly from (0,100). (a) Ca=1.0, (b) Ca=0.5, (c) Ca=0.35, (d) Ca=0.25.

(c)

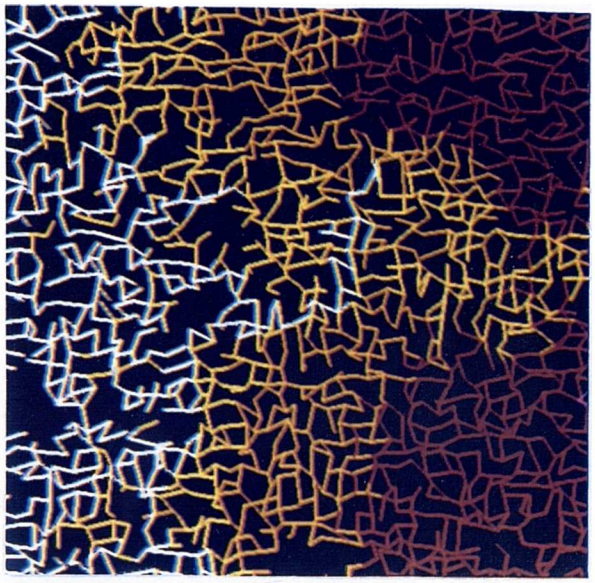

(d)

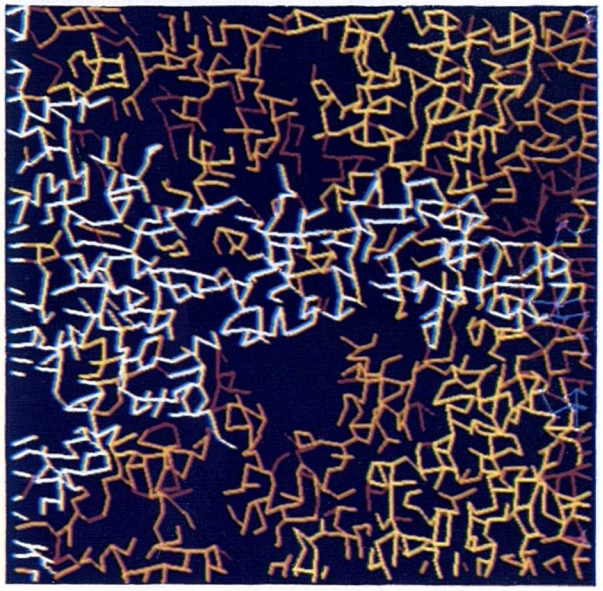

Figure 6.5 (Continued)

(a)

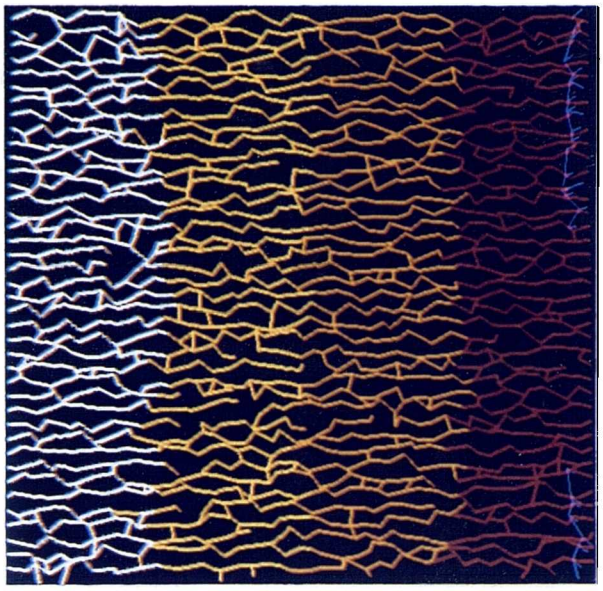

(b)

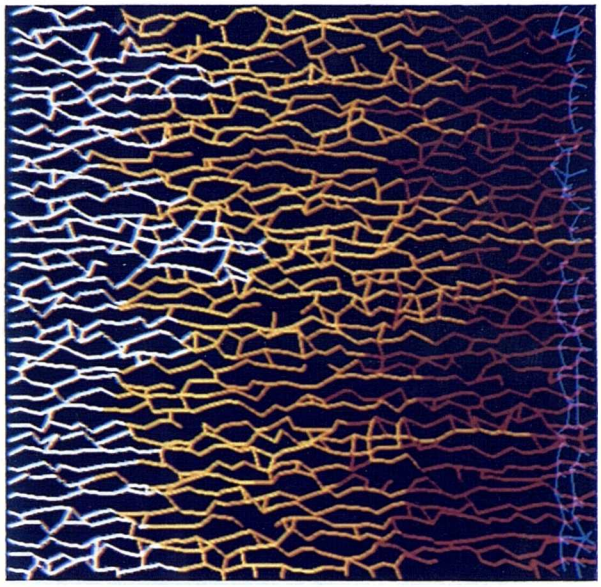

(c)

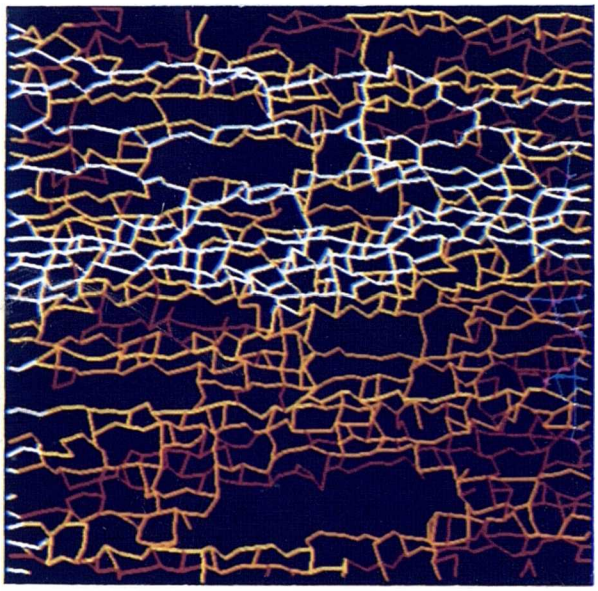

Figure 6.6 Drainage simulations on a 40x40 distorted network, showing the effect of network heterogeneity upon residual saturation and displacement efficiency. The sequence of displacement is white-yellow-orange-red, the trapped phase is black. Radii are now chosen from (40,60). (a) κ=0.01, (b) κ=1.0, (c) κ=100.

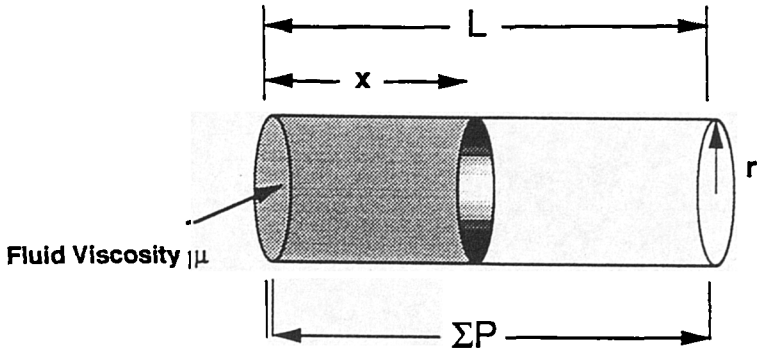

Figure 6.7 Water of viscosity μ displaces air from a capillary tube of radius r. ΣP is the total effective pressure.

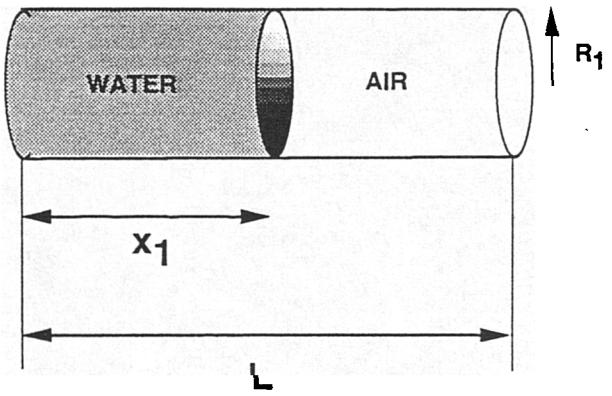

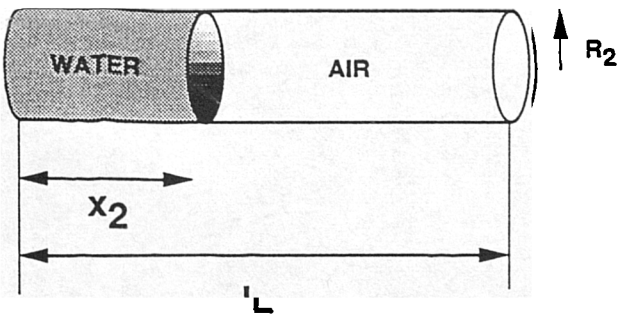

Figure 6.8 Two tubes of differing radius filling under viscous domination. The penetrated lengths satisfy the equation $x_1=(R_1/R_2)x_2$.

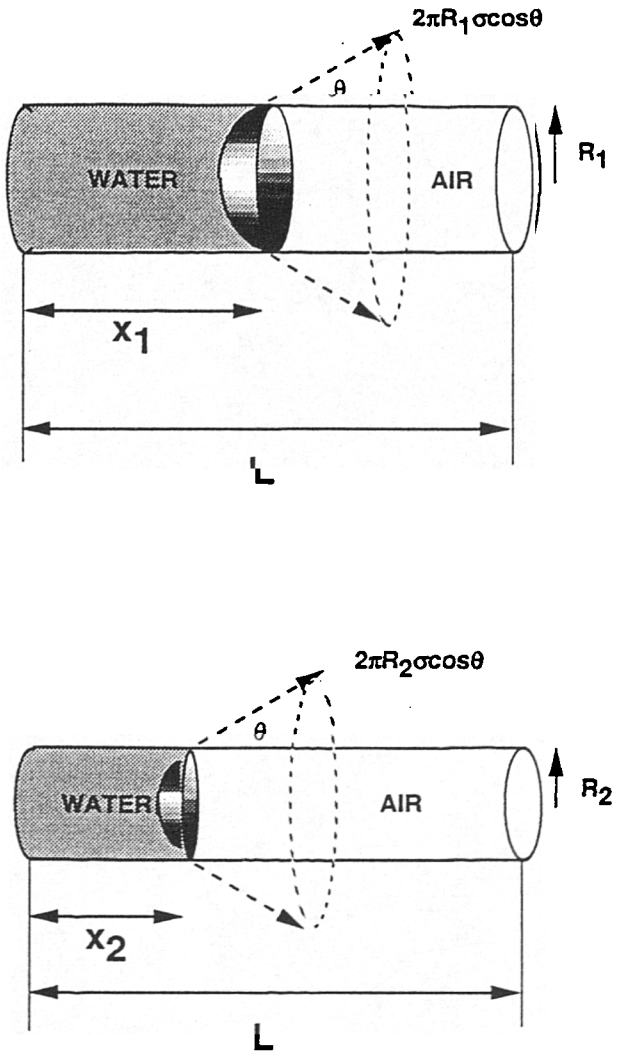

Figure 6.9 Two tubes of differing radius filling under capillary control. The penetrated lengths now satisfy the equation $x_1=(R_1/R_2)^{1/2}\ x_2$.

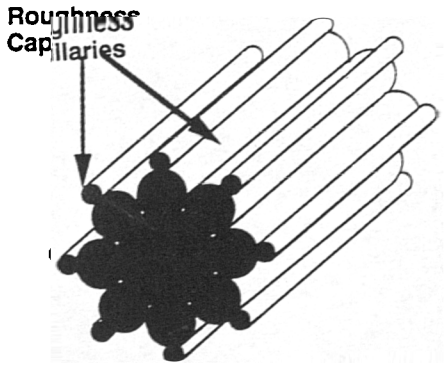

Figure 6.10 Typical pore element used for imbibition simulations. Two sets of roughness capillaries are used to explicitly model film-flow along surface irregularities.

(a)

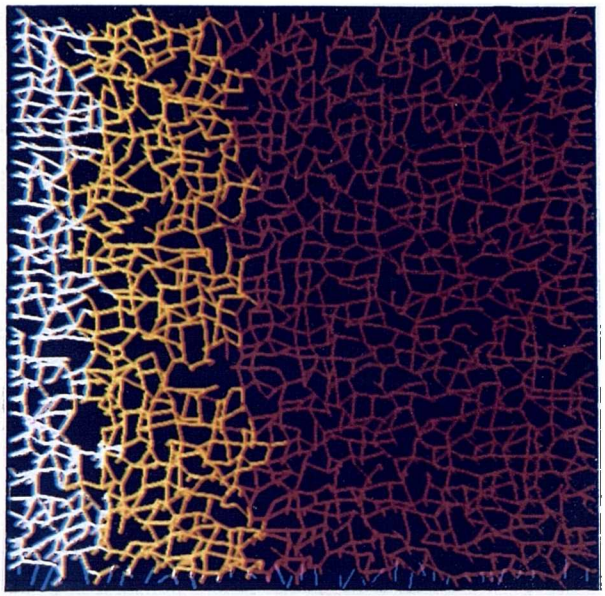

(b)

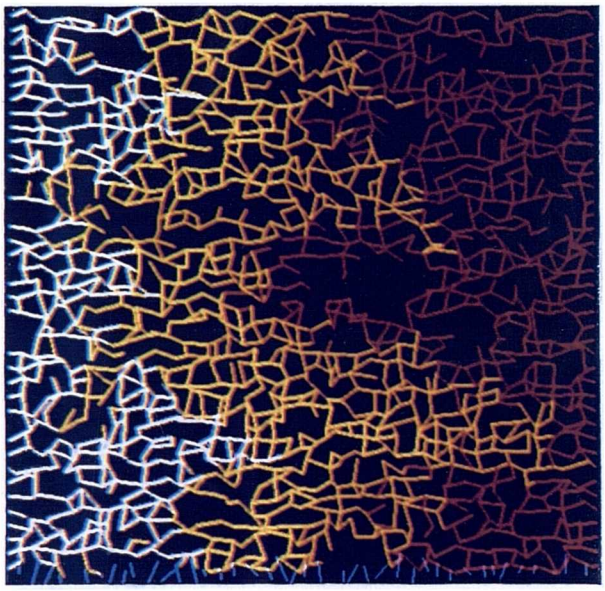

(c)

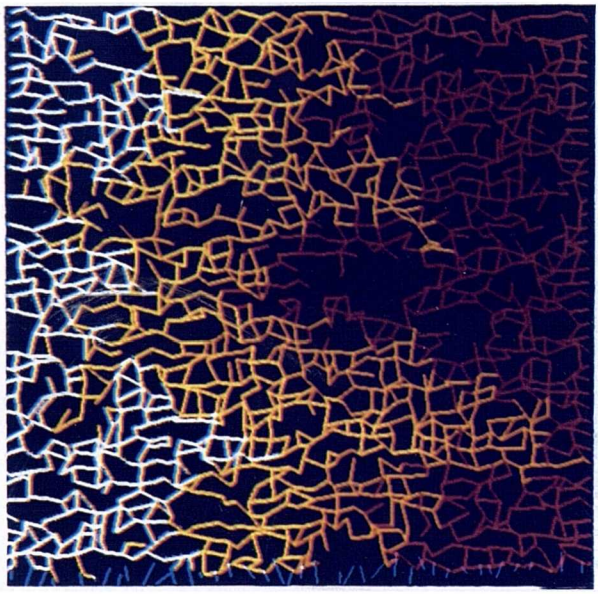

Figure 6.11 Network simulations of waterfloods in homogeneous water-wet media using the Washburn approximation: (a) capillary-dominated, (b) viscous/capillary regime, (c) viscous-dominated.

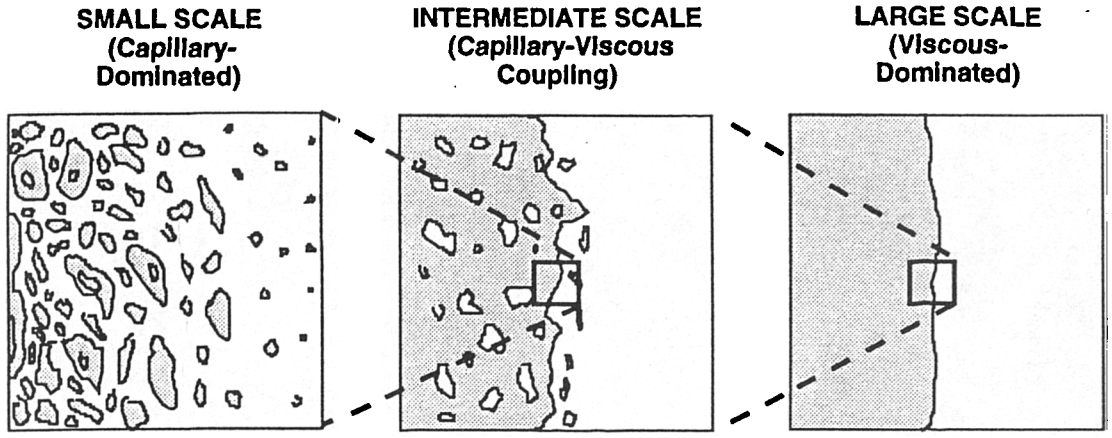

Figure 6.12 The scale-dependency of the viscous/capillary force balance — from the pore-scale to the reservoir-scale.

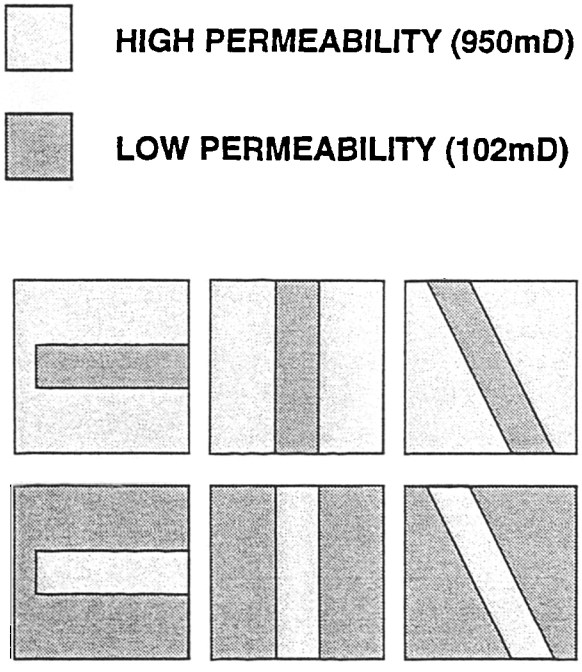

Figure 6.13 The six heterogeneous systems used in this study: each contains an orientated layer of contrasting permeability.

(a)

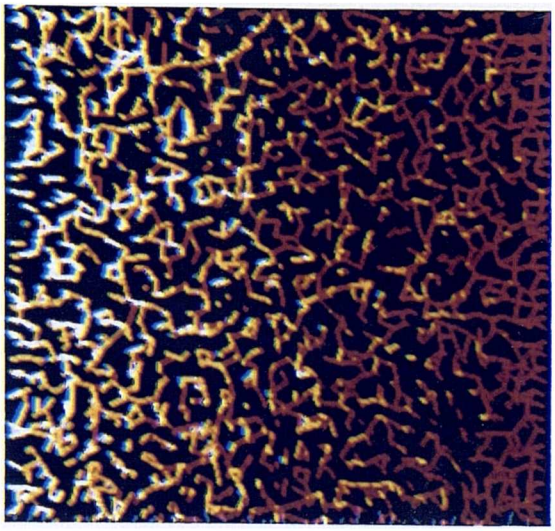

(b)

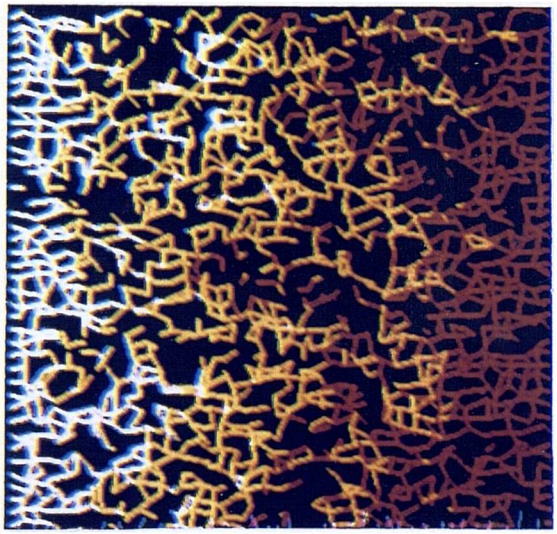

(c)

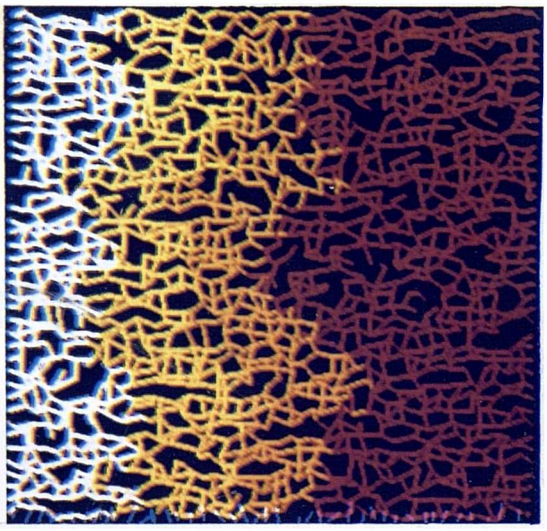

Figure 6.14 Network simulations of waterfloods in homogeneous water-wet media using the extended Washburn equation: (a) capillary-dominated flow(scattered capillary fringe), (b) viscous/capillary coupling (frontal advance together with a narrow capillary fringe), (c) viscous-dominated flow (frontal advance).

(a)

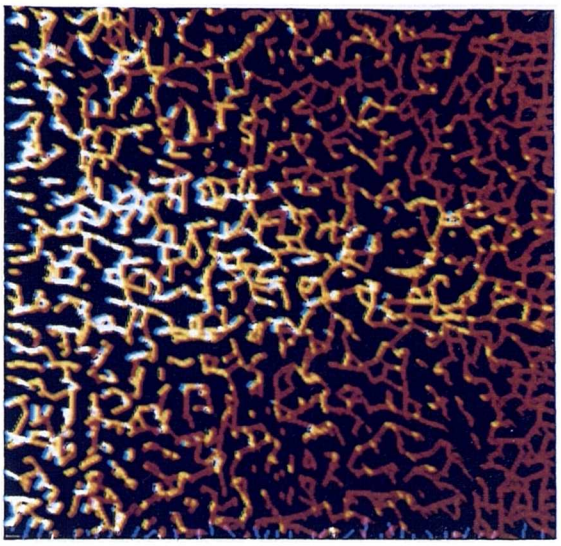

(b)

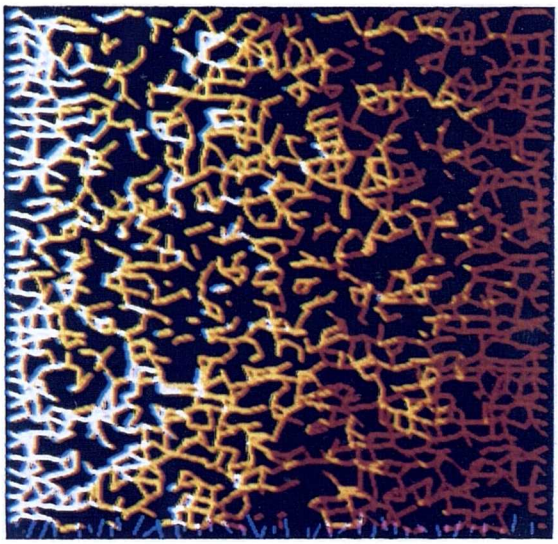

(c)

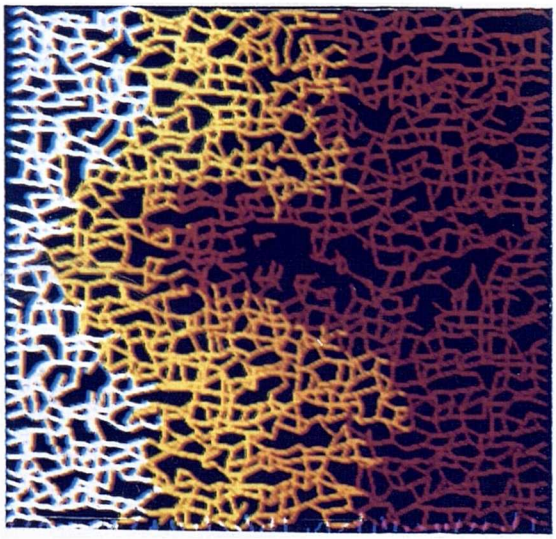

Figure 6.15 Waterflood simulations in heterogeneous water-wet systems containing orientated layers of low permeability. Viscous forces increase vertically downwards: (a)-(c) low permeability horizontal, (d)-(f) low permeability vertical, (g)-(i) low permeability diagonal.

(d)

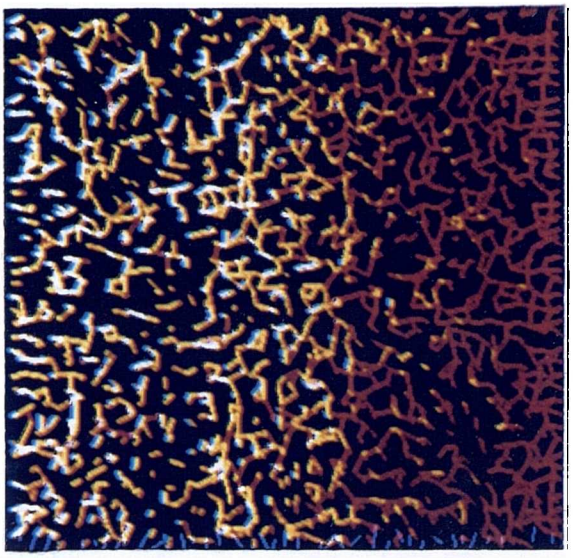

(e)

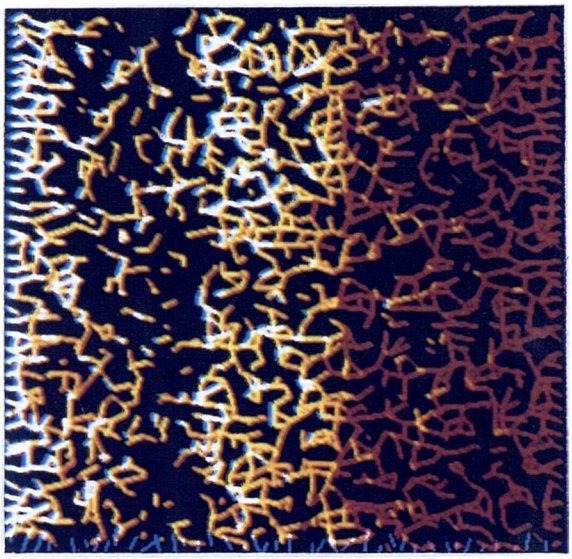

(f)

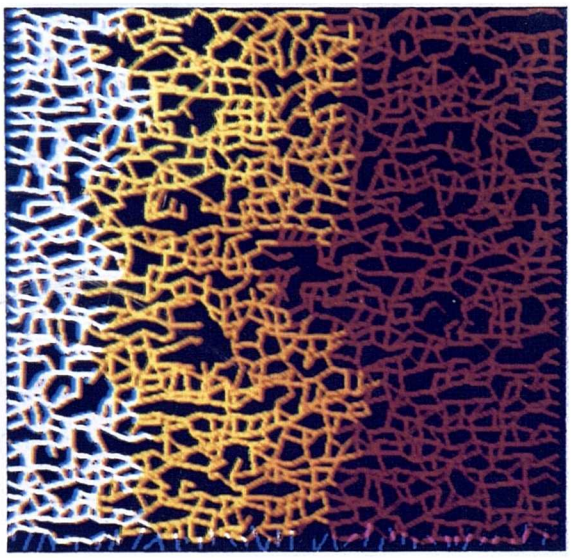

Figure 6.15 (Continued)

(g)

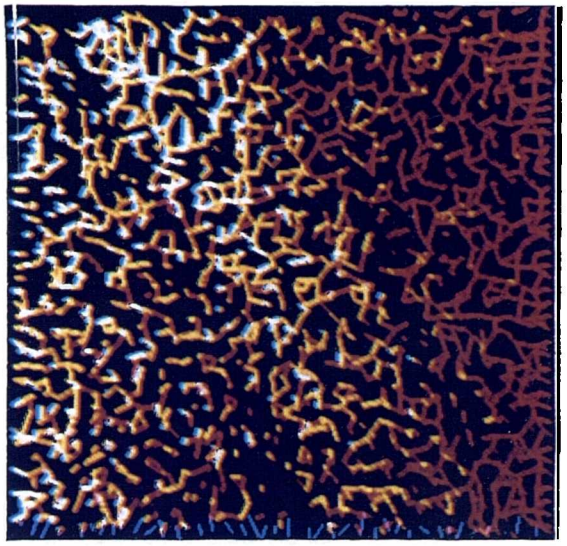

(h)

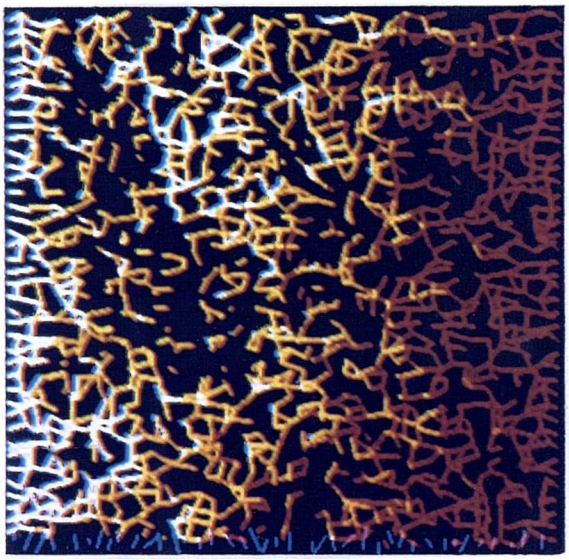

(i)

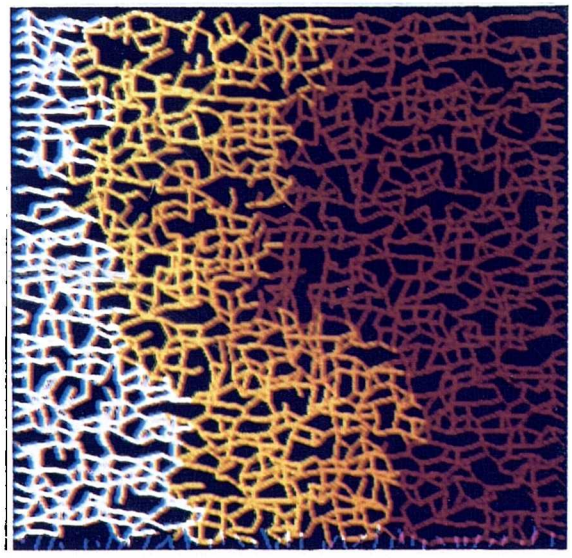

Figure 6.15 (Continued)

(a)

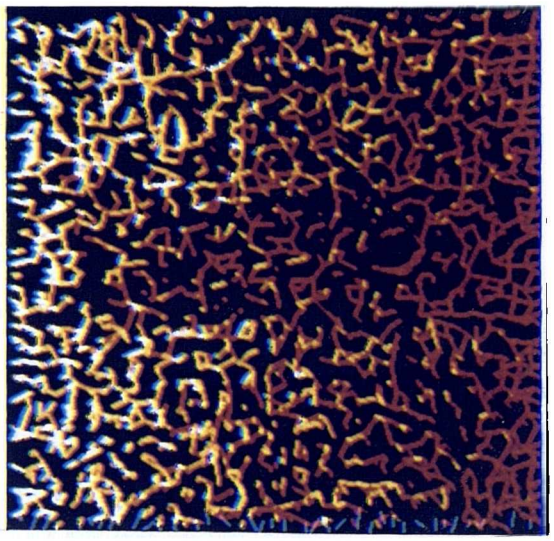

(b)

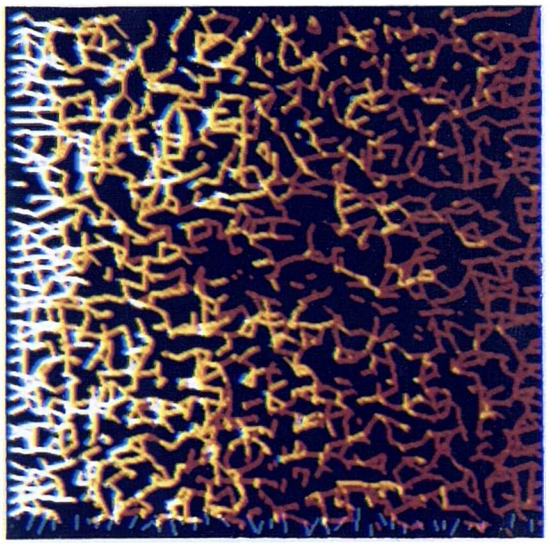

(c)

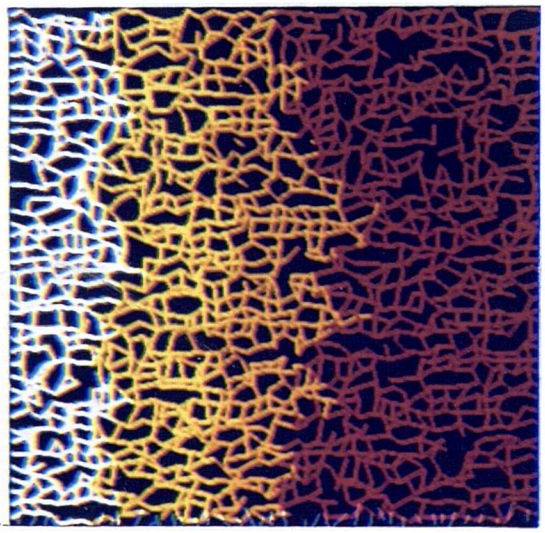

Figure 6.16 Waterflood simulations in heterogeneous water-wet systems containing orientated layers of high permeability. Viscous forces increase vertically downwards: (a)-(c) high permeability horizontal, (d)-(f) high permeability vertical, (g)-(i) high permeability diagonal.

(d)

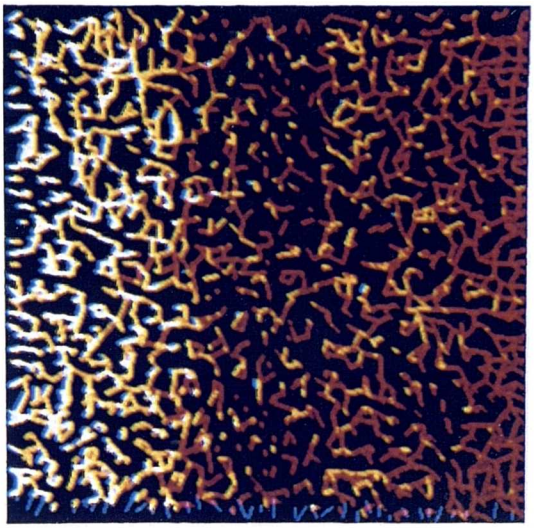

(e)

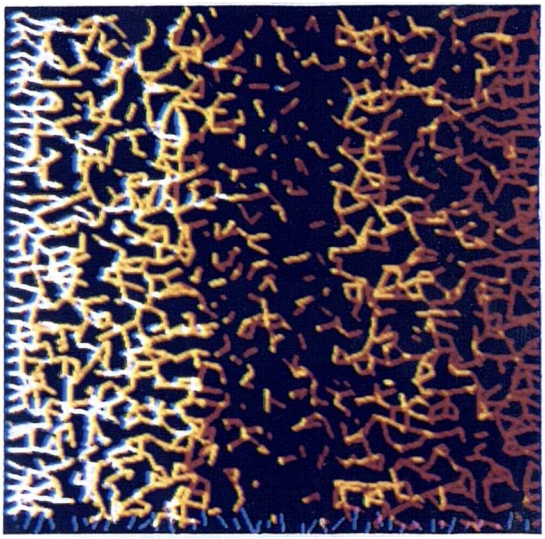

(f)

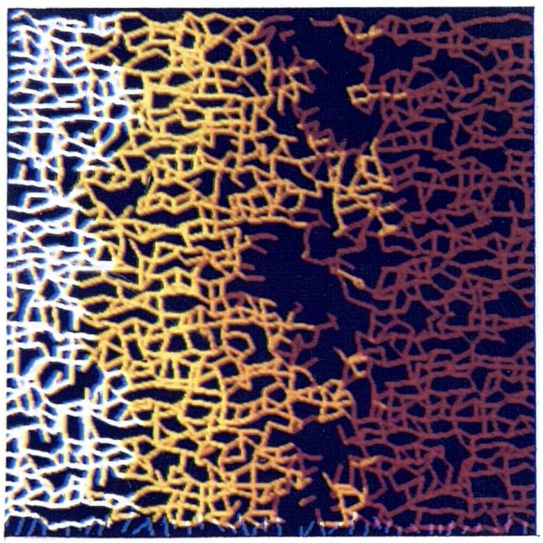

Figure 6.16 (Continued)

(g)

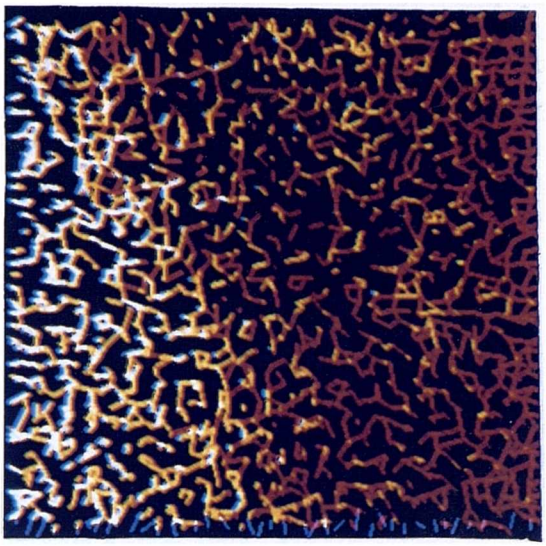

(h)

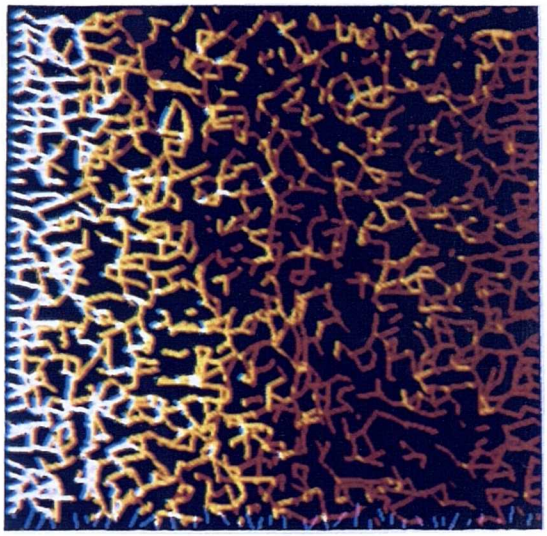

(i)

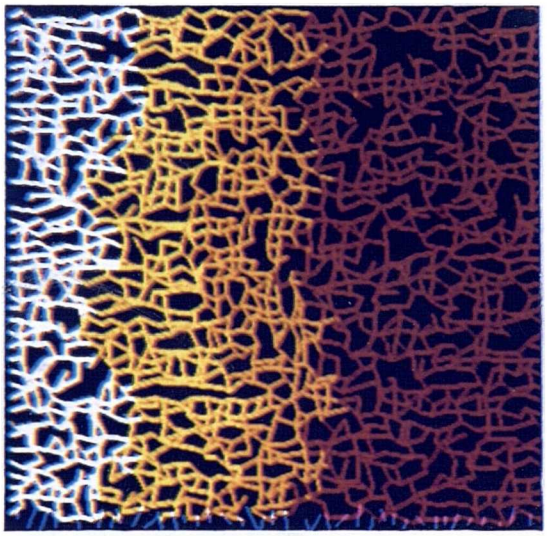

Figure 6.16 (Continued)

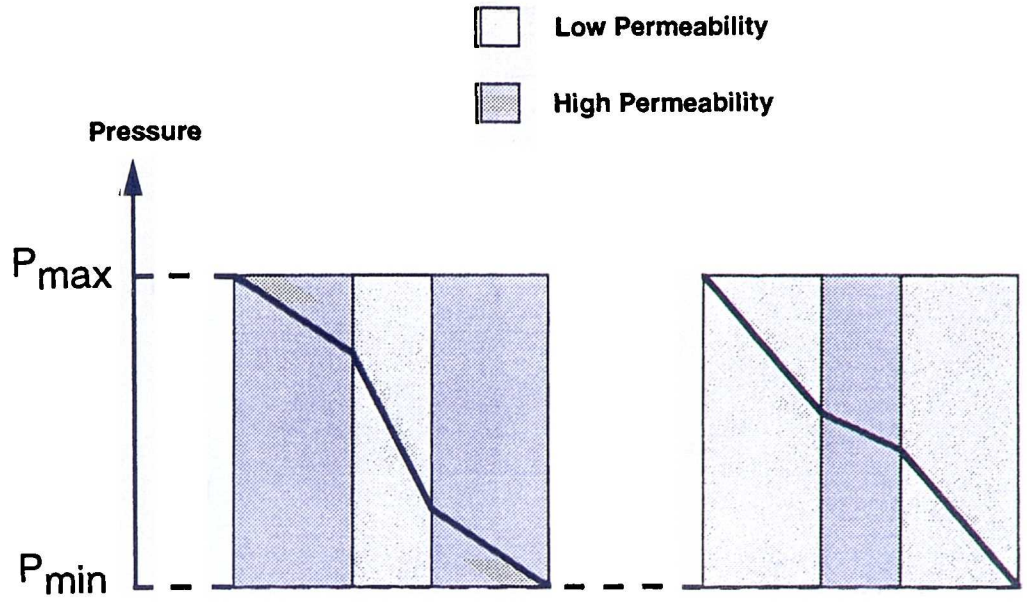

Figure 6.17 Schematic showing the difference in viscous pressure gradients across layered systems. Darcy's law shows that pressure gradients will be greatest across low permeability layers.

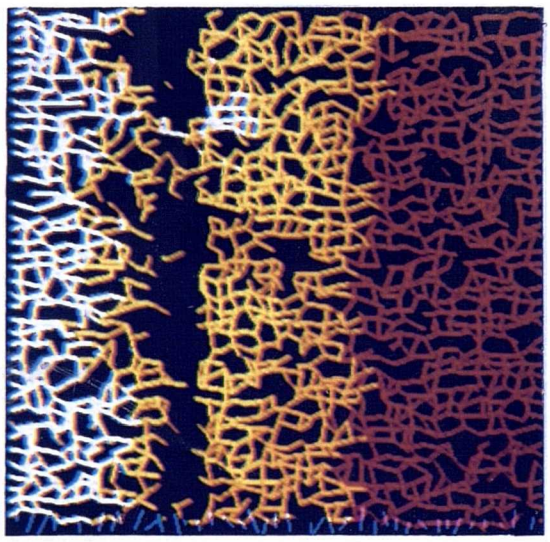

Figure 6.18 Viscous-dominated waterflood of a water-wet system containing a vertical layer of low permeability. The permeability contrast between layers is approximately 100:1.

(a)

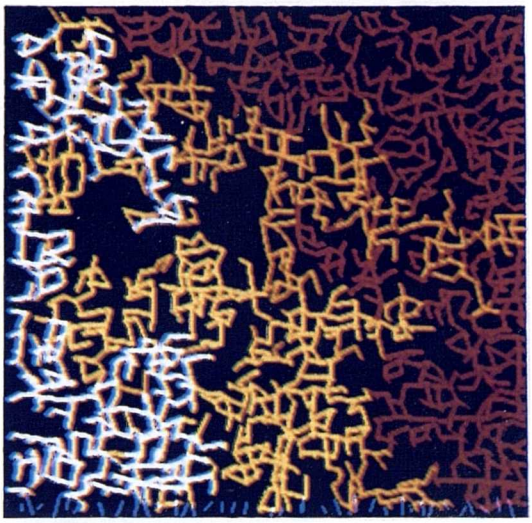

(b)

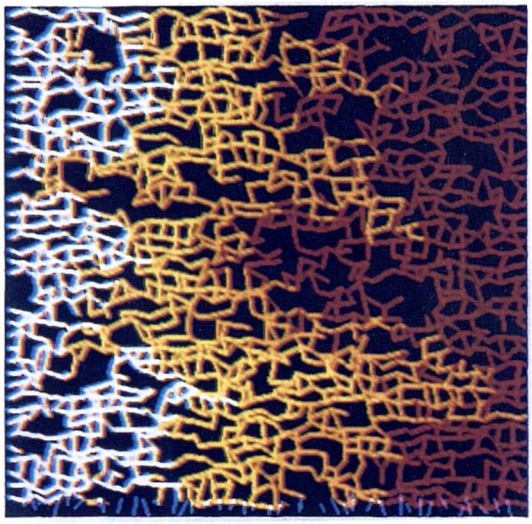

(c)

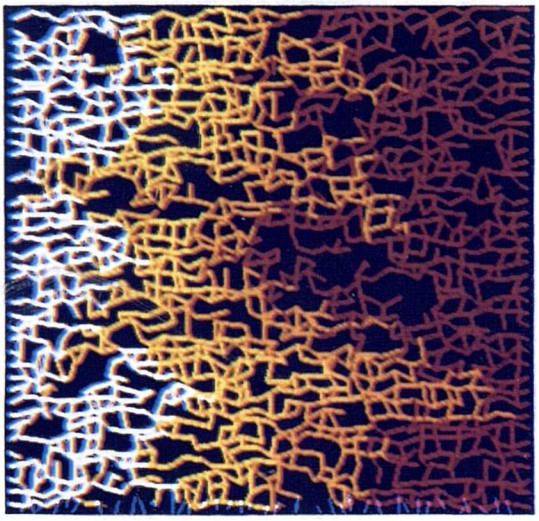

Figure 6.19 Network simulations of waterfloods in homogeneous oil-wet media: (a) capillary-dominated flow (capillary fingering), (b) viscous/capillary coupling, (c) viscous-dominated flow.

(a)

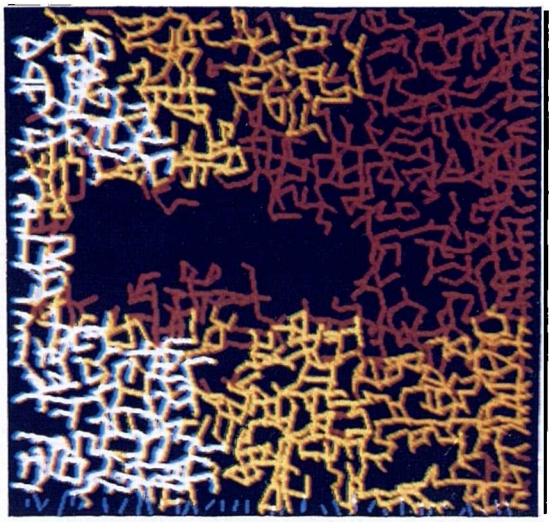

(b)

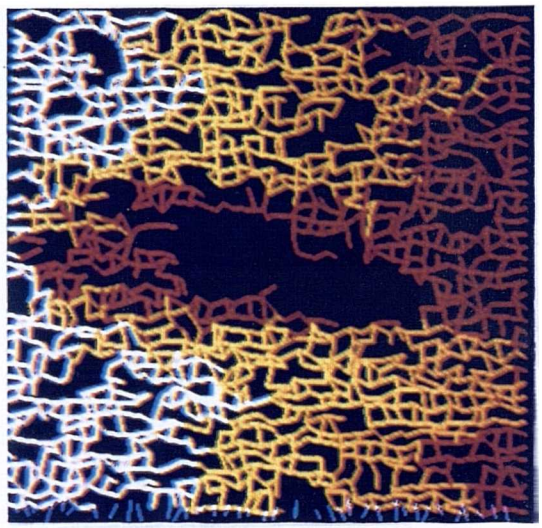

(c)

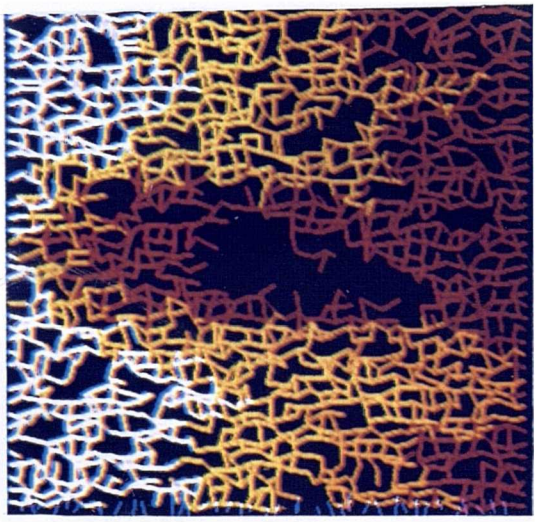

Figure 6.20 Waterflood simulations in heterogeneous oil-wet systems containing orientated layers of low permeability. Viscous forces increase vertically downwards: (a)-(c) low permeability horizontal, (d)-(f) low permeability vertical, (g)-(i) low permeability diagonal.

(d)

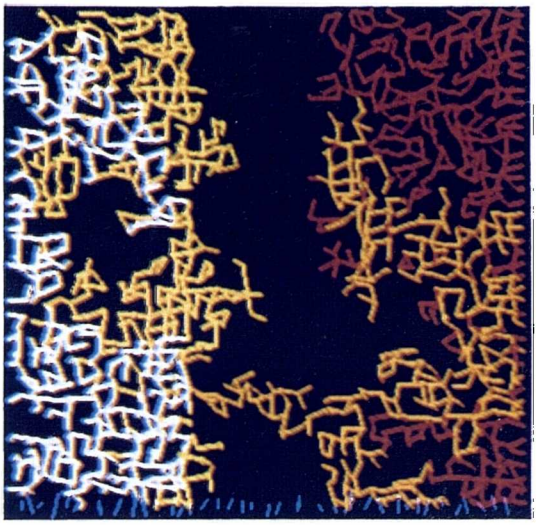

(e)

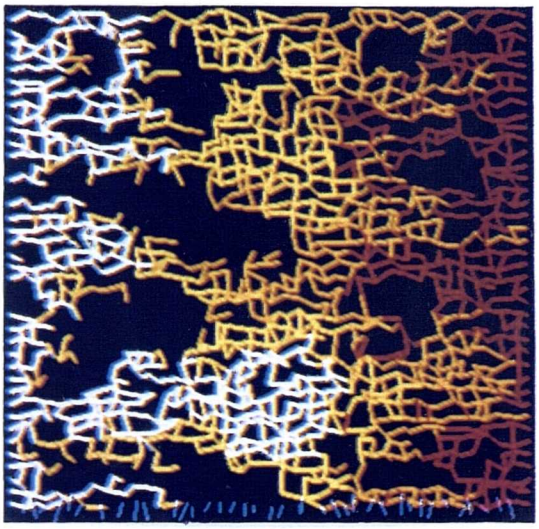

(f)

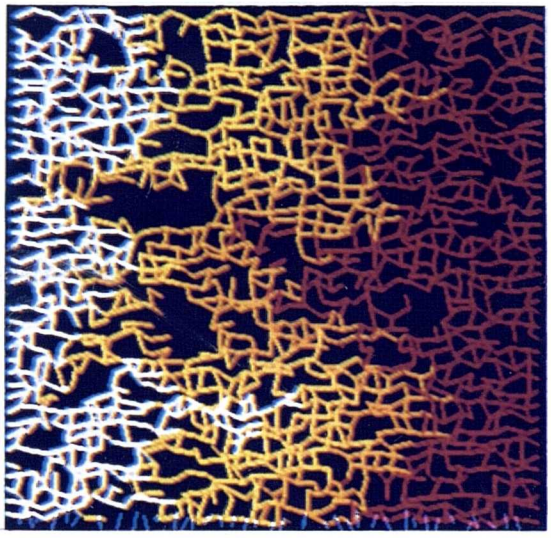

Figure 6.20 (Continued)

(g)

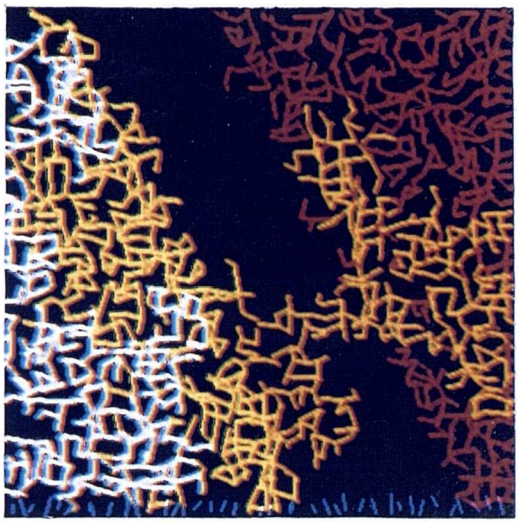

(h)

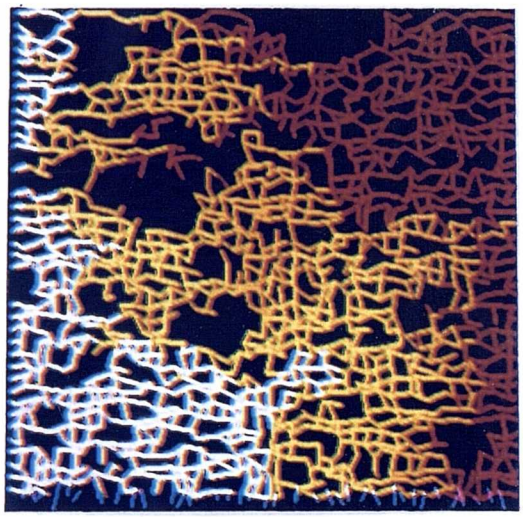

(i)

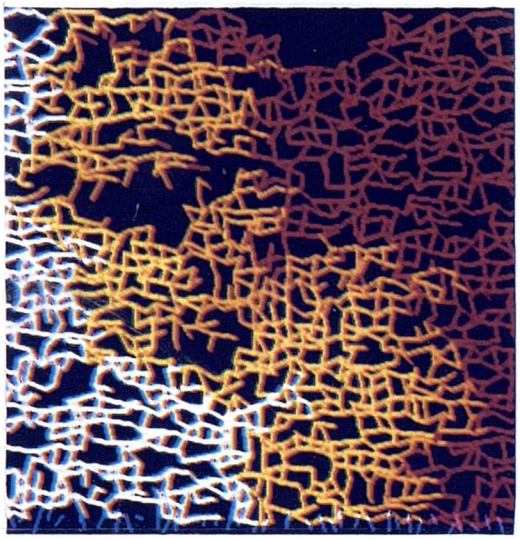

Figure 6.20 (Continued)

(a)

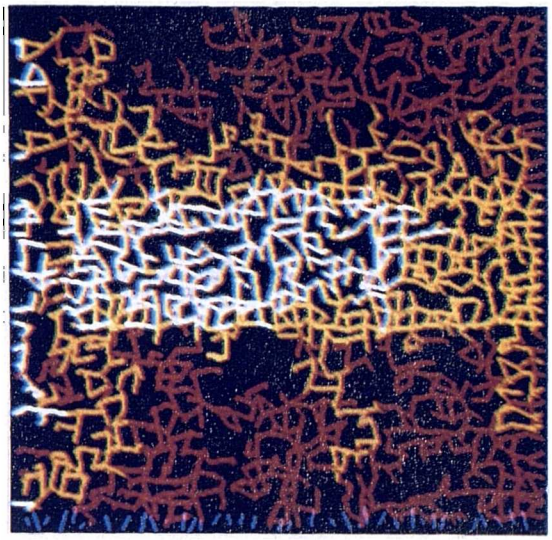

(b)

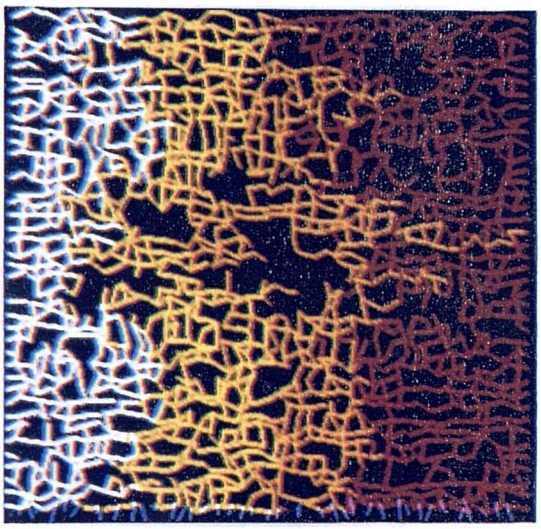

(c)

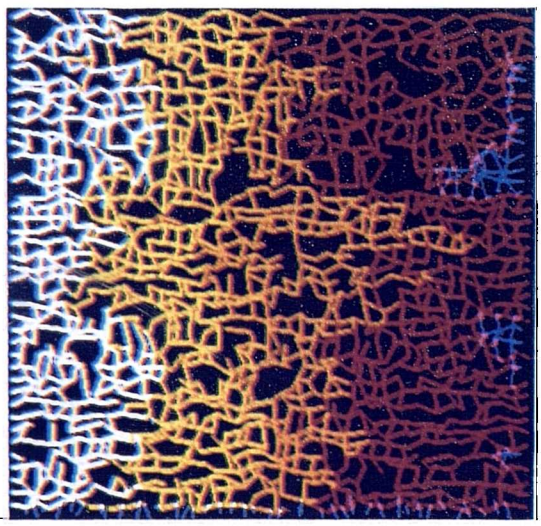

Figure 6.21 Waterflood simulations in heterogeneous oil-wet systems containing orientated layers of high permeability. Viscous forces increase vertically downwards: (a)-(c) high permeability horizontal, (d)-(f) high permeability vertical, (g)-(i) high permeability diagonal.

(d)

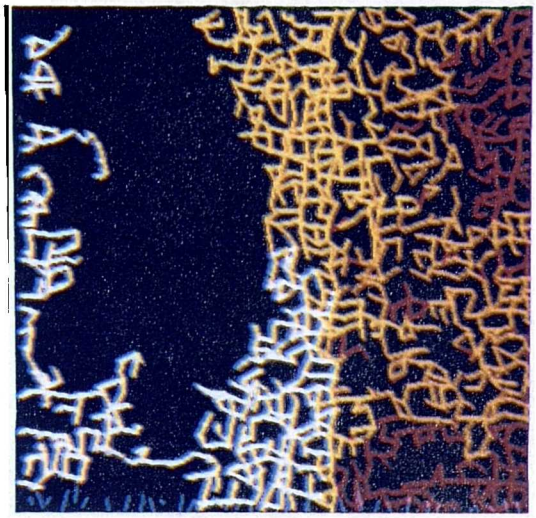

(e)

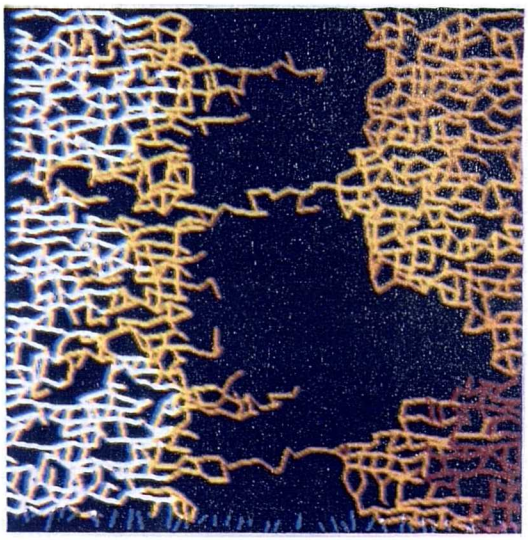

(f)

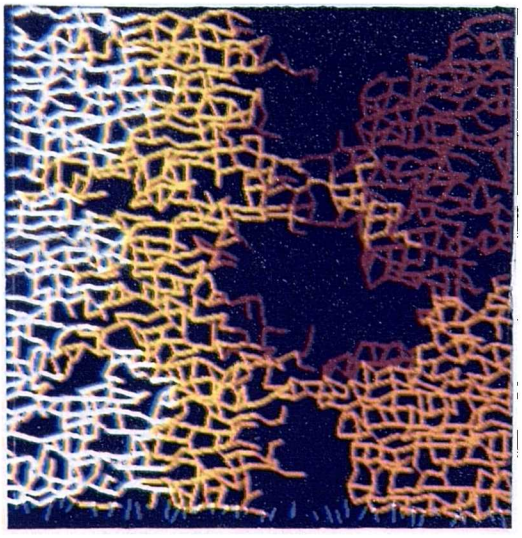

Figure 6.21 (Continued)

(g)

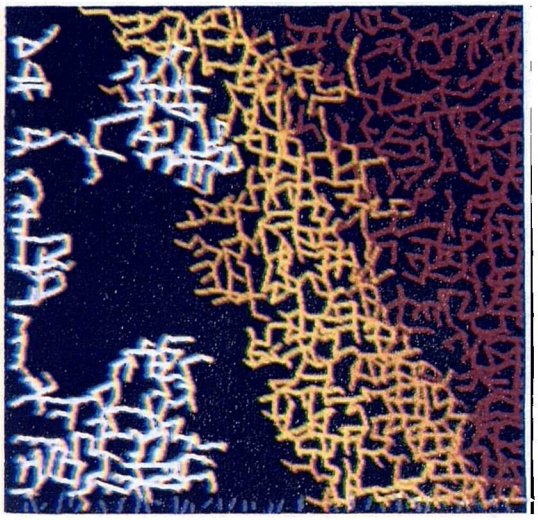

(h)

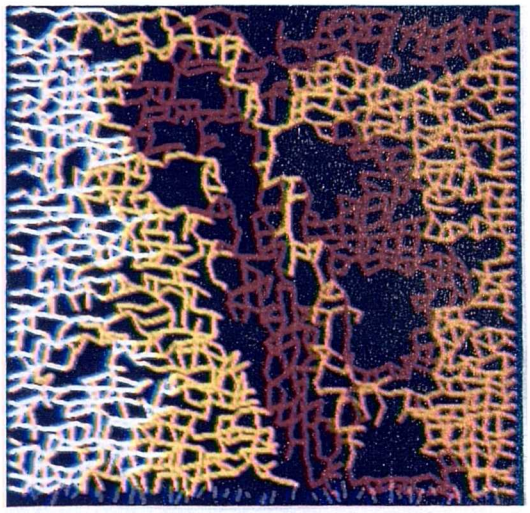

(i)

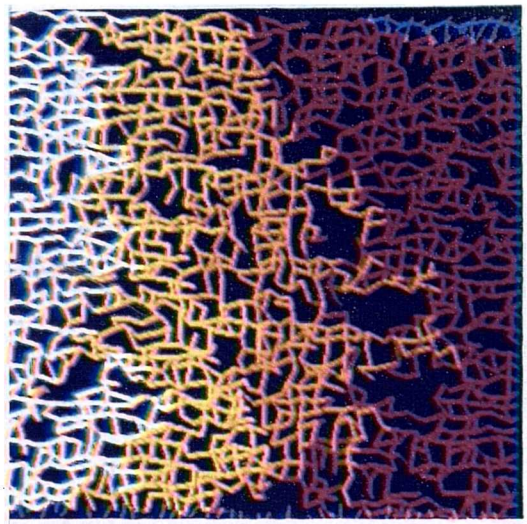

Figure 6.21 (Continued)

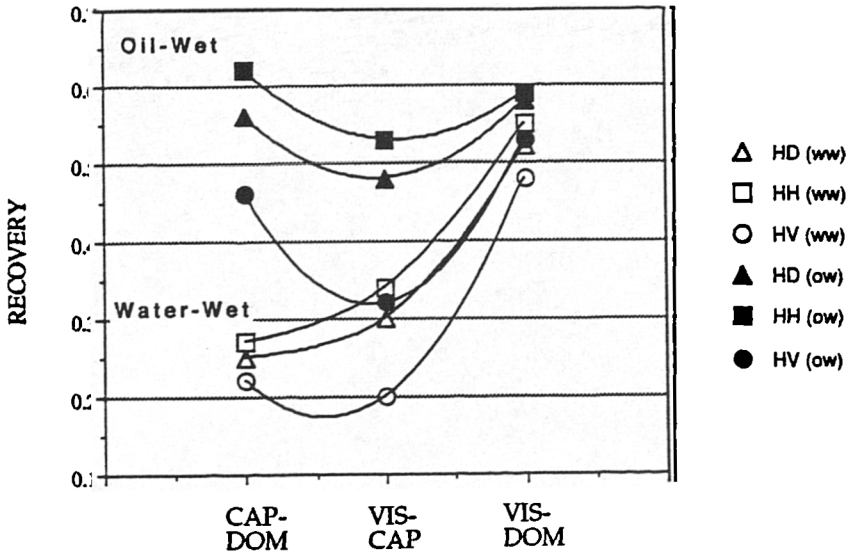

(a)

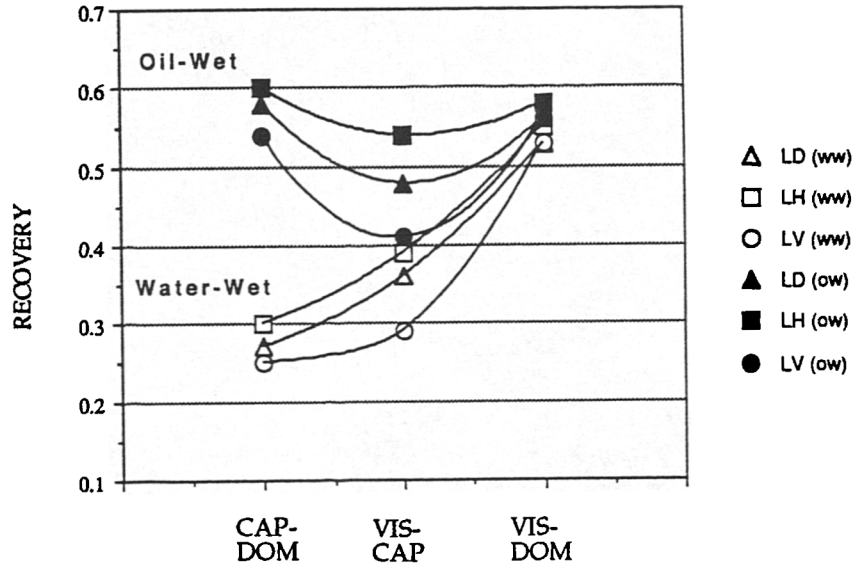

(b)

Figure 6.22 Plots showing recovery as a function of the viscous/capillary force balance: (a) systems containing low permeability heterogeneities, (b) systems containing high permeability heterogeneities

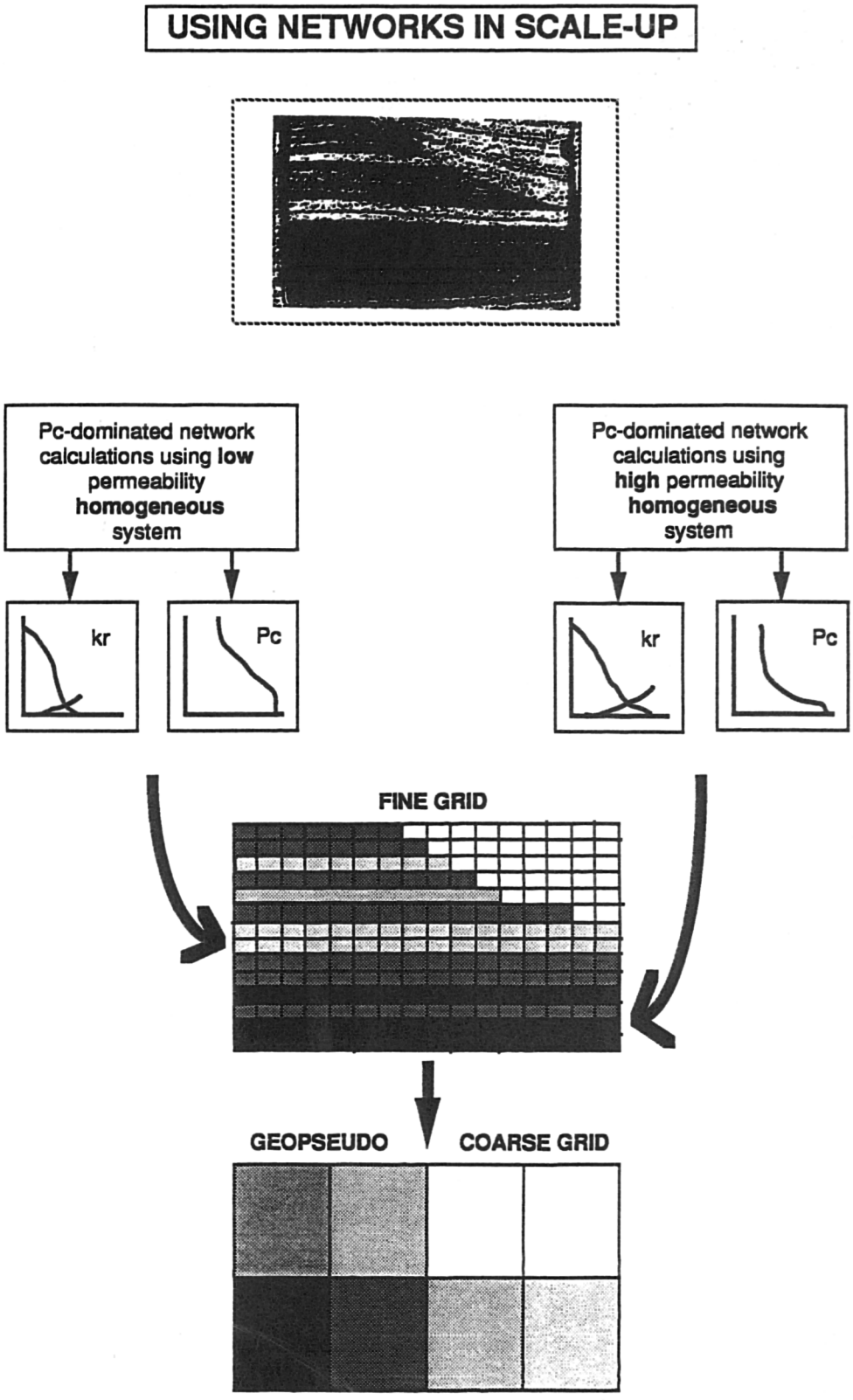

Figure 6.23 Network calculations can best be used for obtaining small-scale capillary-dominated flow parameters. These can then be used as input data for "geopseudo" scale-up studies.

CHAPTER 7 THREE-PHASE FLOW

7.1 Introduction

This chapter sets out to describe the current confusion surrounding a variety of three-phase flow phenomena and suggests a possible way forward towards greater understanding of three-phase flow generally. By focussing attention upon the relevant microscopic flow physics, it provides a cogent explanation as to why so much experimental work is inconsistent and contradictory.

Three-phase flow may occur under a wide range of operating conditions; blow-down in dissolved-gas or retrograde gas-condensate reservoirs, CO_2 injection, steam drive, WAG processes, etc. Of more immediate interest, perhaps, is a recent proposal involving depressurisation of the Brent field (Braithwaite and Schulte, 1992), which is expected to increase oil and condensate recovery by some 30MMstb. Such proposals, however, have wide bands of uncertainty associated with them, especially when three phases are involved. It is vital, therefore, to be able to assess risk as accurately as possible, and to interpret three-phase laboratory measurements in a realistic and meaningful way. A simple analysis of the problem, however, serves to highlight the intrinsic difficulties associated with interpreting such experiments: whereas in two-phase flow regimes there are only two possible contacting histories (either water or oil contacts the sample first) and two possible saturation histories (imbibition and drainage), in three-phase flow there are *six* contacting histories and *thirteen* saturation histories. The numerous combinations of these lead to a vast range of disparate flow behaviour — a range which is yet to be fully appreciated and researched. Such a multiplicity of flooding conditions must surely be responsible for much of the contradictory experimental evidence of the past.

The first part of this chapter begins by examining previous experimental work and looks at the chronological development of three-phase flow research generally. The existing analytical models are then discussed and their shortcomings highlighted. It should be noted that none of the currently available analytical techniques incorporates the relevant flow physics; in fact, many are little more than empirical correlations. The next section explains the need for an integrated research programme which builds upon our existing knowledge in a systematic way — from the pore-scale to the core-scale. The case for network modelling studies is also discussed. This is followed by some simulation results, which have been used to examine the role played by connate water and the spreading coefficient during three-phase displacements.

7.2 Current Difficulties Associated with Three-Phase Flow

Even after the briefest glance through the three-phase literature, it soon becomes apparent to the interested reader that general predictions are virtually non-existent. In fact, each paper seems to throw up more questions than it answers. Contradictory results are commonplace, and occur for a variety of reasons: different studies tend to utilise different fluids; experiments are carried out on different rock types; flooding is done at different rates; different core conditioning procedures are used. Consider the last of these (core conditioning): recent micromodel work by Idris (1990) has clearly demonstrated that contacting history can greatly affect the wettability characteristics of a system and hence the flow of fluids through it (see Table 7.1). It is therefore no great surprise that systems conditioned in different ways do not behave analogously. Failure to recognise the thirteen possible three-phase saturation histories, summarised in Table 7.2, must also be a source of much confusion. The extent of this confusion is exemplified in the following review of three-phase studies that have taken place to date.

7.2.1 Contradictory Experimental Results

Many unresolved discrepancies exist throughout the associated literature, from the early pioneering work of Leverett and Lewis (1941) to the more recent studies of Longeron et al (1993). These differences are fundamental: for instance, even the basic structure of three-phase "isoperms" is not yet known — are they convex, linear, or concave in nature? A chronological list of important experimental work, containing procedural information related to each study is presented in Table 7.3. The main areas of conflict are now discussed below.

Three-Phase Relative Permeability — Most three-phase relative permeability studies have concentrated on displacements in water-wet media. The earliest investigations utilised sandpacks (Leverett and Lewis, 1941; Snell, 1962), whilst subsequent work seems to have concentrated mainly on the use of core samples (Corey et al, 1956; Saraf and Fatt, 1967; Oak et al, 1988; Oak, 1990; Dria et al, 1990). Unfortunately, comparison between studies is wholly inappropriate, as saturation histories are often inconsistent and experimental conditions extremely variable — the resulting contradictions are perfectly understandable. Consider first water isoperms. Some investigators have reported that the relative permeability to water in a three-phase system depends upon water saturation only (Schneider and Owens, 1970; Oak, 1990; Dria and Pope, 1990; inter alia), whilst others show it to be a function of all three phase saturations (Donaldson and Dean, 1966; Van Spronsen, 1982; inter alia). A variety of water isoperms are presented in Figure 7.1; the structural differences between them clearly makes generalisation impossible.

A similar conflict arises when attempting to compare three-phase gas relative permeabilities: are these functions of gas saturation only (Corey et al, 1956; Narahara et al, 1990) or do they too depend upon all three saturations (Reid, 1956; Snell, 1963; Berry et al, 1992)? A range of gas isoperms is shown in Figure 7.2. Notwithstanding the evidence of Figures 7.1 and 7.2, water and gas

isoperms are generally assumed to be linear with respect to the ternary saturation diagram.

There appear to be no consistent results whatsoever concerning oil relative permeabilities: oil isoperms have been shown to be concave (Oak, 1990; Kokal and Maini; 1990), linear (Sarem, 1966), and convex (Saraf and Fatt, 1967) in form. Oil relative permeabilities from several studies are shown in Figure 7.3; those from Oak et al (1988) also clearly demonstrate the importance of saturation history. The need for a systematic study of three-phase relative permeability is obvious.

Effect of Initial Gas Saturation — A few studies have attempted to quantify the effect of initial gas saturation upon residual oil (Holmgren and Morse, 1951; Kennedy and Guerrero, 1954; Kyte et al, 1956). Once again, however, conclusions are contradictory: Kennedy and Guerrero showed that residual oil saturations decreased with decreasing initial gas saturations, whereas the other two studies concluded exactly the opposite (namely an *increase* in residual oil with decreasing gas saturations).

Effect of Connate Water — The role played by a connate water saturation has also recently been examined; once again, studies yield inconsistent results. Narahara et al (1990) found that gas/oil relative permeabilities (expressed as functions of *liquid* saturation) measured with an initial water saturation present were the same as those measured without water present. Berry et al (1992), however, indicate that both gas and oil relative permeabilities *are* affected by the presence of connate water. The effect of connate water upon capillary pressure curves has also recently been re-examined (Longeron et al, 1993); yet again, results appear to be at odds with earlier work (Dumoré and Schols, 1974).

Other Issues —

(1) It has recently been shown that the choice of injected gas (air, N_2, CO_2) can also dramatically modify relative permeability measurements (Dria et al, 1990).

(2) During depressurisation, the *rate* of depressurisation has a profound effect upon critical gas saturation and oil recovery (Stewart et al, 1954; Dumoré, 1970; Moulu and Longeron, 1989; Kortekaas and van Poelgeest, 1989).

(3) Relative permeability to gas appears to depend upon whether steady-state or unsteady-state displacements are undertaken (Schneider and Owens, 1970).

(4) Capillary end effects are a major problem in most studies and are seldom adequately accounted for.

The points outlined above clearly indicate that further progress in this area will only be possible if some standardisation of three-phase flow measurements can be achieved. The current variations in experimental procedure must inevitably lead to more confusion and more experimental cul de sacs.

7.3 Existing Analytical Models and Their Limitations

Large-scale simulation studies require three-phase relative permeabilities to accurately model a variety of multiphase flow processes in the reservoir. It will now be apparent, however, that the laboratory measurement of such parameters is fraught with difficulty and subject to a large degree of uncertainty. As a result, a number of analytical methods have been derived which attempt to predict three-phase relative permeabilities from the more accessible two-phase data. A chronological listing of these is given in Table 7.4 (a comparative study of seven of them is given by Delshad and Pope (1989)).

Analytical models generally seek to use two-phase data together with a mixing rule dependent upon normalised saturations. The most commonly used

methods are those due to Stone (Stone, 1970, 1973) which implicitly assume strongly water-wet conditions (conditions which now appear to be the exception rather than the rule). Water and gas relative permeabilities are taken to be functions of their own saturations only, whereas oil relative permeabilities can depend upon the saturations of all three phases. Although Stone's methods have proven inadequate for three-phase flow predictions, they have nevertheless become the industry standard.

Stone's Method I

In this method, oil relative permeability is considered to be a modified linear function of normalised oil saturation:

$$k_{ro} = S_o^* \beta_w \beta_g \tag{7.1}$$

where

$$\beta_w = \frac{k_{row}}{1 - S_w^*} \quad (2-\text{Phase}) \tag{7.2}$$

$$\beta_g = \frac{k_{rog}}{1 - S_g^*} \quad (2-\text{Phase}) \tag{7.3}$$

and the normalised saturations are given by:

$$S_o^* = \frac{S_o - S_{or}}{1 - S_{wc} - S_{or}} \tag{7.4}$$

$$S_w^* = \frac{S_w - S_{wc}}{1 - S_{wc} - S_{or}} \tag{7.5}$$

and

$$S_g^* = \frac{S_g}{1 - S_{wc} - S_{or}} \tag{7.6}$$

Stone's Method II

The second model makes the assumption that the sum of all three relative permeabilities in a three-phase system, can be written in terms of water-oil data obtained at $S_g=0$ and oil-gas data obtained at $S_w=S_{wc}$. Hence:

$$\left[k_{ro}+k_{rw}+k_{rg}\right]_{3-Phase}=\left[(k_{ro}+k_{rw})\right]_{oil-water}\times\left[(k_{ro}+k_{rg})\right]_{oil-gas} \qquad (7.7)$$

As water and gas relative permeabilities are assumed to be the same if two or three phases are present, this equation can be rearranged to give the three-phase relative permeability to oil as

$$\left[k_{ro}\right]_{3-Phase}=\left[(k_{ro}+k_{rw})\right]_{oil-water}\times\left[(k_{ro}+k_{rg})\right]_{oil-gas}-\left[k_{rw}+k_{rg}\right]_{2-Phase} \qquad (7.8)$$

In general, the results obtained by using these methods are not very accurate and comparisons with experimental work are poor (Van Spronsen, 1982; Fayers and Matthews, 1984; Kokal and Maini, 1990; Oak, 1990). In fact, Oak's results completely contradict the assumption that two-phase data can be used to predict three-phase relative permeabilities at all.

The inadequacies associated with Stone's methods I and II have led to a variety of modifications. Dietrich and Bondor (1976) and Aziz and Settari (1979) renormalised Stone's equations using the endpoint oil relative permeability at connate water saturation derived from two-phase oil-water data. More recently, Fayers and Matthews (1984) suggested an algebraic form for the residual oil saturation term in Stone's method I. Fayers (1987) further extended this model in an attempt to improve the reliability of the method at low oil saturations. None of these modifications gives any physical insight into the true nature of three-phase displacements, however: they completely ignore the fact that very different pore-scale interactions take place when a third phase is present within the porespace.

Althougn useful three-phase relative permeability correlations may well exist, variations in wettability, contacting history and/or saturation history mean that the *general* applicability of any of these methods is extremely questionable. It is clear that further examination of fundamental three-phase flow physics is essential if predictive uncertainties are to be minimised in the future.

7.4 A Possible Solution Strategy: From Pore-Scale to Core-Scale.

The ability to perform cheap, quick and accurate three-phase petrophysical measurements under reservoir conditions would surely be one of the most important advances for any major oil company. Unfortunately, three-phase experiments are costly, time-consuming, and notoriously difficult to carry out. Consequently, companies tend to perform very few three-phase experiments themselves and rely heavily upon the inadequate analytical methods outlined above; methods that take no account of the complex three-phase interactions actually taking place. Indeed, it is staggering that so little importance has been attached to the governing multiphase fluid dynamics in the past, and not surprising that valid interpretation of coreflood work has proven somewhat difficult.

The complexity of the flow physics governing three-phase processes is immense and needs to be unravelled in a systematic way. Fortunately, there are three complementary techniques which can be utilised towards this end: micromodel visualisation, network modelling, and laboratory coreflooding. It is the author's belief that the key to successful three-phase prediction lies in the identification of relevant microscopic displacement mechanisms and their accurate implementation in a 3-dimensional pore-scale simulator. By "anchoring" the simulator to real coreflood data, it should be possible to perform a range of sensitivity analyses (wettability, flowrate, pore structure, etc.) and return a suite of production profiles for further consideration.

The first step is to identify the relevant pore-scale physics.

7.5 Relevant Three-Phase Flow Physics

The variety and complexity of the three-phase flow behaviour outlined above has recently prompted several investigators to return to more fundamental studies using glass micromodels (Henderson et al, 1991; Øren and Pinczewski, 1991; Soll et al, 1993) and capillary tubes (Dawe and Hawes, 1992; Kalaydjian, 1992). These studies have been vital in demonstrating some of the differences between two- and three-phase flow mechanisms, and are currently the only means by which one can readily see what actually happens at the pore-scale. Some key issues will now be discussed.

(1) Spreading Phenomena — A crucial parameter in determining three-phase flow behaviour is the *spreading coefficient* (S). It relates the free surface energies of all three phases at equilibrium and can be used to predict phase hierarchies at the pore-scale. In a completely water-wet medium, the oil spreading coefficient determines whether or not the oleic phase can spread as a film between the gas and water substrate. It is defined in terms of the three interfacial tensions of the system as:

$$S_o = \gamma_{wg} - (\gamma_{og} + \gamma_{ow}) \tag{7.9}$$

The coefficient is normally positive when reservoir oil contacts water, resulting in oil spreading over the water phase and opening up the possibility of oil drainage via film-flow. Hence, for a water-wet medium with positive spreading coefficient, the hierarchy of fluids in a pore is; water spreading on the solid surfaces, oil spreading on the water layer, and gas residing in the centre of the pore space (Figure 7.4a).

The capillary tube studies, together with additional micromodel work by Idris (1990), have clearly demonstrated the implications of spreading phenomena for gasflood efficiency and field optimisation. They have shown that by injecting gas into a watered-out reservoir, trapped oil can be remobilised and an oil bank formed. This is due to isolated oil ganglia becoming reconnected by oil spreading on the water substrate in the presence of injected gas. Efficient film-flow mechanisms have also been observed in micromodel studies of condensate/water/gas systems (Henderson et al, 1991). Pressure depletion below the dew-point leads to condensate dropout and, in systems with $S_o>0$, its subsequent spreading results in high condensate recovery

Micromodel displacements characterised by a *negative* spreading coefficient have been studied by Øren et al (1990), Kalaydjian and Tixier (1991), and Kalaydjian (1992). These studies show that with $S_o<0$, water-gas interfaces can be formed, leading to slug-type flow behaviour and high residual oil saturations (Figure 7.4b). The efficiency of a gasflood in systems with $S_o<0$ is generally reported to be much lower compared to that observed in systems where $S_o>0$.

Note that none of the analytical models currently in use take account of the spreading coefficient.

(2) *Gravity Drainage* — In systems where oil can form films, the role of gravity is an important one. Once contacted by invading gas, oil may be able to drain vertically and form a rich oil bank at the bottom of the reservoir. There is evidence that this *gravity drainage* process can be almost complete, and so an understanding of the relevant pore-level physics is vital. Work on this aspect of three-phase flow is still in its infancy and related experimental work is rather thin on the ground (Dullien et al, 1991). Associated core work on oil recovery by gravity segregation in low IFT systems has identified a crossover from

capillary-driven to gravity-stabilised imbibition which depends upon interfacial tension and core permeability (Schechter et al, 1991). This work also demonstrates how *gradients* in interfacial tension can also substantially affect flow behaviour (the so-called Marangoni effect).

(3) *Bubble Growth and Critical Gas Saturation* — An important feature of pressure depletion in oil reservoirs is the development of the gaseous phase via the nucleation and growth of gas bubbles. There is little understanding of this phenomenon and only a few investigations have been undertaken to study it (see, for example, Firoozabadi et al, 1992). One theory takes a thermodynamic approach to predict the appearance of a bubble (Kashchiev and Firoozabadi, 1993), whilst a second assumes that microbubbles already exist in cavities within the pore walls (Yang and Kim, 1988; Yortsos and Parlar, 1989). A micromodel study by Yousfi et al (1991) identified four steps in the kinetic growth of a bubble: pre-existence of microbubbles, growth and capillary trapping in wall roughness, site activation, and growth by diffusion. Comparisons between internal and external gas drives have been reported by Danesh et al (1987) and Kamath and Boyer (1993). No definitive theory yet exists which can completely model bubble growth, and much work remains to be done in this area if realistic estimates for critical gas saturations are to be predicted.

7.6 The Role of Network Modelling

Although 2-dimensional micromodels are indispensable for observing pore-scale behaviour, their quantitative contribution should not be over-estimated: in real porous media, the third dimension plays a major role in determining phase connectivity and residual saturations. However, by using microscopic observations as a rule base for *3-dimensional* network models, these fundamental studies can be incorporated at a practical reservoir engineering level.

Earlier chapters have discussed how network modelling has been utilised by the author in an attempt to discover the true nature of two-phase relative permeability and to explain how this is influenced by the various microscopic flow processes that occur in a porous medium. Many interesting results have emerged and many experimental observations have been successfully simulated. The work described next concentrates on extending the two-phase simulator to incorporate the simultaneous flow of oil, water, and gas. The accurate calculation of three-phase transport coefficients in terms of associated pore-scale parameters is an extremely difficult task. The purpose of the pore-scale simulations presented here is *not* to calculate these parameters for a specific rock, but once again to predict what the significant controls are on them from a microscopic viewpoint.

Successful modelling of two-phase flow has been made possible by recognising and implementing physically realistic displacement mechanisms. As outlined above, recent micromodel experiments using condensate/water/gas systems (Henderson et al, 1991) and laboratory studies of "conventional" oil/water/gas systems (Øren and Pinczewski, 1991; Dawe and Hawes, 1992; Kalaydjian, 1992) have identified much of the relevant three-phase pore-scale behaviour, and these observations form a basis for the latest three-phase models.

Although some of the programming elements required for unsteady-state three-phase studies are already firmly in place, the results presented in the following sections relate mainly to capillary-dominated three-phase flow in water-wet systems. This will enable the effects of spreading coefficient and connate water to be seen in isolation, away from the added confusion caused by unsteady-state dynamics.

7.7 The Effect of Connate Water and Spreading Co-efficient Upon Gas/Oil Capillary Pressure Measurements.

7.7.1 Introduction

Capillary pressure curves are of great importance in the field of reservoir engineering for two main reasons. Firstly, they help to characterise transition zones within the associated reservoir, and secondly, they are used in reservoir simulators as constitutive pressure relationships. Ideally, such curves should be measured using reservoir fluids and reservoir-state core at reservoir conditions — in practice, however, this is seldom the case. Imposed limitations on both time and cost often mean that indirect mercury injection tests have to be conducted using cleaned core at ambient conditions. The mercury-air data is then scaled using the Young-Laplace equation, yielding an approximate water/oil, gas/oil, or gas/water curve for use in subsequent simulation studies.

The question arises as to whether such scaled curves are truly representative of reservoir conditions. Although early work suggested that indirect measurements *were* acceptable for two-phase systems (Leverett, 1941; Dumoré and Schols, 1974), doubts have recently been raised (Da Silva, 1989). Indeed, current research suggests that the Young-Laplace equation itself may be inappropriate for scaling low IFT systems (Christoffersen et al, 1992).

If a third phase is present within the porespace (a scenario which is often the case in real reservoirs), the general applicability of scaled measurements is even more doubtful. Recent experimental work by Kalaydjian and Tixier (1991) and Longeron et al (1993) has highlighted some of the inconsistencies. In particular, they have discussed the important role played by the spreading coefficient during gas/oil drainage experiments in systems containing connate water. These observations have motivated the present study, which utilises network

modelling techniques to examine the combined effects of connate water, spreading coefficient and pore topology more closely.

7.7.2 Simulation Details

The precise details of the basic network model have been described in earlier chapters and will not be given here. In this section, the earlier 3-dimensional model has been extended further to incorporate variable co-ordination number and variable pore geometry options (Figure 7.5). Although the model is capable of simulating displacements at any given rate, the capillary pressure simulations described below have been carried out at ultra low rates: such conditions are characteristic of the reservoir in regions well away from the wellbore. A variety of network configurations has been examined, and gas/oil displacements in the presence of connate water have been conducted under both positive and negative spreading conditions (see Figure 7.6). If $S<0$ oil can only escape if it is *hydraulically* connected to the outllet, whereas $S>0$ also permits film-flow of oil around a pathway of gas bubbles.

Simulations were carried out in the following order:

(1) Capillary-dominated gas/oil drainage flood without connate water (base case).

(2) Capillary-dominated oil/water drainage flood (to get connate water saturation).

(3) Capillary-dominated gas/oil drainage flood in the presence of connate water ($S<0$).

(3') Capillary-dominated gas/oil drainage flood in the presence of connate water ($S>0$).

Details are summarised in Table 7.5 and some sample two-dimensional simulations are shown in Figures 7.7 and 7.8. These clearly demonstrate the dramatic differences between displacements characterised by positive and negative spreading coefficients.

7.7.3 Results and Discussion

The simulated three-dimensional capillary pressure curves are shown in Figures 7.9 and 7.10 The effects of spreading coefficient, pore geometry, co-ordination number and connate water are self-evident. Various combinations of these clearly give rise to a wide range of flow behaviour and results serve to underline just how diverse three-phase flow processes can be. Before attempting to interpret any contradictory experimental work, however, it is important to first examine the data obtained from the simulations more closely.

Begin by considering what is actually being measured during a two-phase capillary pressure experiment: namely, the pressure difference between the displacing and displaced fluid, and the volume of injected fluid. Which pore-scale parameters affect each measurement? The first depends upon interfacial tension, contact angle, and the distribution of throat diameters, whilst the second is mainly governed by the distribution of elemental pore volumes within the sample. Interfacial tension and contact angle have been kept constant in this work (their effect is well understood, except possibly in low IFT systems), and so the main parameters governing the structure of the model capillary pressure curves would appear to be the "pore size distribution functions" associated with throat diameter and elemental pore volume. This is indeed the main reason for the differences between Figures 7.9 and 7.10 — the slopes of the curves in the former are less than those in the latter mainly because of the different pore geometries associated with each.

The physical parameters listed above are not the only things influencing capillary pressure measurements, however. There is another important issue that must be considered; namely, *accessibility*. The concept of accessibility is summarised in Appendix A. During capillary pressure measurements, some of

the larger pores cannot be accessed immediately by the invading phase because they are effectively *shielded* by smaller pores which can only be entered at higher pressures. Hence, only a fraction of the larger pores are initially accessible to the invading phase. As more and more pores become invaded, however, accessibility becomes less of an issue (in well-connected systems), as the dendritic structure of the invading phase allows it to gain access to almost all "available" pores. Hence, in well-connected systems, accessibility mainly affects the early part of a displacement. In less well-connected systems, however, this is no longer the case. Accessibility now plays a major role *throughout* a displacement, and can alter capillary pressure curves dramatically (Figure 7.11).

Interpreting the three-phase curves of Figures 7.9 and 7.10 is quite straightforward once accessibility issues have been considered. It is important to recognise, however, that accessibility to the invading phase can be restricted in a number of subtle ways. The *effective connectivity* of the gas/oil system can be lowered by:

(1) a reduction in the physical co-ordination number of the network.

(2) the presence of connate water.

(3) denying gas access to any oil-filled pores that are not hydraulically connected to the outlet (i.e. disallowing oil flow through films).

Larger residual oil saturations are the natural result of a lowering in effective connectivity: compare the residual saturations obtained under positive and negative spreading conditions, for example. Conversely, the larger the effective connectivity of a system, the more efficient the subsequent displacement.

7.7.4 Comparisons with Published Data

To date, there appears to be very little published work concerning the systematic study of three-phase capillary pressure curves. This is not too

surprising, perhaps, when one considers the high costs associated with such measurements, yet the contradictory evidence discussed below again demonstrates the need for further investigation.

One of the first series of experiments was carried out by Dumoré and Schols (1974), and their results have been reproduced in Figure 7.12. Their rather surprising conclusion, was that neither connate water nor the value of the spreading coefficient greatly affect the shape of gas/oil drainage curves. Even more surprising, was the fact that very low residual oil saturations were obtained *even in a negative spreading system.* No suggestions were given as to why this should be the case. More recent work by Longeron et al (1993) also describes cases where almost all of the oil has been recovered from negative spreading systems, but once again no explanation is given. Moreover, their experimental capillary pressure curves exhibit large hysteresis effects when connate water is present within the sample (Figure 7.13). The reasons for this also remain a mystery, and the simulation results presented here would tend to disagree with such findings.

The situation becomes even more confused when presented with associated work by Kalaydjian and Tixier (1991), whose results contradict those of the other studies but agree well with the simulated trends presented here: they report a definite increase in residual oil as the spreading coefficient becomes more negative (Figure 7.14).

The three-phase network modelling approach described in this chapter is still in the development stage and is constantly being updated as new pore-scale physics become available. The final model should produce a clearer understanding of a variety of three-phase flow processes.

7.8 Concluding Remarks on Three-Phase Flow

This chapter set out to describe the current confusion concerning three-phase flow experiments and to stress the need for a structured, focussed research programme. By describing a variety of pore-scale phenomena, it has hopefully gone some way in clarifying why so much experimental work appears inconsistent and contradictory. It has also shown how current analytical methods take no account of such phenomena and how many are no more than empirical correlations.

Every year, more and more three-phase experiments are reported in the literature; every year, the situation becomes more and more confusing. By integrating micromodel visualisation, network modelling and coreflood work, there is perhaps an opportunity for a clearer, more interpretable picture to emerge.

Table 7.1 The Effect of Contacting History Upon Micromodel Wettability (After Idris, 1990)

Contacting History	Resulting Wettability of Untreated Glass Micromodel	Resulting Wettability of Silane-Treated Glass Micromodel
Water - Oil - Gas	Water-Wet	Mixed-Wet
Water - Gas - Oil	Water-Wet	Mixed-Wet
Oil - Water - Gas	Oil-Wet	Oil-Wet
Oil - Gas - Water	Oil-Wet	Oil-Wet
Gas - Water - Oil	Water-Wet	Mixed-Wet
Gas - Oil - Water	Mixed-Wet	Oil-Wet

Table 7.2 Possible Saturation Histories During Three-Phase Displacements (After Saraf et al, 1982)

Regime	Gas Saturation	Oil Saturation	Water Saturation	Field Example
1	Increasing	Decreasing	Constant	Gas injection at connate water
2	Increasing	Constant	Decreasing	Gas injection into watered-out reservoir
3	Decreasing	Increasing	Constant	Oil migration into gas-cap at connate water
4	Decreasing	Constant	Increasing	Water injection at residual oil into reservoir below the bubble point
5	Constant	Decreasing	Increasing	Waterflood of oil reservoir with trapped gas
6	Constant	Increasing	Decreasing	Oil migration with trapped gas below critical saturation
7	Increasing	Decreasing	Decreasing	Gasflood
8	Decreasing	Increasing	Decreasing	Oil migration with trapped gas above critical saturation
9	Decreasing	Decreasing	Increasing	Waterflood of oil reservoir with mobile gas
10	Decreasing	Increasing	Increasing	Intermediate regime during WAG process (oil bank formation)
11	Increasing	Decreasing	Increasing	WAG process
12	Increasing	Increasing	Decreasing	Oil and gas migration into aquifer
13	Constsnt	Constsnt	Constsnt	Steady-state flow

	One phase saturation constant
	Two phase saturations decreasing
	Two phase saturations increasing
	Steady-state regime

Table 7.3 Chronological Listing Of Three-Phase Relative Permeability Experiments.

Ref. No.	Date	Author	Rock Properties				Fluids			Exptal. Method	No. Of Data Pt.	Sat. History	Rel. Perm Dependency			Isoperms		
			Type	Poro (%)	k mD	Wett.	Water	Oil	Gas				krw	kro	krg	Water	Oil	Gas
146	1941	Leverett and Lewis	Uncons. sandstone	42	5000 to 160000	Water-wet	0.24M NaCl	Kerosene	N_2	Dyn. SS	64	w/o prim. dr.	Sw	All	All	Linear	Concave	Convex
35	1951	Caudle et al	Cons. sandstone	23	25	Oil-wet	N/R	Oil	Air	SS	N/R	w/o/g IDI	All	All	All	Concave	Concave	Convex
52	1956	Corey et al	Berea	N/R	N/R	Water-wet	CaCl Brine	N/R	N/R	SS (Hassler)	62	w/o/g DDI	Sw	All	Sg	N/R	Concave	Linear
185	1956	Reid	Uncons. sandstone	35	31000	Water-wet	0.1M NaCl	Diesel	Air	SS	98	w/o prim. dr.	All	All	All	Concave	Convex	Concave
209	1962	Snell	Uncons. sandstone	35	7100	Water-wet	5g/l NaCl	Diesel	Air	SS	250	w/o prim. dr.	All	All	All	Concave	Convex	Convex
199	1966	Saraf	Berea	20	275	Water-wet	0.2M NaCl	Soltrol 130	Air	USS	70	w/o/g DDI	Sw	So	Sg	Linear	Linear	Linear
68	1966	Donaldson and Dean	Berea, Limestone	19 11	N/R 42.5	Water-wet	0.1M NaCl	Soltrol	Air	USS	120	w/o/g DDI	All	All	All	Concave	Concave	Convex
198	1967	Saraf and Patt	Boise sandstone	26	1450	Water-wet	Heavy water	Kerosene	N_2	SS	81	w/o/g DDI	Sw	All	Sg	N/R	Convex	Linear
202	1970	Schneider and Owens	Torpedo sandstone	24	370	Water-wet	Brine	H-C Fraction	N_2	SS	N/R	w/o/g DDI IDD	Sw	All	All	Linear	N/R	N/R
222	1982	van Spronsen	Berea, Weeks ss	21.3 26	480-600 21.3-26	W-wet Oil-wet	Water and glycol	N/R	CO_2	SS	N/R	N/R	All	All	N/R	Concave	Concave	N/R
197	1982	Saraf et al	Fired Berea	23	510-580	Water-wet	Distilled water	Non-polar oil	N_2	SS and USS	N/R	w/o/g DDI	Sw	All	Sg	Linear	Concave	Linear
174	1988	Oak et al	Fired Berea	N/R	160-210	Water-wet	N/R	N/R	N_2	SS	N/R	w/o/g DDI, IID	Sw	All	All	Linear Linear	N/R Linear	N/R Linear
173	1990	Oak	Fired Berea	N/R	200, 800, 1000	Water-wet	5%wt NaCl+ 0.5% CaCl	Mineral or dodecane	N_2	SS	9000	8 Cases	Sw	All	Sg	Linear	N/R	Convex
170	1990	Narahara et al	Berea	21.5	635-860	W-wet and Mixed	2.5% NaCl+ CaCl	Refined white oil	Helium Air	USS	N/R	g/o prim. drain.	Sw	So	Sg	N/R	N/R	N/R
72	1990	Dria et al	Dolomite	20.2	24	Water-wet	2%wt CaCl	Decane	CO_2	SS	23	w/o/g DDI	Sw	So	Sg	N/R	N/R	N/R
157	1991	Marek et al	Limestone	23.4	N/R	Mixed-wet	5000ppm CaCl	dodecane /headeca ne	N_2	SS	10	w/o/g IDI	N/R	N/R	N/R	N/R	Convex	N/R

Table 7.4 Chronological Listing Of Three-Phase Relative Permeability Models.

REF	DATE	AUTHOR	FORMULA
52	1956	Corey et al	$K_{ro} = \{(S_l - S_w)^3 / (1 - S_{lr})^4\} - (S_w + S_l - 2S_{lr})$
169	1961	Naar and Wygal	$K_{ro} = S^{*3}_{of}(S^*_{of} + 3S^*_{fw})$ $S^*_{of} = (S_o - S_{ob}) / (1 - S_{wi})$ $S^*_{fw} = ((S_w - S_{wi}) / (1 - S_{wi})) + S_{ob}$ $S_{ob} = (1 - S_{wi}) \int_0^{1-a} x\,dx$ $\quad a = (1 - S_w) / 1 - S_{wi}$
139	1968	Land	-- if Sw increases at the expense of So while the Sg remains constant $k_{ro} = S_{of}^3(2S_w + S_{of})$ -- If all gas contained by the porous media is trapped : $k_{ro} = S^{*3}_{of}(2S^*_w + S^*_{of}) - S^{*2}_{of}\{S^{*2}_{gr} + 2/C\,(S^*_{gr} + 1/C \ln S_{gr})\}$
214	1970	Stone's Method I	$K_{ro} = S^*_o \beta_w \beta_g$ $\quad \beta_w = K_{row} / (1 - S^*_w)$ $\quad \beta_g = K_{rog} / (1 - S^*_g)$ $S^*_o = (S_o - S_{om}) / (1 - S_{wc} - S_{om})$ $\quad S^*_w = (S_w - S_{wc}) / (1 - S_{wc} - S_{om})$ $S^*_g = S_g / (1 - S_{wc} - S_{om})$
215	1973	Stone's Method II	$K_{ro} = (K_{row} + K_{rwo})(K_{rog} + K_{rgo}) - (K_{rwo} + K_{rgo})$
65	1976	Dietrich and Bondor	$K_{ro} = ((K_{row} + K_{rwo})(K_{rog} + K_{rgo}) / K_{rocw}) - (K_{rwo} + K_{rgo})$
59	1976	Hirasaki	$K_{ro} = (K_{row} K_{rog}) - S_g (1 - K_{row})(1 - K_{rog})$
59	1977	Nolen	$K_{ro} = K_{rocw}\{(K_{row}/K_{rocw} + K_{rw})(K_{rog}/K_{rocw} + k_{rgo}) - (K_{rw} + Kr_g)\}$
13	1979	Aziz and Settari	- For Stones method I : $K_{ro} = S^*_o (K_{row} + K_{rog}) / K_{rocw} (1 - S^*_w)(1 - S^*_g)$ - For Stones method II : $K_{ro} = \{(K_{row} + \alpha K_{rwo})(K_{rog} + \alpha K_{rgo}) - \alpha(K_{rwo} + K_{rgo}\}$ $\quad \alpha = K_{rocw} / K$

Table 7.4 (Continued)

87	1979	Fayers and Matthews	- For Stones Method I : $S_{om} = \alpha S_{orw} + (1 - \alpha) S_{org}$ $\alpha = 1 - (S_g / (1 - S_{wc} - S_{org}))$ - In the presence of trapped gas :water -wet sandstone : $S_{om} = S_{orw} - 0.5 * S_g$
2	1984	Aleman	$K_{ro} = K_{ro}(I)^{-\Delta}$ $K_{ro}(I)$ = Kro predicted by Stone's I $\Delta = \frac{S^*_o (K^*_{row} - 1)(k^*_{rog} - 1)(K^*_{row} K^*_{rog} - K^*_{rwo} K^*_{rgo})}{(k^*_{rgo} -)(K^*_{row} - K^*_{rwo}) - (K^*_{row} - 1)(K^*_{rgo} - K^*_{rog})}$
59	1986	Aleman	- For Stones method I : $S_{om} = S_{orw} \{ (S_w - S_{wc}) / (1 - S_{wc} - S_{orw}) \}^{\alpha} + S_{org} \{ S_g / (1 - S_{wc} - S_{org}) \}^{\beta}$
86	1987	Fayers	- For Stones Method I : $S_{om} = S_{orw} - \{(S_{orw} - S_{org}) / ((1 - S_{wc} - S_{org}))S_g - \alpha \{(1 - S_{wc} - S_{org})S_g - S_g^2\}$ $\alpha = \{ a - (S_{orw} - S_{org}) / (1 - S_{wc} - S_{org}) \} / (1 - S_{wc} - S_{org})$ $0 < a < 0.5$
181	1987	Parker et al	$K_{ro} = S^*_o{}^{0.5} \{ (1 - S^*_w{}^{1/m})^m - (1 - S^*_t{}^{1/m})^m \}^2$
14	1989	Baker	$K_{ro} = \{ (S_w - S_{wr}) K_{row} + (S_g - S_{gr}) K_{rog} \} / \{ (S_w - S_{wr}) + (S_g - S_{gr}) \}$
72	1989	Pope	$K_{ro} = K_{rocw} \{ a S_o^{\alpha} (1 - S_w)^{\beta} + (1 - a) S_o^{\gamma} (1 - S_g)^{\delta} \}$ $S_o = (1 - S_w - S_g - S_{or}) / X$ $S_w = (S_w - S_{wr}) / X$ $S_g = (S_g - S_{gr}) / X$ $X = 1 - S_{wr} - S_{gr} - S_{or}$
137	1989	Lake	$K_{ro} = K^o_{ro} \{ (S_o - S_{or}) / (1 - S_{wr} - S_{gr} - S_{or}) \}^{e_o}$ $K^o_{ro} = K^o_{rg} + G (K^o_{rw} - K^o_{rg})$ $e_o = e_g + G (e_w - e_g)$: $S_{or} = S_{gr} + G (S_{wr} - S_{gr})$: e_i=Exponent of phase i $G = (S_g - S_{gr}) \{ 1 - (S_w - S_{wr}) \} / \{ (S_g - S_{gr}) + (S_w - S_{wr}) \}$
59	1989	Corey-type	$K_{ro} = K^o_{ro} \{ \frac{S_o - S_{or}}{1 - S_{wr} - S_{gr} - S_{or}} \}^{e_o}$ where $S_{or} = F(S_g, S_w)$
157	1991	Marek et al	$K_{ro} = (S_{wf} / S_{wf} + S_g) K_{row}(S_{oew}) + (S_g / S_{wf} + S_g) K_{rog}(S_{oeg})$ $S_{oew} = S_o + S_w S^n_{wf} S_g^{2-n} / (S_{wf} + S_g)$ $S_{oeg} = S_o + S_g S^n_{wf} S_g^{2-n} / (S_{wf} + S_g)$

Table 7.5 Details of Simulation Runs and Residual Oil Saturations

Gas/Oil Drainage Run	Average Coordination Number (z)	S_{wi}	Spreading Coefficient	Pore Geometry	S_{or}
1	6	0.0	N/A	Cylindrical	0.045
2	6	0.045	-ve	Cylindrical	0.135
3	6	0.045	+ve	Cylindrical	0.0
4	4	0.0	N/A	Cylindrical	0.111
5	4	0.111	-ve	Cylindrical	0.334
6	4	0.111	+ve	Cylindrical	0.007
7	2.8	0.0	N/A	Cylindrical	0.27
8	2.8	0.27	-ve	Cylindrical	0.46
9	2.8	0.27	+ve	Cylindrical	0.033
10	6	0.0	N/A	Biconical	0.22
11	6	0.22	-ve	Biconical	0.231
12	6	0.22	+ve	Biconical	0.0
13	4	0.0	N/A	Biconical	0.331
14	4	0.331	-ve	Biconical	0.305
15	4	0.331	+ve	Biconical	0.011
16	2.8	0.0	N/A	Biconical	0.456
17	2.8	0.456	-ve	Biconical	0.327
18	2.8	0.456	+ve	Biconical	0.026

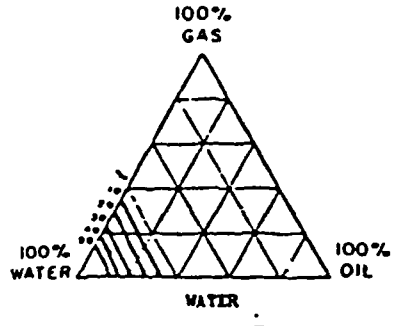

Leverett and Lewis (1941)

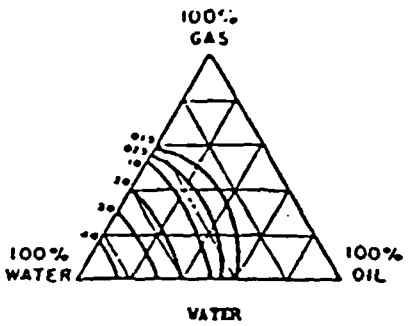

Caudle et al (1951)

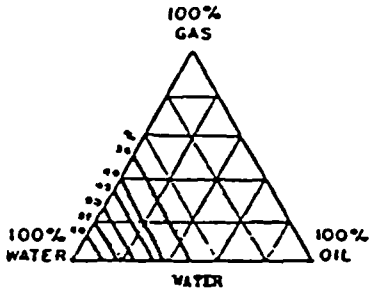

Corey (1954)

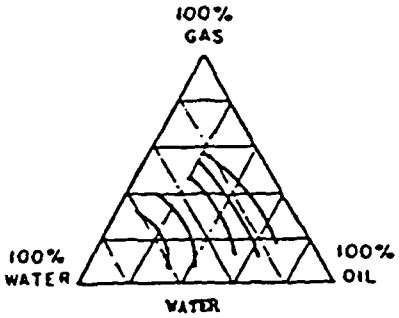

Reid (1956)

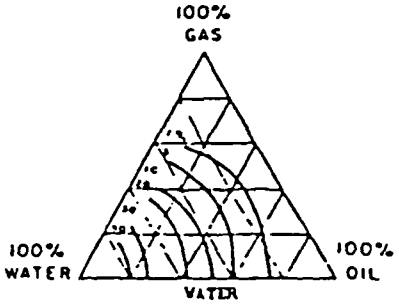

Snell (1962)

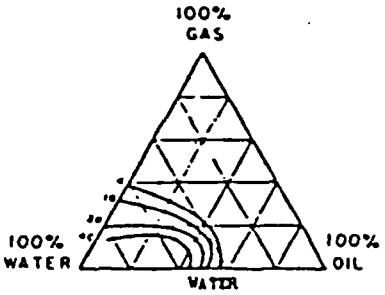

Donaldson and Dean (1966)

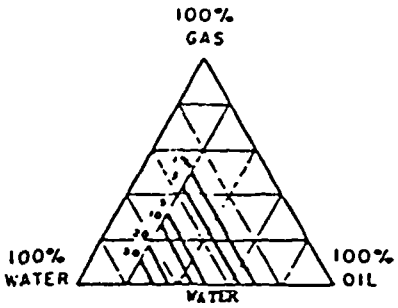

Saraf and Fatt (1967)

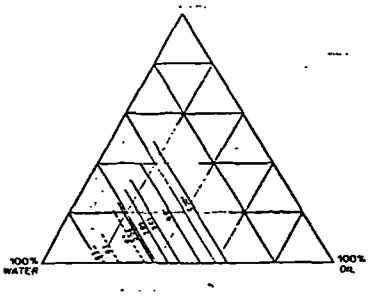

Saraf et al (1982)

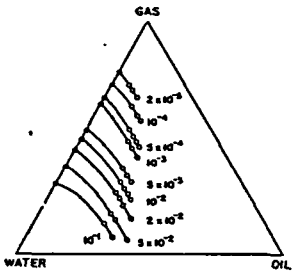

Van Spronsen (1982)

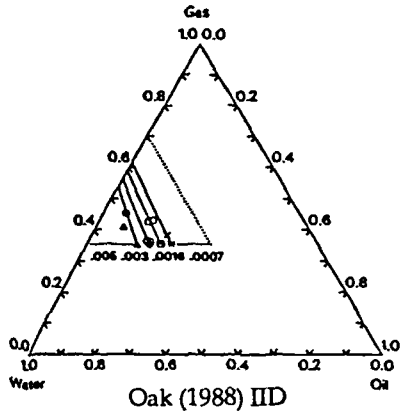

Oak (1988) IID

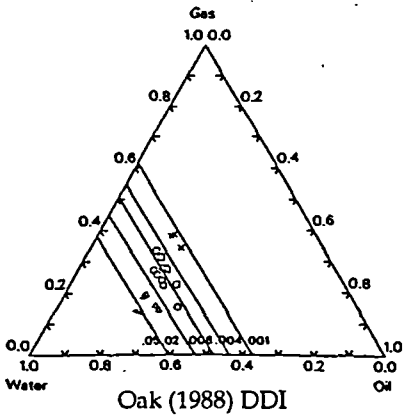

Oak (1988) DDI

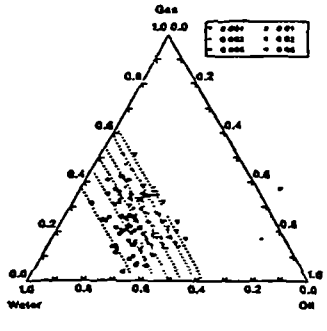

Oak (1990)

Figure 7.1 A collection of water isoperms from the current literature.

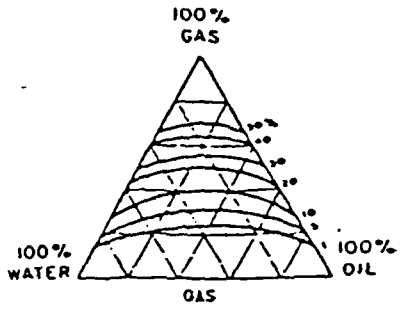

Leverett and Lewis (1941)

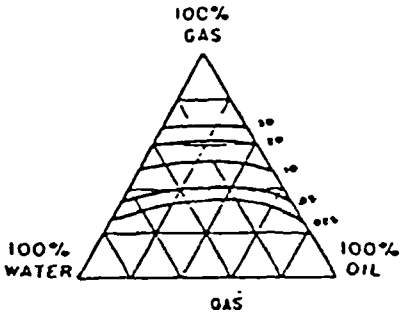

Caudle et al (1951)

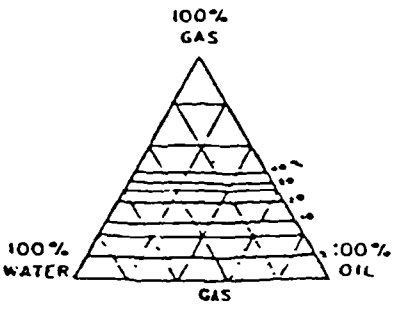

Corey (1954)

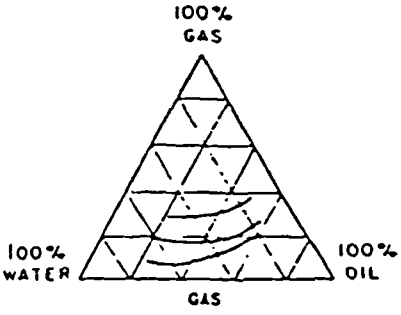

Reid (1956)

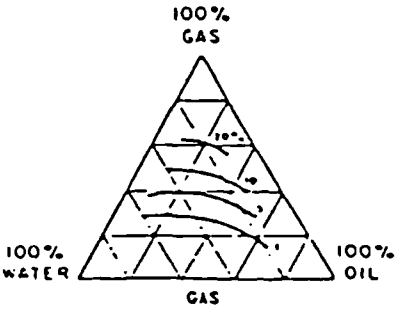

Snell (1962)

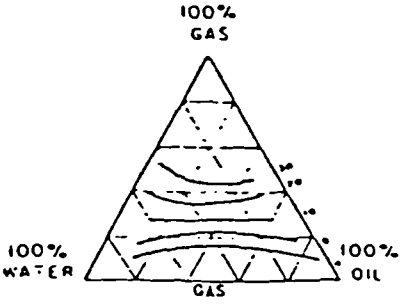

Donaldson and Dean (1966)

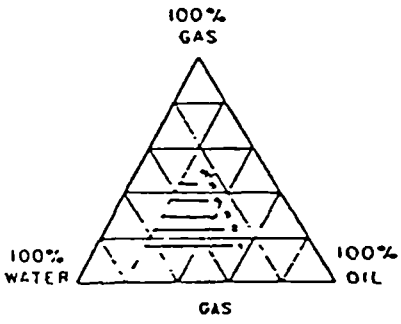

Saraf and Fatt (1967)

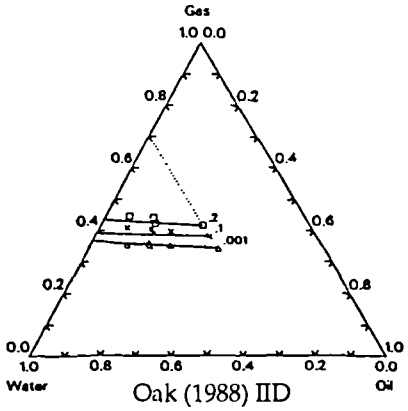

Oak (1988) IID

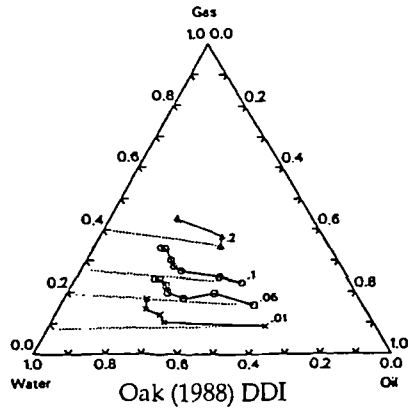

Oak (1988) DDI

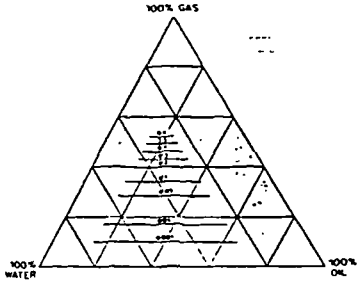

Saraf et al (1982)

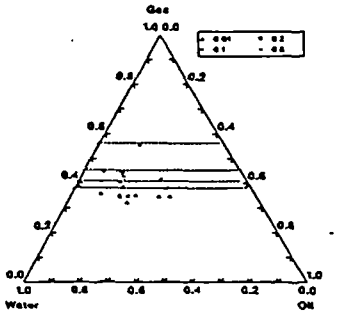

Oak (1990)

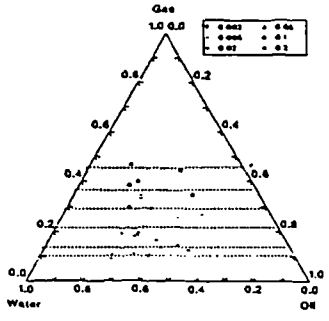

Oak (1990)

Figure 7.2 A collection of gas isoperms from the current literature.

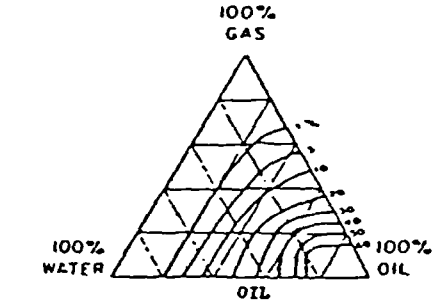

Leverett and Lewis (1941)

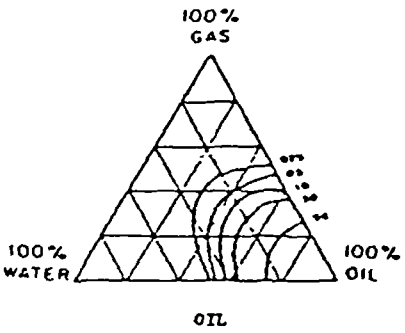

Caudle et al (1951)

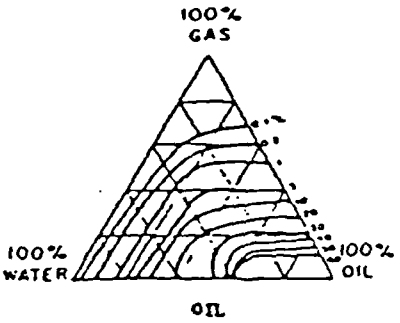

Corey (1954)

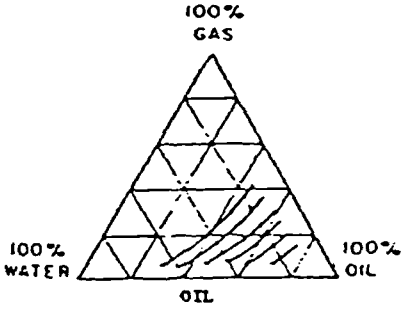

Reid (1956)

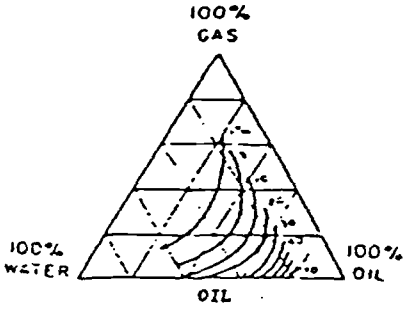

Snell (1962)

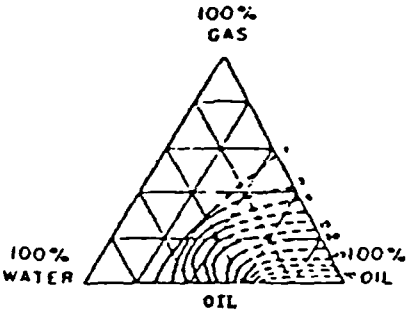

Donaldson and Dean (1966)

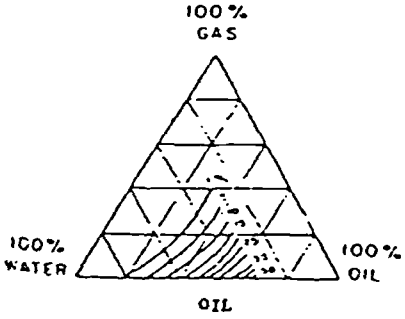

Saraf and Fatt (1967)

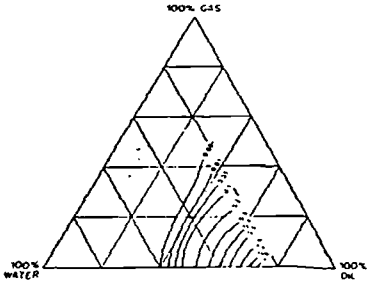

Saraf et al (1982)

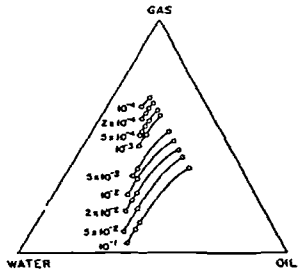

Van Spronsen (1982)

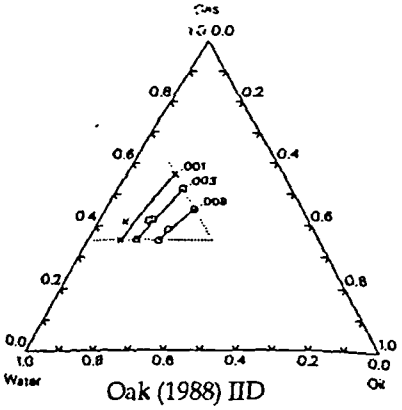

Oak (1988) IID

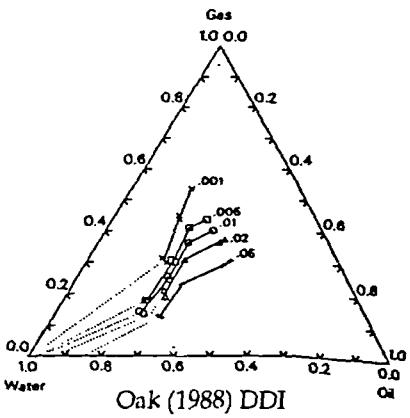

Oak (1988) DDI

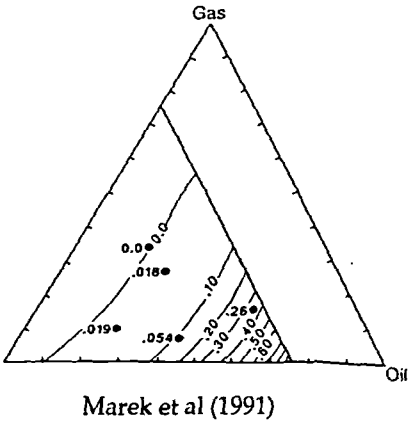

Marek et al (1991)

Figure 7.3 A collection of oil isoperms from the current literature.

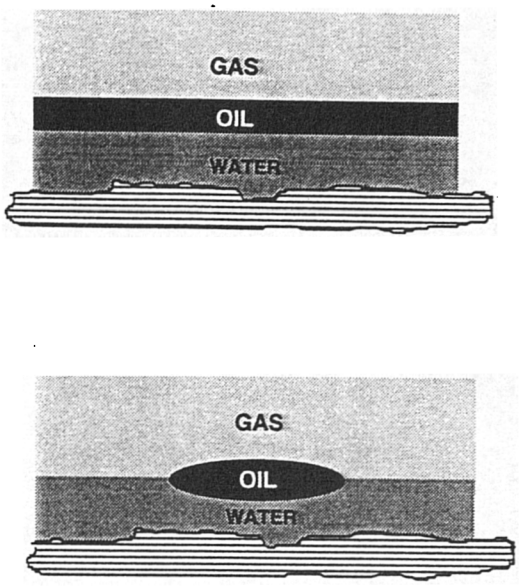

Figure 7.4 Fluid hierarchies at the pore-scale: (a) positive spreading coefficient, (b) negative spreading coefficient.

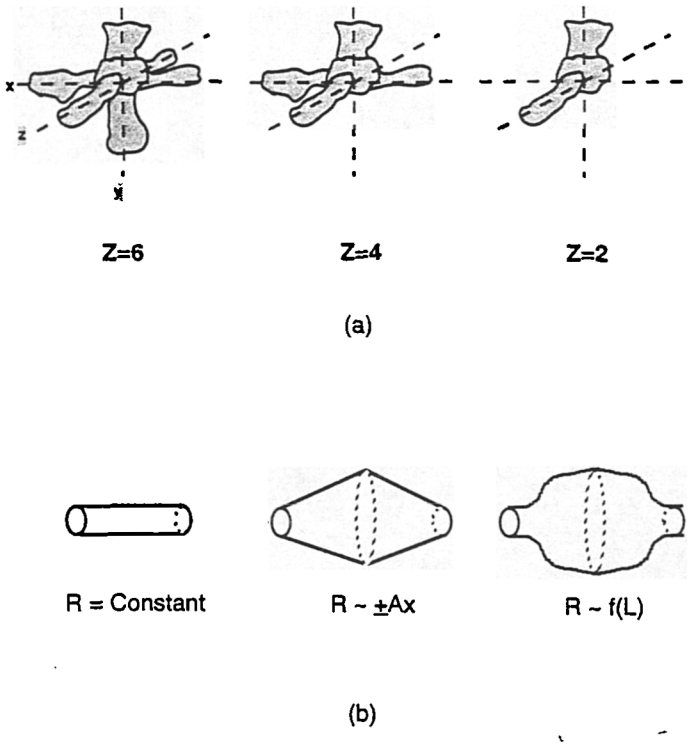

Figure 7.5 (a) Various co-ordination numbers, (b) different pore geometries (cylindrical, biconical, general).

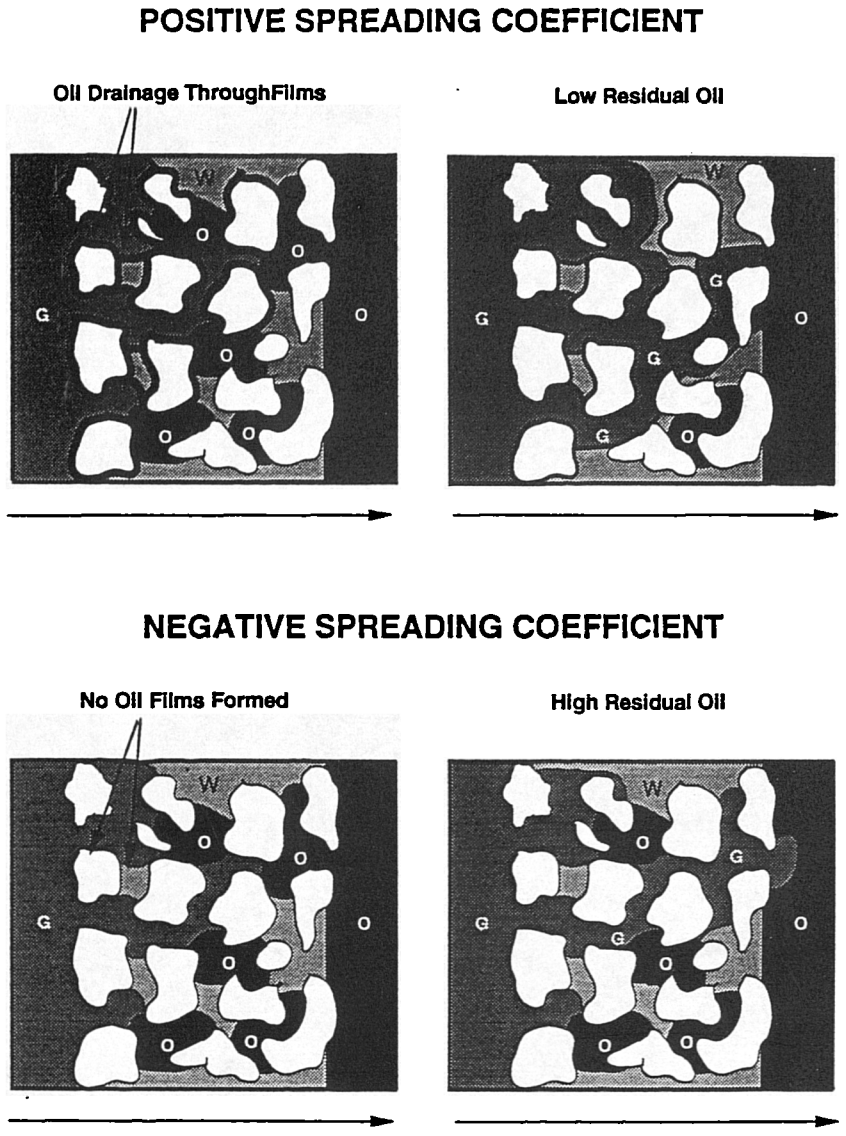

Figure 7.6 Schematic showing how oil films can improve displacement efficiency in a positive spreading system.

(a)

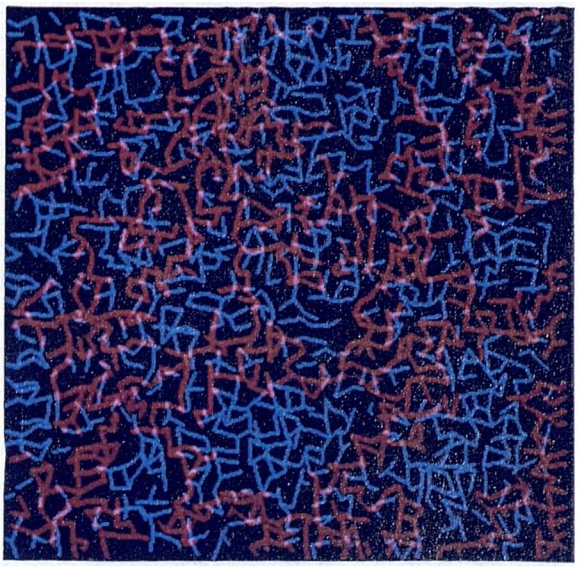

(b)

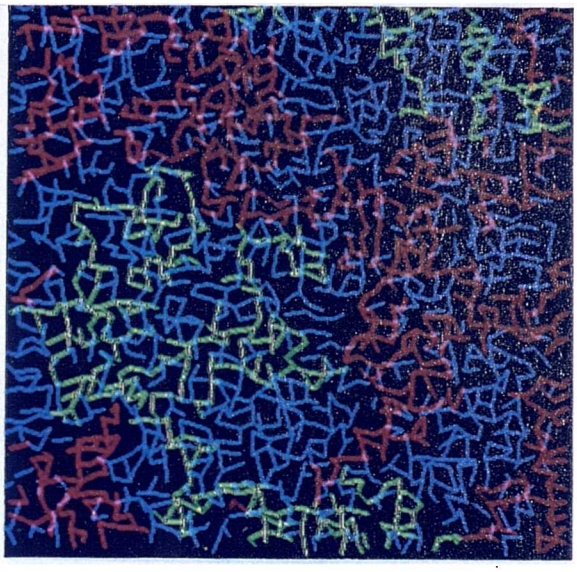

(c)

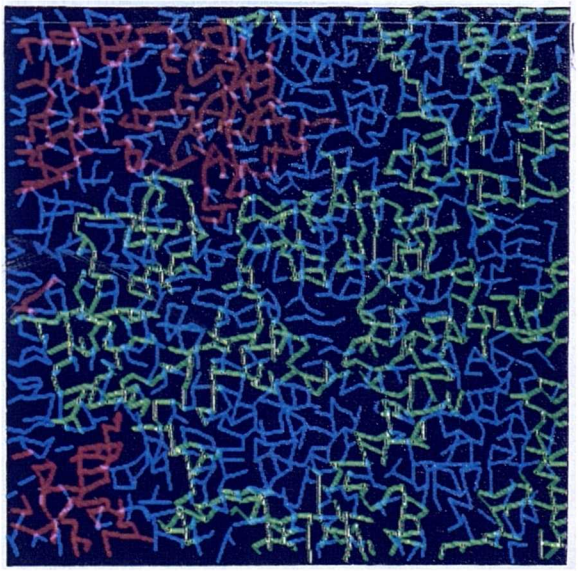

Figure 7.7 Series of network simulations of external gas drive with S>0 (blue-water, red-oil, green-gas): (a) primary oil-water drainage, (b) external gas drive up to breakthrough, (c) end of gas drainage (red oil clusters remain trapped).

(a)

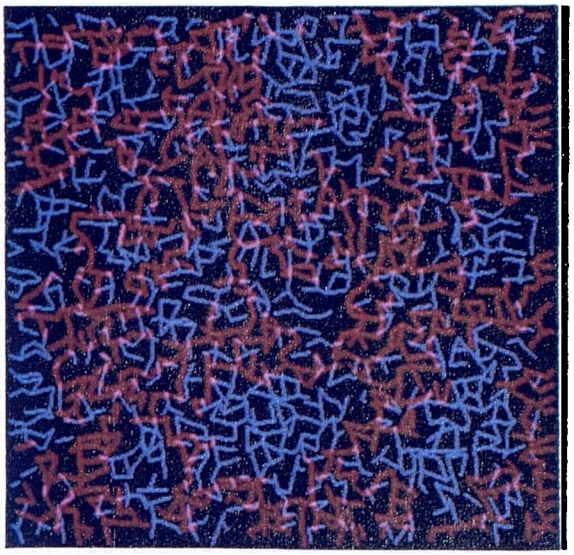

(b)

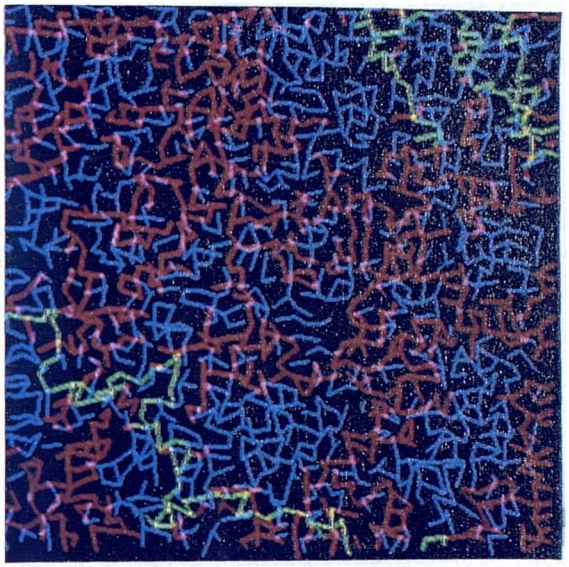

(c)

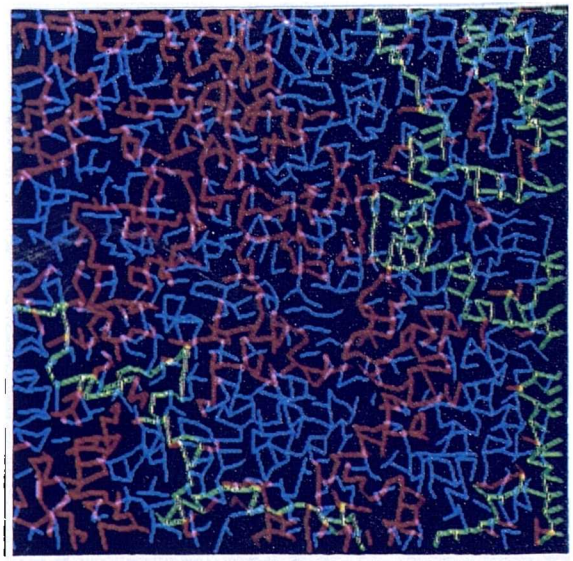

Figure 7.8 Series of network simulations of external gas drive with S<0 (blue-water, red-oil, green-gas): (a) primary oil-water drainage, (b) external gas drive up to breakthrough, (c) end of gas drainage (large number of red oil clusters remain trapped).

(a)

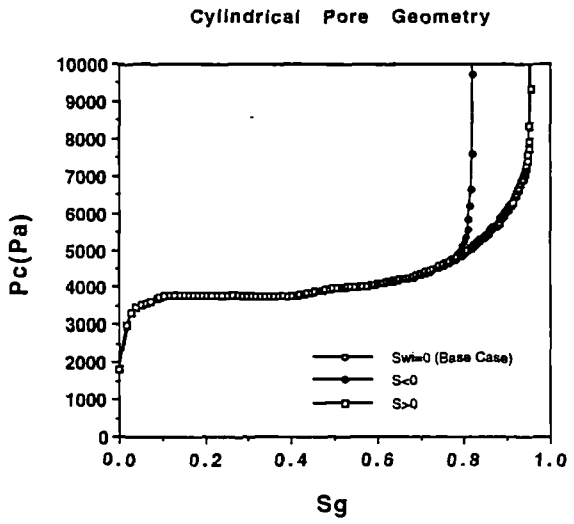

(b)

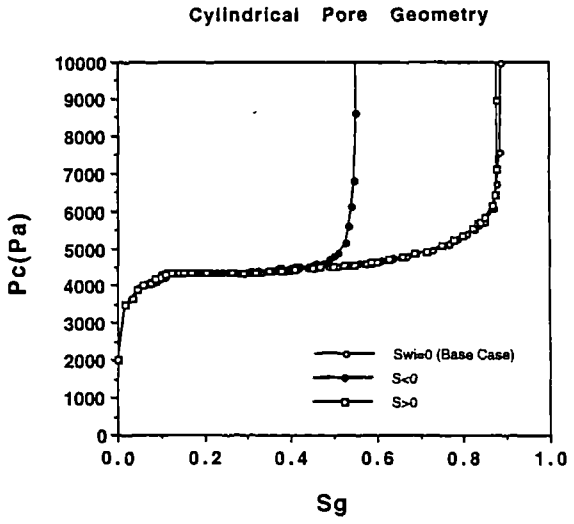

(c)

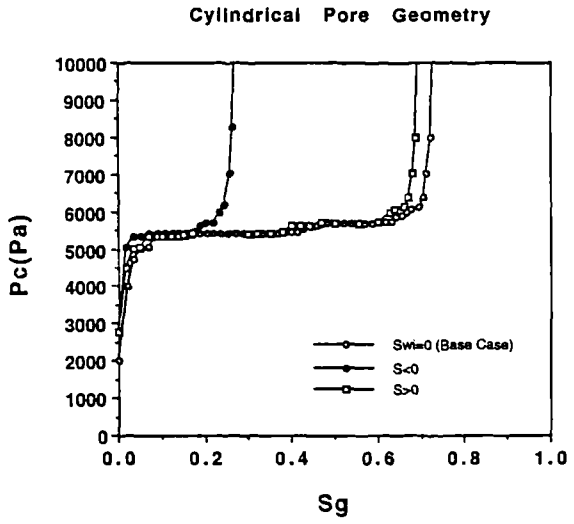

Figure 7.9 Simulated capillary pressure curves for a variety of co-ordination numbers, showing the effects of connate water and spreading coefficient **(cylindrical pore geometry)**: (a) z=6, (b) z=4, (c) z=2.8.

(a)

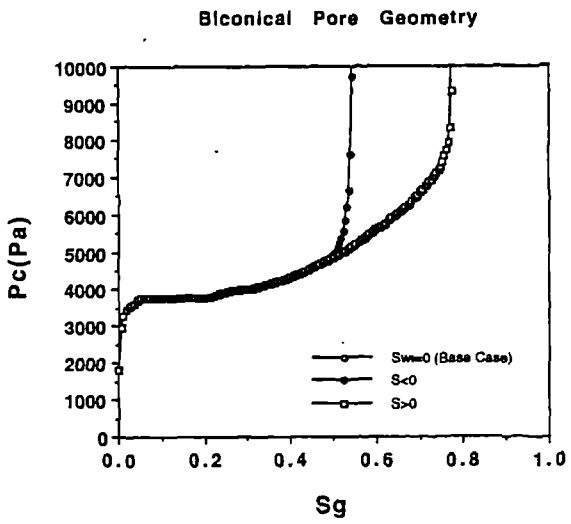

(b)

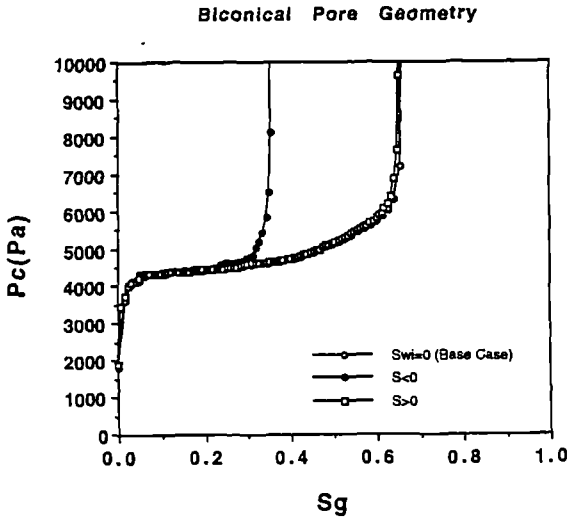

(c)

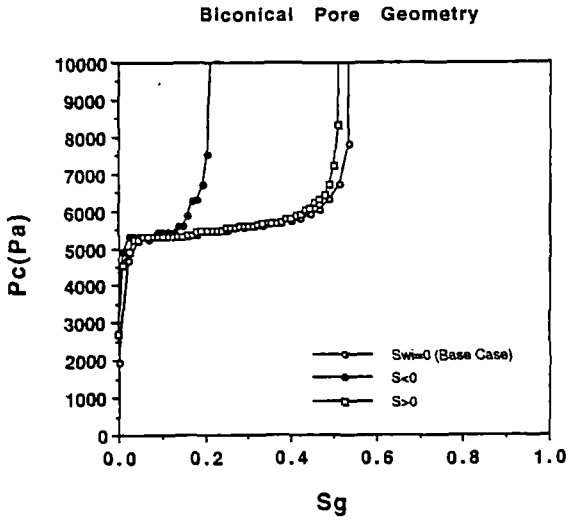

Figure 7.10 Simulated capillary pressure curves for a variety of co-ordination numbers, showing the effects of connate water and spreading coefficient **(biconical pore geometry)**: (a) z=6, (b) z=4, (c) z=2.8.

(a)

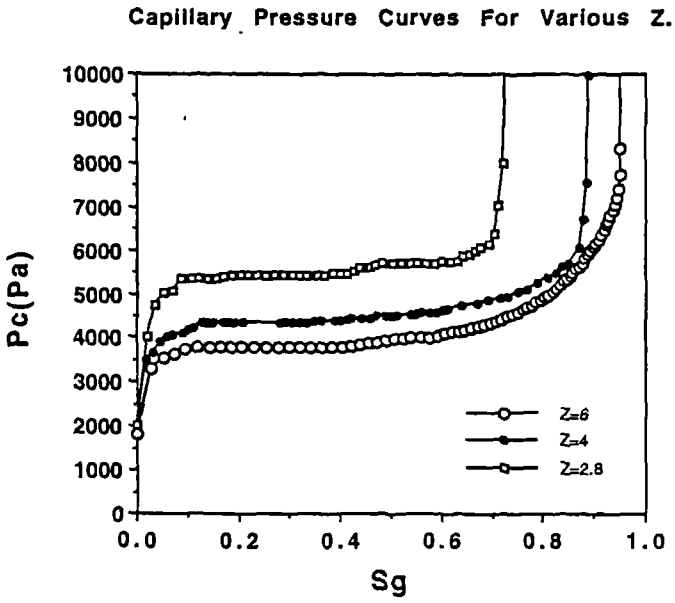

(b)

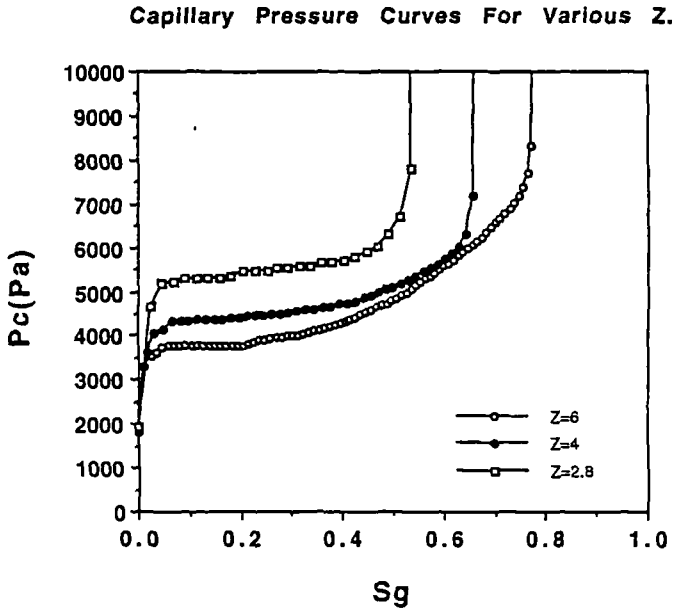

Figure 7.11 Effect of z upon gas/oil capillary pressure curves (S_{wi}=0): (a) cylindrical pore geometry, (b) biconical pore geometry.

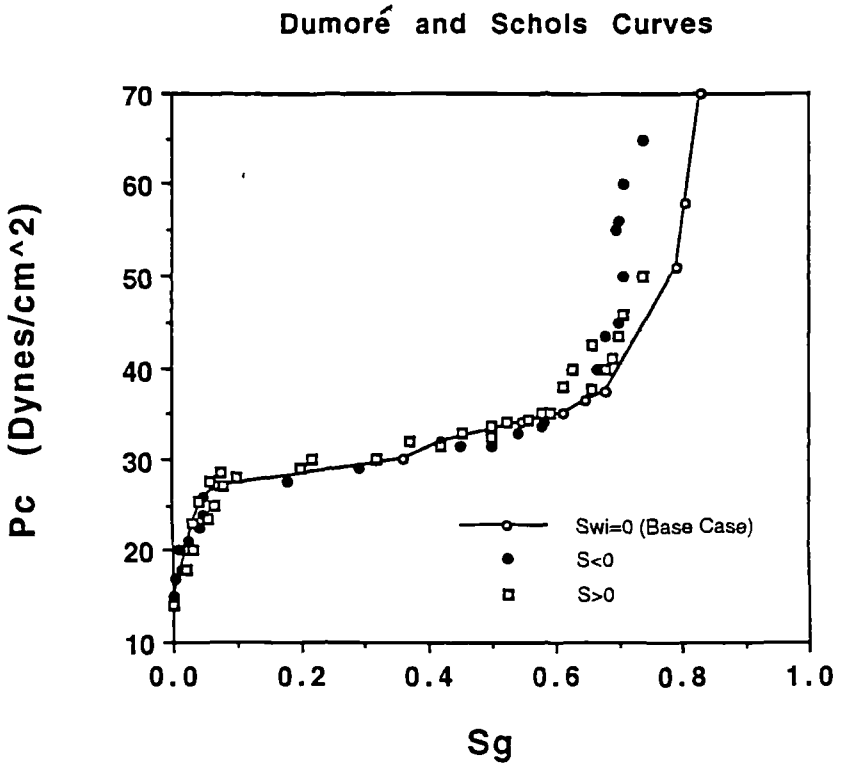

Figure 7.12 Experimental data of Dumoré and Schols (1974) showing the effects of connate water and spreading coefficient upon gas/oil capillary pressure curves. Bentheim cores and kerosene/Ondina17/water/air used.

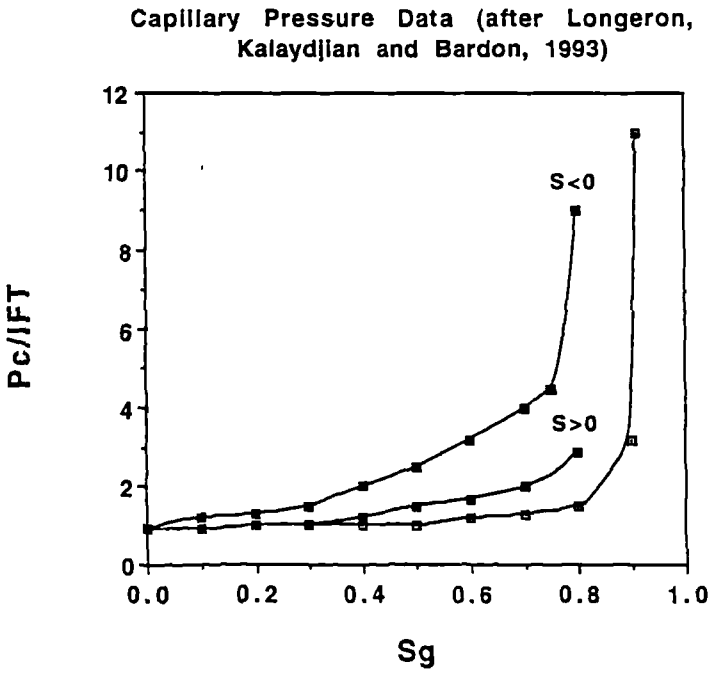

Figure 7.13 Capillary pressure data from Longeron et al (1993). Clashach cores and *n*-heptane/methane mixtures used.

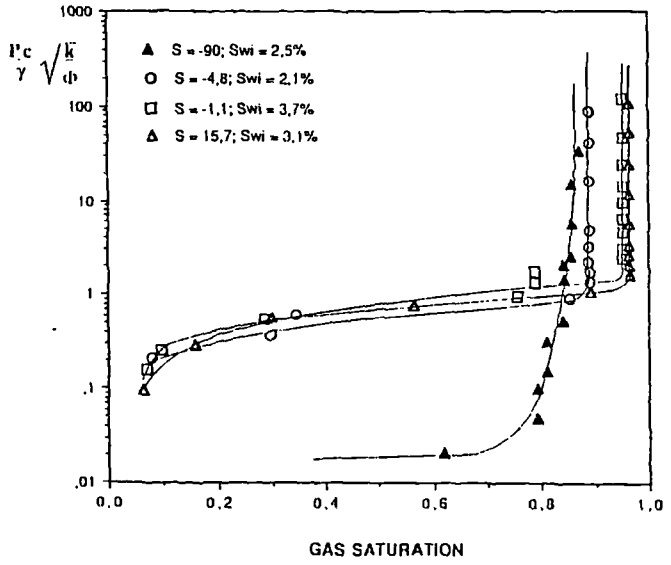

Figure 7.14 Capillary pressure data from Kalaydjian and Tixier (1991) using unconsolidated sandpacks.

CHAPTER 8 CONCLUSIONS AND AREAS FOR FUTURE STUDY

The intrinsic difficulties associated with the experimental investigation of a variety of flow phenomena have prompted the current study. This thesis has consequently set out to report upon the development and implementation of a pore-scale simulator capable of modelling a variety of physical processes relating to multiphase immiscible flow in porous media. Many interesting results have emerged and many experimental observations have been successfully simulated. Moreover, as well as modelling and explaining observed phenomena, the network model has been used in a *predictive* capacity: by demonstrating how production efficiency may be expected to vary with rock wettability, for example. More specific conclusions are outlined below.

8.1 Single Phase Flow

From a geometrical point of view it has been demonstrated that in order to simulate the interconnectedness of a porous medium, it is necessary to use a network flow analogue. It has been shown that the flow is determined not only by the associated macroscopic parameters (pressure, liquid viscosity and dimensions), but also by the microgeometry. This microgeometry is characterised by the mean and variance of the pore-size distribution, and this result allows the flow to be predicted for any given network. Thus a formula for the network permeability can be written and has been shown to be valid for a wide range of microgeometries (pore radius distributions). The connection between this result and those of Effective Medium Theory and Percolation Theory has been demonstrated and some novel analysis has shown that all three approaches are, in fact, very closely related. Again it should be emphasised that the model developed here results in a formula that is independent of many details of the given microgeometry; it depends only upon the mean pore radius and the distribution variance. Apart from the elegance of this result it is very practical: calculations on a large network require a great

deal of computer time, whereas this formula allows the total flow to be calculated directly for a given network.

8.2 Two-Phase Flow in Strongly Water-Wet Systems

8.2.1 Primary Processes

During the study of primary processes, various qualitative phenomena have been described. The work has demonstrated that very different rule-bases can give almost identical relative permeability curves. In all cases, however, this is due to the combined effects of saturation and permeability shifts which may act to cancel one another. The true nature of a displacement can only be properly understood if the associated R-plots are analysed. The way in which relative permeability curves are constructed effectively disguises the underlying pore-scale dynamics of such processes.

Investigations into imbibition studies have shown that the resulting relative permeability curves appear to be insensitive to the actual displacement mechanism used. Trapping of the nonwetting phase *does* play an important role, however, causing the nonwetting curve to experience a small shift towards lower water saturations. The wetting curves essentially remain unaffected (save for premature termination at $S_w = 1-S_{or}$). At the end of the displacement, the trapped oil is contained in the largest pores and so the residual oil saturation is given to a good approximation by:

$$S_{or} \approx \frac{\int_{R_f}^{R_{max}} V(r)\, f(r)\, dr}{V_{tot}}$$

where V(r) is the volume function, f(r) the pore radius distribution, and R_f satisfies $p(R_f) = P_f$, the floodout percolation threshold.

In contrast to imbibition, drainage relative permeability curves appear to remain unaffected by phase trapping, but are strongly dependent upon the method of displacement used. It is therefore essential to ascertain the precise pore-scale mechanics governing such processes: top-down invasion percolation would appear to be the most appropriate model for such studies. Topological considerations show that the irreducible water saturation can be accurately determined from the integral:

$$S_{wi} \approx \frac{\int_{R_{min}}^{R_c} V(r)\, f(r)\, dr}{V_{tot}}$$

where R_C satisfies $p(R_C) = P_C$.

Two very important topological results have emerged from this work, the first of which relates to cluster growth. Once approximately 50% of the pores have been invaded, the network essentially consists of only two clusters; one wetting, the other nonwetting. The implication here is that from this point onwards, the filling regime is no longer of any importance: by this stage, all pores available for invasion are now accessible to the invading cluster. The second important finding concerns trapping of the displaced phase. Trapping only *begins* to occur once approximately 50% of the pores have been invaded and only becomes significant as the floodout threshold is approached (about 75% in this case). Note that these figures relate to systems with an average co-ordination number of six — they can be generalised with recourse to Equation (3.22), however, which relates percolation and floodout thresholds to the co-ordination number and dimensionality of the network.

8.2.2 Secondary Processes

Consider now, the simulation of secondary imbibition displacements. A large hysteresis effect is found to occur when primary drainage is followed by a waterflood in a water-wet system. In such cases the nonwetting relative permeability curve is shifted towards much lower water saturations, whilst the wetting curve appears to remain unaffected. Many theories have been proposed in an attempt to explain such phenomena, including: pore structure, contact angle hysteresis, and matrix cementation. It has been demonstrated here that such behaviour can be explained quite simply in terms of the wettability characteristics assigned to the network. By assuming that the network is strongly wetted by one particular phase (water in this case), the primary drainage mechanism is one of piston-like invasion percolation, whilst the secondary imbibition is a pure bond percolation problem. This assumption alone ensures hysteresis between the nonwetting curves, solely because of the limited accessibility associated with an invading nonwetting cluster. Note that trapping of oil during the secondary stage contributes only slightly to the hysteresis and is *not* the main cause. The wetting phase curves appear unchanged simply because corresponding shifts in water saturation and relative permeability act to cancel one another. It is important to realise that such subtle effects remain hidden because of the way in which relative permeability curves are constructed. Heiba et al (1982) performed similar calculations using a Bethe lattice with co-ordination number z=5, but they did not reach any conclusions relating to the causes of the observed hysteresis effect.

8.3 Two-Phase Flow in Mixed-Wet and Fractionally-Wet Systems

The intrinsic difficulties associated with the experimental determination of matrix wettability have prompted the current investigation using numerical simulations at the pore scale. This thesis has reported upon the development and implementation of a pore-scale simulator capable of modelling multiphase

flow in porous media of nonuniform wettability, pore wettability characteristics having been explicitly incorporated into a steady-state model. Results have been presented which show how α (the fraction of pores which are assigned oil-wet characteristics) affects waterflood capillary pressure curves, relative permeability curves, and recovery efficiency.

Simulated capillary pressure data have demonstrated that standard wettability tests (such as Amott-Harvey and free imbibition) may give spurious results when the sample is fractionally-wet in nature. Results describing spontaneous imbibition in *mixed*-wet media, however, show that the amount of imbibition should give a more reliable indication of wettability. An interesting aspect of the waterflood capillary pressure curves is the existence of a discontinuity as the process switches from imbibition to drainage. This discontinuity would appear to be more marked for mixed-wet media, although the assumption of perfectly wetting and perfectly nonwetting fluids may have exaggerated the effect.

Relative permeability curves have also been computed for a variety of α values. For fractionally-wet networks, it was found that as the oil-wet pore fraction increased, the curves (and the crossover point) experienced a general shift towards lower water saturations. The oil curves changed from being convex to concave in appearance whilst the water curves exhibited the reverse behaviour. All curves lay within the 100% water-wet/100% oil-wet envelope. Increasing the oil-wet pore fraction had two effects: at low water saturations the oil permeability decreased with increasing α, whilst at high water saturations the water permeability *increased* with α. The general trend was not quite as obvious when the networks were made mixed-wet. Although the oil curve lost curvature and the water curve gained curvature, the crossover point no longer moved towards lower water saturations as α increased. For α between 0 and

0.5, it actually shifted to higher saturations; only beginning to move back towards lower values once $\alpha > 0.5$.

The waterflood relative permeability curves have been used in the conventional fractional flow equations enabling the construction of a family of fractional flow curves. Buckley-Leverett analyses have subsequently been carried out to uncover how the microscopic displacement efficiency was influenced by the wettability of the system. In both fractionally-wet and mixed-wet cases, recovery has been shown to be maximum in networks consisting of 50% oil-wet pores and 50% water-wet pores. The variation in recovery at breakthrough was shown to be approximately 7% for fractionally-wet systems and about 15% for mixed-wet systems — minimum recoveries occurring for strongly oil-wet networks. Furthermore, the recovery data from waterfloods carried out on mixed-wet networks have been shown to be in excellent qualitative agreement with the recent experimental studies of Jadhunandan and Morrow (1991). This appears to be the first time that a network model has been used in the systematic study of both fractionally- and mixed-wet media in order to explain waterflood performance, and it would appear that the essential physics underlying the relative permeability concept is included in the rule based steady-state simulator.

A novel test has been proposed which it is hoped could be used to determine the wettability of both fractionally-wet *and* mixed-wet porous media. To date, no such satisfactory test appears to exist. The test would not require the determination of phase saturations but would involve the controlled imbibition of water into an oil-saturated sample. Such a controlled waterflood may be possible by incrementally decreasing capillary pressure and allowing the spontaneous imbibition of water up to a certain pore radius. Measurement of oil relative permeability at each capillary pressure value would then allow the

construction of R-k_{ro} curves ($R \propto 1/p_c$), which could then be used for wettability measurement as outlined in Section 5.7.

8.4 Unsteady-State Flow and the Viscous/Capillary Force Balance

The earlier steady-state, capillary-dominated models have been extended to deal with *un*steady-state dynamics, producing a simulator capable of interpreting a wide variety of multiphase laboratory displacements. Both unsteady-state drainage *and* imbibition models have been considered. For the imbibition case, some new analysis has been presented which shows up the inadequacy of the Washburn equation at the pore-scale. The new formulation also demonstrates the importance of *inertial* effects during pore-filling events (these had always been considered negligible in the past). Sensitivity analyses relating to a variety of flow parameters have been considered, including; viscosity ratio, flowrate, and pore-scale heterogeneity. Results support and extend related work by Lenormand et al (1988).

A variety of layered models has been used to give some qualitative indication as to the combined effect of capillary and viscous forces on waterflood displacement efficiency in finely laminated porous media. Both water-wet and oil-wet systems have been studied, and results have clearly demonstrated how both the small-scale lamination structure and the associated local displacement mechanisms govern the distribution of residual oil. More specifically, it has been shown that:

(i) Under capillary (and "intermediate") flow conditions, flooding across laminae in both water-wet and oil-wet systems is less efficient than flooding along laminae. Thus, the network simulations confirm the results of Kortekaas (1983) and Ringrose et al (1993) from purely microscopic considerations. Such variations in recovery may prove to be an important factor in applications which involve across-layer flow such as in cross-bedded clastic sediments.

(ii) In waterfloods of layered water-wet media, displacement efficiency tends to increase as viscous forces become more dominant. It should be stressed, however, that the viscous/capillary force balance has only been examined using simple layered models at each scale. In general, reservoir geology tends to be *aggregated* (not stretched), and so small-scale structure can therefore still impact upon reservoir predictions.

(iii) In waterfloods of laminated *oil*-wet media, waterfloods appear to be *least* efficient at a scale where both capillary *and* viscous forces are coupled i.e. at the "intermediate" scale considered here.

8.5 Three-Phase Flow

The many problems associated with three-phase flow have been described and a possible route towards greater understanding of these has been suggested. There are clearly many factors affecting three-phase flow at the pore-scale and it is extremely difficult to isolate these for experimental study. The network simulator described here provides a "clean" environment in which to carry out a variety of sensitivity analyses, and has been used to elucidate any topological effects which may be influencing the flow behaviour. The beauty of microscopic simulation is that many system attributes, such as wettability, connectivity and pore geometry, can be assigned to each element individually. This flexibility has facilitated the systematic study of displacements running under a wide range of operating conditions.

The combined effects of connate water, spreading coefficient, and pore topology upon gas/oil capillary pressure curves have been investigated. Meaningful interpretation of these curves has been shown to depend upon the notion of *effective connectivity*. The effective connectivity of the gas/oil system can be affected by: the physical co-ordination number of the system, the presence of connate water, and the spreading characteristics of the oil. Larger

residual oil saturations have been shown to be the result of a lowering in effective connectivity.

8.6 Practical Significance

The practical significance of the work presented in this thesis effectively relates to two different areas: (i) implications for experimental practice and interpretation, and (ii) issues concerning microscopic modelling itself.

Specific contributions regarding the former have included: giving valuable microscopic insights into a range of displacement processes, suggesting new ways of plotting standard relative permeability and capillary pressure data, and the proposal of a new wettability test. More generally, results support the argument that only cores which have the "correct" reservoir wettability state should be used for laboratory analysis. Any alteration in matrix wettability will invariably lead to inaccurate (and possibly very costly) conclusions: the use of cleaned cores for capillary pressure measurements could give very inaccurate results and lead to an overestimate of the height of the transition zone in a reservoir, whilst waterfloods performed on cleaned or weathered material would almost certainly result in an erroneous prediction of reservoir efficiency. As far as routine petrophysical measurements are concerned, one of the most valuable results from this thesis has been the demonstration of the inadequacy of the standard Ritter and Drake analysis (Appendix A); an analysis which forms the basis for the interpretation of all conventional porosimeter data.

The main contribution towards microscopic modelling itself has been the extended Washburn equation, which clearly demonstrates the importance of inertial effects at the pore-scale. If such effects are disregarded (as has been common practice in the past), then pore-filling sequences will generally be

incorrectly predicted. This result is so fundamental, that it impinges upon all attempts to model microscopic imbibition processes successfully.

8.7 Areas for Future Study

The basic single-phase transport model has gradually been extended, resulting in a three-dimensional, three-phase pore-scale simulator that is now capable of incorporating: phase trapping, film-flow/spreading, wettability effects, viscous/capillary coupling, geological heterogeneity, and variable pore connectivity/geometry/orientation. There are, however, a great many related problems yet to be tackled. The modelling of bubble growth during depressurisation, for example, would help towards a better understanding of how a critical gas saturation forms. The effects of reservoir stress could be incorporated to facilitate the modelling of faults and fractures, thereby giving some indication as to the way in which fracture and matrix interact during flooding. The influence of wettability upon electrical resistivity measurements is also a possible area for further study. The complete control afforded by network modelling gives a much clearer insight into a wide variety of flow behaviour and can hopefully lead to a vastly improved predictive capability in many areas. It is to be hoped that the model developed here could prove to be a useful starting point for these future investigations.

APPENDIX A PORE SHIELDING AND THE LIMITATIONS OF STANDARD MERCURY POROSIMETRY

Introduction

Mercury porosimetry is one of the most routinely performed techniques in the petroleum industry, yet the interpretation of any mercury intrusion curve still has a large degree of uncertainty associated with it. This appendix sets out to discuss the pitfalls of mercury porosimetry and gives analytical results which show that the pore size distribution functions derived from it are seldom valid. Network simulations of the process will demonstrate how mercury intrusion could function most effectively as a diagnostic tool, giving valuable information about the geological structure of a variety of porous media.

Laboratory Determination of Pore Size Distributions

Mercury injection is carried out using a porosimeter, which essentially forces mercury into a porous sample at incrementally higher pressures. Good quality data is dependent upon the ability of the porosimeter to accurately measure both the volume of mercury taken up by the sample and the corresponding pressure at which this occurs. This is generally achieved by sealing the porous material in a glass sample cell (penetrometer) which has a fine bore capillary extending from one end (Figure A1). The capillary and penetrometer are first evacuated and then filled with mercury — the sample is now effectively surrounded by a nonwetting fluid. Next, depending upon the pressure range required, either a pneumatic or hydraulic pressure source is connected to the open end of the capillary, and the pressure incrementally increased. A cylindrical capacitor surrounding the capillary is used to measure the corresponding incremental change in the height of the mercury column, and so the injected volume can be immediately inferred. Pressures can typically range from low vacuum to about 60,000psi.

About 50 pairs of data are typically plotted on semi-log axes giving a cumulative P_c-S_{Hg} graph, which is subsequently converted into a cumulative "radius" distribution through Laplace's equation:

$$R = \frac{2\sigma\cos\theta}{P_c}. \qquad \text{(A1)}$$

The differential or log-differential of the resulting curve is then assumed to give the correct pore size distribution. The limitations of this (almost universally adopted) approach will soon become apparent during the following discussion.

Pore Shielding and the Accessibility Issue

Consider the network of pores shown in Figure A2. The capillaries all have different radii which consequently governs the order in which they are filled during a capillary-dominated displacement. The expected filling sequence during mercury injection is shown in Figure A3, where it is clear that most of the larger pores cannot be immediately accessed by the invading mercury, because they reside at the interior of the sample: they are effectively *shielded* by smaller pores which can only be entered at higher pressures. The initial inaccessibility of these pores means that their cumulative volume will be incorrectly assigned when the resulting intrusion curve is analysed. That is to say, the number of smaller pores will invariably be overestimated by the process. The issue of accessibility is an important one, because it can play a subtle role in a variety of different displacement processes; for example, it appears to be one of the major factors responsible for hysteresis effects in relative permeability and capillary pressure curves (see Chapter 4).

Counter-Examples to the Standard Ritter and Drake Analysis

The way in which mercury intrusion curves are used for the derivation of pore size distributions was briefly touched upon above. The relevant analysis will now be discussed in greater depth and some counter-examples will serve to

highlight the inadequacy of current techniques (accessibility issues notwithstanding).

Consider an *ideal* porous medium consisting of cylindrical capillary tubes with capillary entry radii, $r \in [R_{min}, R_{max}]$. This example serves two purposes:

(i) it is an assumption of the standard Ritter and Drake (1945) analysis, which is still used in porosimeters today.

(ii) it allows the volume of a pore to be written as $V(r)=\pi r^2 l$, where l is the length of the cylindrical pore, i.e. the volume of each pore is known exactly.

If the pore radii are chosen from a uniform probability f(r), then the intrusion process can be represented schematically as shown in Figure A4. Remembering that f(r) is a *number* density function, the saturation S_{Hg} at a given r (i.e. R_{cap}) can be written as:

$$S_{Hg} = \int_{R_{cap}}^{R_{max}} V(r) f(r) A(r)\, dr \qquad \text{(A2)}$$

per unit volume of the sample (i.e. the equation has been divided through by V_{tot}). The only additional quantity to appreciate is A(r), which is the accessibility function. This is a geometrical factor describing the fraction of porespace that *is* occupied at the capillary entry radius, r, as a function of the porespace which *could* be occupied. In Figure A5 the quantity A(r) is the fraction shown inset.

For the present analysis, the accessibility issue will be ignored, although it could easily be included. This then permits the integration of Equation A2 to obtain:

$$S_{Hg} = \int_{R_{cap}}^{R_{max}} \frac{\pi r^2 l}{(R_{max} - R_{min})} dr = \frac{\pi l}{3(R_{max} - R_{min})}(R_{max}^3 - R_{cap}^3) \qquad \text{(A3)}$$

For mercury intrusion, R_{cap} can be directly related to the capillary pressure, P_c, through Laplace's equation, and so, by rearrangement S_{Hg} and P_c can be directly related to give:

$$S_{Hg} = \frac{\pi l}{3(R_{max} - R_{min})}\left(R_{max}^3 - \left(\frac{2\sigma\cos\theta}{P_c}\right)^3\right) \qquad \text{(A4)}$$

This relationship can be viewed as the "experimental" S_{Hg}/P_c curve (neglecting the accessibility issue) and is shown in Figure A6. Note that this relationship is derived from a known and clearly defined pore size distribution. Thus the application of any approach to the analysis of mercury intrusion data must reproduce this known pore size distribution.

Hence, application of the standard Ritter and Drake analysis to the "perfect data" generated by this model system (i.e. Equation A4), should reproduce the original pore size distribution exactly. Ritter and Drake used the following formula:

$$D(r) = \frac{P_c}{r}\left(\frac{dS_{Hg}}{dP_c}\right) \qquad \text{(A5)}$$

where D(r) is the "pore size distribution". The assumptions of this method are:

(i) The system is made up of cylindrical pores of capillary radius, r (which for a cylinder is the same as the tube radius).

(ii) The pores are all accessible.

Both of these assumptions are *true* for the model data generated above. Thus the derivative of Equation A4 can be directly substituted into Equation A5 to obtain the Ritter and Drake quantity, D(r). Going through this process gives:

$$D(r) \propto r^2 \tag{A6}$$

Hence the Ritter and Drake approach leads to a *quadratic* form of "pore size distribution" instead of the uniform distribution which was input. Similarly, a log-uniform *input* distribution:

$$f(r) = \frac{1}{r \log(R_{max}/R_{min})} \tag{A7}$$

yields a *linear* Ritter and Drake output distribution.

These problems arise because the pore size distribution is not defined in terms of both the capillary radius and the volume function: i.e. the Ritter and Drake results are actually*volume-weighted* distributions. A more meaningful procedure would involve a modified formula of the form:

$$D_{mod}(r) = \frac{\frac{p_c}{r}\left(\frac{dV_{int}}{dp_c}\right)}{V(r)} \int_{R_{min}}^{R_{max}} V(r) D_{mod}(r)\, dr \tag{A8}$$

where the integral is simply a constant which is unimportant when examining the *functional* r-dependency of the distribution. This equation acknowledges the fact that the pore entry radius, r, is distinct from the volume function, V(r). For cylindrical pores, $V(r)=\pi r^2 l$, as noted above, but for pores of more general shape the volume function may contain other factors (aspect ratio, etc.). However, if the modified equation is applied to the cylindrical pore model which has a uniform pore size distribution, the result is:

$$D_{mod}(r) = \frac{1}{(R_{max} - R_{min})} \qquad \text{(A9)}$$

which is precisely the input function. Thus, unlike the Ritter and Drake formulation, the analysis presented here can "close the loop" between input and output data; this must be a prerequisite of any improved analytical method. Although this approach requires some foreknowledge of the form of the pore volume function, a range of different pore shapes could be analysed and used as options in the analysis of a particular rock.

Different variants of the Ritter and Drake formula (Equation A5) have been proposed, but these do not generally help. Indeed, certain commercially available "solutions" can make the predicted pore size distributions even *worse*. For example, the current ethos for obtaining a distribution curve is to differentiate the S_{Hg}/R_{cap} intrusion curve with respect to $\log_{10}r$ instead of just r (as is the case for Ritter and Drake). Closer examination of this method, however, shows that the output distribution, D*(r) is related to the Ritter and Drake distribution, D(r), via the simple expression:

$$D^*(r) = (r \log_e 10).D(r) \approx 2.3rD(r) \qquad \text{(A10)}$$

In effect, this current "improvement" actually gives *even more* weighting to larger pores.

Network Simulations of Mercury Injection in Geological Media

Theoretical problems associated with mercury injection capillary pressure can be divided into the following two concerns in relation to geological media:

(i) the correct interpretation of the mercury intrusion data in terms of a pore size distribution where there is *genuinely* a single unimodal population of

pore sizes. This requires an improved analysis relative to that of Ritter and Drake.

(ii) the more complex problem of how to separate certain observed features of the intrusion curve, when there is a suspicion that the behaviour is influenced by factors on various lengthscales, e.g. *multimodal* distributions associated with lamination.

Issue (i) has been addressed above and will not be considered further. The second problem has been examined by utilising the capillary-dominated drainage network simulator to generate mercury intrusion curves for three rock classes. These are shown in Figure A7 and comprise contrasting pore size distributions (and hence permeabilities) in systems distributed in the following ways:

(a) a laminated sample (Case 1, Figure A7a)

(b) an isolated surrounded clast (Case 2, Figure A7b)

(c) a genuinely randomly distributed bimodal pore size distribution (Case 3, Figure A7c).

All three of these models are made up of two permeability types, each of which has its own pore size distribution:

— High permeability (24mD) - pore size range is 0.42-1.06μm, skewed normal distribution.

— Low permeability (2mD) - pore size range is 0.21-0.53μm, skewed normal distribution.

Numerical mercury P_c curves have been generated for a series of cases with varying fractions of high permeability vs low permeability regions (or, in the case of a randomly dispersed bimodal distribution, a randomly mixed fraction

from the two distributions). In these simulations, mercury totally surrounds the sample as in real intrusion experiments.

The main results from the S_{Hg} vs P_c curves are as follows:

(i) Figures A8 and A9 show that curves with a pronounced step are obtained for both the laminated and the isolated surrounded clast models. Indeed, these are identical, showing that it is the *order of accessibility* induced by the gross structure of the system that governs this step behaviour. The order is the same in both structures, since the mercury can penetrate virtually all of the high permeability regions before entering the low permeability lamina or clast. Note, however, that if the *higher* permeability clast were isolated in the centre, then the resulting capillary pressure curve would be very different.

(ii) Figure A10 shows that a genuine bimodal pore size distribution may lead to a characteristically different form of mercury intrusion curve. Curves exhibit an initial "ramp-type" behaviour, rather than the rapid steep rise onto an intermediate plateau, typical of the "step-type" behaviour.

These results clearly demonstrate how mercury intrusion curves can give valuable information pertaining to the sedimentological (and diagenetic) structure of a variety of porous samples. However, when structure is present, there is no analysis — such as that described earlier — to back out a unique set of pore size distributions. Thus, although the mercury intrusion curves are useful, they must be interpreted very carefully.

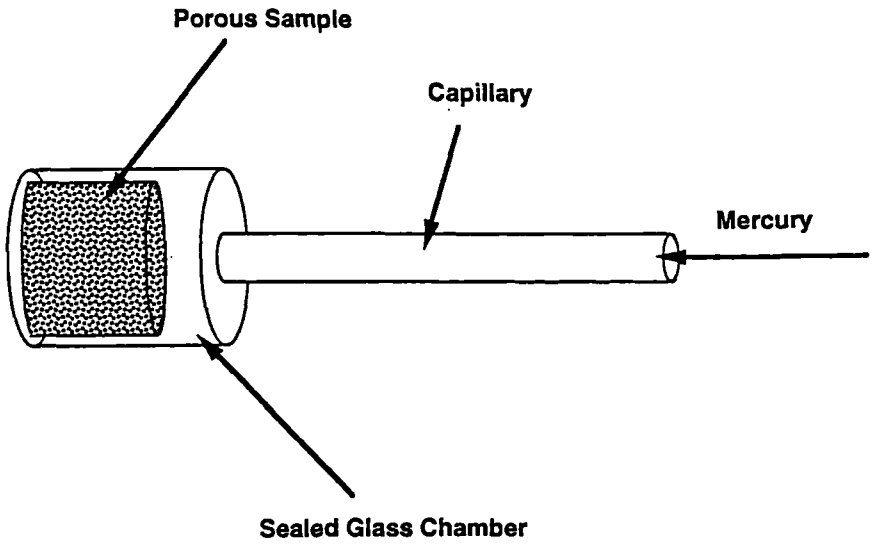

Figure A1 Schematic of penetrometer used in mercury injection experiments.

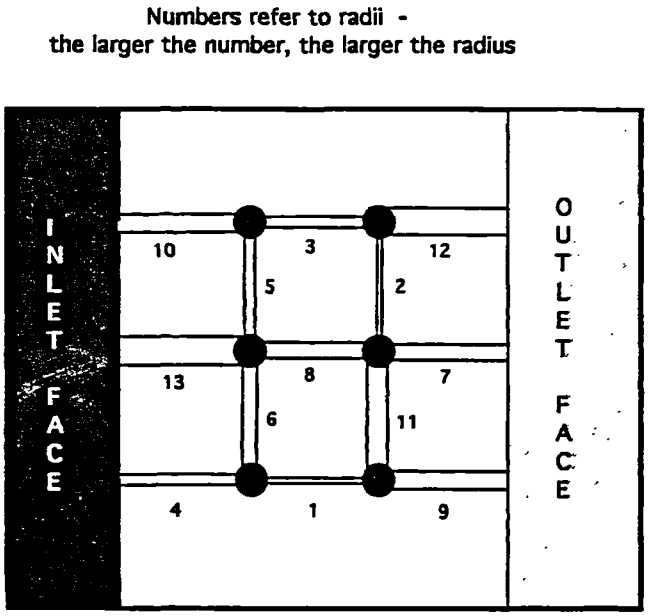

Figure A2 Pore network consisting of tubes of different radii (numbers refer to relative sizes).

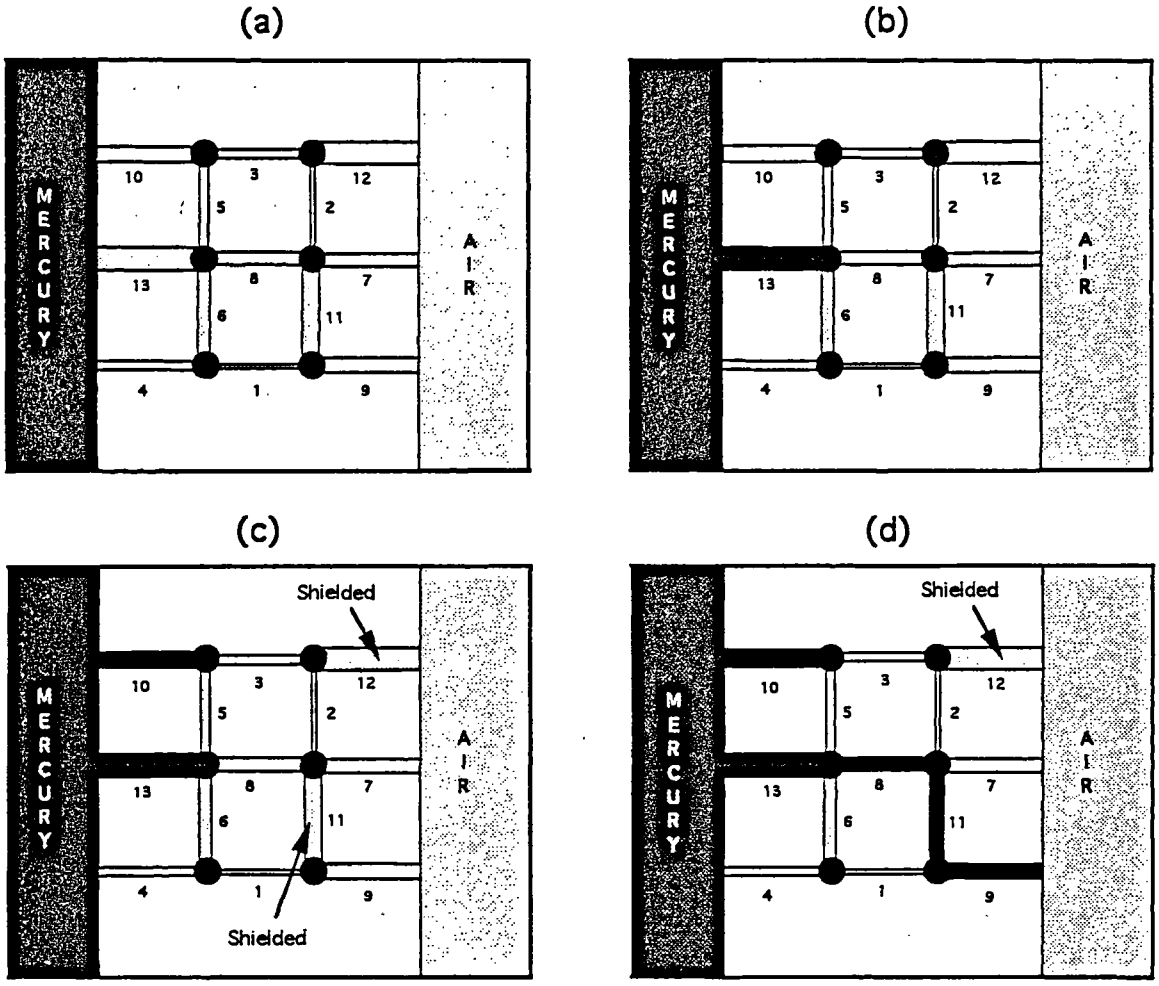

Figure A3 Mercury injection into the pore network.

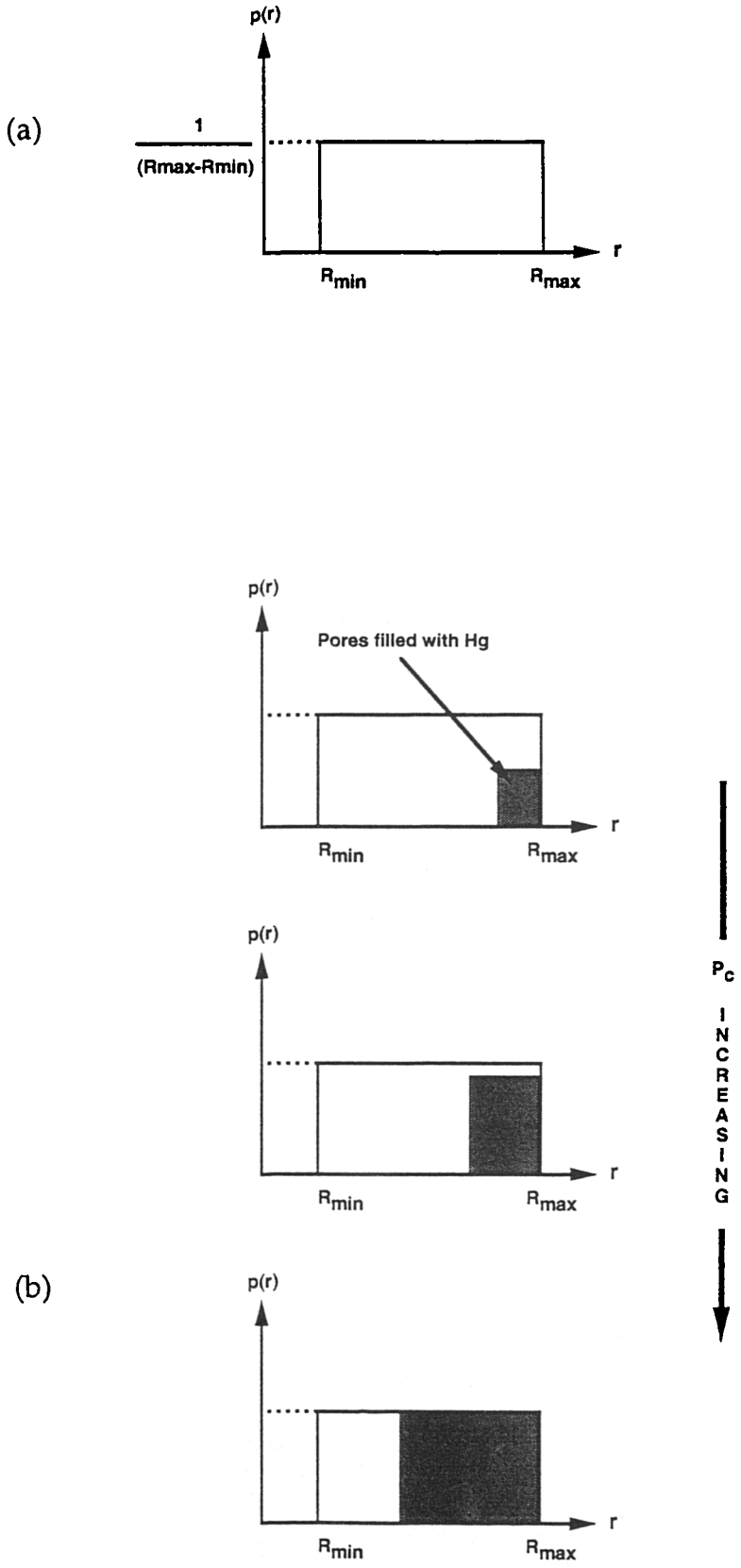

Figure A4 (a) Uniform pore size distribution, (b) mercury intrusion schematic as P_c increases.

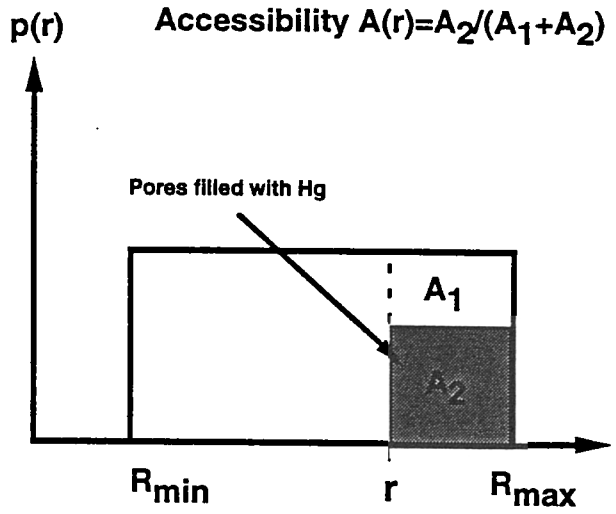

Figure A5 Illustration of the meaning of the Accessibility function, A(r), during the injection process.

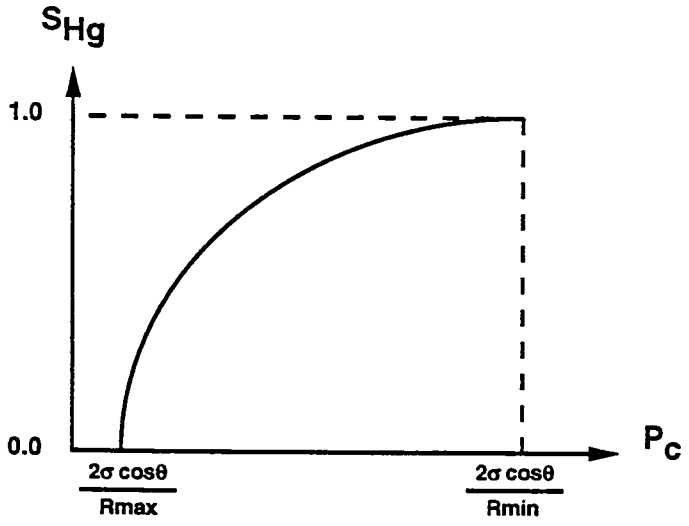

Figure A6 The predicted S_{Hg} vs P_c relationship for a Uniform pore size distribution.

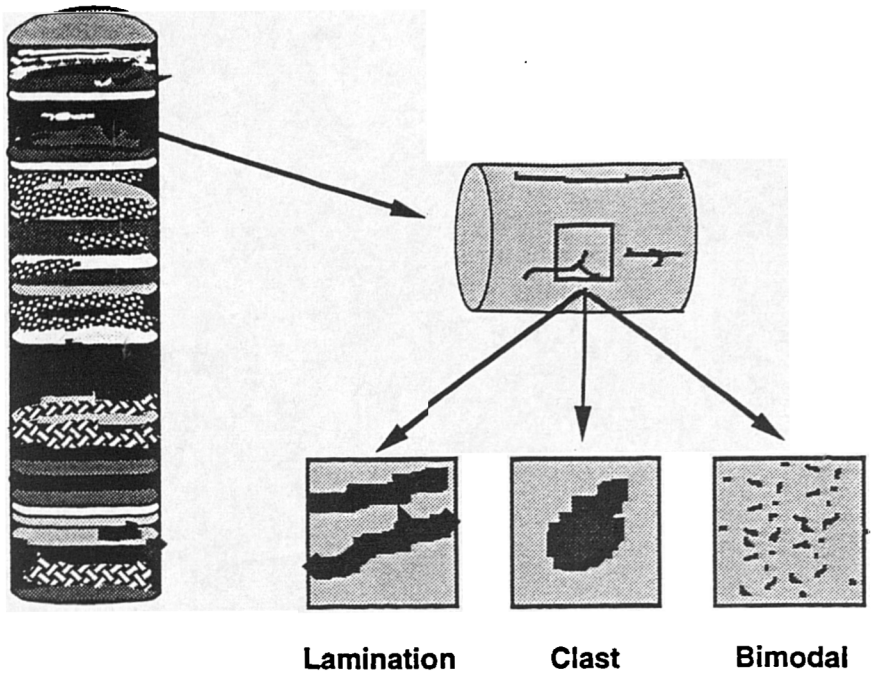

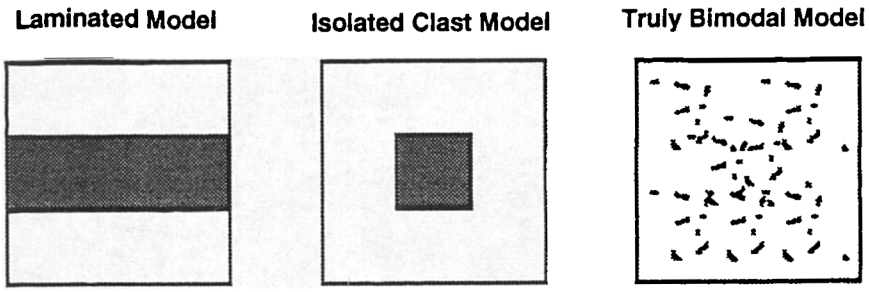

Figure A7 The three classes of heterogeneity considered in this study.

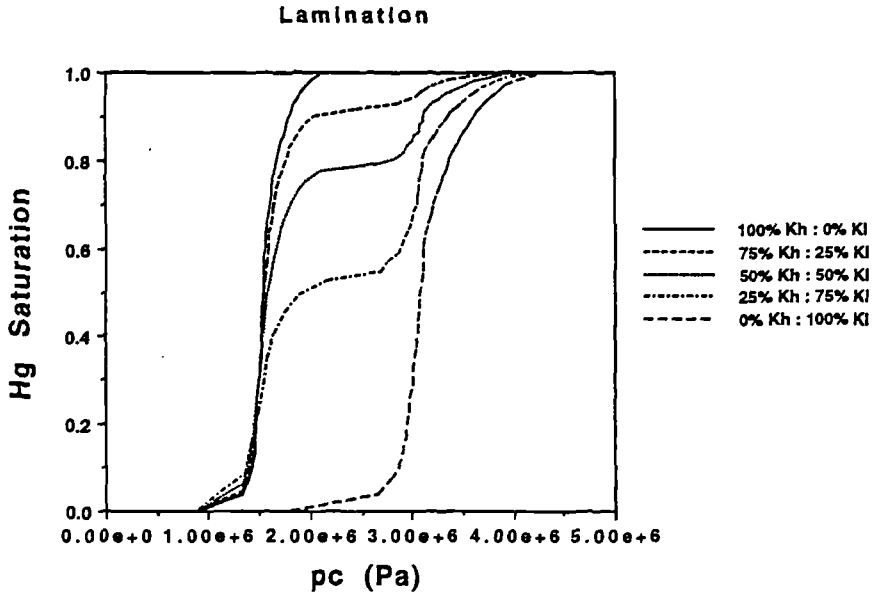

Figure A8 Simulated mercury intrusion curves for the laminated model. Each curve corresponds to a different ratio of low permeability to high permeability.

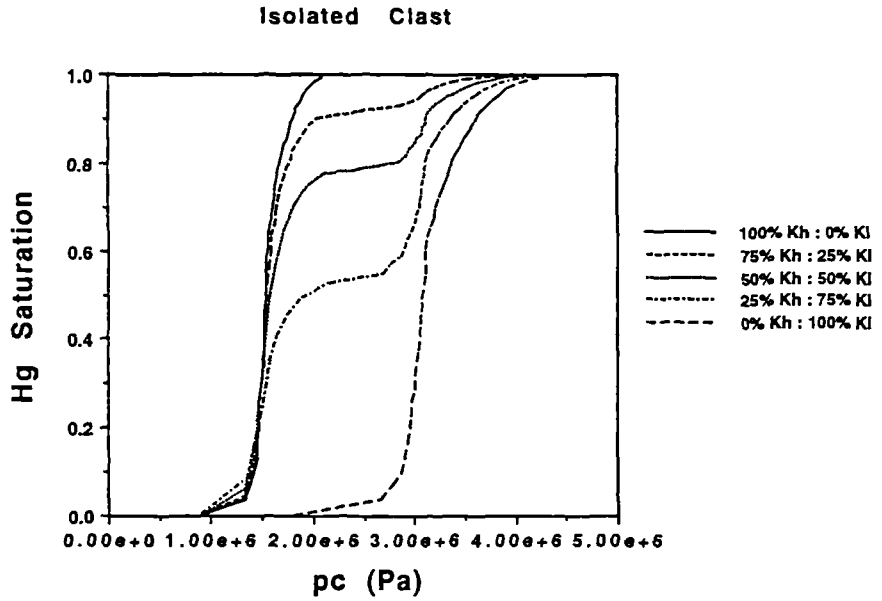

Figure A9 Simulated mercury intrusion curves for the isolated clast model.

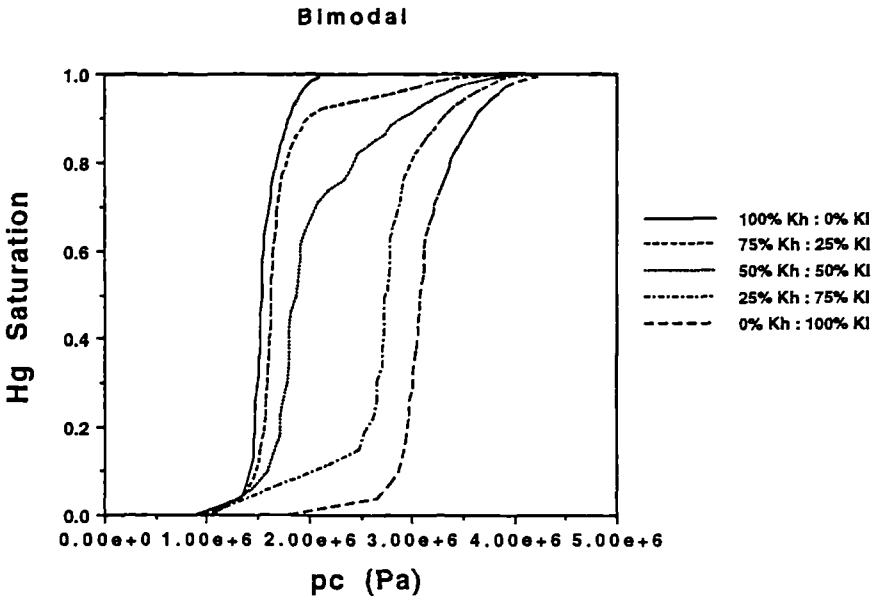

Figure A10 Simulated mercury intrusion curves for the truly bimodal model.

APPENDIX B THE EXTENDED WASHBURN EQUATION AND ITS APPLICATION TO OIL/WATER DISPLACEMENTS

The Washburn approximation has been discussed briefly in Chapter 6 of the main text. Equation (6.7) can easily be integrated to give the "pore" filling time, t_f, in the presence of only viscous forces, ΔP (and $\varepsilon=0$), as:

$$t_f = \frac{4L^2\mu}{r^2\Delta P} \tag{B1}$$

where L is the total tube length. Likewise, when the flow is entirely capillary dominated, the time for complete penetration is given by:

$$t_f = \frac{2\mu L^2}{r\sigma\cos\theta} \tag{B2}$$

Note that, under either viscous or capillary domination, the Washburn approximation predicts that wide tubes fill quicker than narrow ones; that is, $t_f \sim 1/r^2$ and $t_f \sim 1/r$ for viscous and capillary dominated systems, respectively.

There are two issues, however, which have led the authors to question the general applicability of the Washburn approximation: (i) Equation (6.7) predicts an infinite velocity at x=0 (t=0), which is physically impossible, and (ii) if Washburn is valid, why does imbibition begin with the wetting phase filling the *smallest* pores of a porous medium? It should also be remembered that the Washburn approximation assumes steady-state flow either side of the meniscus - a simplification which may lead to errors at the pore-scale. It was noted in the main text that this may partly be explained in terms of "metering effects" due to the limited supply of wetting fluid. This may indeed be important, but there are also some other issues as discussed below.

A more rigorous analysis of the capillary rise problem, with water displacing air, was carried out by Szekely et al (1971). By considering the energy balance of the system, they were able to derive the following equation governing the advance, x(t), of the wetting front in a capillary:

$$\left(x+\frac{7}{6}r\right)\ddot{x}+1.225\dot{x}^2+\frac{8\mu}{\rho r^2}x\dot{x}=\frac{1}{\rho}\left(\frac{2\sigma\cos\theta}{r}-\rho g x\right) \qquad \text{(B3)}$$

The three terms on the left hand side of equation (B3) represent (a) inertial effects relating to the net influx of kinetic energy; (b) the formation of a vena contracta at the tube inlet, and (c) the work expended overcoming viscous forces. The right hand side consists of a capillary force term and gravitational potential term. The velocity singularity at t=0 is no longer a problem in this formulation. Their numerical solutions led Szekely et al to conclude that "...the Washburn equation would be appropriate for the interpretation of capillary penetration rates for most systems of practical interest".

Consider now, water displacing air under capillary control (i.e. $\Delta P_V = 0$ and g = 0) in two capillaries of radii r_1 = 0.01cm (100μm) and r_2=0.001cm (10μm). How do the solutions of the Washburn equation and equation (B3) compare? The results are presented in Figure B1, and it is quite clear that both give very similar predictions for the tube filling time: under capillary control, the wider tube fills first.

Notice that the penetrated lengths shown in Figure B1 range from 0cm to 0.6cm, i.e. the tubes are very long and thin. In a porous medium, however, pore lengths are very small (L~100μm, say): how do the two formulations compare at this scale? The rather surprising comparison is shown in Figure B2. The Washburn approximation again predicts that the wider tube will fill first, whilst the solutions of Equation (B3) exhibit more complex behaviour. They predict a *critical penetration length*: if the two tubes are less than about 250μm long, then

the narrower tube will fill first; if the tubes are longer than 250μm, the wider tube will fill first. *This shows that time taken for a pore to fill is dependent upon its aspect ratio (r/L).*

The author has extended this early work to two-phase (oil-water) displacements under the influence of capillary, gravitational and viscous forces (McDougall et al, in preparation). The final governing equation takes the form:

$$\left(x(\rho_w-\rho_o)+\rho_o L+\frac{7}{6}r(\rho_w+\rho_o)\right)\ddot{x}+1.225\rho_w\dot{x}^2+$$

$$\frac{8[x(\mu_w-\mu_o)+\mu_o L]}{r^2}\dot{x}= \qquad \text{(B4)}$$

$$\left(\frac{2\sigma\cos\theta}{r}+\Delta P_{vis}-gx(\rho_w-\rho_o)\right)$$

Some special cases can be considered:

(i) If $\ddot{x}=\dot{x}=0$ and $\Delta P_v=0$, then

$$x=\frac{2\sigma\cos\theta}{\rho g(\rho_w-\rho_o)} \qquad \text{(B5)}$$

This is the well-known capillary rise result.

(ii) With $\rho_O=\rho_W=\rho$ and $\mu_W=\mu_O=\mu$, Equation (B4) can be solved analytically to give:

$$x(t)=\frac{\left(\frac{2\sigma\cos\theta}{r}+\Delta P_v\right)}{8\mu L}r^2\left\{t-A\left(1-\exp^{-\frac{t}{A}}\right)\right\} \qquad \text{(B6)}$$

where,

$$A=\frac{\rho r^2\left(L+\frac{7}{3}r\right)}{8\mu L} \qquad \text{(B7)}$$

This solution contains a transient term (exp-(t/A)) which becomes very small at large times. Once this transient period is over, the penetration varies approximately linearly with time. These two limits can be extracted in a straightforward manner to give analytical formulae relating pore filling time to system parameters.

For t<<A, a limit corresponding to short, fat pores (i.e. large aspect ratio) the filling time is given by:

$$t_f = L\sqrt{\frac{2\rho\left(L+\frac{7r}{3L}\right)}{\left(\frac{2\sigma\cos\theta}{r}+\Delta P_v\right)}} \qquad \text{(B8)}$$

This predicts narrower pores filling before wider ones. For large t, a limit corresponding to long, thin pores (i.e. small aspect ratio, r/L), the filling time becomes:

$$t_f = \frac{8\mu L^2}{r^2\left(\frac{2\sigma\cos\theta}{r}+\Delta P_v\right)} + \frac{\rho r^2\left(L+\frac{7}{3}r\right)}{8\mu L} \qquad \text{(B9)}$$

The first term in (B9) corresponds to the Washburn approximation, whilst the second relates to the transient part of the solution. The above analysis shows that the Washburn equation is generally inadequate for flow modelling at the pore scale: it is only approximately valid for flow calculations in uncommonly long, thin pores. The simulations reported in this paper are based upon the new physics described by (B8) and (B9). A fuller account of this work coupled with pore metering effects, where a free supply of wetting fluid is unavailable, will be reported in a forthcoming paper (McDougall et al, in preparation).

Washburn

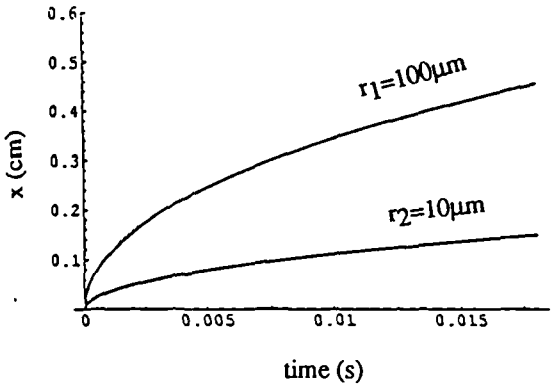

Szekely *et al*

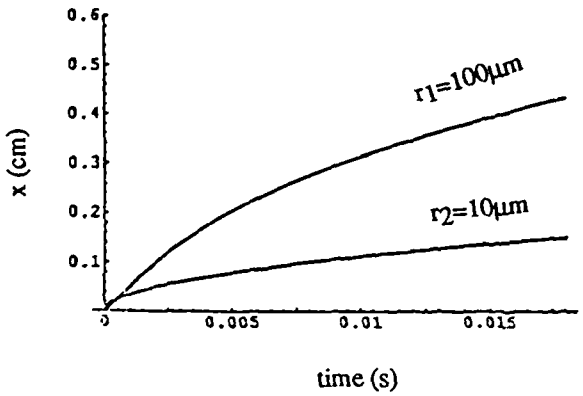

Figure B1 Comparison between the Washburn approximation and the full energy equation for two capillary tubes of radii r_1=100μm and r_2=10μm. x(cm) is the penetrated length.

Washburn

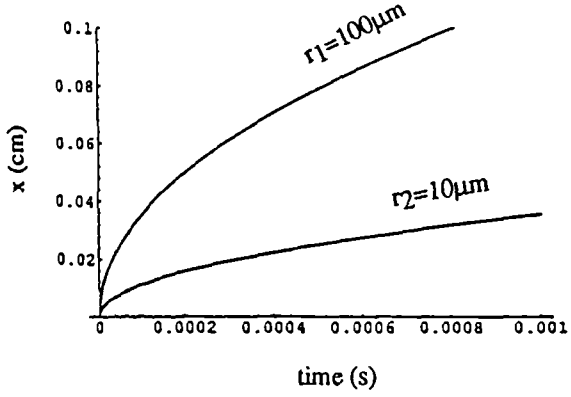

Szekely *et al*

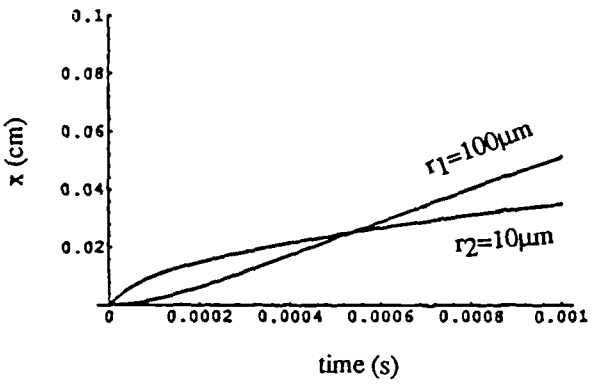

Figure B2 Blown-up region of Figure B1. The Washburn equation still predicts wider tubes filling first, but the full energy equation predicts more complex behaviour.

APPENDIX C SCALEUP AND THE VISCOUS/CAPILLARY FORCE BALANCE.

An immiscible displacement in a porous medium is governed by viscous, capillary and gravitational forces. It is clear, however, that the relative importance of these forces is scale-dependent in that different force balances are prevalent in systems of different sizes. At the lamina scale (<1cm), displacements are usually entirely governed by capillarity: drainage processes are dominated by capillary entry thresholds, whilst imbibition tends to occur via film-flow and snap-off. As the system size increases, however, viscous and gravitational forces become more and more important. At the lamina set scale (~ 1-50cm), both viscous *and* capillary forces may affect the displacement, whilst larger systems tend to lie in the viscous-gravity regime. Clearly, cross-over regimes must exist at some scale, but these are difficult to quantify and the best approach is to utilise consistently defined scaling groups.

The appropriate scaling groups for a system in which there is incompressible, immiscible, two-phase flow are quite well known. The main group as far as this work is concerned is the viscous/capillary scaling group as follows:

$$\frac{q\Delta x\mu_w}{k_x\Delta y\Delta z\left(\frac{dP_c}{dS_w}\right)} \qquad \text{(C1)}$$

There is also a viscous/gravity group and, in 3D, two aspect ratio groups, of the form:

$$\frac{k_x}{k_y}\left(\frac{\Delta y}{\Delta x}\right)^2 \text{ and } \frac{k_x}{k_z}\left(\frac{\Delta z}{\Delta x}\right)^2 \qquad \text{(C2)}$$

which account for geometrical factors (Δx, Δy, Δz are the system dimensions, k_x, k_y, k_z are the anisotropic permeabilities, q is the total flow rate, μ_w the water viscosity, and dP_c/dS_w the capillary pressure gradient). If these scaling groups can be matched for two different systems, then both will behave in completely analogous ways: that is, saturation profiles and production data will be perfectly reproduced at homologous times.

The above groups come from the *continuum* two phase flow equations. Thus, in the context of "discrete" network simulation, these groups can only be applied consistently *if the effective flow behaviour in a region of the network in some sense reproduces the average continuum behaviour*. This is clearly an approximation and would generally be valid only for very large networks. However, these scaling groups can be used — particularly the capillary/viscous group — to give some indication of the *lengthscales* at which various phenomena apply.

There have been many attempts to incorporate the viscous/capillary force balance into a single dimensionless number — the capillary number. Unfortunately, relatively few capillary numbers take account of the full flow equations, and generally take the form:

$$Ca = \frac{v\mu}{\sigma \cos\theta} \qquad \text{(C3)}$$

where v is the frontal velocity of the displacing phase, μ its viscosity, σ the interfacial tension and θ the contact angle.

Equation (C1) gives a more physically-based representation of the viscous/capillary force balance, as it is derived directly from the governing flow equations. In this case, capillary effects are represented by the slope of the associated capillary pressure curve, the nature of which is intrinsically linked to the underlying structure of the porous medium. Network simulations

comparing systems with differing pore-size distributions can be used to give some qualitative insight into the form of $P_C(S_W)$. The (k, ϕ) dependence is given by:

$$\frac{dP_c}{dS_w} \sim \frac{\phi^m}{k^n} \tag{C4}$$

Leverett (1941) found a correlation with m=n=1/2 (the Leverett J-function), and this appears to be an acceptable approximation for well-connected systems. This leads to a generalised capillary number which should express the viscous/capillary force balance in a somewhat more meaningful way. For isotropic media, this takes the form:

$$\frac{q\Delta x\mu_w}{\Delta y\Delta z\sigma\cos\theta\sqrt{k\phi}} \tag{C5}$$

Thus, scale-up can be achieved by increasing the total network flow rate. That is to say, if the prototype system (which may be a gridblock, for example) has dimensions that are N times larger than those of the network, then the force balance acting at the prototype scale can be reproduced in the network simply by increasing the *network* frontal velocity by a factor N. Hence, the viscous dominated *network* simulations may be interpreted as representing an identical laminar system at a much larger scale. Note, however, that if capillary-induced trapping is predicted at the (small) lamina scale, and the bedform is an *aggregate* of such lamina sets, then capillary trapping will also be an important feature at the larger scale.

APPENDIX D RADIUS PROBABILITY DISTRIBUTION FUNCTIONS

A complete list of all distributions:

(1) Uniform

$$f(r)=\begin{cases}\dfrac{1}{R_{max}-R_{min}} & R_{min}\le r\le R_{max}\\ 0 & \text{otherwise}\end{cases}$$

(2) Triangular

$$f(r)=\begin{cases}\alpha(r-R_{min}) & R_{min}\le r\le c\\ \beta(R_{max}-r) & c\le r\le R_{max}\\ 0 & \text{otherwise}\end{cases}$$

where $c=(\alpha R_{min}+\beta R_{max})/(R_{min}+R_{max})$

(3) Cubic

$$f(r)=\begin{cases}Nr^3 & R_{min}\le r\le R_{max},\\ 0 & \text{otherwise}\end{cases}\qquad N=4/(R_{max}^4-R_{min}^4)$$

(4) Log-Uniform

$$f(r)=\begin{cases}N/r & R_{min}\le r\le R_{max},\\ 0 & \text{otherwise}\end{cases}\qquad N=1/\ln(R_{max}/R_{min})$$

(5) Exponential

$$f(r)=\begin{cases}Ne^{-r} & R_{min}\le r\le R_{max},\\ 0 & \text{otherwise}\end{cases}\qquad N=1/(e^{-R_{min}}-e^{-R_{max}})$$

(6) Truncated Normal (TN)

$$f(r) = N(R_{max} - r)(r - R_{min}) \exp\left[\frac{-(r-m)^2}{2d^2}\right] \quad R_{min} \le r \le R_{max}$$

N is a normalisation factor: this is a normal distribution cut off at R_{min} and R_{max}.

(7) Rayleigh

$$f(r) = \frac{2(r - R_{min})\, e^{\frac{-(r-R_{min})^2}{\beta}}}{\beta\left(1 - e^{\frac{-(R_{max}-R_{min})^2}{\beta}}\right)} \qquad r \in [R_{min}, R_{max}]$$

(8) Bimodal Uniform

$$f(r)\begin{cases} \dfrac{\alpha}{(R_2 - R_1)} & R_1 \le r \le R_2 \\ \dfrac{\beta}{(R_4 - R_3)} & R_3 \le r \le R_4 \end{cases}$$

where $\alpha+\beta=1$.

APPENDIX E COMPUTATIONAL ALGORITHMS AND PROGRAMMING DETAILS

Introduction

This appendix describes the computational principles and details underpinning the various simulators used throughout this thesis. All simulators utilise the simple network model as a starting point, with each successive extension adding to its complexity and range of application. Models range from the basic single-phase analogue to the more complex unsteady-state three-phase system. The justification for each model is discussed in the relevant chapter; it is the functional details of the programs which are dealt with here. Throughout this discussion, the term "bond" refers to any capillary element.

The basic code 1PHASE calculates the total flow of a single fluid through a given distribution of bonds. Program PERC can be used to investigate critical exponents near percolation threshold. This is achieved by initially blocking all of the bonds and then opening an increasing percentage until there is full network flow.

The models for capillary-dominated two-phase flow (oil/water) are generally built upon the assumption that oil occupies the larger bonds and water the smaller bonds. There are two codes available to calculate flow behaviour: one for imbibition and the other for drainage displacements. Program IMBIBITION begins with all of the bonds filled with oil and proceeds to fill them with water beginning with the smallest bonds (wherever they are in the network). Program DRAINAGE begins with all bonds initially water-filled, and proceeds to fill the largest bonds *connected to the inlet face of the network* with oil. This invading oil cluster is then grown by filling progressively smaller bonds that happen to be connected to it. The results from these programs can be used to calculate oil/water relative permeabilities for a given network.

The program MIXWET is used to simulate capillary-dominated waterfloods of mixed-wet and fractionally-wet networks. Water is allowed to spontaneously imbibe along water-wet clusters and proceeds to fill the smallest *accessible* bond. Once imbibition has been completed, water is forced into the largest available oil-wet pore and the waterflood continues as a drainage process. The clustering analysis is clearly more involved in MIXWET, as phase clusters *and* wettability clusters have to be examined.

Unsteady-state imbibition and drainage displacements are simulated using the UNSTEADY(IMB) and UNSTEADY(DR) codes. Whilst drainage processes are still characterised by pistonlike meniscus advance, imbibition may also require film-flow dynamics (depending upon the flowrate used). Both viscous and capillary forces are accounted for, and surface roughness has been explicitly incorporated.

Even more complex clustering is required to follow three-phase flow processes. Clustering algorithms capable of reproducing the effects of positive and negative spreading oils have been developed and are implemented in the program 3PHASE.

The following sections describe how important parts of the codes function. Details are given of how radii are sampled from probability distribution functions, the labelling of neighbours and clusters is also described. Details of each code are then clarified with flowcharts. Finally there is a description of the associated software and hardware.

The Model

The network consists of a three-dimensional cubic lattice of capillary tubes (referred to as bonds), which meet at $N_X \times N_Y \times N_Z$ nodes. The total number of

bonds is Nbond = $3N_xN_yN_z + N_yN_z$ (Figure E1). The bond radii and lengths are selected from given probability distributions. A pressure difference is maintained in the x-direction allowing fluid to enter and exit on y-z planes. In order to eliminate finite size effects, periodic boundary conditions are imposed across x-y and x-z boundaries. It would also be possible to set all flows equal to zero on the boundaries as, for large enough systems, these boundary conditions are equivalent; i.e. they do not affect the total flow through the system.

Conservation of mass at each node means that the total flow there must be zero. If Q_{ij} denotes the flow from a given bond j into node i, then:

$$\sum_{j=1}^{6} Q_{ij} = 0 \qquad (i = 1, N_x N_y N_z) \qquad \text{(E1)}$$

In order to solve these equations, a relationship is required which connects the flow through a single tube and the various parameters associated with it. It is assumed that Poiseuille's law holds so that

$$Q_{ij} = \frac{\pi R_{ij}^4}{8\eta L_{ij}} \Delta P_{ij} \qquad \text{(E2)}$$

Where ΔP_{ij} is the pressure difference across the bond, R_{ij} the radius of the bond, L_{ij} its length and η the fluid viscosity. The equations defined by Equation (E1) is a set of sparse simultaneous linear equations; these are solved by using either: (a) a NAG routine for sparse linear systems based on the Lanczos algorithm, or (b) an in-house routine based upon the incomplete Cholesky decomposition method. The latter is much faster and was used for the more complex multiphase problems.

Once the linear equations have been solved, the pressure field throughout the network is determined. From this, the total flow parallel to the pressure gradient can then be derived: this, then, simulates the flow of a single liquid through a connected network of capillary tubes.

Labelling of the Nodes

One of the first problems encountered in the development of the basic model was the labelling of nodes and bonds. For the purposes of assigning bond radii and solving the network pressure field, it was convenient to base the labelling scheme on the nodes and to distinguish between the x, y and z directions. For example, XBR (i, j, k) is the radius of the bond in the x-direction entering node (i, j, k) (Figure E2).

This labelling scheme is used repeatedly throughout the program. Note, however, that there are N_X+1 bonds in the x-direction compared to N_y and N_Z in the other orthogonal directions. At each face of the network there are "dangling" x-bonds which allow fluid to enter and exit the network. This means that for example, YBR (N_X+1, j, k) and ZBR (N_X+1 , j, k) do not exist, leading to continuity problems. These difficulties are overcome by assigning periodic boundary conditions, so that:

$$YBR (i, N_y+1, k) = YBR (i, 1, k),$$
$$ZBR (i, j, N_Z+1) = ZBR (i, j, 1),$$

This numbering scheme is illustrated in Figure E3.

Labelling of the Bonds.

When considering the labelling of the bonds for clustering, it is convenient to use a different method. All of the x-bonds are numbered first, then the y and z bonds. Begin by counting the x-bonds as shown in Figure E4. In each row there

are N_X+1 bonds and on each x-y plane (N_X+1).N_y bonds. This leads to the following expression for x-bond labelling:

$$xLabel = i + (j-1)(N_X+1) + (k-1)(N_X+1)N_y$$

where $1 \le i \le (N_X+1)$, $1 \le j \le N_y$, $1 \le k \le N_Z$. The total number of x-bonds is

$$xTotal = (N_X+1)\, N_y N_Z.$$

Moving on to the y-bonds there are N_X in each row and $N_y N_X$ in each plane; the labelling, *starting at NTX+1*, is given by:

$$yLabel = i+(j-1)\, N_X + (k-1)\, N_X N_y + xTotal$$

where $1 \le i \le N_X$, $1 \le j \le N_y$, $1 \le k \le N_Z$. The total number of y-bonds is:

$$yTotal = N_X N_y N_Z$$

The label for z-bonds is similarly:

$$zLabel = i+(j-1)\, N_X+(k-1)\, N_X N_y + xTotal + yTotal$$

where $1 \le i \le N_X$, $1 \le j \le N_y$, $1 \le k \le N_Z$ giving a total of $N_X N_y N_Z$ z-bonds.

This effectively means that all x-bonds are numbered between 1 and xTotal, all y-bonds between (xTotal+1) and (xTotal+yTotal), and all z-bonds between (xTotal+yTotal+1) and (Nbond).

Sometimes, it is necessary to find the unknown Cartesian coordinates of a numbered bond. Given a bond label m, is it possible to work out which bond it

is; i.e. to which node it is attached and whether it is an x, y or z bond. The type of bond can easily be checked;

$1 \le m \le xTotal$	x-bond
$xTotal+1 \le m \le xTotal+yTotal$	y-bond
$xTotal+yTotal+1 \le m \le Nbond$	z-bond

Now, if it transpires that m is an x-bond, its k label can be found from:

$$k = INT\left[\frac{FLOAT\,(m)-\delta}{FLOAT\left((N_x+1)N_y\right)}\right]+1$$

where δ is a small number less than 1.

Setting $m = m - (k-1)(N_X+1)\,N_Y$ allows the j label to be found similarly from:

$$j = \mathrm{INT}\left[\frac{FLOAT(m)-\delta}{FLOAT(N_x+1)}\right]+1$$

Finally, i is given by $i= m - (j-1)(N_X+1)$. So for a given bond label, the node to which it is attached, as well as its "Cartesian identity", can be found. Therefore the two methods for labelling nodes and bonds are simply related. This bond labelling is used extensively throughout the programs.

Sampling Radii from a Probability Distribution

Given a distribution of bond radii, the network values must be assigned randomly to each element. The problem of sampling from a distribution is now discussed. Suppose that the bond radii are distributed according to the probability density f(r) in the interval [a,b] as shown in Figure E5. Thus the

probability of a bond chosen at random having a radius in [r, r+dr] is given by f(r)dr. The probability of the radius being in the interval [a,R] is:

$$P(R) = \int_a^R f(r)dr \qquad \text{(E3)}$$

where P(b) = 1, P(R) is the *cumulative probability function* of f(r). If a number P is chosen at random in (0,1) then there is a number R such that:

$$P = \int_a^R f(r)dr = F(R) - F(a) \qquad \text{(E4)}$$

implying that $R = F^{-1}[P+F(a)]$. Take the case of a uniform distribution:

$$f(r) = \begin{cases} \dfrac{1}{b-a} & a \le r \le b \\ 0 & otherwise \end{cases}$$

and so:

$$P(R) = \frac{1}{b-a}\int_a^R dr = \frac{1}{(b-a)}(R-a).$$

So a random variable (radius) from the distribution f(r) can be found via the linear transformation:

$$R = a + P(b-a)$$

where P is uniformly generated in (0,1). Another example is the cubic distribution defined by:

$$f(r) = \begin{cases} \dfrac{4}{(b^4-a^4)}r^3 & a \le r \le b \\ 0 & otherwise \end{cases}$$

Now,

$$P(R)=\frac{4}{(b^4-a^4)}\int_a^R r^3\,dr=\frac{R^4-a^4}{(b^4-a^4)}$$

and

$$R=\left[a^4+P(b^4-a^4)\right]^{1/4}$$

However, it is not always possible to invert the probability distribution analytically. For example, the truncated normal distribution is not even analytically integrable; in the program, a NAG routine is used to integrate numerically.

Clusters and Clustering

Identifying Bond Types — Investigating flow behaviour near the percolation threshold (P_C) leads to a situation where there are isolated clusters, a spanning cluster and a flowing backbone cluster (which is a subset of the spanning cluster). At different times during a displacement, isolated, spanning and flowing clusters of all phases must be considered. In order to follow the progress of the system, each bond type is assigned a label Bond(i):

0 - water

1 - water in spanning cluster

2 - water in flowing cluster

10 - oil

11 - oil in spanning cluster

12 - oil in flowing cluster.

With this labelling scheme, relevant quantities can easily be calculated for each of the bond types.

Cluster Labelling — The next problem concerns the labelling of *clusters* of bonds in the network. In order to understand the problem, consider a specific example. Suppose that there exists a network of oil and water bonds. As mentioned above, the identifying labels are 10 for the oil bonds and 0 for the water bonds. An algorithm is required that will scan the network and assign a cluster label to each isolated group of bonds of a given type.

The simplest method is to move systematically through the network taking each bond, identifying all neighbours of the same type and assign them a cluster label (each bond has ten neighbours in three dimensional systems). At each step a check must be made to see if connections are being made to an already-labelled cluster. This can lead to problems, however, even in two dimensions. Take a simple example to illustrate this point. Figure E6 shows a two dimensional array of oil and water bonds, the shaded areas represent oil bonds. Begin at A and, moving horizontally, assign cluster labels (Iclus(i)) to all bonds connected the the first row of nodes. Moving across the first row there are three distinct clusters. So far so good! On the second row it is apparent that, when cluster 5 is reached, it is connected to cluster 1 and cluster 6 is connected to cluster 2. When the top row is scanned, it is discovered that cluster 2 is connected to cluster 1 (at B). So, a return journey has to be made in order to relabel all of cluster 2. With larger systems, even more confusion can arise, resulting in the network having to be scanned many times. In a large three dimensional network this can be a long laborious task occupying a large amount of memory (storing all of the cluster information) and using massive amounts of CPU time.

Fortunately there is a simple method that circumvents these difficulties. The algorithm was developed by Hoshen and Kopelman (1976) for two dimensional networks. This has been extended here to deal with three dimensional systems.

In order to understand this method, return to Figure E6 and start again. There is no difference with the previous method until (B) is reached, where clusters 1 and 2 join. Instead of going back and relabelling all of the clusters, an array of "improper labels", NP(i), is used to denote the fact that they have joined. Setting NP(2) = 1 records the fact that all the bonds in cluster 2 are actually connected to cluster 1.

By using this method, the network has only to be examined once. Although some of the labels in the array Iclus are incorrect, the correct connections are held in NP. When all of the bonds have been labelled, a sweep is made through the network and clusters are relabelled correctly using NP(i). For further reading see Stauffer and Aharony(1992) and references therein.

Trapping — The fluid within a pore remains trapped if it cannot escape to the outlet face of the network. The clustering algorithm is primarily used to determine whether or not a bond contains trapped fluid: if the cluster number of the bond in question does not match any cluster numbers of the outlet bonds, then the bond is trapped. Trapping criteria need not necessarily be applied in all cases, however; escape via film-flow may be allowed in some instances. By further adapting the clustering process, accessibility along water-wet pathways during waterfloods of mixed- and fractionally-wet systems can also be examined.

Neighbours — Another problem encountered during clustering concerns the identity of bond neighbours. Given the *node* (i, j, k) it is easy to list its six nearest neighbours; (i-1, j, k), (i+1, j, k) etc.. Consider, however, the difficulties associated with finding the neighbours of a *bond* .

Take the example of an x-bond entering node (i, j, k). With end effects and periodic boundary conditions, great care must be taken when listing its neighbours:

Case (i) x-neighbours:

(a)	$i = 1$	XBR(2, j, k)
(b)	$i = N_X+1$	XBR(N_X, j, k)
(c)	$i \neq 1, N_X + 1$	XBR(i-1, j, k) and
		XBR(i+1, j, k)

Case (ii) y-neighbours:

(a)	$i = 1$	YBR(1, N_y, k)
	$j = N_y$	YBR(1, 1, k)
(b)	$i = 1$	YBR(1, j, k)
	$j \neq N_y$	YBR(1, j+1, k)
(c)	$i = N_X + 1$	YBR(N_X, N_y, k)
	$j = N_y$	YBR(N_X, 1, k)
(d)	$i = N_X+1$	YBR(N_X, j, k)
	$j \neq N_y$	YBR(N_X, j+1, k)
(e)	$i \neq 1, N_X + 1$	YBR(i-1, N_y, k)
	$j = N_y$	YBR(i, N_y, k)
		YBR(i-1, 1, k)
		YBR(i, 1,k)

(f) all other cases	YBR(i-1, j, k)
	YBR(i, j, k)
	YBR(i-1, j+1, k)
	YBR(i, j+1, k)

Case (iii) z neighbours: these are found in a similar way to the y-neighbours.

The neighbours are enumerated in subroutines *NeighX, NeighY, NeighZ* where they are used to find adjacent bonds of the same type.

Software and Hardware

General — All non-graphics programs are written in FORTRAN 77 and utilise NAG library routines for random number generation and linear solving. They have been run exclusively on SUN systems, although some sections were developed and tested with Microsoft Fortran on a Macintosh SE/30. The running time associated with a simulation depends upon the size of the network considered, whether the displacement is steady- or unsteady-state, and whether or not cluster analysis is being carried out. For a 15x15x15 network the running time can vary from 5 seconds (single-phase, steady-state flow), up to several hours (unsteady-state, multi-phase flow in systems of non-uniform wettability). All calculations were performed on a SPARC 2 under Unix. This machine has a main memory of 32Mb, virtual memory of 414Mb and runs FORTRAN 77 version 1.4. Output data is transferred to a Macintosh 180c Powerbook and graphs obtained using Cricket Graph.

Graphics Interface — All FORTRAN 77 programs were linked to an in-house graphics program coded using X Windows under C. Graphical output could be displayed directly from the SPARC 2 workstation, enabling the on-screen visualisation of an entire displacement as it happened.

Note on NAG Routines Used — The use of NAG routines in this program is essential for selecting random numbers and solving the pressure field equations. The routine G05CAF(X) is used to choose a number uniformly from (0,1). Calling G05CCF at the beginning of the program ensures that a *different* sequence of random numbers will be chosen each time the program is run. This means that the program will produce different networks albeit with the same radial distribution. Note that the same sequence could be repeated by calling G05CBF(X). The set of $N_x N_y N_z$ linear equations expressing conservation of flow at each node are solved using F04MBF. This routine is specifically designed to solve a set of sparse linear equations using the Lanczos algorithm.

Flow Diagrams of Programs

A series of flowcharts for each of the programs is presented in Figures E7 to E14. A separate chart, Figure E15, describes the clustering algorithm used in all cases. More precise details relating to a particular flow regime can be found in the relevant chapter.

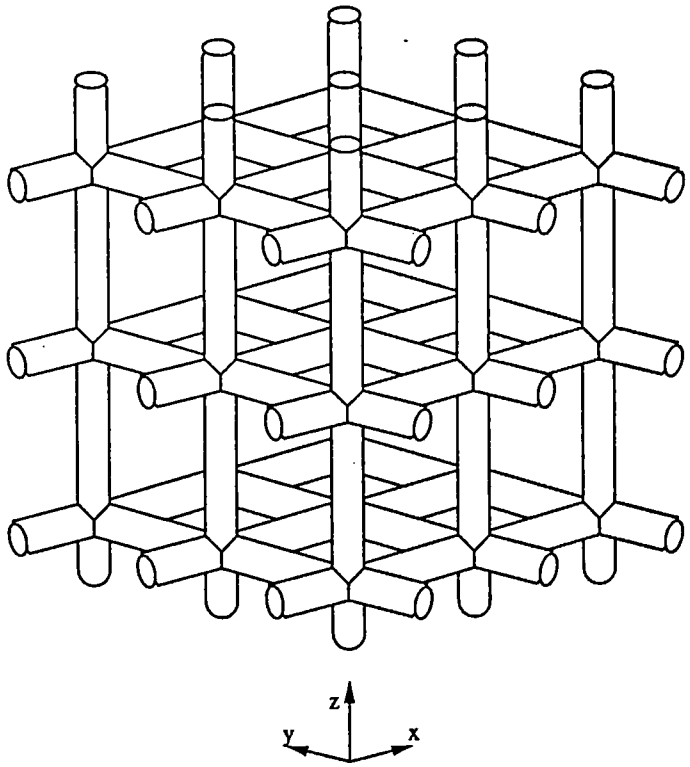

Figure E1 Three-dimensional pore network of nodal dimensions $N_x x N_y x N_z$.

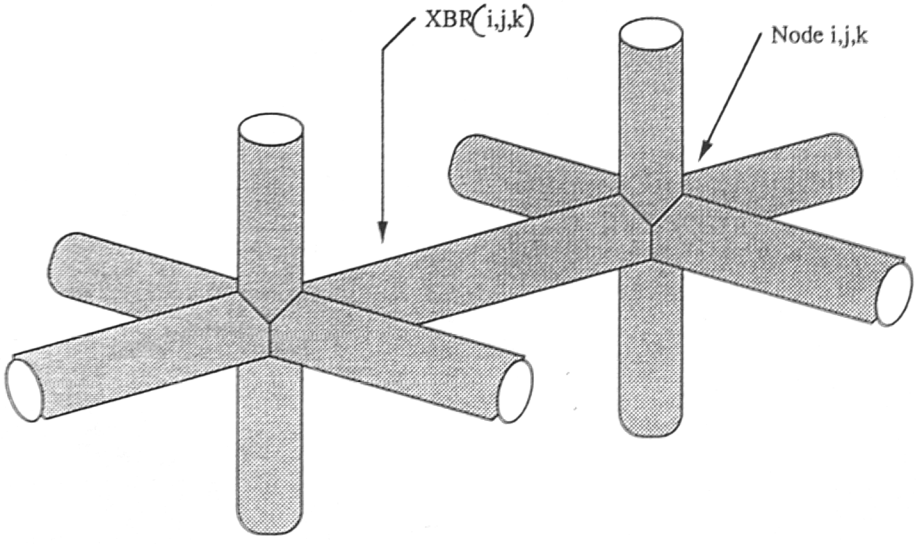

Figure E2 Illustration of how bonds and nodes are identified.

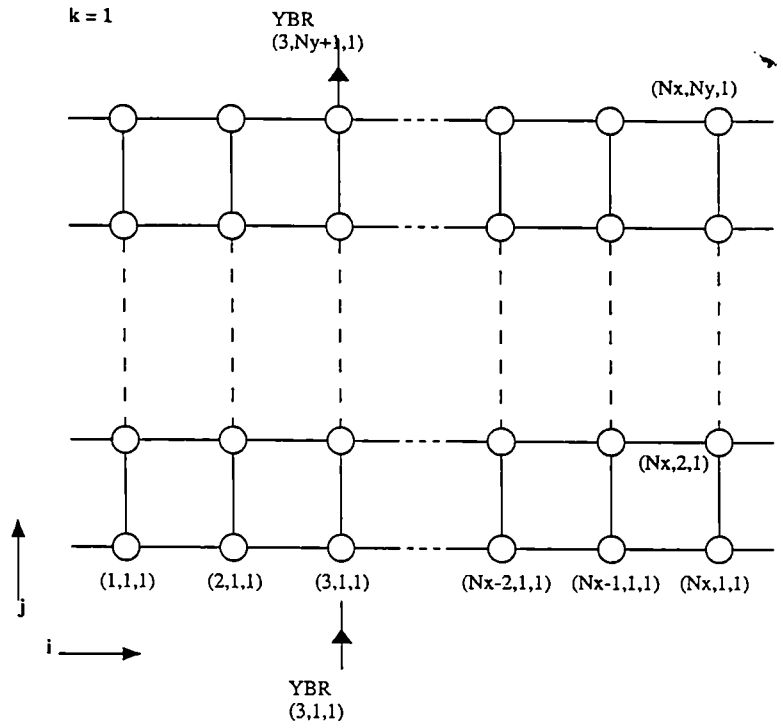

Figure E3 Labelling of the nodes.

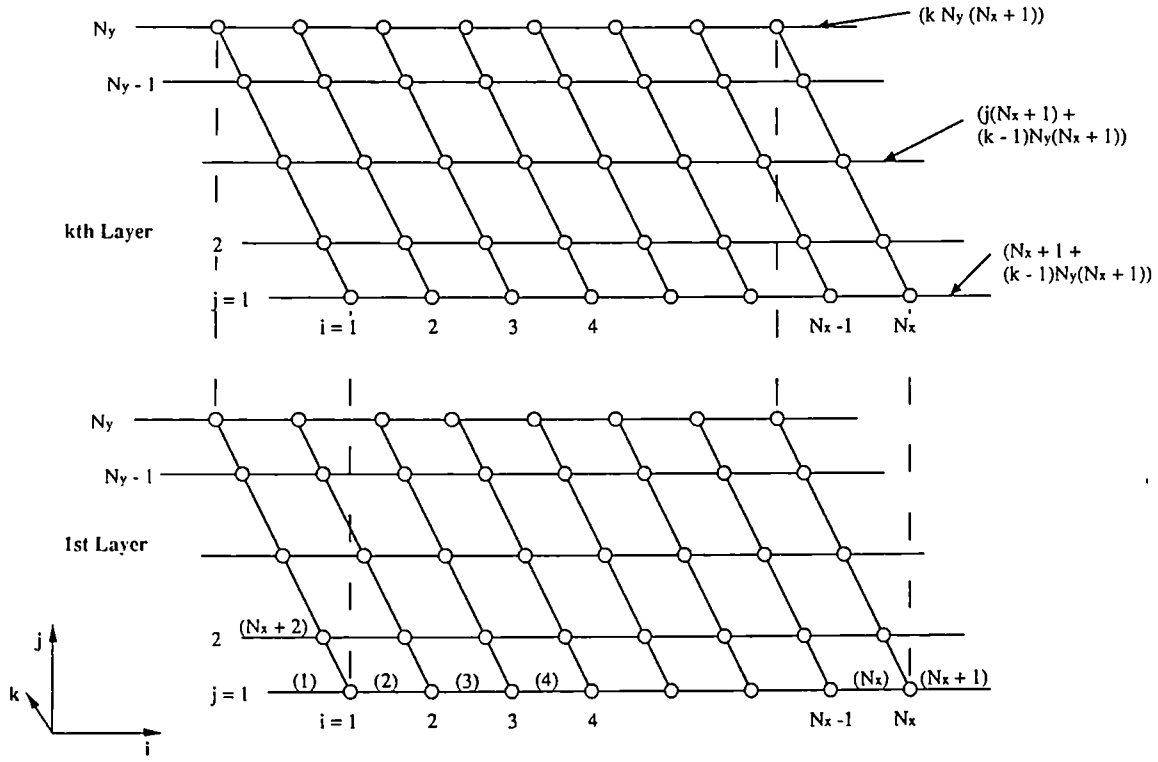

Figure E4 Labelling of the bonds.

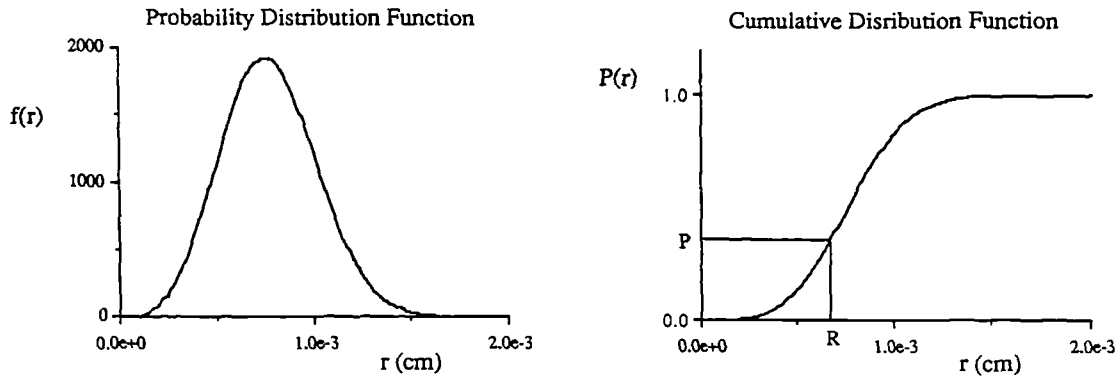

Figure E5 (a) Probability density function for the bond radii, (b) the cumulative probability distribution.

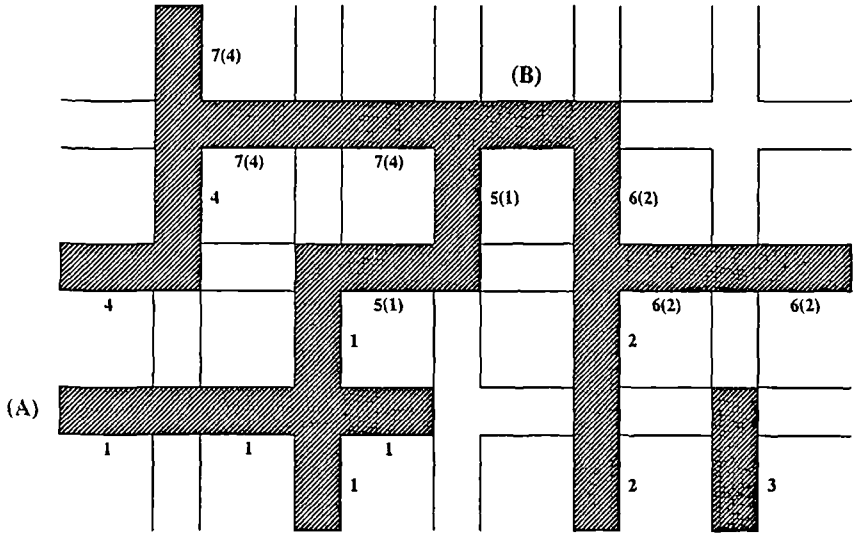

Figure E6 Example of cluster labelling.

FLOWCHART FOR 1PHASE

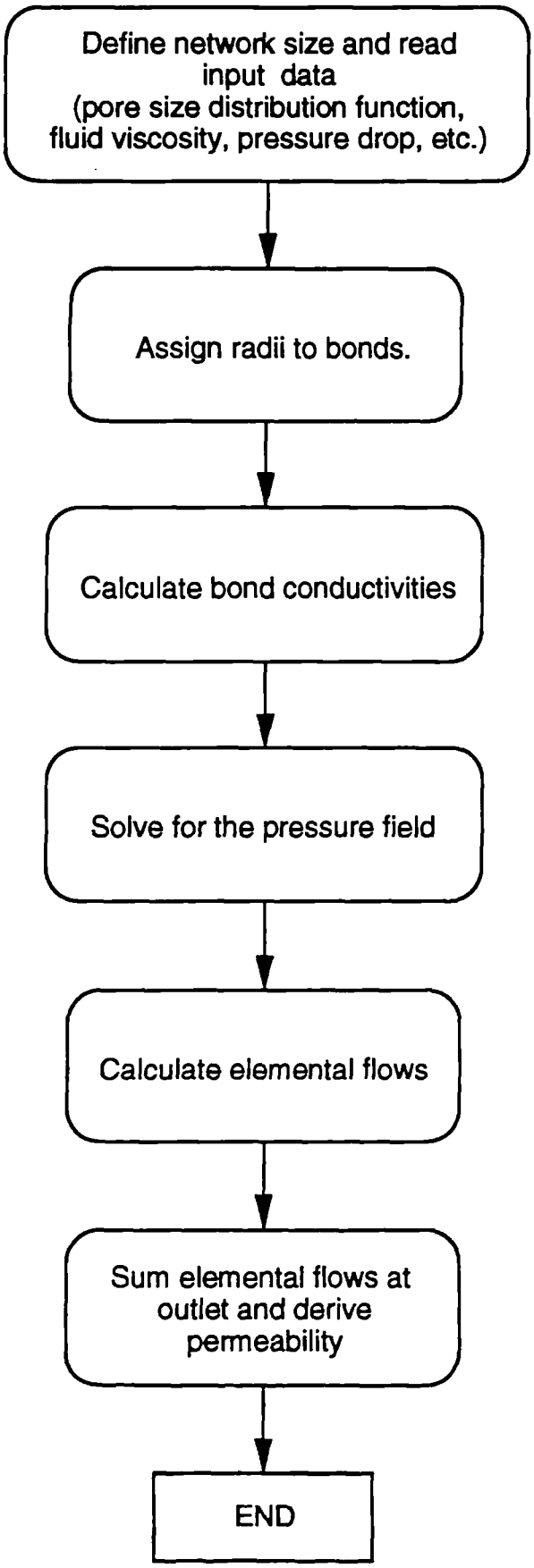

FLOWCHART FOR PERC

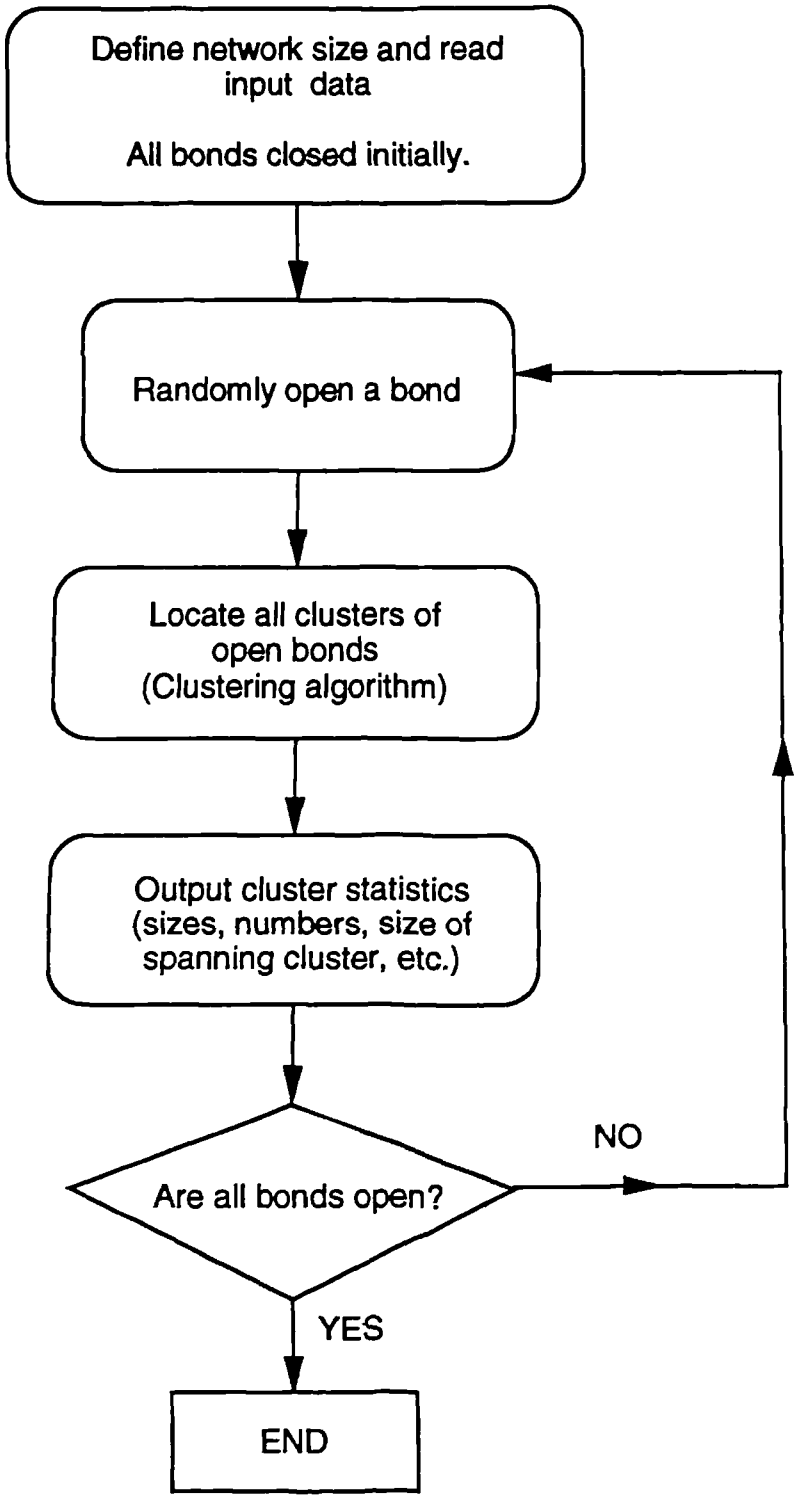

FLOWCHART FOR DRAINAGE

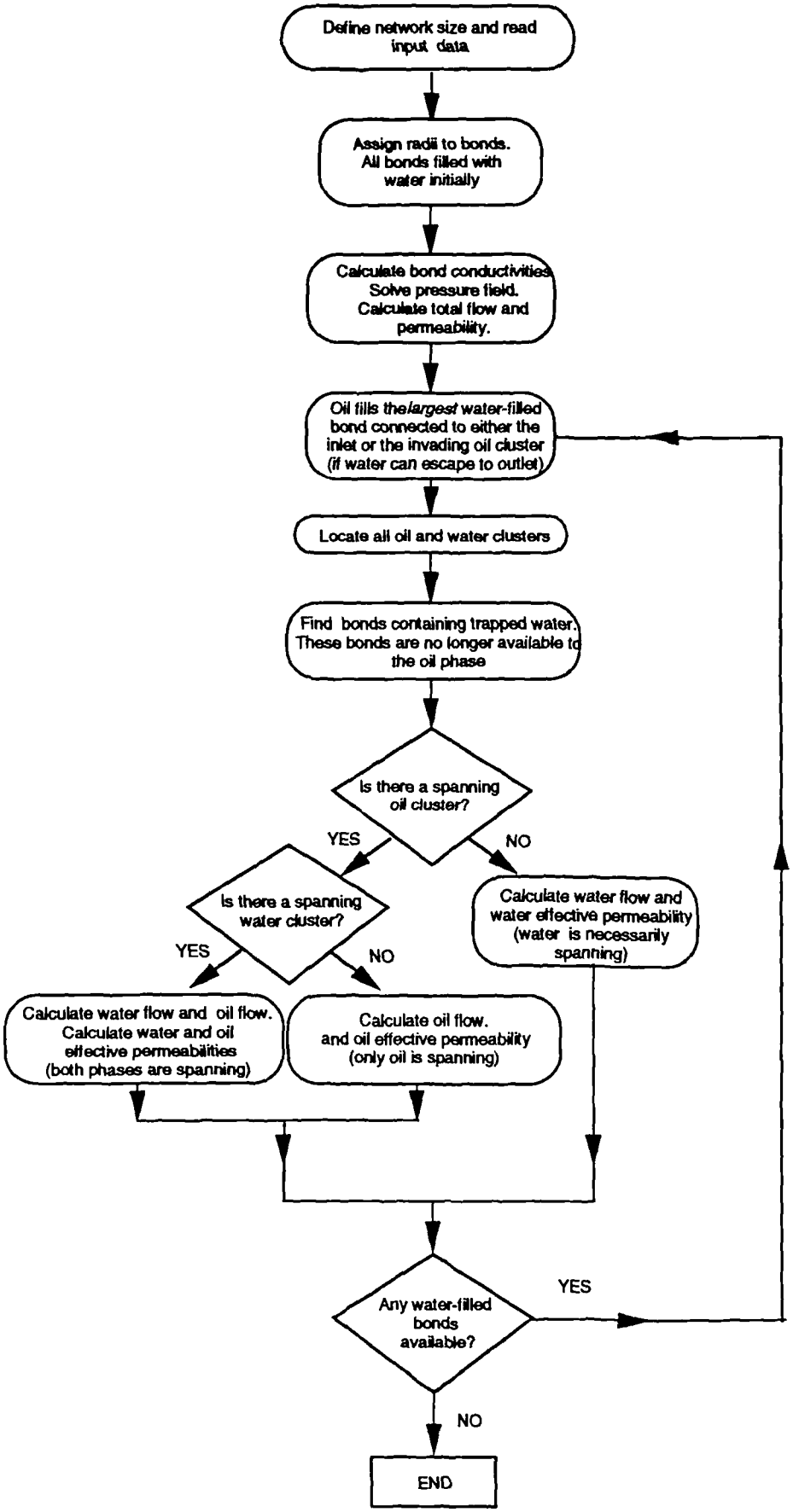

FLOWCHART FOR IMBIBITION

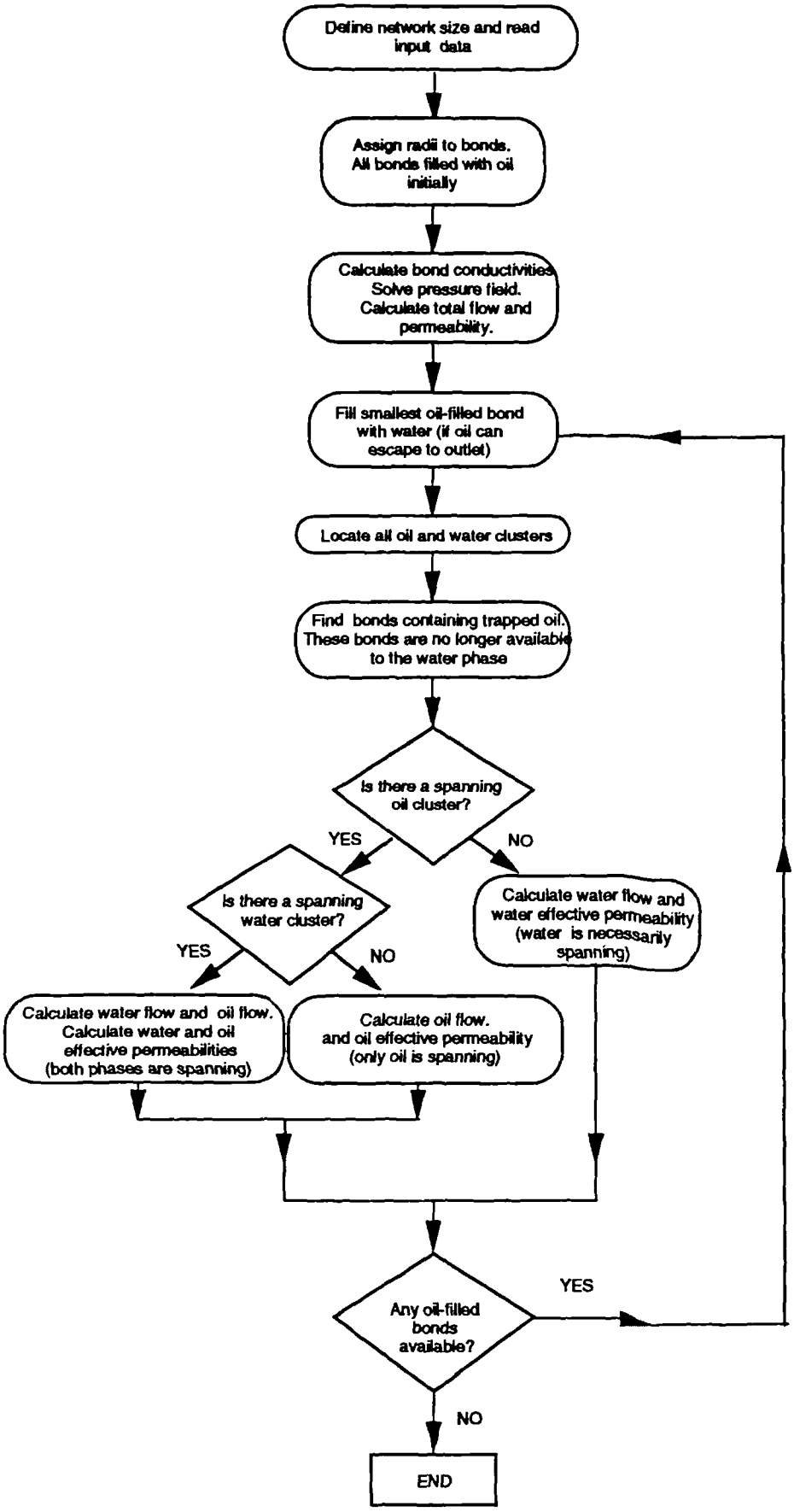

FLOWCHART FOR MIXWET

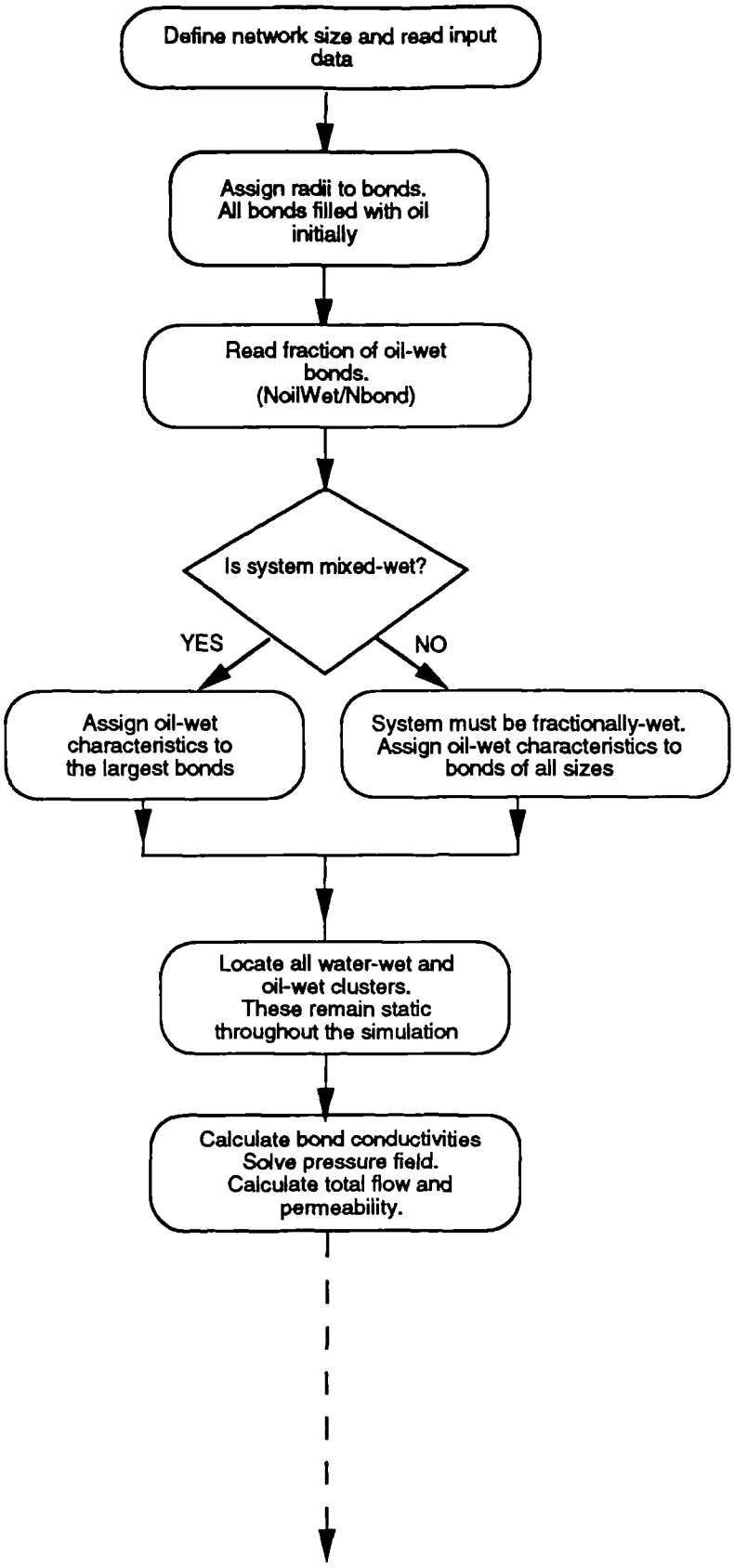

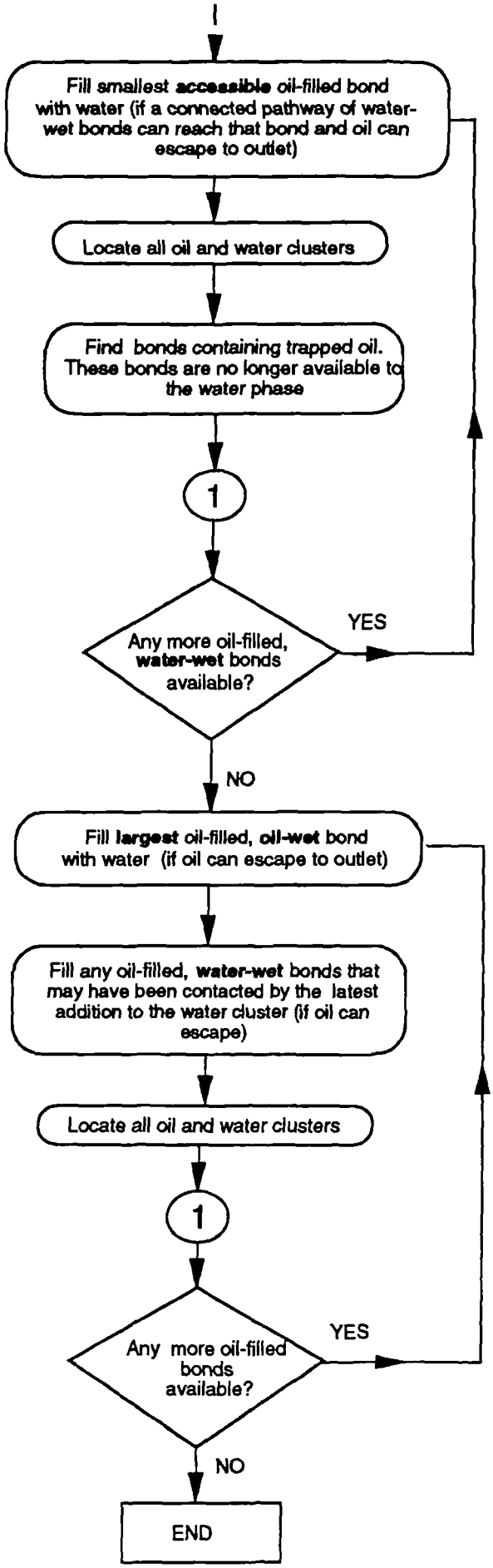
I
Fill smallest accessible oil-filled bond with water (if a connected pathway of water-wet bonds can reach that bond and oil can escape to outlet)
Locate all oil and water clusters
Find bonds containing trapped oil. These bonds are no longer available to the water phase
1
Any more oil-filled, water-wet bonds available?
YES
NO
Fill largest oil-filled, oil-wet bond with water (if oil can escape to outlet)
Fill any oil-filled, water-wet bonds that may have been contacted by the latest addition to the water cluster (if oil can escape)
Locate all oil and water clusters
1
Any more oil-filled bonds available?
YES
NO
END

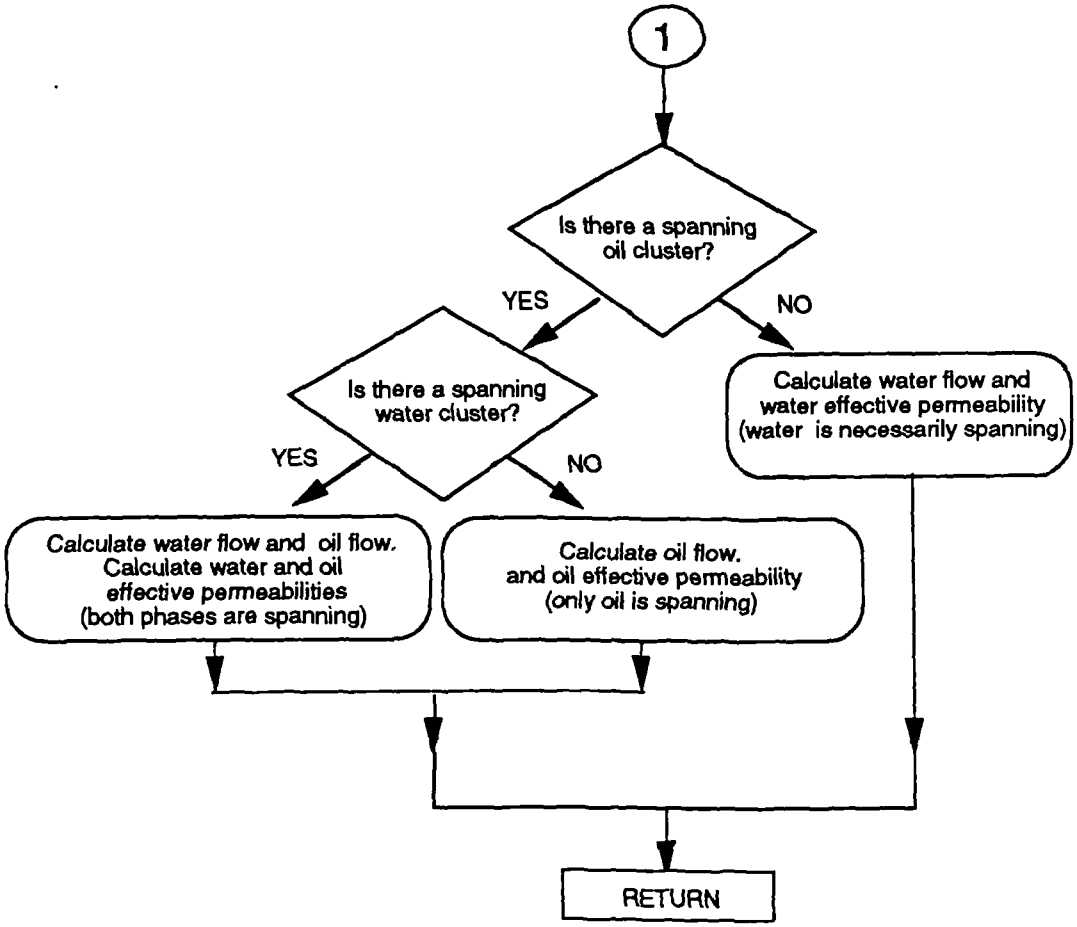
1
Is there a spanning oil cluster?
YES
NO
Is there a spanning water cluster?
Calculate water flow and water effective permeability (water is necessarily spanning)
YES
NO
Calculate water flow and oil flow. Calculate water and oil effective permeabilities (both phases are spanning)
Calculate oil flow. and oil effective permeability (only oil is spanning)
RETURN

FLOWCHART FOR UNSTEADY(DR)

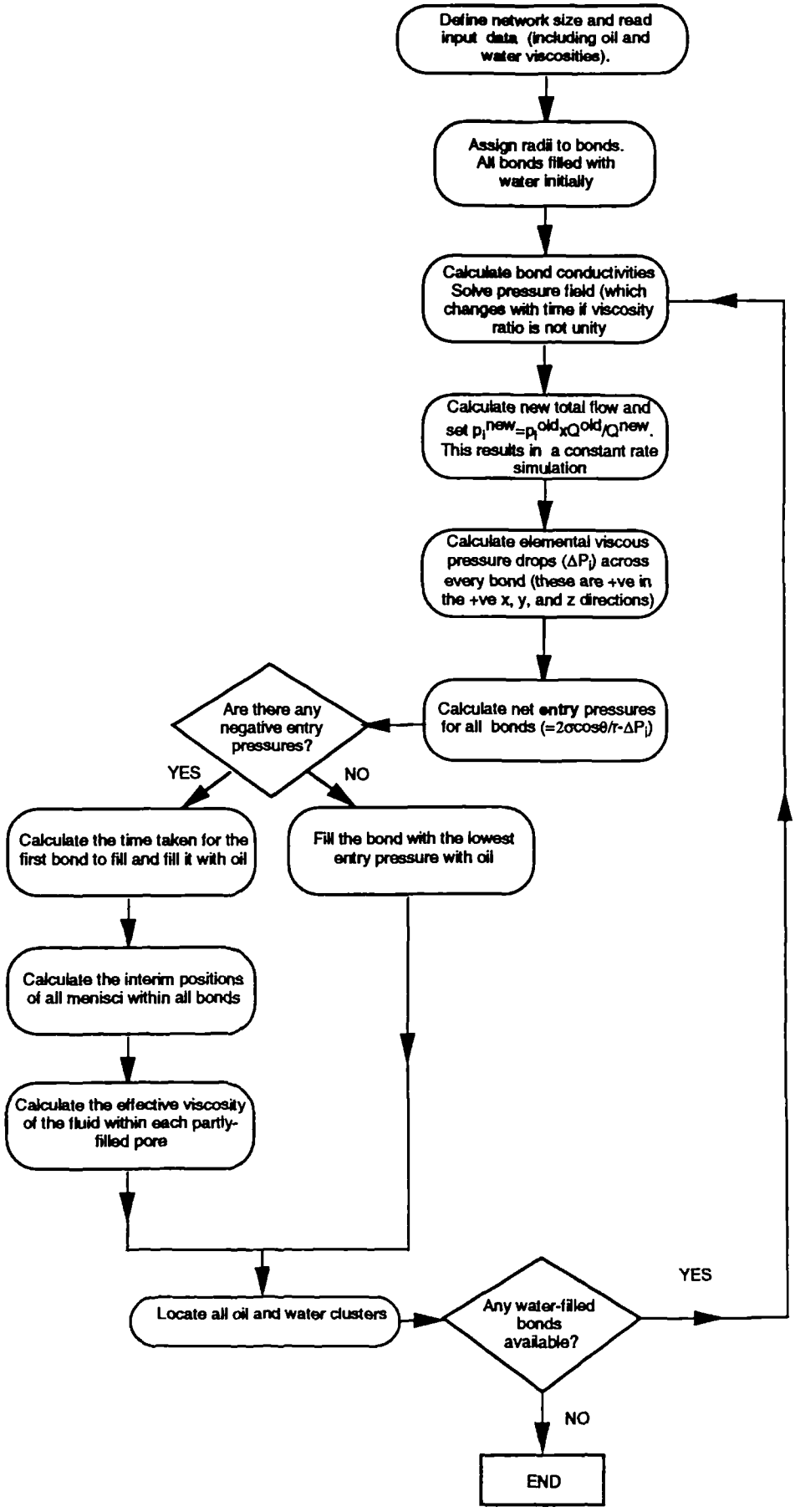

FLOWCHART FOR UNSTEADY(IMB)

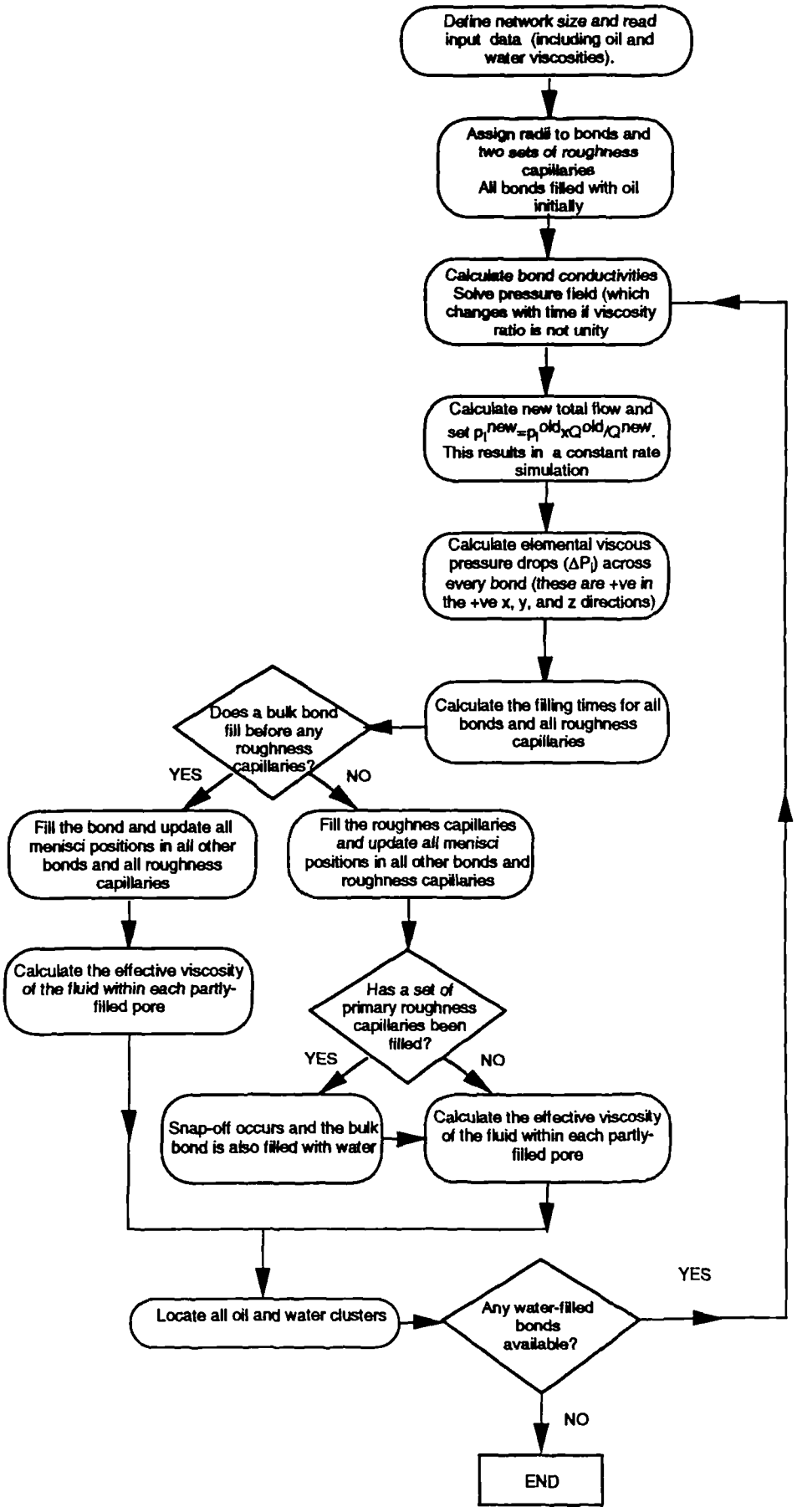

FLOWCHART FOR 3PHASE

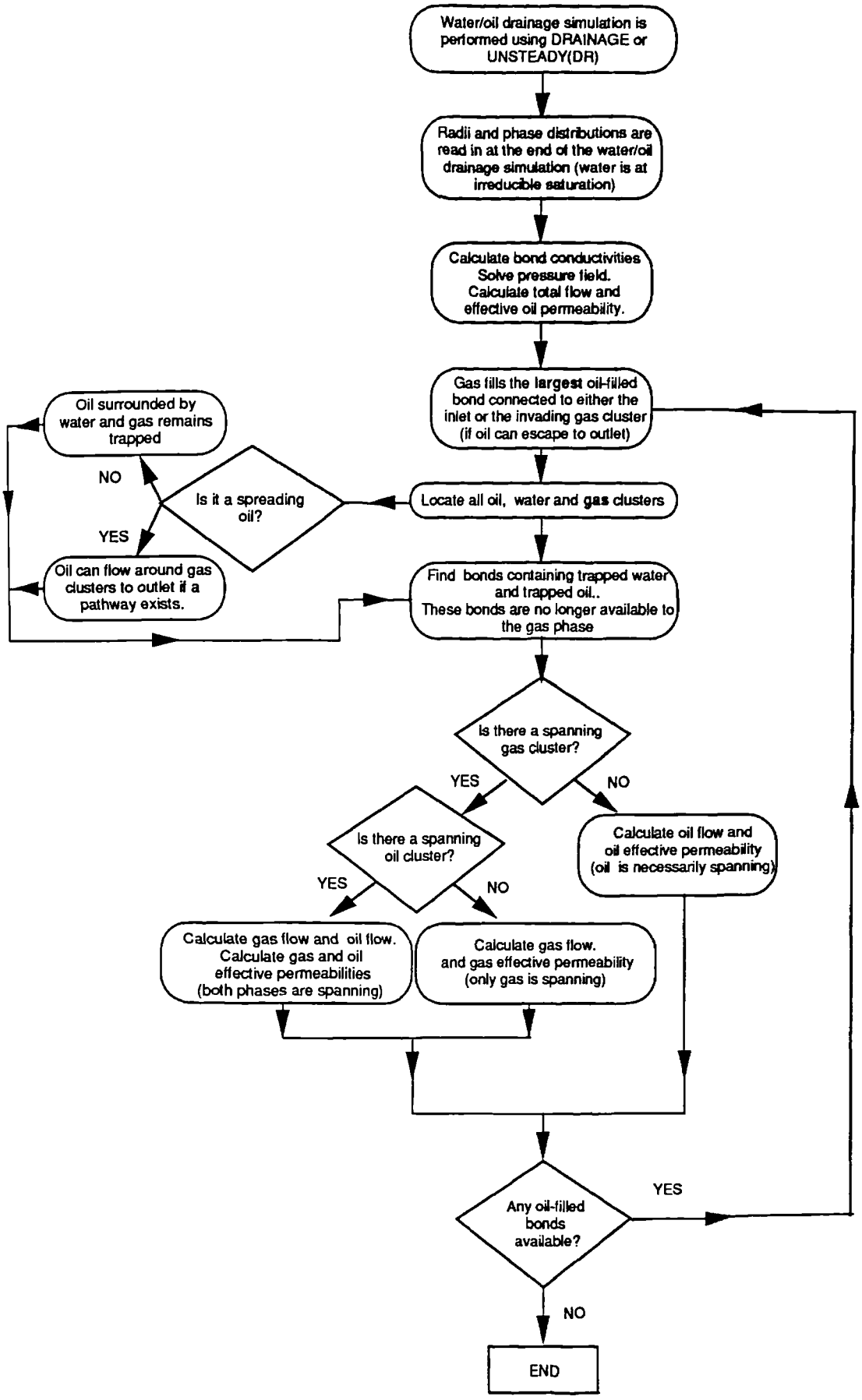

FLOWCHART FOR CLUSTERING

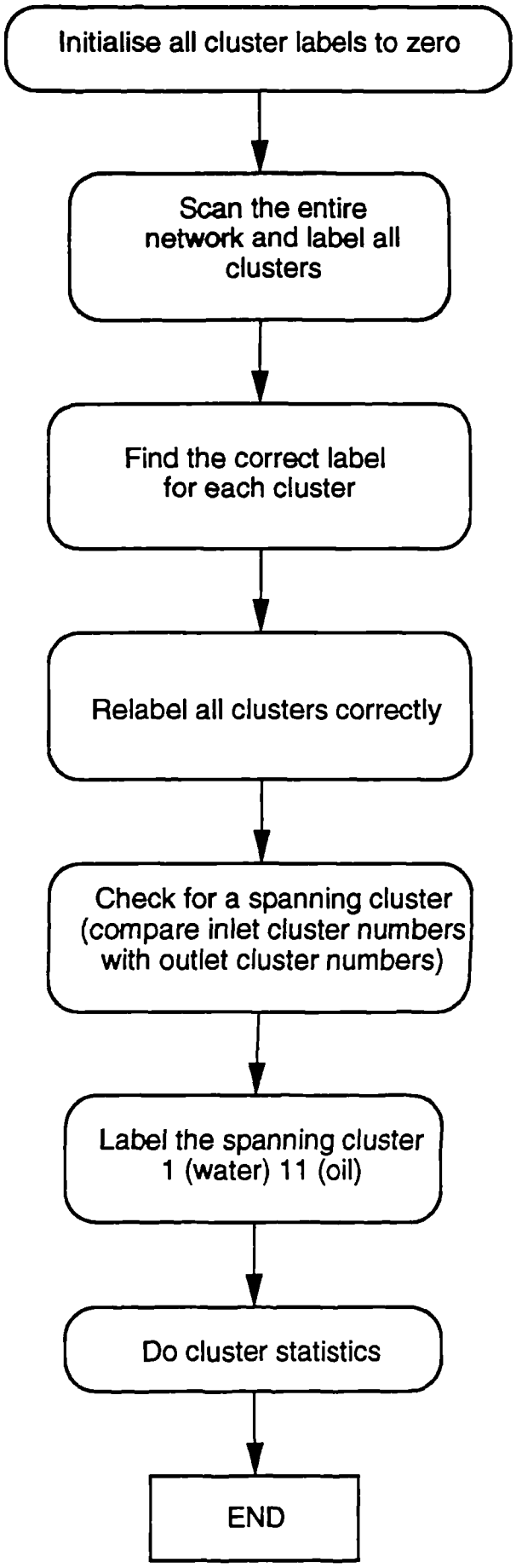

REFERENCES

[1] Adler, P. M., Jacquin, C. G. and Quiblier, J. A., "Flow in Simulated Porous Media", Int. J. Multiphase Flow **16**, 691 (1990).

[2] Aleman, M.A., Ramamahan, T.R. and Slattering, J.C. , " A Statistical Structural Model For Unsteady-State Displacement in Porous Media", Paper **SPE 13265** Presented at the SPE Annual Technical Conference and Exhibition, Houston TX, Sept 16-19, (1984).

[3] Allen, J. R. L., *Sedimentary Structures: Their Classification and Physical Basis*, Vols. 1 and 2, Elsevier, Amsterdam, Netherlands, (1982).

[4] Ambegaokar, V., Halperin, B. I. and Langer, J. S., "Hopping Conductivity in Disordered Sysrems", Phys. Rev. B, **4**, 2612 (1971).

[5] Amott, E., "Observations Relating to the Wettability of Porous Rock", Trans AIME **216**, 156 (1959).

[6] Anderson, W.G., "Wettability Literature Survey-Part 1: Rock/Oil/Brine Interaction and the Effects of Core Handling on Wettability", JPT (Oct 1986), 38, 1125.

[7] Anderson, W.G., "Wettability Literature Survey-Part 2: Wettability Measurement", JPT (Nov 1986), 38, 1246.

[8] Anderson, W.G., "Wettability Literature Survey-Part 3: The Effects of Wettability on Electrical Properties of Porous Media", JPT (Dec 1986), 38, 1371.

[9] Anderson, W.G., "Wettability Literature Survey-Part 4: The Effects of Wettability on Capillary Pressure", JPT (Oct 1987), 39, 1283.

[10] Anderson, W.G., "Wettability Literature Survey-Part 5: The Effects of Wettability on Relative Permeability", JPT (Nov 1987), 39, 1453.

[11] Anderson, W.G., "Wettability Literature Survey-Part 6: The Effects of Wettability on Waterflooding", JPT (Dec 1987), 39, 1606..

[12] Archer, J. R. and Wong, S. W., "Interpretation of Laboratory Waterflood Data by Use of a Reservoir Simulator", preprint for the 46th SPE Annual Technical Conference and Exhibition. Op. cit. Dullien, F. A. L. (1979).

[13] Aziz, K. and Settari, T., *Petroleum Reservoir Simulation* , pp 30-38, Applied Science Publisher, London, (1979) .

[14] Baker, L.E., "Three-Phase Relative Permeability Correlations", **SPE/DOE 17369**, presented at the SPE/DOE Symposium on Enhanced oil Recovery, Tulsa, Oklahoma, April 17-20, 1988.

[15] Bardon, C. and Longeron, D., "Influence Of Very Low Interfacial Tensions On Relative Permeability", SPE 7609, presented at the 53rd SPE Annual Technical Conference and Exhibition, Houston, TX., (1978).

[16] Benner, F. C. and Bartell, F. E., "The Effect of Polar Impurities Upon Capillary and Surface Phenomena in Petroleum Production", Drill. Prod. Pract. **341**, 209 (1941).

[17] Berman, D., Orr, B. G., Jaeger, H. M. and Goldman, M.,"Conductance of Filled Two-Dimensional Networks", Phys. Rev. B, 33, 4301 (1986).

[18] Berry, J.F., Little, A.J.H., and Skinner, R.C., "Differences in Gas/Oil and Gas/Water Relative Permeability", submitted to the 8th SPE/DOE Symposium on Enhanced oil Recovery, Tulsa, Oklahoma, April 21-24, 1992.

[19] Blunt, M.J. and King, P., "Macroscopic Parameters from Simulations of Pore Scale Flow", Phys. Rev. A., **42**, 8, 4780 (1990).

[20] Blunt, M.J. and King. P., "Relative Permeabilities from Two and Three Dimensional Pore Scale Network Modelling", Transport in Porous Media, **6**, 407 (1991).

[21] Blunt, M. J., King, M. J., and Scher. H., "Simulation and Theory of Two Phase Flow in Porous Media", Phys Rev A, **46**, No 12, 7680, (1992).

[22] Boneau, D.F. and Clampitt, R.L., "A Surfactant System for the Oil-Wet Sandstone of the North Burbank Unit", JPT (May 1977), 501.

[23] Braithwaite, C.I.M. and Schulte, W.M., "Transforming The Future of the Brent Field: Depressurisation - The Next Development Phase.", **SPE 25026**, presenred at EUROPEC, Cannes, France, 16-18 Nov. 1992.

[24] Broadbent, R. and Hammersley, J. M., "Percolation Processes, Crystals and Mazes", Proc. Camb. Phil. Soc. **53**, 629 (1957).

[25] Brooks, R. H. and Corey, A. T., "*Hydraulic Properties of Porous Media*", Hydrology papers No. 3 Colorado State University, Colorado (1964).

[26] Brown, R.J.S. and Fatt, I., "Measurements of Fractional Wettability of Oilfield Rocks by the Nuclear Magnetic Relaxation Method", Trans AIME **207**, 262 (1956).

[27] Bruggemann, D. A. G., "Berechung Verschiededer Physikalischer Konstanten von Heterogenen Substanzen. I. Dieletrizitatskonstanten und Leitfahigkeiten der Mischkorper aus Isotropen Substanzen", Ann. Phys. (Leipz.), **24**, 636 (1935).

[28] Bryant, S. and Blunt, M., "Prediction of Relative Permeability in Simple Porous Media", Phys. Rev. A **46**, 2004 (1992).

[29] Büche, W., Z. Ver. deuts. Ing. Beih. Verfahrenstech, **1937**, 155 (1937). Op. cit. Scheidegger, A. E. (1963).

[30] Buckley, S. E. and Leverett, M. C., "Mechanism of Fluid Displacement in Sands", Trans. AIME **146**, 107, (1942).

[31] Burdine, N. T., "Relative Permeability Calculations from Pore Size Distribution Data", Trans. AIME **198**, 71 (1953).

[32] Carmen, P.C., "Fluid Flow Through Granular Beds", Trans. Inst. Chem. Eng., London, **15**, 150 (1937).

[33] Carmen, P.C., "Determination of the Specific Surface of Powders", J. Soc. Chem. Ind., **57**, 225 (1938).

[34] Carmen, P.C. , "Flow Of Gases Through Porous Media," Butterworths, London (1956).

[35] Caudle .B.H, Slobod.R.L. and Brownscamb.E.R ., " Further Development in the Laboratory Determination of Relative Permeability", Trans .AIME **192**, 145-50 (1951).

[36] Chandler, R., Koplik., J., Lerman, K. and Willemsen, J.F., "Capillary Displacement and Percolation in Porous Media", J. Fluid Mech., **119**, 249 (1982).

[37] Chang, K. S. and Dullien, F. A. L., "Section Diameter Method for Non-Spherical Objects", J. Microsc. **108**, 61 (1976).

[38] Chatzis, I., M. A. Sc. Dissertation, Univ. Of Waterloo, Canada (1976).

[39] Chatzis, I., PhD Thesis, Univ. Of Waterloo, Canada (1980).

[40] Chatzis, I. And Dullien, F.A.L. , "Modelling Pore Structure by 2D and 3D Networks with Application to Sandstone", J. Can. Pet. Technol., **16**, 97 (1977).

[41] Chatzis, I. and Dullien, F.A.L., "Dynamic Immiscible Displacement Mechanisms in Pore Doublets: Theory Versus Experiment", J. Coll. Int. Sci. **91**, 1, 199, (1983).

[42] Chilingar, G.V. and Yen, T.F., "Some Notes on Wettability and Relative Permeabilities of Carbonate Reservoir Rocks II", Energy Sources **1**, 67 (1983).

[43] Chen, J-D. and Koplik, J. , "Immiscible fluid displacement in Small Networks", J. Colloid Int. Sci., **108**, 304, (1985).

[44] Chen, J-D. and Wilkinson, D. , "Pore-Scale Viscous Fingering in Porous Media", Phys. Rev. Lett., **55**, 1892, (1985).

[45] Childs, E. C. and Collis-George, N., "The Permeability of Porous Materials", Proc. R. Soc. Lond Ser. A **201**, 392 (1950).

[46] Cieplak, M. and Robbins, M.O., "Dynamical Transition in Quasistatic Fluid Invasion in Porous Media", Phys. Rev. Lett., **60**, 2042 (1988).

[47] Cohen, M.H. And Lin, C. , *Macroscopic Properties Of Disordered Media*, Eds. R. Burridge, S. Childress And G. Papanicolaou, Springer-Verlag, Berlin (1983).

[48] Collins, R. E., *Flow of Fluids Through Porous Materials*, Van Nostrand-Reinhold, Princeton, NJ (1961).

[49] Corbett, P. W. M., Ringrose, P. S., Jensen, J.L. and Sorbie, K. S., "Laminated Clastic Reservoirs; The Interplay of Capillary Pressure and Sedimentary Architecture", **SPE 24699** presented at the SPE 67th Annual Technical Conference, Washington, DC, 4-7 Oct 1992.

[50] Corey, A.T., "The Interrelation Between Gas and Oil Relative Permeabilities", Prod. Monthly **19**, 38 (1954).

[51] Corey, A.T. and Rathjens, C.H., "The Effect of Stratification on Relative Permeability", Trans. AIME **207**, (358) 69 (1956).

[52] Corey, A.T., Rathjens, C.H., Henderson, J.H. and Wyllie, M.R.J., "Three-Phase Relative Permeability", Trans AIME **207**, 349 (1956).

[53] Craig, F.F., *The Reservoir Engineering Aspects of Waterflooding*, Monograph Series, SPE, Richardson, TX 3 (1971).

[54] Christoffersen, K.R., Whitson, C.H, Da Silva, F.V., and Haldoupis, A.J., "Measuring Capillary Pressure of Chalk Samples at Elevated Pressures and Varying Interfacial Tension", 4th North Sea Chalk Symposium, Sept. 21-23, Deauville, France (1992).

[55] Danesh, A., Peden, J.M., Krinis, D., and Henderson, G.D., "Pore Level Visual Investigation of Oil Recovery by Solution Gas Drive and Gas Injection", **SPE 16956**, presented at the 62nd Annual Technical Conference and Exhibition of the SPE, Dallas, TX, Sept. 27-30, 1987.

[56] Da Silva, F.V., "Primary and Enhanced Recovery of Ekofisk Field: A Single and Double- Porosity Numerical Simulation Study", **SPE 19840**, presented at the 1989 SPE Annual Technical Conference and Exhibition, San Antonio,TX, Oct 8-11.

[57] David, C., Gueguen, X. and Pampoukis, G., "Effective Medium Theory and Network Theory Applied to the Transport Properties of Rock", J. Geophys. Research 95, 6993 (1990).

[58] Dawe, R.A. and Hawes, R.I., "Fluid/Solid and Fluid/Fluid Interfacial Phenomena in Three Phase Flow in Porous Media", Presented at the 2nd

International Symposium on Evaluation of Reservoir Wettability and Its Effect on Oil Recovery, Edinburgh, Scotland, 21-23 September 1992.

[59] Delshad, M. and Pope, G.A., " Comparison of Three-phase Oil Relative Permeability Models", Transport in Porous Media **4** , 59-83 (1989).

[60] Dias M.M. and Payatakes, A.C., "Network Models for Two-Phase Flow in Porous Media. Part 2. Motion of Oil Ganglia", Journ. Fluid Mech., **164**, 337 (1986).

[61] Dias M.M. and Payatakes, A.C., "Network Models for Two-Phase Flow in Porous Media. Part 1. Immiscible Microdisplacement of Nonwetting Fluids", Journ. Fluid Mech., **164**, 305 (1986).

[62] Dias, M.M. and Wilkinson, D. , "Percolation with Trapping", J. Phys. A., **19**, 3131 (1986).

[63] Diaz, C.E., Chatzis, I. and Dullien, F.A.L. , "Simulation of Capillary Pressure Curves Using Bond Correlated Site Percolation on a Simple Cubic Network", Transport in Porous Media, **2**, 215, (1987).

[64] Dietrich, J.K., "Relative Permeability During Cyclic Steam Stimulation of Heavy Oil Reservoirs", **SPE 7968**, presented at SPE California Regional Meeting, Ventura, April 18-0, 1979.

[65] Dietrich, K. and Bondor, P.L., "Three-Phase Oil Relative Permeability Models", **SPE 6044**, paper presented at the 51st SPE Annual Technical Conference and Exhibition, New Orleans, LA, 3-6 Oct (1976).

[66] Dodd, C.G. and Kiel, O.G. , "Evaluation of Monte Carlo Methods in Studying Fluid-Fluid Displacement and Wettability in Porous Rock", J. Phys. Chem., **63**, 1646 (1959).

[67] Donaldson, E.C., "Oil-Water-Rock Wettability Measurement", Proc. Am. Chem. Soc. 26, No.1, 110 (1981)

[68] Donaldson, E. C. and Dean, G. W., "Two-and Three-Phase Relative Permeability Studies", RI6826, USBM (1966).

[69] Donaldson, E.C. and Thomas, R.D., "Microscopic Observations of Oil Displacement in Water-Wet and Oil-Wet Systems", Paper SPE 3555 presented at the 1971 SPE Annual Technical Conference and Exhibition, New Orleans, Oct 3-6.

[70] Donaldson, E.C., Thomas, R.D., and Lorenz, P.B., "Wettability Determination and Its Effect on Recovery Efficiency", SPEJ (March 1969), 13.

[71] Doyen, P.M., "Permeability, Conductivity, and Pore Geometry of Sandstone", J. Geophys. Res. **93**, B7 7729 (1988).

[72] Dria, D.E., Pope, G.A. and Sepehnoori, K., "Three-Phase Gas/Oil/Brine Relative Permeabilities Measured Under Carbon Dioxide Flooding Conditions", **SPE/DOE 20184** presented at the Seventh Symposium on Enhanced Oil Recovery, Tulsa, Oklahoma, April 22-25 (1990).

[73] Dullien, F.A.L., "*Porous Media, Fluid Transport and Pore Structure,*", Academic Press Inc., New York (1979)

[74] Dullien, F.A.L., In proceedings of "Physics of Granular Media", Les Houches, France (1990).

[75] Dullien, F.A.L., Catalan, L., Chatzis, I., and Collins, A., "The Effect of Wettability and Heterogeneities on the Recovery of Waterflood Residual Oil With Low Pressure Inert Gas Injection, Assisted by Gravity Drainage", Presented at the 6th European IOR-Symposium, Stavangar, Norway, May 21-23, 1991.

[76] Dullien, F.A.L. and Dhawan, G.K., "Characterisation of Pore Structure by a Combination of Quantitative Photomicrography and Mercury Porosimetry", J. Coll. Int. Sci., **47**, 2, 337 (1974).

[77] Dumoré, J.M., "Development of Gas Saturation During Solution-Gas Drive in an Oil Layer Below a Gas Cap", SPEJ (Sept), 211-218, (1970).

[78] Dumoré, J.M. and Schols, R.S., "Drainage Capillary Pressure Functions and the Influence of Connate Water", SPEJ (Oct) 437-444 (1974).

[79] Efros, A. L., *Physics and Geometry of Disorder,* Mir, Moscow, (1986).

[80] Eijpe, R. and Weber, K.J., "Mini-Permeameters for Consolidated Rock and Unconsolidatad Sand", Amer. Assoc. Pet. Geol. Bull. **55**, 2, 307 (1971).

[81] Emery, L.W., Mungan, N. and Nicholson, R.W., "Caustic Slug Injection in the Singleton Field", JPT Dec 1970, 1569.

[82] Evans, A.J., Sorbie, K.S., and Clifford, P.J., "Scaling Relations for Water and Polymer Floods in Stratified Systems", AEE Winfrith Report M2143, Winfrith, UK, (1985).

[83] Fatt, I. , "The Network Model of Porous Media", Trans. AIME, **207**, 144 (1956)

[84] Fatt, I. and Dykstra, H., "Relative Permeability Studies", Trans. AIME. **192**, 249 (1951).

[85] Fatt, I. and Klikoff, W.A., "Effect of Fractional Wettability on Multiphase Flow Through Porous Media", Trans. AIME **216**, 426 (1959).

[86] Fayers, F.J. , "Extension of Stone's Method I and Conditions for Real Characteristics in Three-Phase Flow", SPE Reservoir Engineering (Nov) 437 (Also **SPE 16965**) (1987).

[87] Fayers, F.J. and Matthews, J.D., "Evaluation of Normalised Stone's Methods for Estimating Three-Phase Relative Permeabilities", SPEJ (April) 224-232 (1984).

[88] Ferrand, L.A. and Celia, M.A., "The Effect of Heterogeneity on the Drainage Capillary Pressure-Saturation Relation", Water Resources Research, **28**, 859, 1992.

[89] Firoozabadi, A., Ottesen, B., and Mikkelsen, M., "Measurements of Supersaturation and Critical Gas Saturation", SPE Formation Evaluation (Dec), (1992).

[90] Fischmeister, H. F., In *Pore Structure and Properties of Materials* (Proc. Int. Symp. RILEM/UPAC, Prague, Sept. 18-21), Part II, pp C435-C476 (1974).

[91] Fisher, L.R. and Lark, P.D., "An Experimental Study of the Washburn Equation For Liquid Flow in Very Fine Capillaries", J. Coll. Int. Sci. **69**, 486-492 (1979).

[92] Fritz, W. J. and Moore, J. N., *Basics of Physical Stratigraphy and Sedimentology*, John Wiley and Sons Inc., (1988).

[93] Geffen, T. M., Owens, W. W., Parrish, D. R. and Morse, R. A., "Experimental Investigation of Factors Affecting Laboratory Relative Permeability Measurements", Trans. AIME **192**, 99 (1951).

[94] Goddin, C.S., Craig, F.F., Wilkes, J.O, and Tek, M.R., "A Numerical Study of Waterflood Performance in a Stratified System with Crossflow", JPT (June), 765, 1966.

[95] Golshan, H., Ph.D. Thesis, University Of Manchester, UK (1979).

[96] Grimmett, G., *Percolation*, Springer-Verlag, Berlin (1989)

[97] Guin, J. A., Kessler, D. P. and Greenkorn, R. A., "Average Pore Velocities in Porous Media", Phys. Fluids, **14**, 4 (1971a)

[98] Guin, J. A., Kessler, D. P. and Greenkorn, R. A., "The Permeability Tensor for Anisotropic Non-Uniform Porous Media", Chem. Eng. Sci. , **26**, 1475 (1971b)

[99] Habesch, S. M., "Pore Geometry Evaluation by Petrographic Image Analysis", In *Microcomputer Applications in Geology* 2, Vol. 6 (eds. Hanley, J. T. and Merriam, D. F.), Pergamon Press New York (1990).

[100] Haring, R. E. and Greenkorn, R. A., "A Statistical Model of a Porous Medium with Non-Uniform Pores", AIChE J. **16**, 477 (1970).

[101] Hartkamp-Bakker, C.A., "Capillary Oil Entrapment in Crossbedded Sedimentary Structures of Fluvial Sandstone Reservoirs", **SPE 22761** presented at the 66th Annual Conference.of the SPE, Dallas, Texas, 1991.

[102] Hassler, G. L., U.S. Patent 2,345,935 (1944).

[103] Heiba, A.A., Davis, H.T. and Scriven, L.E., "Effect of Wettability on Two-Phase Relative Permeabilities and Capillary Pressures", Paper **SPE 12172** presented at the 58th Annual Conference of the SPE, San Francisco, CA, 5-8 Oct. (1983).

[104] Heiba, A.A., Sahimi, M., Scriven, L.E., and Davis, H.T., "Percolation Theory of Two-Phase Relative Permeability", Paper **SPE 11015** presented at the 57th Ann. Tech. Conf. of the SPE of AIME, New Orleans, L.A., Sept. 26-29 (1982).

[105] Henderson, G.D., Danesh, A. and Peden, J.M. (1991), "An Experimental Investigation of Waterflooding of Gas Condensate Reservoirs and Their Subsequent Blowdown", Presented at the 6th European IOR-Symposium, Stavangar, Norway, May 21-23, 1991.

[106] Hoimyr, O., Kleppe, A, and Nystuen, J., "Effects of Heterogeneities in a Braided Stream Channel Sandbody on the Simulation of Oil Recovery: a Case Study From the Lower Jurassic Statfjord Formation, Snorre Field, North Sea", from *Advances in Reservoir Geology* (ed. Ashton) Geological Society special publication No 69, 105, 1993.

[107] Holbrook, O.C. and Bernard, G.C., "Determination of Wettability by Dye Adsorption", Trans AIME **213**, 261 (1958).

[108] Holmgren, C.R. and Morse, R.A., "Effect of Free Gas Saturation on Oil Recovery by Waterflooding", Trans AIME **192**, 135 (1951).

[109] Honarpour, M., Koederitz, L., and Harvey, A.H., *Relative Permeability of Petroleum Reservoirs*, CRC Press Inc., Boca Raton, Florida (1986).

[110] Hoshen, J. and Kopelman, R., "Percolation and Cluster Distribution. I. Cluster Multiple Labelling Technique and Critical Concentration Algorithm", Phys. Rev. B **14/8**, 3438 (1976).

[111] Idris, A.K., PhD Thesis, Imperial College of Science, Technology and Medicine, UK (1990).

[112] Jadhunandan, P. and Morrow, N.R., "Effect of Wettability on Crude Oil/Brine/Rock Systems", Presented at the 66th Annual Technical Conference of SPE, Dallas, TX, Oct 6-9 (1991).

[113] Johnson, E. F., Bossler, D. P. and Naumann, V. O., "Calculation of Relative Permeability From Displacement Experiments", Trans. AIME **216**, 370 (1959).

[114] Jones, S. C. and Roszelle, W. O., "Graphical Techniques for Determining Relative Permeability From Displacement Experiments", J. Pet. Technol. **5**, 807 (1978).

[115] Kalaydjian, F. (1992), "The Spreading Coefficient, a Key Parameter Ruling the Efficiency of an Oil Recovery Process by Gas Injection in Three-Phase Flow Conditions", Presented at the 2nd International Symposium on Evaluation of Reservoir Wettability and Its Effect on Oil Recovery, Edinburgh, Scotland, 21-23 September (1992).

[116] Kalaydjian, F. and Tixier, M., "Effect of the Spreading Coefficient on Gas-Oil Capillary Pressure Curves in Presence of Connate Water", Paper presented at the 5th Annual SCA Technical Conference, San Antonio, USA, Aug 20-22 (1991).

[117] Kamath, J. and Boyer, R.E., "Critical Gas Saturation and Supersaturation in Low Permeability Rocks", SPE 26663, presented at the 68th Annual Technical Conference and Exhibition of the SPE, Houston, TX, Oct. 3-6, (1993).

[118] Kashchiev, D. and Firoozabadi, A., "Kinetics of the Initial Stage of Isothermal Gas Phase Formation", J. Chem. Phys. **98** (6), (1993).

[119] Katz, A. J. and Thompson, A. H., "Quantitative Prediction of Permeability in Porous Rock", Phys. Rev. B, **34**, 8179-8181 (1986).

[120] Katz, A. J. and Thompson, A. H., "Prediction of Rock Electrical Conductivity From Mercury Injection Measurements", J. Geophys. Research, **92**, 599-606 (1987).

[121] Katz, A. J., Thompson, A. H., and Ratschke, R. A., "Numerical Simulation of Resistance Steps for Mercury Injection Under the Influence of Gravity", Phys. Rev. A **38**, 4901 (1988).

[122] Kennedy, H.T., Burja, E.O., and Boykin, R.S., "An Investigation of the Effects of Wettability on the Recovery of Oil by Waterflooding", J, Phys. Chem. **59**, 867 (1955).

[123] Kennedy, H.T. and Guerrero, E.T., "The Effect of Surface and Interfacial on the Recovery of Oil BY Waterflooding", Trans AIME **201**, 124 (1954).

[124] Kirkpatrick, S., "Percolation and Conduction", Rev. Mod. Phys. **45**, 574 (1973)

[125] Klinkenberg, L. J., "The Permeability of Porous Media to Liquids and Gases", API Drill. and Prod. Practice, pp200ff (1941).

[126] Kokal, S.L. and Maini, B.B., "An Improved Model For Estimating Three-Phase Oil-Water Gas Relative Permeabilities From Two-Phase Oil-Water and Oil-Gas Data", J. Can. Pet. Tech. **29** (1990).

[127] Koplik, J., "On the Effective Medium Theory of Random Linear Networks", J. Phys. C., **14**, 4821 (1981).

[128] Koplik, J.,,"Creeping Flow in Two-Dimensional Networks", J. Fluid Mech. **119**, 219 (1982).

[129] Koplik, J. and Lasseter, T.J. (1982), "Two-Phase Flow in Random Network Models of Porous Media", **SPE 11014** presented at the 57th Annual Conference of the SPE, New Orleans, Louisiana, (1982).

[130] Koplik, J., Lin, C. and Vermette, M., "Conductivity and Permeability From Microgeometry", J. App. Phys. **56**, 3127 (1984).

[131] Kortekaas, T.F.M., "Water/Oil Displacement Characteristics in Cross-Bedded Reservoir Zones", SPE 12112 presented at the 58th Technical Conference of the SPE, San Francisco, (1983).

[132] Kortekaas, T.F.M. and van Poelgeest, F., "Liberation of Solution Gas During Pressure depletion of Virgin and Watered-Out Oil Reservoirs", *SPE 19693, presented at the 64th Annual SPE Fall Meeting, Oct. 8-11,* (1989).

[133] Kozeny, J., "Über Kapilläre Leitung des Wassers im Boden", Royal Academy of Science, Vienna, Proc. Class 1, **136**, 271 (1927).

[134] Kumar, J., Fatt, I., and Saraf, D.N., "Nuclear Magnetic Relaxation Time of Water in a Porous Medium with Heterogeneous Surface Wettability", J. Appl. Phys. **40**, No. 10, 4165 (1969).

[135] Kyte, J.R., Stanclift, R.J, Stephan, S.C. and Rapoport, L.A., "Mechanisms of Waterflooding in the Presence of Free Gas", Trans AIME **207**, 215 (1956).

[136] Laidlaw, W.G. and Wardlaw, N.C., "A Theoretical and Experimental Investigation of Trapping in Pore Dublets", Can. J. Chem. Eng. , **61**, 719, (1983).

[137] Lake, L. W., *Enhanced Oil Recovery*, Prentice Hall N.J., (1989).

[138] Lake, L. W., Carroll, H. B. J. and Wesson, T. C. W. (eds.), *Reservoir Characterisation II,* Academic Press Inc., (1991).

[139] Land, C.S., " Calculation Of Imbibition Relative Permeability for Two- and Three- Phase Flow From Rock Properties", SPEJ (June) , 149-156 (1968).

[140] Landauer, R. J., "The Electrical Resistance of a Binary Layer", J. Appl. Phys. **23**, 779 (1952).

[141] Larson, R.G, Davis, H.T., and Scriven, L.E., "Displacement of Residual Nonwetting Fluid From Porous Media", Chem. Eng. Sci. **36**, 75, (1981).

[142] Lenormand, R., Touboul, E. and Zarcone, C. , "Numerical Models and Experiments on Immiscible Displacements in Porous Media", J. Fluid Mech., **189**, 165, (1988).

[143] Lenormand, R. and Zarcone, C., "Role of Roughness and Edges During Imbibition in Square Capillaries", Paper **SPE 13264**, paper presented at the 59th SPE Technical Conference and Exhibition, Houston, Texas, 16-19 Sept. (1984).

[144] Leverett, M.C., "Capillary Behaviour in Porous Solids", Trans. AIME **142**, 152 (1939).

[145] Leverett, M.C., "Capillary Behaviour in Porous Media", Trans AIME **142**, 341 (1941).

[146] Leverett, M.S. and Lewis, W.B., "Steady Flow of Gas-Oil-Water Mixtures Through Unconsolidated Sands", Trans. AIME **142**, 107 (1941).

[147] Levine, J. S., "Displacement Experiments in a Consolidated Porous System", Trans. AIME **201**, 57 (154).

[148] Lin, C.Y. and Slattery, J.C., "Three-Dimensional, Randomised, Network Model for Two-Phase Flow Through Porous Media", AIChE J., **28**, 311 (1982).

[149] Longeron, D., Kalaydjian, F. and Bardon, C., "Gas-Oil Capillary Pressure Measurements at Reservoir Conditions: Effect of Interfacial Tension and Connate Water Saturation", presented at the 7th European IOR Symposium, Moscow, Russia, 27-29 Oct, (1993).

[150] Loomis, A. G. and Crowell, D. C., "Relative Permeability Studies: Gas-Oil and Water-Oil Systems", U.S. Govt. Printing Office, Bulletin 599,1,Washington D.C. (1962).

[151] MacDonald, I. F., Kaufmann, P. and Dullien, F. A. L., "Quantitative Image Analysis of Finite Porous Media. II. Specific Genus of Cubic Lattice Models and Berea Sandstone", J. Microsc. **144** 297 (1986).

[152] McDougall, S.R. and Sorbie, K.S., "Network Simulations of Flow Processes in Strongly Wetting and Mixed-Wet Porous Media", Paper presented at the 3rd European Conference on the Mathematics of Oil Recovery, 17-19 June 1992, Delft, The Netherlands.

[153] McDougall, S.R. and Sorbie, K.S., "The Prediction of Waterflood Performance in Mixed-Wet Systems From Pore-Scale Modelling and Simulation", SPE 25271 presented at the 12th SPE Symposium on Reservoir Simulation, New Orleans, Louisiana, Feb 28 - Mar 3 (1993a).

[154] McDougall, S.R. and Sorbie, K.S., "The Combined Effect of Capillary and Viscous Forces on Waterflood Displacement Efficiency in Finely Laminated Porous Media", SPE 26659, presented at the 68th Annual Technical Conference and Exhibition of the SPE, Houston, TX, Oct. 3-6, (1993b).

[155] McDougall, S.R., Sorbie, K.S. and Wu, Y.Z., paper in preparation.

[156] Manjnath, A. and Honarpour, M.M., "An Investigation of Three-Phase Relative Permeability", Paper **SPE 12915** presented at the 1984 Rocky Mountain Regional Meeting held in Casper, Wy, May 21-23 (1984).

[157] Marek, B.F., Hartman, K.J. and McDonald, A.E., " Three-Phase Relative Permeability of Limestones Having Bimodal Pore-Size Distribution " Paper SPE 21374 Presented at the SPE Middle East Oil Show , Bahrain , November 16-19 (1991).

[158] Marshall, T. J., "A Plummet Balance for Measuring the Size Distribution of Soil Particles", J. Soil Sci. **9**, 1 (1958).

[159] Mavis, F. T. and Wilsey, E. F., Eng. News Rec., **118**, 299 (1937). Op. cit. Dullien, F. A. L. (1979).

[160] Millington, R. J. and Quirk, J. P., "Permeability Of Porous Solids", Trans. Faraday Soc. **57**, 1200 (1961).

[161] Mohammadi, S., Sorbie, K.S., Danesh, A. And Peden, J.M., "Pore-Level Modelling of Gas-Condensate Flow Through Horizontal Porous Media", **SPE 20479** paper presented at the 65th SPE Annual Technical Conference and Exhibition, New Orleans, LA, 23-26 Sept. (1990)

[162] Mohanty, K. K. and Salter, S. J., "Multiphase Flow in Porous Media: II Pore-Level Modelling, **SPE 11018** presented at the 57th Annual Conference of the SPE, New Orleans, Louisiana, (1982).

[163] Mohanty, K.K. and Salter, S.J., "Multiphase Flow in Porous Media: III. Oil Mobilisation, Transverse Dispersion, and Wettability", Paper **SPE 12127** presented at the 58th Annual Conference of the SPE, San Francisco, CA, 5-8 Oct. (1983).

[164] Morrow, N.R. (ed), *Interfacial Phenomena in Petroleum Recovery*, Surfactant Science Series 36, Marcel Dekker Inc., New York (1991).

[165] Morse, R. A., Terwillinger, P. L. and Yuster, S. T., "Relative Permeability Measurements on Small Samples", Oil Gas J. **46**, 109 (1947).

[166] Moulu, J.C. and Longeron, D., "Solution Gas Drive: Experiments and Simulation", Proceedings of the 5th European Symposium on Enhanced Oil Recovery, Budapest, Hungary, 1989.

[167] Mungan, N., "Interfacial Effects in Immiscible Liquid-Liquid Displacement in Porous Media", SPEJ (Sept 1966) 247, Trans. AIME **237**.

[168] Muscat, M. and Meres, M. W., Physics 7, 346 (1936). Op. cit. Honarpour, M. et al (1986)

[169] Naar, J., and Wygal, R.J., "Three-Phase Imbibition Relative Permeability", SPEJ (Dec), 253-258 (1961).

[170] Narahara, G.M., Pozzi, A.L. and Blackshear Jr , T.H., " Effect of Connate Water on Gas/Oil Relative Permeability For Water-Wet And Mixed-Wet Berea Rock, "Paper SPE 20503 presented at the 65th Annual Technical Conference and Exhibition, New Orleans, LA, September 23-26, (1990).

[171] Nutting, P.G., "Physical Analysis of Oil Sands", Bull. Am. Assoc. Pet. Geol., **14**, 10, 1337 (1930)

[172] Nutting, P.G., "Some Physical and Chemical Properties of Reservoir Rocks Bearing on the Accumulation and Discharge of Oil", Problems of Petroleum Geology, W.E. Wrather and F.H. Lahee (eds), AAPG, Tulsa 825 (1934).

[173] Oak, M. J., "Three-Phase Relative Permeability Of Water-Wet Berea", Paper **SPE/DOE 20183** presented at the Seventh Symposium on Enhanced Oil Recovery, Tulsa, Oklahoma, April 22-25 (1990).

[174] Oak, M. J., Baker, L. E. and Thomas, D. C., "Three-Phase Relative Permeability of Berea Sandstone", Paper **SPE 17370** presented at the SPE/DOE Enhanced Oil Recovery Symposium, Tulsa, Oklahoma , April 17-20 (1988).

[175] O'Carroll, C. and Sorbie, K. S., "Generalisation of the Poiseuille Law for One- and Two-Phase Flow in a Random Capillary Network", Phys. Rev. E **47**, 3467 (1993).

[176] Odeh, A. S.,"Effect of Viscosity Ratio on Relative Permeability", Pet. Trans. AIME **216**, 346 (1959).

[177] Oren, P.E., Billiotte, J., and Pinczewski, W.V., "Mobilisation of Waterflood Residual Oil By Gas Injection For Water-Wet Conditions", **SPE 20185**, presented at the 7th SPE/DOE Symposium on Enhanced Oil Recovery, Tulsa, Oklahoma, April 22-25, (1990).

[178] Oren, P.E. and Pinczewski, W.V., "The Effect of Film-Flow on the Mobilisation of Waterflood Residual Oil by Gas Flooding", Presented at the 6th European IOR-Symposium, Stavangar, Norway, May 21-23, (1991).

[179] Owens, W.W., Parish, D. R. and Lamoreaux, W. E., "An Evaluation of a Gas Drive Method for Determining Relative Permeability Relationships", Trans. AIME **207**, 275 (1965).

[180] Owens, W.W and Archer, D.L., "The Effect of Rock Wettability on Oil-Water Relative Permeability Relationships", JPT (July 1971), Trans. AIME **251**, 873.

[181] Parker, J.C., Lenhard, R.J., and Kuppusamy, T., " A Parametric Model for Constitutive Properties Governing Multi-Phase Flow in Porous Media", Water Resources Research **23**, 618-624 (1987).

[182] Pettijohn, F. J. and Potter, P. E., *Atlas and Glossary of Primary Sedimentary Structures*, Springer-Verlag, New York, 1964.

[183] Purcell, W. R., "Capillary Pressures — Their Measurement Using Mercury and the Calculation of Permeability Therefrom", Trans. AIME **186**, 39-48 (1949).

[184] Rapoport, L.A., "Scaling Laws for Use in Design and Operation of Water-Oil Flow Models", Trans AIME **204**, 143, 1955.

[185] Reid .S.: " The Flow Of Three Immmmiscible Fluids in Porous Media." PhD Dissertation. U. of Birmingham U.K (1956).

[186] Richardson, J. G., Kerver, J. K., Hafford, J. A. and Osoba, J. S., "Laboratory Determination of Relative Permeability", Trans. AIME **195**, 187 (1952).

[187] Ringrose, P. S., Sorbie, K. S., Feghi, F., Pickup, G. E. and Jensen, J. L., "Relevant Reservoir Characterisation: Recovery Process, Geometry and Scale", In Situ, **17** (1) 55 (1993a).

[188] Ringrose, P.S., Sorbie, K.S., Corbett, P.W.M., and Jensen, J.L., "Immiscible Flow Behaviour in Laminated and Cross-Bedded Sandstones", J. Pet. Sci. Eng. 9(2), 103- 1993b.

[189] Ritter, L. C. and Drake, R. L., "Pore Size Distribution in Porous Materials", Ind. Eng. Chem. An. Ed. 17, 782 (1945).

[190] Ritter, L. C. and Drake, R. L., "Macropore Size Distributions in Some Typical Porous Substanes", Ind. Eng. Chem. An. Ed. 17, 782 (1945).

[191] Rose, H. E., "An Investigation into the Laws of Flow of Fluids Through Beds of Granular Material", Proc. Inst. Mech. Eng. Appl. Mech. **153**, 5, 141 (1945).

[192] Rose, W. , Studies of Waterflood Performance, Vol. III, Use of Network Models, Illinois State Geology Survey, Circ. No. 237, Urbana, Illinois (1957).

[193] Salathiel, R.A., "Oil Recovery by Surface Film Drainage in Mixed-Wet Rocks", JPT (Oct 1973) 1216. Trans AIME, **155**.

[194] Salter, S.J. and Mohanty, K.K.,"Multiphase Flow inPorous Media: I. Macroscopic Observations and Modelling", **SPE 11017**, paper presented at the 57th SPE Annual Technical Conference and Exhibition, New Orleans, LA, 26-29 Sept. (1982).

[195] Saraf, D.N. and Fatt, I., "Three -Phase Relative Permeability Measurement Using a Nuclear Ma gnetic Resonance Technique for Estimating Fluid Saturations. " SPEJ (Sept) 235-42. Trans AIME 240 (1967).

[196] Saraf, D.N. and McCaffery, F. G., "Two- and Three-Phase Relative Permeabilities: a Review", Petroleum Recovery Institute Report #81-8, Calgary, Canada (1982).

[197] Saraf. D.N et al., "An Experimental Investigation Of Three-Phase Flow Of Water/Oil/Gas Mixtures Through Water Wet Sandstones .", Paper **SPE 10761** presented at the SPE California Regional Meeting, San Francisco, March 24-26, 1982.

[198] Saraf, D.N. and Fatt, I., "Three-Phase Relative Permeability Measurement Using a NMR Technique For Estimating Fluid Saturation", Soc. Pet. Eng. J. (Sept) 235 (1967).

[199] Sarem, A.M., " Three -Phase Relative Permeability Measurement by the Unsteady-State Method" SPEJ (Sept) 199-205: Trans AIME 237 (1966).

[200] Schechter, D.S., Zhou, D., and Orr, F.M., "Capillary Imbibition and Gravity Segregation in Low IFT Systems", presented at the 12th Workshop and Symposium of the International Energy Agency Collaborative Project on Enhanced Oil Recovery, Bath, England, Oct. 28-30, (1991).

[201] Scheidegger, A.E. , "The Physics Of Flow Through Porous Media", Univ. Of Toronto Press, Toronto, Canada (1963).

[202] Schneider, F.N and Owens ,W.W., " Sandstone and Carbonate Two and Three-Phase Relative Permeability Characteristics", Soc.Pet.Eng.J (March) 75-184 ; Trans AIME vol.249 (1970).

[203] Shankar, P.K. and Dullien, F.A.L., "Experimental Investigation of Two-Liquid Relative Permeability and Dye Adsorption Capacity Versus Saturation Relationships in Untreated and DRIFILM-treated Sandstone Samples", Surface Phenomena in Enhanced Oil Recovery, D.O. Shah (ed), Plenum Press, NY City 453 (1981).

[204] Sharma, M.M. and Wunderlich, R.W., "The Alteration of Rock Properties Due to Interactions with Drilling Fluid Components", paper **SPE 14302** presented at the 60th SPE Annual Technical Conference and Exhibition, Las Vegas, NV, 22-25 Sept. (1985).

[205] Shaw, D. J., *Introduction to Colloid and Surface Chemistry*, 2nd Edition, Butterworths and Co. Ltd., London.

[206] Shook, M., Li, D. and Lake, L. W., "Scaling Immiscible Flow Through Permeable Media by Inspectional Analysis", In Situ **16**, 4, 311, (1992).

[207] Simon, R. and Kelsey, F. J., "The Use of Capillary Tube Networks in Reservoir Performance Studies: I. Equal Viscosity Miscible Displacements", SPE J., **11** (2) , (1971).

[208] Snell, R.W, "Three-Phase Relative Permeability in an Unconsolidated Sand", J. Inst. Pet. **48**(459) (1962).

[209] Snell, R.W., "The Saturation History Dependence of Three-Phase oil Relative Permeability",: J. Inst .Pet. **49**, 81-84(March 1963).

[210] Soll, W.E., Celia, M.A., and Wilson, J. L., "Micromodel Studies of Three-Fluid Porous Media systems: Pore-Scale Processes Relating to Capillary Pressure- saturation Relationships", Submitted to Water Resources Research, (1993).

[211] Stauffer, D. and Aharony, A., *Introduction To Percolation Theory*,, Taylor and Francis, London And Philadelphia (1992).

[212] Stewart, C.R., Hunt, E.B., Schneider, F.N., and Berry, V.J., "The Role of Bubble Formation in Oil Recovery by Solution Gas Drives in Limestones", Trans AIME Vol **201**, 294-301, (1954).

[213] Stiles, W.E., "Use Of Permeability Distribution in Waterflood Calculations", Trans AIME **186**, 9-21, (1949).

[214] Stone, H.L., "Probability Model For Estimating Three-Phase Relative Permeability", JPT 22 (Feb), 214-218 (1970).

[215] Stone, H.L., "Estimation of Three-Phase Relative Permeability and Residual Oil Data", J. Can. Pet. Tech. **12**, 53-61 (1973).

[216] Szekely, J., Neumann, A.W., and Chuang, Y.K., "The Rate of Capillary Penetration and the Applicability of the Washburn Equation", J. Coll. Int. Sci. **35**, 2, 273, (1971).

[217] Thompson, A. H., Katz, A. J. and Ratschke, R. A., "Mercury Injection in Porous Media: A Resistance Devil's Staircase with Percolation Geometry", Phys. Rev. Lett. **58**, 29 (1988).

[218] Trantham, J.C. and Clampitt, R.L., "Determination of Oil Saturation After Waterflooding in an Oil-Wet Reservoir - The North Burbank Unit, Tract 97 Project", JPT (May 1977), 491.

[219] Treiber, L.E., Archer, D.L., and Owens, W.W.,"A Laboratory Evaluation of the Wettability of Fifty Oil Producing Reservoirs", SPEJ (Dec 1972) 531, Trans. AIME **253**.

[220] Tzakiroglou, R.D. and Payatakes, A.C., "A New Simulator of Mercury Porosimetry for the Characterisation of Porous Materials", J. Colloid Int. Sci., **137**, 135 (1990).

[221] Van Batenburg, D.W., Bruining, J, Bakken, H, and Palmgren, C.T.S., "The Effect of Capillary Forces in Heterogeneous "Flow "Units": a Streamline Approach", **SPE 22588** presented at the 66th Annual Conference.of the SPE, Dallas, Texas, (1991).

[222] van Spronsen. E., "Three-Phase Relative Permeability Measurements Using the Centrifuge Method", Paper **SPE 10688** Presented at the

SPE/DOE Symposium on Enhanced Oil Recovery, Tulsa April 4-7, (1982).

[223] Washburn, E.W., "The Dynamics of Capillary Flow", Phys Rev **17**, 273-283 (1921).

[224] Weber, K.J., "How Heterogeneity Affects Oil Recovery", in *Reservoir Characterisation II* (eds Lake and Carroll), Academic Press Inc., (1991).

[225] Welge, H. J., "A Simplified Method for Computing Recovery by Gas or Water Drive", Trans. AIME **195**, 91 (1952).

[226] Wilkinson, D.,"Percolation Effects in Immiscible Displacement", Phys. Rev. A., **34**, 1380 (1980).

[227] Wilkinson, D., in *Mathematics in Oil Production*, eds, S. Edwards and P. R. King, Clarendon, Oxford, 343 (1988).

[228] Wilkinson, D. and Willemsen, J.F., "Invasion Percolation: a New Form of Percolation", J. Phys. A., **16**, 3365 (1983).

[229] Woodside, W. and Messmer, J. H., "Thermal Conductivity of Porous Media. I. Unconsolidated Sands", J. Appl. Phys. **32**, 1688 (1961).

[230] Wykoff, R. D., Botset, H. G., Muscat, M. and Reed, D.W., "The Measurement of the Permeability of Porous Media for Homogeneous Fluids", Rev. Sci. Inst. **4**, 394, (1933).

[231] Wykoff, R. D. and Botset, H. G., "The Flow of Gas-Liquid Mixtures Through Unconsolidated Sands", Physics **9**, 325 (1936).

[232] Wyllie, M. R. J. and Gardner, G. H. F., "The Generalised Kozeny-Carman Equation, Its Application to Problems of Multi-Phase Flow in Porous Media", World Oil **146**, 121 (1958).

[233] Yang, S.R. and Kim, R.H., "A Mathematical Model of the Pool Boiling Nucleation Site Density in terms of the Surface Characteristics", Int. J. Heat Mass Transfer, **31**, 1127-1135 (1988).

[234] Yanuka, M., Dullien, F. A. L. and Elrick, D.E., "A Geometrical and Topological Model of Porous Media Using a Three-Dimensional Joint Pore Size Distribution", J. Coll. Int. Sci. **112**, 24 (1986).

[235] Yortsos, Y.C. and Parlar, M, "Phase Change in Binary Systems in Porous Media: Appilication to Solution Gas Drive", **SPE 19697**, paper presented at the 64th SPE Technical Conference and Exhibition, San Antonio, Texas, 8-11 Oct. (1989).

[236] Yousfi, A.E., Zarcone, C., Bories, S. and Lenormand, R., "Mecanismes de Formation d'une Phase Gazeuse par Detente d'un Liquide en Milieu Poreux", Mecanique des Fluides (1991).

[237] Ypma, J.G.J., "Analytical and Numerical Modelling of Immiscible Gravity-Stable Gas Injection into Stratified Reservoirs", **SPE 10109** presented at the SPE Fall Meeting, San Antonio, (1983).

[238] Zapolitsky, J. G., "Monte Carlo Evidence Against the Alexander-Orbach Conjecture for Percolation Conductivity", Phys. Rev. B 30, 4077 (1984).

"The sun is a gigantic nuclear power station which radiates energy in the form of sunshine. When we burn coal and oil we are using up part of the solar radiation which was received by the earth many millions of years ago, converted into chemical energy by photosynthesis, and in part stored up as natural fuels. We are, in fact, living at an alarmingly extravagant rate on an inheritance of capital that cannot be renewed. The present accelerating rate of consumption of energy per head of the world population, which itself is explosively increasing, stands high amongst the many causes of anxiety and embarrassment for the future well-being of our race."

Arthur Holmes, from *Principles of Physical Geology*, 1965.

Visual Monitor and Printer Check

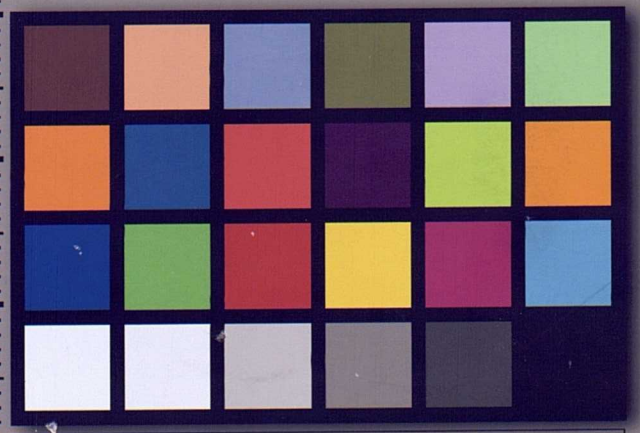

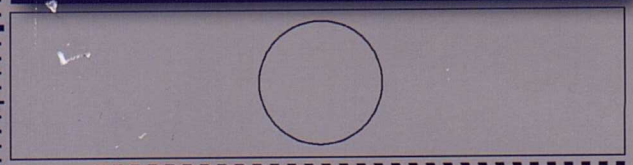

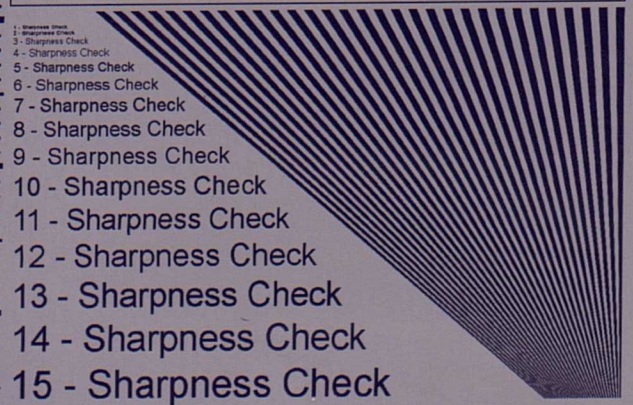

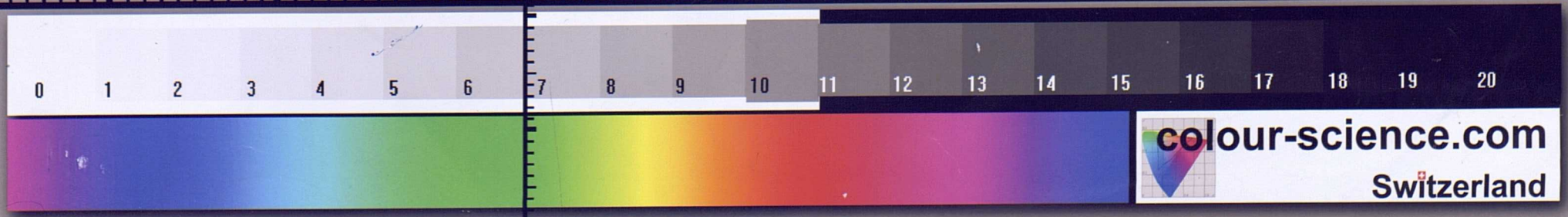

colour-science.com

Switzerland